The Tropical Tropopause

Amanda Marie Kerr-Munslow

Brasenose College

University of Oxford

A thesis submitted to the Faculty of Physical Sciences for the degree of Doctor of Philosophy at the University of Oxford.

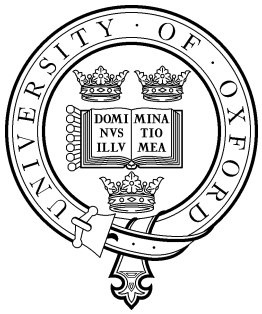

Trinity Term, 2004

Atmospheric, Oceanic and Planetary Physics

Department of Physics

University of Oxford

The Tropical Tropopause

Amanda Kerr-Munslow, Brasenose College, University of Oxford
Submitted for the degree of Doctor of Philosophy, Trinity Term 2004.

Abstract

The annual cycle in lower stratospheric tropical temperatures is examined using ECMWF re-analysis fields and UK Met Office Unified Model data in order to find the processes driving the large annual cycle (changes of over 8 K near 90 hPa) at the tropical tropopause.

By examining the balances in the transformed Eulerian mean (TEM) thermodynamic equation, it is shown that changes in adiabatic cooling caused by changes in vertical motion are driving the changes in temperature. Then, by considering the mass continuity equation, it is shown that changes in tropical mass divergence local to the tropical tropopause have a dominant influence on the annual cycle in vertical motions near the tropical tropopause.

By considering the TEM momentum equation, it is shown that these changes in mass divergence are predominantly caused by Eliassen-Palm flux (EP flux) divergence at the edges of the tropics. Furthermore, it is shown that stationary waves with zonal wavenumbers greater than three are responsible for the changes in EP flux. It is shown that both horizontal and vertical components of EP flux divergence and both northern and southern contributions are important.

By examining the longitudinal distribution of the eddy flux components of the EP flux divergence and comparing this with the stream function, it is shown that the annual cycle in the EP flux divergence is linked to the annual cycle in the upward extension of the monsoon circulations.

The monsoon anticyclones are nearly symmetric about the equator in northern hemisphere winter whereas the Asian monsoon anticyclone in northern hemisphere summer is pushed well off the equator. The changes in the monsoon circulations over the course of the year affect the stationary wave structure in the tropical lower stratosphere, giving an annual cycle in EP flux divergence in the tropics.

The monsoon circulations in the Unified Model data are less tightly bound to the equatorial regions, giving a less strong annual cycle in EP flux divergence.

Acknowledgements

I would like to thank my supervisors, Warwick Norton, David Andrews and Vicky Pope for their support, advice and encouragement, especially my main supervisor, Warwick.

Thank you to Alan Iwi for help with the ECMWF data and advice on optimising the processing of the data and Nathan Gillett for help with modifications to the Unified Model to obtain Eliassen-Palm flux diagnostics,

Thank you to David Tan, Alison Pamment and Rachel Stratton of the Met Office for their assistance with using the Unified Model and to Stuart Webster of the Met Office for advice on the use and meaning of gravity wave diagnostics in the Unified Model.

Many thanks are due to my friends in Oxford and in Guiding for their support, encouragement and provision of chocolate and hugs, as required.

The greatest thanks are due to Ganesh Sittampalam and my family for their continuing support and love, in many different ways, and without whom I most probably would not have come this far.

The D. Phil. was funded by the Natural Environment Research Council and sponsored by the UK Met Office.

Contents

Chapter 1

Introduction

1.1 Overview

This research is an investigation of the causes of the annual cycle in tropical tropopause and tropical lower stratosphere temperatures. The tropical tropopause region is a key region for exchange between the troposphere and the stratosphere. The processes affecting troposphere-stratosphere exchange are not fully understood, including the effects due to variability of the tropical tropopause region. The tropical tropopause has an annual cycle in temperature and height; it is colder and higher in northern hemisphere winter than summer. There have been a number of theories as to what causes this annual variation, including variations in convection and in upwelling driven by wave-breaking. This research investigates this annual cycle in temperature, looking at the possible driving by wave-breaking in a different way to previous authors.

In section 1.2 the troposphere, stratosphere and tropopause will be described, including the annual cycle seen in the tropical tropopause region. In section 1.3 exchange between the stratosphere and troposphere will be discussed, showing the importance of the tropopause for exchange. Section 1.4 describes the current understanding of the annual cycle in the tropical tropopause. Finally, the aims and layout of this thesis are described in section 1.5.

1.2 The troposphere, stratosphere and tropopause

The troposphere is the lower-most region of the atmosphere where the temperature decreases with altitude at a nearly constant lapse rate. At the upper boundary of this region is the "tropopause"—a region of temperature minimum marked by a sharp change in the lapse rate. Above the tropopause the temperature is nearly constant and then increases with altitude in the stratosphere. The tropopause is at an altitude of about 16–18 km near the equator, 10–13 km in mid-latitudes and 8–10 km near the poles.

Figure 1.1 shows a pressure against latitude cross-section of the time mean zonal mean temperature from 22 years of analysis data from the European Centre for Medium Range Weather Forecasts (ECMWF). The potential temperature is plotted using solid contours. The temperature is at a minimum in the tropics near 100 hPa, i.e. in the tropical tropopause region. The 380 K potential temperature isentrope lies within this region.

The troposphere is characterised by convective overturning with baroclinic forcing in the extra-tropics. Convection is deeper in the tropics. One definition of the troposphere is as a region where the atmosphere has been in recent contact with the boundary layer (near the Earth's surface) through convection or rapid vertical motion (Shepherd, 2002; Gettelman and Forster, 2002). Transport timescales are relatively fast, ranging from hours for convectively driven transport to a few days for baroclinically driven transport (Holton *et al.*, 1995). Stability to vertical displacements is weak and heat transfer is turbulent and rapid. Chemicals are rapidly mixed from the surface throughout the troposphere due to the fast transport timescales. There are low mixing ratios of ozone and high mixing ratios of water vapour. There is mean upwelling in the tropics and downwelling in the extra-tropics (with the strongest descent at latitudes of 25–30° in the winter hemisphere (James, 1994)). This is the Hadley circulation and is driven by latitudinal gradients in thermal forcing (Held and Hou, 1980; Plumb, 2002). There are also zonal circulations due to non-uniform heating. Air rises at longitudes of heating, for example over Indonesia, and sinks at longitudes of cooling, for example over the east Pacific (Salby, 1996). These circulations are called Walker circulations.

In contrast, the stratosphere is close to dynamical and radiative equilibrium with perturbations from this equilibrium due to external forcings, such as from

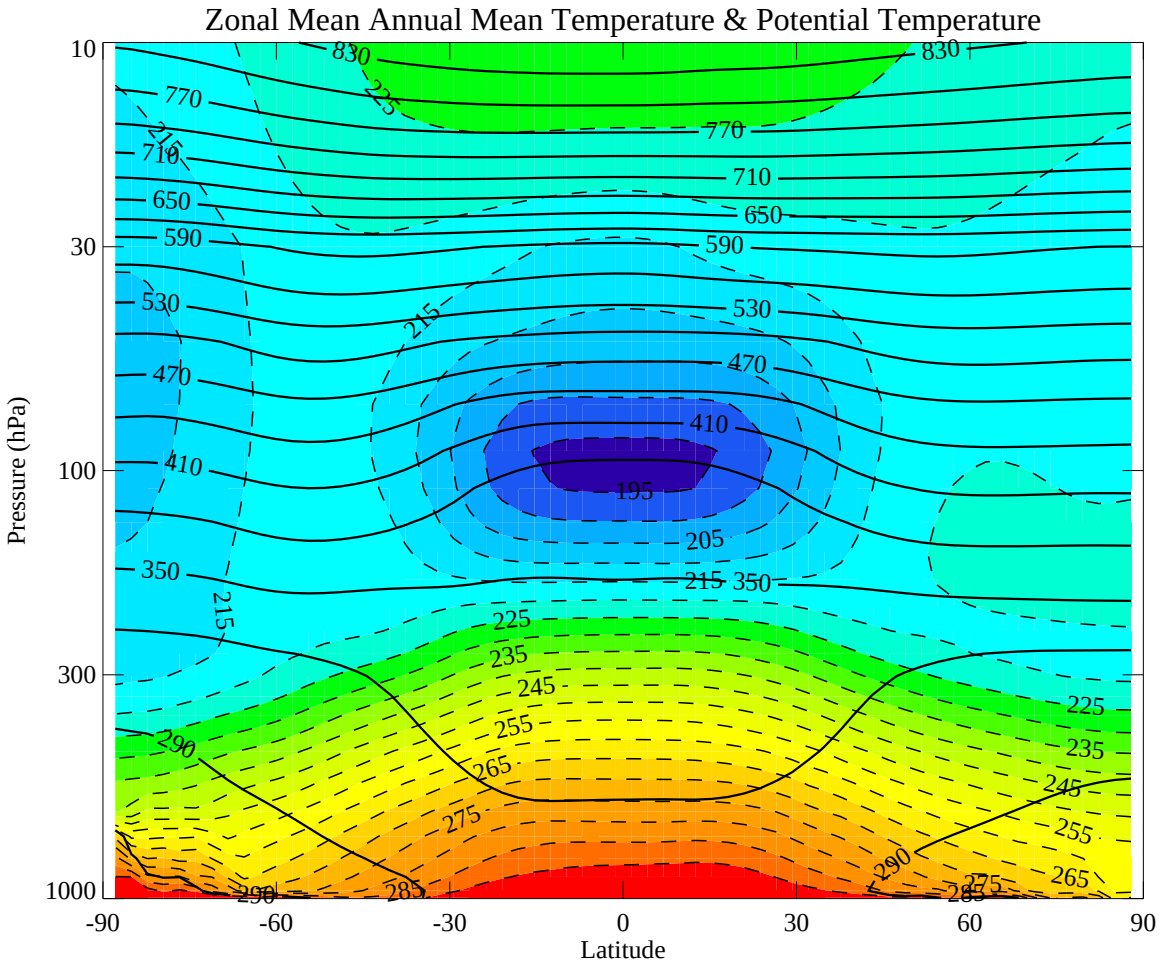

Figure 1.1: Pressure-latitude cross-section for the time average of 22 years of ECMWF analysis data. The dashed contours with colour filling represent temperature, with a contour interval of 5 K, and the solid contours represent potential temperature, with a contour interval of 30 K (after Holton *et al.*, 1995).

waves propagating up from the troposphere (Shepherd, 2002). There is a slow wave-driven circulation from planetary-scale Rossby waves, which drive an equator-to-pole mass circulation (Andrews *et al.*, 1987; Holton *et al.*, 1995), with upwelling in the tropics and downwelling in the extra-tropics. This is the Brewer-Dobson circulation. Heating is internal, by the absorption of solar radiation by constituents such as ozone. Longwave cooling then responds to the change in temperatures forced by the vertical motion. Static stability is much greater in the stratosphere than the troposphere, determined by radiative equilibrium. It is strongly stable due to the vertical distribution of ozone heating (Shepherd, 2002). Vertical velocities are much less in the stratosphere than the troposphere and transport timescales are months to years in the stratosphere compared with days to months in the

troposphere. This contrast in transport timescales can be seen in the spatial distribution of many chemical species. For example, there is a rapid increase in ozone mixing ratio and a rapid decrease in water vapour mixing ratio with height above the tropopause (Holton *et al.*, 1995).

Although the dynamics of the troposphere and stratosphere are inseparable (Holton *et al.*, 1995), the chemical compositions and thermal structures are distinguishable and it is still useful to consider them separately.

The tropopause is the boundary between the well-mixed, turbulent troposphere and the stably stratified stratosphere. Traditionally this has been thought of as a thin layer, which may be appropriate for the extra-tropics but is less appropriate in the tropics. Recently the concept of a "tropical tropopause layer" (TTL) has been discussed. Various different tropopause definitions give different heights for the tropopause, highlighting different properties, and the TTL encompasses a transition zone between different tropopause definitions based on different physical processes.

The World Meteorological Organisation (WMO) definition of the tropopause is "the lowest level at which the temperature lapse rate decreases to $2\,\mathrm{K\,km^{-1}}$ or less and where the average lapse rate between this level and all higher levels within the next 2 km does not exceed $2\,\mathrm{K\,km^{-1}}$" (Holton *et al.*, 1995). This characterises the tropopause by an increase in static stability from the troposphere to the stratosphere. This is the most commonly used definition and gives a tropical tropopause height of approximately 16–17 km (Reid and Gage, 1985). However, this is not the only possible definition of the tropopause. The transition from tropospheric lapse rates to stratospheric ones can extend over several kilometres in the vertical, as opposed to the specific height suggested by this definition (Bethan *et al.*, 1996).

The temperature minimum is an obvious, easy to identify point, especially in the tropics. It is important for Stratosphere-Troposphere Exchange (STE), determining the amount of freeze-drying of air entering the stratosphere (Selkirk, 1993). The temperature minimum or "cold point" definition gives a tropical tropopause height usually higher than that of the lapse-rate, between about 16 and 18 km (Highwood and Hoskins, 1998; Gettelman and Forster, 2002). In assimilated data with limited vertical resolution the tropopause may be between different levels depending on the definition used. The exact choice of levels used is significant as to whether the lapse-rate tropopause and temperature minimum are between the same levels, and the interpolation method used can affect the properties

of these surfaces (Highwood and Hoskins, 1998). The temperature minimum tropopause definition is only reliable when the lower stratosphere is not close to being isothermal, i.e. within the deep tropics (Highwood and Hoskins, 1998). Satellite measurements also have problems resolving the temperature minimum (SPARC Report 3, 2002).

The top of the convective-heating region indicates the top of the active troposphere. This can be considered to be more physically meaningful than the lapse-rate tropopause because it indicates the top of the rapid dynamical overturning of the troposphere. Observationally, the top of the Hadley circulation is at about 150 hPa or 13 km (James, 1994). In a simple radiative-convective model the top of the convection is lower than the lapse-rate tropopause by about 1-2 km and lower than the temperature minimum by about 3-4 km (Thuburn and Craig, 1997; Forster *et al.*, 1997).

The 100 hPa surface is used as a proxy for the tropical tropopause because it is a level directly available from models, though this definition can produce problems. Frederick and Douglass (1983) showed that using 100 hPa temperatures as a proxy for the tropopause gave different stratospheric water vapour mixing ratios to those of the true tropopause. Because the tropopause can be anywhere between 75 and 130 hPa, the 100 hPa surface can be in the troposphere at some times and the stratosphere at others (Reid and Gage, 1985). The time average of an atmospheric variable calculated at 100 hPa would then be including both tropospheric and stratospheric properties.

The 380 K potential temperature isentrope in the annual mean corresponds approximately to the annual mean tropical tropopause, with the 2 Potential Vorticity Units (PVU) potential vorticity surface corresponding approximately to the extra-tropical tropopause (Holton *et al.*, 1995). Danielsen (1968) discusses a definition based on a large gradient in potential vorticity (PV). He showed that PV gives a good indication of air of recent stratospheric origin and that a PV based tropopause definition can be more useful than the thermal lapse rate definition. Using a PV gradient eliminates the problem of the lapse rate definition tropopause moving erratically between different stable layers when waves propagate through the atmosphere. Tropospheric values of PV are typically below 1.5 PVU, jumping to stratospheric values of more than 4 PVU at the tropopause (Hoskins *et al.*, 1985). However, it is hard to map tropopause folds when using the PV gradient definition (Danielsen, 1968). The 2 PVU tropopause definition is useful in high latitudes and can be used to within 10° of the equator, but not in the deep tropics

where the PV surfaces are nearly vertical (Highwood and Hoskins, 1998).

Transport timescales are much longer in the stratosphere than the troposphere, such that even weak chemical processes can occur in the stratosphere giving a chemical ageing effect. This is reflected in the distributions of many chemical species, so that the tropopause is sometimes defined by the change in chemical composition (Shepherd, 2002). For example, the ozone concentration sharply increases from the troposphere to the stratosphere and Shepherd (2002) shows that the meridional gradient of N_2O has a sharp change at the mid-latitude tropopause on the 320 K isentrope.

Bethan *et al.* (1996) proposed a tropopause based on ozone concentration. This was based on the much higher ozone concentration in the stratosphere than the troposphere and the sharp increase in the concentration gradient at the base of the stratosphere. Their ozone tropopause was usually near or below to the WMO tropopause. They showed that it can have advantages over the WMO definition in locations where the WMO tropopause is not particularly well defined, such as near jet streams and in winter high latitudes.

The clear-sky radiative tropopause (CSRT) is a possible radiative-dynamical tropopause. This is the transition between the tropospheric balance between clear-sky radiative cooling and convective heating and the stratospheric balance between clear-sky radiative heating and adiabatic cooling from upwelling. Rather than these two regimes overlapping, the CSRT is sharpened due to a rapid decrease of convective outflow and rapid increase of background upwelling with altitude (Haynes and Shepherd, 2001).

Thuburn and Craig (2000) note that most of the definitions of the tropopause are empirical in nature due to a lack of physical understanding of the tropopause. They suggest one physically based definition as the separation of two regions with qualitatively different heat budgets.

The justification for using definitions such as those above is that the tropopause behaves, chemically speaking, as a material surface over timescales of a few days (Holton *et al.*, 1995; Thuburn and Craig, 1997). The various definitions of the tropopause provide a range of altitudes in the tropics. In these latitudes the troposphere is at similar altitudes to the mid-latitude stratosphere. In some studies multiple tropopause levels have been found, indicating the possibility of a tropopause transition zone (Highwood and Hoskins, 1998). Chemically, the tropopause in the tropics does not behave like a material surface but more like a transition zone (Gettelman *et al.*, 2002, and references therein). In this transition

zone the air has not come into contact with the surface of the Earth recently, unlike tropospheric air, but it has chemically aged to some extent—though less so than stratospheric air (Shepherd, 2002). The tropical tropopause layer can be defined as a transition region between the convective equilibrium of the troposphere and the radiative equilibrium of the stratosphere (Gettelman *et al.*, 2001). It is the region between the main convective outflow or lapse rate minimum (at 10–12 km) to the temperature minimum or cold point (at 16–17 km) (Gettelman and Forster, 2002). Below the TTL the tropical troposphere is dominated by convection. Above the TTL in the stratosphere, adiabatic cooling from upwelling and radiative heating are important. In the TTL convection, radiation and large-scale upwelling are all important (Thuburn and Craig, 1997) and there is a transition between the tropospheric and stratospheric regimes (Shepherd, 2002). However, from the CSRT point of view, the TTL lies entirely within the stratosphere and does not have a radiative-dynamical significance (Haynes and Shepherd, 2001). Thuburn and Craig (2002) defined the TTL as a region where radiation is more important than convection, but convection more important than chemical production of ozone.

There is a strong annual cycle in the temperature of the atmosphere in the tropical tropopause region (Reid and Gage, 1981; Yulaeva *et al.*, 1994; Holton *et al.*, 1995; Highwood and Hoskins, 1998). Figure 1.2 shows the anomaly in the annual cycle of the zonal mean temperature at the equator for 22 years of ECMWF analysis data. There is a large annual cycle near the tropopause, between 120 and 50 hPa. This annual cycle is a maximum at 70 hPa, with temperatures reaching 5.1 K above the mean in northern hemisphere (NH) summer and 3.6 K below the mean in NH winter (an 8.7 K variation). At 90 hPa the temperature anomalies vary between -2.6 K and 4 K (a 6.6 K variation), with a 4 K variation at 100 hPa. For comparison, Randel *et al.* (2002) (figure 1) shows a 6 K variation in temperature over the year for 10°N–10°S at 68 hPa, which is a smaller variation than the one shown here. They show a 4 K variation at 100 hPa which compares well with that of this data but both are smaller than the 5 K variation seen for the tropics in Reid and Gage (1996) (figure 4a). SPARC Report 3 (2002) (figure 24) shows the annual cycle in equatorial temperatures for 100 hPa. It shows that ECMWF assimilated data agrees well with radiosonde observations in terms of both temperature values and annual variation (about 4 K), whereas other assimilated data sets such as those of the US National Centers for Environmental Prediction (NCEP) and the UK Met Office have the correct annual variation but overestimate the temperatures by 2–3 K.

Annual cycles in the height of the tropopause have also been noted, being about 1-2 km higher in NH winter than NH summer (Staley, 1962; Cole, 1975; Reid and Gage, 1981). The annual cycle in this region will be discussed further in section 1.4.

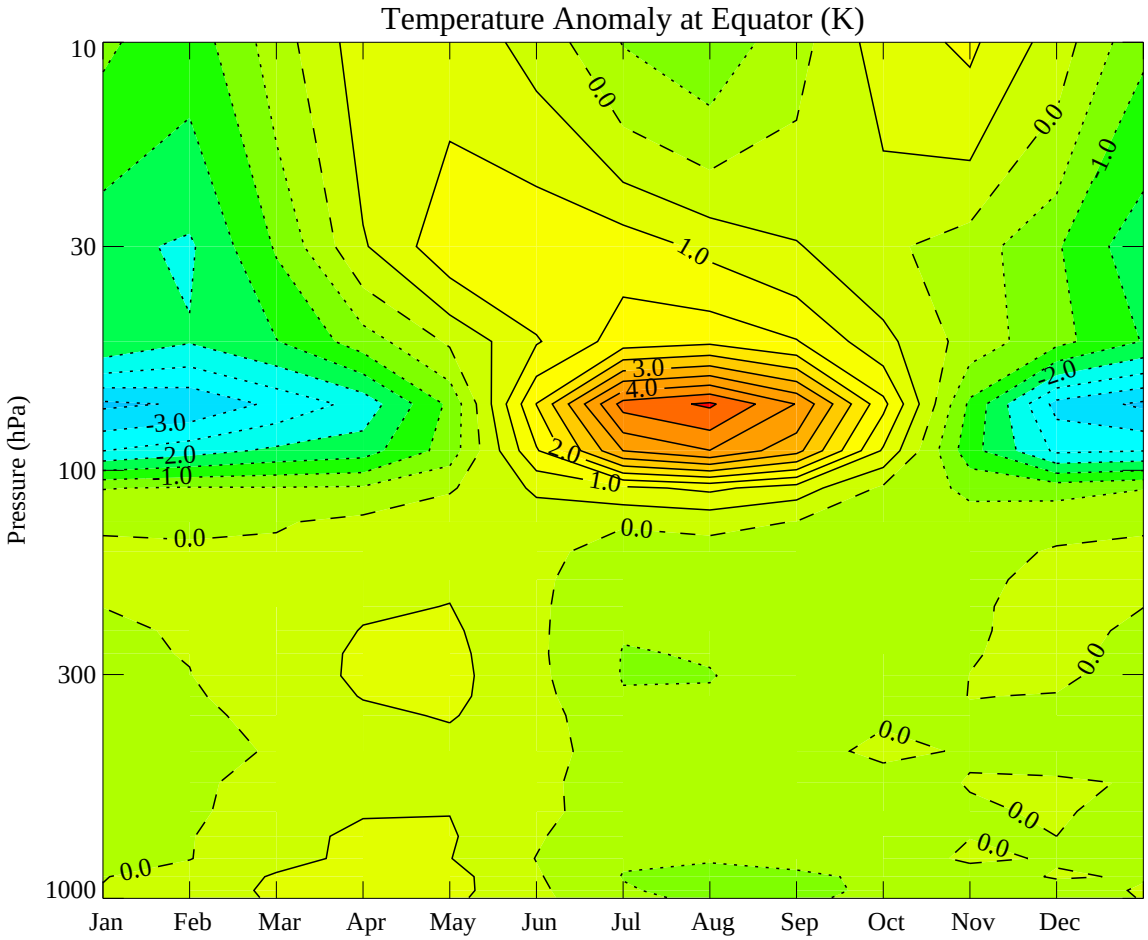

Figure 1.2: The mean annual cycle of the zonal mean temperature anomaly at the equator. The contour interval is 0.5 K. Solid contours indicate positive anomalies, dashed contours indicate zero anomaly and dotted contours indicate negative anomalies.

At higher altitudes, a different temperature structure can be seen in figure 1.2. There is a semi-annual cycle in the temperatures from 20 hPa upwards. This implies that different processes may be responsible for the temperature structure at these levels, however the resolution of the data is poor at these higher levels.

The tropopause region is important because of the coupling between the troposphere and stratosphere. The processes involved in this coupling need to be understood for the prediction of global change (Holton *et al.*, 1995). Stratosphere-

troposphere exchange will be discussed further in section 1.3.

The climatological mean structure and position of the tropopause is determined by radiative-convective adjustment in the tropics and additionally by synoptic scale baroclinic eddies in the extra-tropics (Holton *et al.*, 1995). This balance can be affected by changes to properties of either the troposphere or the stratosphere and by STE.

1.3 Stratosphere-troposphere exchange

As previously mentioned, the tropopause region is important because of the coupling between the troposphere and lower stratosphere. This coupling is dynamical, chemical and radiative. Chemical and radiative timescales are relatively long so that dynamical forcings including chemical transport and adiabatic cooling are important. As a result, temperature is very sensitive to changes in radiative heating rates and chemical concentrations are affected by the slower chemical processes (Haynes and Shepherd, 2001). The processes feed back on each other; changes in the transport of chemical species will influence the chemical composition of the middle atmosphere, which will influence the thermal structure and therefore the radiative coupling between the troposphere and stratosphere. Changing the thermal structure, the temperature profile and thermodynamics of the troposphere and stratosphere may influence the general circulation in these regions and therefore influence transport of chemical species (Andrews *et al.*, 1987). It is not just the transport across the tropopause which is important, the rate at which air is moved to and from regions of chemical sources and sinks is important as well (Holton *et al.*, 1995).

Understanding the processes of stratosphere-troposphere exchange is important because these processes may be affected by climate change. For example, there has been an increase in stratospheric water vapour which cannot be explained by increases in methane or changes in tropical tropopause temperatures (Gettelman *et al.*, 2001; Shepherd, 2002). Total hydrogen is approximately conserved in the stratosphere (Sherwood and Dessler, 2001). Ozone and water vapour are both present in the tropopause region, allowing production of the OH radical which is important in chemistry relevant to climate change (Haynes and Shepherd, 2001). Water vapour is also important in the stratosphere, affecting the radiative balance and ozone chemistry. For these reasons, being able to understand and predict the variability of water vapour entering the stratosphere is important. How chemicals

which are released at the surface, by anthropogenic causes such as industry or by natural causes such as volcanic eruptions, will be transported to other regions of the atmosphere is of interest. For example, a volcanic eruption causes enhanced aerosol concentrations in the tropical lower stratosphere which lead to local heating and enhanced tropical upwelling in the short term followed by higher tropopause temperatures and increased stratospheric water vapour on longer timescales (Shepherd, 2002). How anthropogenic ozone destroying chemicals reach the ozone layer in the stratosphere has also been cause for concern. The tropical lower stratosphere is very close to radiative equilibrium, so small changes in the diabatic heating can have significant effects on adiabatic upwelling and thus the distribution of chemical species across the globe (Olaguer *et al.*, 1992).

Holton *et al.* (1995) discuss possible routes for STE, including adiabatic transport along isentropes, which cross the steeper part of the tropopause in the subtropics, and diabatic transport across isentropes. These exchanges can be in either direction. The global circulation gives large scale ascent in the tropics and descent in the extra-tropics. Smaller scale processes for transport may include tropopause folding in the subtropics, overshooting tropical convection and turbulent eddies. The large scale, global circulation is useful for understanding chemical species with sources and sinks far from the tropopause, whereas for species with sources near the tropopause the smaller scale processes need to be considered. In the stratosphere the chemical compositions of the tropics and extra-tropics are different, which indicates that there is little exchange between the tropics and extra-tropics in this region. There is a strong correlation between global-scale vertical velocity and chemical mixing ratios in each of the tropics and extra-tropics, which indicates the importance of the global, mean meridional circulation.

It is generally accepted that the tropical tropopause region is the source region for the majority of the air entering the stratosphere (Callis *et al.*, 1987; Holton *et al.*, 1995; Highwood and Hoskins, 1998; Gettelman *et al.*, 2002, and others). Brewer (1949) showed that the amount of water vapour entering the stratosphere is determined in the tropical tropopause region. Upward transport from the surface to the tropopause in the tropics is due to ascent in deep convective clouds. However, the balance of processes which regulate STE across the tropical tropopause is uncertain (Gettelman *et al.*, 2001). The stratosphere is dry with a water vapour mixing ratio of less than three parts per million by volume (ppmv). The tropical upper troposphere has typical mixing ratio values of ten ppmv. Given the lack of sinks for water vapour in the stratosphere, the air must be dried before it enters

the stratosphere (Highwood and Hoskins, 1998).

Water is a chemical species which is a very important atmospheric constituent. Convective latent heat release from the condensation of water vapour plays a major part in driving the large scale circulation in the tropics (Zhang, 1993). Water vapour provides a good monitor of dynamical effects at low temperature, such as those in the lower stratosphere, because its saturation is strongly dependent on temperature. The hydrogen budget in the middle atmosphere is made up of water vapour, methane and molecular hydrogen. This budget is useful in monitoring motions and conditions in the middle atmosphere (Jackson *et al.*, 1998).

There have been various mechanisms hypothesised as to how moist tropospheric air may be dehydrated to produce the low mixing ratios of the stratosphere. Danielsen (1982) hypothesised that tropical cumulus or cumulonimbus clouds, which have vigorous deep convection, can penetrate above the tropopause level. Evidence for this was provided in Danielsen (1993). This overshooting of clouds mixes moist tropospheric air into the stratosphere. The water vapour in the moist air freezes into ice crystals at these very cold temperatures. Radiative overturning allows the ice crystals to grow so that they become too heavy and fall out of the cloud and down into the troposphere before they can sublime. Thus the air is dried. However zonally averaged tropical tropopause temperatures are not cold enough to freeze-dry the air to give the lower stratospheric water vapour mixing ratios which have been observed (Russell *et al.*, 1993). Newell and Gould-Stewart (1981) hypothesised that ascent from the troposphere to the stratosphere occurred in limited regions, which were cold enough to freeze-dry the air. However, the results of the Stratosphere-Troposphere Exchange Project (STEP) (Russell *et al.*, 1993) show that there wasn't sufficient cirrus cloud or cold enough temperatures at these locations. The STEP results imply that dehydration occurs on a convective scale, with ice crystals sedimenting out of the top of overshooting convective clouds as hypothesised by Danielsen (1982), although with a lower minimum temperature, and this occurs regionally, over Australia rather than the west Pacific suggested by Newell and Gould-Stewart (1981). Holton and Gettelman (2001) and Plumb (2002) suggest that horizontal transport may allow air parcels to pass through the coldest parts of the atmosphere, causing dehydration in locations other than where the air entered the stratosphere and even in locations of local downward motion. There are several possible processes which could cause the freeze-drying of the air and this subject is still widely debated.

The amount of water vapour entering the stratosphere varies over the course

of the year by this freeze-drying effect (Mote *et al.*, 1996). Because of slow ascent and slow mixing in the stratosphere, this gives a signal of alternately high and low water vapour on a vertical profile of tropical stratospheric air. The signal is retained by the air parcels as they rise through the stratosphere for up to 18 months, giving a "tape recorder" signal. Understanding how the annual cycle in water vapour is driven is important for predicting changes in the hydrogen budget in the stratosphere. The amount of freeze-drying of the air is controlled by the temperatures where the water vapour enters the stratosphere. A better understanding of how the annual cycle in tropical tropopause temperature is driven may help to understand the annual cycle and processes of dehydration of air entering the stratosphere.

1.4 The annual cycle

As previously mentioned, there is a strong annual cycle in the temperature of the atmosphere in the tropical tropopause region and an annual cycle in the height of the tropopause, giving a colder, higher tropopause in NH winter. Various theories have been put forward to explain this.

Reed and Vlcek (1969) hypothesised that the annual cycle in temperatures was driven by changes in the intensity of the NH Hadley cell, with stronger upwelling causing increased adiabatic cooling. The Hadley circulation of the NH is more intense in NH winter than summer, possibly due to changes in the thermal contrast in the tropics due to heating of the land surfaces. Reid and Gage (1981), using the lapse rate definition of the tropopause, hypothesised that the annual cycle in tropopause heights was a response to changes in tropical sea surface temperature (SST) forced by an annual cycle in absorbed solar radiation; this annual cycle in solar radiation being due to the ellipticity of the Earth's orbit. Changes to the SST affects the humidity of the troposphere and thus heating by latent heat release. The subsequent annual cycle in deep cumulus convection combined with the annual cycle in the intensity of the Hadley circulation causes the annual cycle in tropopause height. Reid and Gage (1985) however showed that tropopause temperatures and heights did not have the same relationship at all tropical locations, with temperatures being more sensitive to local conditions. Gage and Reid (1987) showed that tropopause heights were maintained far from the centers of enhanced convection which determine that height, but temperatures increased away from the centres of enhanced convection. Gray and Dunkerton

(1990) and references therein suggested that the annual cycle in temperatures may be a response to gravity wave drag above the NH winter jet stream. Rosenlof (1995) argued that although the timing of the SST minimum and lower stratosphere temperature maximum coincided, the timing of the SST maximum and lower stratospheric temperature minimum did not, implying that it was not a direct effect of SSTs which forced an annual cycle in tropical upwelling.

A different theory is that of "downward control" (Haynes *et al.*, 1991). The residual mean vertical velocity at a given location is controlled by the eddy-induced mean zonal force above that location and by the latitudinal gradient of that force. The extra-tropical/subtropical stratosphere has a non-local effect on the tropical stratosphere by means of the "gyroscopic pump" (McIntyre, 2000). The "gyroscopic pump" has also been referred to as a "stratospheric" or "extra-tropical" pump (Holton *et al.*, 1995; Plumb and Eluskiewicz, 1999) because the driving takes place in the extra-tropical stratosphere. It has also been called the "Rossby wave pump" (Plumb, 2002) although gravity waves may contribute to the driving (Yulaeva *et al.*, 1994; Rosenlof, 1995). Dissipating eddies from breaking Rossby waves and gravity waves cause one-sided forcing due to the rotation of the Earth. This causes air parcels in the extra-tropical stratosphere and mesosphere to move poleward across angular momentum surfaces. The poleward flow is compensated for by drawing air upwards from the tropical lower stratosphere. Thus the extra-tropical/subtropical stratosphere and mesosphere act as a global scale suction pump, removing air from the tropical lower stratosphere. Variations in the strength of the eddy dissipation can lead to variations in the strength of the gyroscopic pump. As more air is pulled upwards, adiabatic cooling of the rising air decreases the temperatures below their radiative equilibrium values (Holton *et al.*, 1995). As the strength of the gyroscopic pump changes, the temperature and height of the tropical tropopause change. "Downward control" has also been called "non-local control" because the driving is not near to the parts of the atmosphere it affects.

Rosenlof and Holton (1993) showed reduced wave activity in SH winter compared with NH winter, to give smaller stratosphere-troposphere mass exchange in SH winter. Rosenlof (1995) suggested that this was due to asymmetries in wave-breaking of planetary-scale waves in the middle and upper stratosphere between the two hemispheres. The forcing of planetary waves in the winter stratosphere is due to orography and contrasts between land and sea surfaces. In the NH these are more effective at forcing such waves (Yulaeva *et al.*, 1994). Wave activity

is also stronger in winter than summer. Thus, there is more wave activity and Eliassen-Palm flux divergence (a measure of wave activity) in NH winter. This gives a stronger gyroscopic pump during NH winter and a corresponding cooler, higher tropopause.

For sufficiently long time averages and large horizontal scales, downward control can estimate the mean meridional residual circulation in the lower stratosphere (Rosenlof and Holton, 1993). Haynes *et al.* (1991) showed that the residual mean vertical velocity at a given level is controlled entirely by the vertical momentum flux across that level and its latitudinal derivative. Rosenlof and Holton (1993) restated this in terms of the mean mass flux across a pressure level being controlled exclusively by dynamical processes above that level. Haynes *et al.* (1991) showed that being able to estimate the vertical velocity at a particular level to within 20% requires information about the dynamics, such as the mean meridional horizontal velocity, for two to three scale heights above that level for most of the globe. At tropical tropopause heights (about 18 km or 100 hPa), information up to 40 km will give a reasonable estimate for the vertical velocity at 100 hPa over most of the globe, but information up to 50 km or 1 hPa will give an accurate estimate (Rosenlof and Holton, 1993).

However, the downward control principle only holds where angular-momentum surfaces span the atmosphere vertically (Haynes *et al.*, 1991). In the tropics, angular-momentum surfaces cannot always span the atmosphere in the vertical and so the downward control principle does not apply. It is only for latitudes greater than 15° that angular-momentum surfaces satisfy this condition for all seasons (Rosenlof and Holton, 1993) and care needs to be taken as to how downward control calculations are done between 15° and 30°. Plumb and Eluskiewicz (1999) however suggest that this extratropical forcing is insufficient to produce the tropical upwelling observed and that it is wave pumping within the tropics which influence tropical upwelling.

Yulaeva *et al.* (1994) showed that the annual cycle in tropical lower stratosphere temperatures was anti-correlated with extra-tropical temperatures and linked this, via wave-driving, to the meridional circulation, with downward motion driving extra-tropical temperatures above radiative equilibrium and upward motion driving tropical temperatures below radiative equilibrium. The annual cycle in the temperatures being therefore driven by the strength of the meridional circulation and the wave-driving. However, upwelling in the tropical lower stratosphere peaks on the summer side of the equator whereas downward control would lead to

maximum upwelling on the winter side (Shepherd, 2000).

Reid and Gage (1996) compared the roles of extra-tropical downward control and tropical convection in the formation and maintenance of the tropical tropopause. Their findings were that the gyroscopic pump cools the upper troposphere by adiabatic cooling of ascending air. This decreases local stability, so that the cumulonimbus clouds can then reach higher levels, entraining stratospheric air and establishing a new, higher tropopause. The relative strengths of these processes still has to be determined. Randel *et al.* (2002) also showed that much of the variability in tropical temperatures can be described by the variability in upwelling calculated from the momentum budget, or from wave-induced forcing. However, Holton *et al.* (1995); Gray and Dunkerton (1990) and Yulaeva *et al.* (1994) showed that an effective location for wave-induced forcing to control an annual cycle in upwelling at the equator is not in the extra-tropics, but rather in the subtropics. Gray and Dunkerton (1990) hypothesised that the annual cycle might be a response to gravity wave drag breaking above the NH winter jet stream. Gettelman *et al.* (2001) also suggested that, with climate change and anthropogenic forcing, the balance of the driving of the annual cycle in temperatures and STE by convection and upwelling may change.

The driving of the annual cycle in tropical tropopause temperatures is still unclear and this research investigates this subject further, putting forward another possible explanation.

1.5 This thesis

This research investigates the annual cycle in tropical tropopause and tropical lower stratospheric temperatures. The transformed Eulerian mean equations, described in section 2.2, are used. These equations were used to investigate downward control by Haynes *et al.* (1991); Rosenlof and Holton (1993); Rosenlof (1995) and Randel *et al.* (2002). However, whereas they estimated the upwelling from approximations to the thermodynamic and momentum equations, this research concentrates on using observational and model data for the tropical upwelling and analysing the balance in all of the terms in these equations to investigate the wave-driven pumping and downward control theories of Haynes *et al.* (1991) and later authors. Two data sets are used for this research; assimilated observational data from the European Centre for Medium–Range Weather Forecasts (ECMWF) and model data from the UK Met Office Unified Model (UM).

The following questions are investigated:

- **What is driving the annual cycle in temperature?**
  Which of the terms in the thermodynamic equation is driving the change in the temperature?

- **What is driving the annual cycle in the strength of the tropical upwelling?**
  Which levels dominate the annual cycle in the outflow which, by mass balance, drives the upwelling—are they close to the tropopause or at much higher altitudes?
  Which of the terms in the zonal momentum equation is driving the net outflow in the tropics?

- **Where do the important wave dissipation regions lie?**
  Is the wave-driven pumping effect remote or "non-local" or is it close to the area affected, confined to a small region?
  Is one hemisphere more important than another? Are particular longitudes significant?

- **Which are the important waves?**
  What type of waves are important? Possibilities include Rossby waves and gravity waves.
  What scales are their wavelengths? Possibilities vary from synoptic scales to planetary scales.
  How and where are they generated?

Chapters 2 to 4 describe the investigation of these questions using ECMWF analysis data. Chapter 2 describes the methodology used for analysing the mean annual cycle in tropical tropopause temperatures using the transformed Eulerian mean form of the primitive equations. The data set used is described in section 2.1. The pressure coordinate form of the transformed Eulerian mean equations is derived in section 2.2. The methods used for processing the data are described in section 2.3.

The results of the investigation as to what is driving the annual cycle in tropical tropopause temperatures in the ECMWF data are described in chapter 3. The thermodynamic equation is studied in section 3.2. In section 3.4 the vertical transport is studied and linked to the zonal momentum equation via mass

continuity. Which vertical levels dominate the annual cycle are also investigated in section 3.4. In section 3.5 the zonal momentum equation is studied, to determine the driving of the tropical upwelling. These results are summarised in section 3.7.

In chapter 4 the tropical wave-driving is studied in more detail. The wave-driving is decomposed in a number of ways. In section 4.2 the wave-driving is decomposed into the contributions from the northern and southern hemispheres. In section 4.3 the contribution from non-conservative mechanical forcings, such as gravity wave drag, is considered. In section 4.4 the Eliassen-Palm flux divergence is considered in greater detail. It is decomposed into different horizontal wavenumbers, horizontal and vertical components and stationary and transient components. The longitudinal structure is also considered. These results are summarised in section 4.5.

Chapters 5 and 6 describe the investigation of the same questions using UM data. Chapter 5 describes the reasons for using model data and the methodology used for analysing the UM data. Section 5.1 describes the problems with and shortcomings of the ECMWF data. Section 5.2 compares the results of using different periods of ECMWF data and section 5.3 one problem with using assimilated data. Section 5.4 describes the Unified Model, the model set-up used for part of this research and the advantages in using such model data. Section 5.5 compares the two data sets. Section 5.6 describes the main differences in data processing to that for the ECMWF data.

In chapter 6 the results of the investigation as to what is driving the annual cycle in tropical tropopause temperatures in the UM data are described and compared to those for the ECMWF data (chapters 3 and 4). The thermodynamic equation is studied in section 6.2. In section 6.3 the vertical transport is studied and linked to the zonal momentum equation via mass continuity. Which vertical levels dominate the annual cycle are also investigated in section 6.3. In section 6.4 the zonal momentum equation is studied, to determine the driving of the tropical upwelling. The zonal momentum equation is decomposed into the contributions from the northern and southern hemispheres in section 6.5. In section 6.6 the contribution from non-conservative mechanical forcings, such as gravity wave drag, is studied. Finally, the Eliassen-Palm flux is studied in section 6.7 and is decomposed into its horizontal and vertical components and eddy flux components. The stream function is studied in section 6.8. These results are summarised in section 6.10.

An overall summary and conclusions are given in chapter 7. Ideas for further work are given in chapter 8.

Appendix A lists the symbols used in this thesis, for quick reference, appendix B derives the second order differencing required for part of the data processing and appendix C derives the decomposition of eddy flux terms into their stationary and transient components.

Chapter 2

Methodology for the transformed Eulerian mean study of the ECMWF analysis data

This chapter describes the methodology for analysing the mean annual cycle in tropical tropopause temperatures. The data set used is a combination of European Centre for Medium–Range Weather Forecasts (ECMWF) re-analysis and operational analysis data, described in section 2.1, and is processed as described in section 2.3. The analysis is done in terms of the transformed Eulerian mean (TEM) form of the primitive equations, described in section 2.2.

The main methodology will be as follows:

- Form a mean annual cycle in potential temperatures from the ECMWF analysis data.
- Analyse the balance of the terms in the TEM thermodynamic equation to find what is driving the temperature changes over the annual cycle. Any terms driving the annual cycle will be in phase with, or leading, the temperature changes.
- Analyse the TEM mass continuity equation to find where the net outflow from the tropics is producing a cycle in tropical vertical ascent.
- Analyse the balance of the terms in the TEM momentum equation to find what forces are driving mass outflow from the tropics.

The results of this analysis will be described in chapter 3.

2.1 ECMWF analysis data

The data used for this study is from the European Centre for Medium–Range Weather Forecasts (ECMWF). A combination of six-hourly analysis and re-analysis data from 1 January 1979 to 31 October 2001 is used.

The ECMWF Re-Analysis (ERA) project is to produce validated data sets of assimilated data using a consistent, unchanging model set-up for the period of the assimilation. The first ERA project produced a fifteen year data set known as "ERA-15". The re-analysis period for ERA-15 was December 1978 to February 1994. The remainder of the data used in this research, from March 1994 to October 2001 is from ECMWF operational analyses. Apart from the horizontal resolution, the ERA-15 data assimilation system was identical to the ECMWF operational system between April 1995 and January 1996. A further project, ERA-40, for the period from mid 1957 to 2001 was under production during the period of this research.

The observations available do not cover the globe evenly so, in order to get an idea of the state of the atmosphere at locations where there are few observations or none, the observational data available is "assimilated" with an atmospheric model which outputs data for the entire globe. Six-hourly forecasts from a numerical forecast model, observations and forcing fields are input to an analysis model. Results from the analysis are initialised and then used as initial conditions for the next forecast.

The ECMWF analysis fields provide a global data set, assimilated from observational data, of the main prognostic variables; geopotential, Φ, zonal and meridional winds, u and v, and temperature, T. The vertical velocity, ω, is somewhat less reliable in the ECMWF analysis data compared with the zonal wind, u, and temperature, T.

2.1.1 ERA-15

ERA-15 is a consistent set of assimilated data. Data sources included satellites, radiosondes, ships and buoys. Observations used included cloud cleared radiance (which gives information about the atmospheric temperature and humidity structure) and cloud track winds, with sea surface temperatures and sea ice cover used as forcing fields. The details of how ERA-15 was set up, which data was selected for the assimilation and why, the model set up and the assimilation system are available in Gibson *et al.* (1999). Other useful texts include Simmons *et al.* (1999)

and ECMWF ERA-15 (2002).

The model uses two different horizontal numerical representations—a spectral representation and a grid point representation. The spectral representation is based on a triangular truncation at wavenumber 106 (T106 spectral resolution). This is used for the representation of upper air fields and the computation of horizontal derivatives within the model. The grid point (Gaussian grid) representation is used for calculating non-linear adiabatic terms and the diabatic physical parametrization. The Gaussian grid is regular in longitude and almost regular in latitude. The T106 spectral resolution corresponds to the N80 Gaussian grid of 1.125° or about 125 km. The N80 reduced Gaussian grid is also used in parts of the model calculation and for storage of surface fields. This has fewer grid points than the N80 Gaussian grid and therefore requires fewer computing resources when running the model and less storage space for output data.

There are thirty-one hybrid model levels in the vertical, from 1015 hPa to 10 hPa. The top five levels are pure pressure levels and the lowest three levels are sigma levels, following the orography. The resolution in terms of geometric height is highest in the planetary boundary layer and lowest in the stratosphere, where the levels are pure pressure levels. There is a smooth transition between the terrain following levels and the pressure levels. See figure 2.4 for a plot of the model levels over orography.

Important features of ERA-15 include:

- **Analysis Period:** December 1978–February 1994.
- **Data Assimilation System:** Intermittent statistical optimum interpolation analysis with 6 hour cycling.
- **Horizontal Resolution:** Spectral T106, Gaussian N80.
- **Vertical Resolution:** 31 hybrid levels.

2.1.2 Operational analyses

From March 1994 ECMWF operational analysis data has been used. The model horizontal resolution increased to T213 in September 1991, to T319 in April 1998 and to T511 in November 2000. However all the data is available at spectral resolution T106 with the N80 reduced Gaussian grid for surface fields and it is this resolution which is used in this research. The data has 31 levels from March 1994 to February 1999, 50 levels from March 1999 to September 1999 and 60 levels from October 1999 to October 2001. This research uses the same set of 31

levels throughout (defined in section 2.3). Between vertical resolutions, some of the exact pressure values for a given surface pressure changed slightly so the data was interpolated onto the selected pressure levels.

In January 1996 the analysis scheme was changed to using a 3-dimensional variational (3D-Var) analysis scheme. This was a new method for the analysis of model-level values of temperature, vorticity, divergence and specific humidity, and surface pressure. There were also some minor changes to the forecast model. In November 1997 a 4-dimensional variational (4D-Var) analysis scheme with 6 hour cycling was introduced. This is known to have had some effect on the residual mean circulation in the stratosphere. The cycling of the 4D-Var was changed to 12 hour in September 2000. Most other changes have been to the model resolution. See ECMWF Analysis (2002) for more information about the changes to the analysis and forecasting system. Further information about the model and analysis system can be found in Simmons *et al.* (1999) and references therein.

Important features of the operational analysis data over the period used include:

- **Analysis Period used:** March 1994–October 2001.
- **Data Assimilation System:** Intermittent statistical optimum interpolation analysis with 6 hour cycling, changing to 3D-Var and then 4D-Var.
- **Horizontal Resolution:** Increases from T106 to T511 over the period used.
- **Vertical Resolution:** Increases from 31 hybrid levels to 60 levels over the period used.

2.1.3 An example diagnostic; zonal mean zonal velocity

Figure 2.1 shows an example diagnostic from the ECMWF data. This is a vertical cross-section of zonal mean zonal velocity, $\overline{u}$, for the means of the 22 years of ECMWF data for December and August. There are clear eastward (westerly) subtropical jets just below 200 hPa near 30° in the winter hemisphere and 45° in the summer hemisphere. The jet reaches stronger values in winter than in summer and is stronger in the summer hemisphere in NH winter than in NH summer. In the stratosphere, there are eastward winds in the winter hemisphere and westward winds in the summer hemisphere.

Other basic diagnostics are shown in figures 1.1, which shows temperature and potential temperature, and 2.2 panels (a) and (b), which shows meridional and vertical velocities.

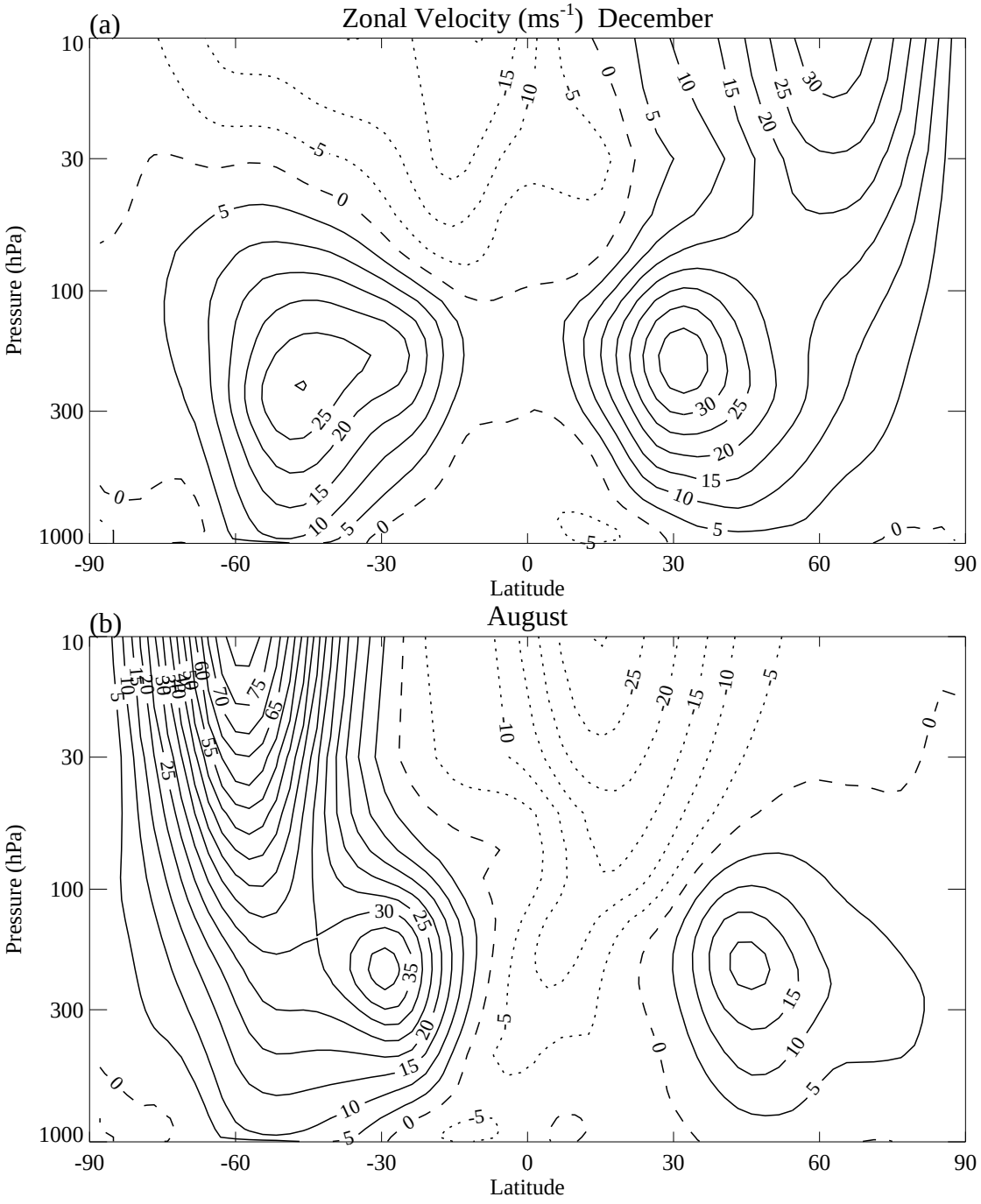

Figure 2.1: Vertical cross-section of zonal mean zonal velocity, $\overline{u}$, for (a) December and (b) August. Positive (eastward) values are shown with solid contours, negative (westward) values with dotted contours. The zero wind line is dashed. The contour interval is $5\,\mathrm{m\,s^{-1}}$.

2.2 Derivation of the transformed Eulerian mean equations

The transformed Eulerian mean (TEM) form of the primitive equations provide a powerful way to describe the response of the atmosphere to wave dissipation or eddy effects. The residual mean meridional circulation, $(0, \overline{v}^*, \overline{\omega}^*)$, discussed in section 2.2.3 and the wave propagation, given by the Eliassen-Palm (EP) flux, $\mathbf{F}$, and wave dissipation, $\nabla.\mathbf{F}$, discussed in section 2.2.5 can also be diagnosed.

For simplicity the log-pressure co-ordinate, z, is often used for the vertical co-ordinate in the primitive equations and derivations of the TEM equations;

$$z \equiv -H \ln\left(\frac{p}{p_s}\right), \tag{2.1}$$

where p is pressure, p_s is a constant reference pressure (=1000 hPa) and $H = RT_s/g_0$ is the scale height. T_s is a constant reference temperature, R is the gas constant for dry air ($= 287\,\mathrm{J\,K^{-1}\,kg^{-1}}$) and g_0 is the global average of gravity at mean sea level ($= 9.80665\,\mathrm{m\,s^{-1}}$). In the middle atmosphere $H = 7\,\mathrm{km}$ corresponding to $T_s \approx 240\,\mathrm{K}$.

Using the log-pressure vertical coordinate can cause problems when processing data on model levels, which are distributed more evenly with respect to pressure than log-pressure. Vertical derivatives are required during processing and such derivatives using finite differencing techniques are better done with more evenly spaced levels. The need to weight many of the terms in the TEM equations with respect to the vertical structure of the atmospheric density is an added complication in using log-pressure levels. For the purposes of this research pressure is a better vertical coordinate, with simpler calculations considering the vertical levels of the data available. The following derivation of the TEM equations is given in pressure coordinates. For a similar derivation in terms of log-pressure see chapter 3 of Andrews *et al.* (1987).

2.2.1 The primitive equations

The equations of motion in a rotating reference frame can be simplified by scale analysis, where the vertical momentum equation is replaced by hydrostatic balance, the Coriolis force associated with the horizontal component of the Earth's rotation is neglected and the distance from a point in the atmosphere to the centre of the Earth can by replaced by a mean radius. Thus, the primitive equations are

formulated (Andrews *et al.*, 1987).

Using spherical coordinates in the horizontal, the primitive equations can be written as:

$$\frac{Du}{Dt} - v\left(f + \frac{u\tan\phi}{R_e}\right) + \frac{\Phi_\lambda}{R_e\cos\phi} = X, \tag{2.2a}$$

$$\frac{Dv}{Dt} + u\left(f + \frac{u\tan\phi}{R_e}\right) + \frac{\Phi_\phi}{R_e} = Y, \tag{2.2b}$$

$$\frac{\partial\Phi}{\partial p} = -\frac{RT}{p}, \tag{2.2c}$$

$$\frac{1}{R_e\cos\phi}\left[\frac{\partial u}{\partial\lambda} + \frac{\partial}{\partial\phi}(v\cos\phi)\right] + \frac{\partial\omega}{\partial p} = 0, \tag{2.2d}$$

$$\frac{D\theta}{Dt} = Q. \tag{2.2e}$$

The independent variables are $(\lambda, \phi, p) = (\text{longitude}, \text{latitude}, \text{pressure})$ with t representing time. The corresponding components of velocity are

$$(u, v, \omega) \equiv \left[(R_e\cos\phi)\frac{D\lambda}{Dt}, R_e\frac{D\phi}{Dt}, \frac{Dp}{Dt}\right]. \tag{2.3}$$

The material derivative, $\frac{D}{Dt}$, is defined as

$$\frac{D}{Dt} \equiv \frac{\partial}{\partial t} + \frac{u}{R_e\cos\phi}\frac{\partial}{\partial\lambda} + \frac{v}{R_e}\frac{\partial}{\partial\phi} + \omega\frac{\partial}{\partial p}, \tag{2.4}$$

where T is temperature and θ is potential temperature. $\Phi = gz$ is the geopotential, R_e is the radius of the Earth ($=6.371\times10^6$ m) and $f = 2\Omega\sin\phi$ is the Coriolis parameter, where Ω is the rotation rate of the Earth ($=7.292\times10^{-5}\,\text{s}^{-1}$).

In the horizontal momentum equations, equations 2.2a and 2.2b, there is the possibility of some non-conservative mechanical forcing, denoted by (X, Y), e.g. friction or unresolved processes such as gravity wave drag. Equation 2.2c expresses hydrostatic balance and 2.2d expresses mass continuity. The thermodynamic relation (2.2e) is expressed simply as the relation between the diabatic heating, Q, and the material rate of change of potential temperature, θ. The diabatic heating rate would include heating from longwave and shortwave radiation and may include a small amount of thermal conduction (Andrews *et al.*, 1987, page 115). Equations 2.2 are similar to those in Andrews and McIntyre (1978) except for the signs of X, Y and Q, due to a difference in notation.

2.2.2 The Eulerian mean equations

Many middle atmosphere phenomena can be considered to be a mean flow with disturbances ("eddies") superimposed. The Eulerian zonal mean is denoted by an over-bar:

$$\overline{u}(\phi,p,t)=\frac{1}{2\pi}\int_0^{2\pi}u(\lambda,\phi,p,t)d\lambda. \tag{2.5}$$

The departure from the zonal mean (i.e. eddy term) is denoted by a prime:

$$u'(\lambda,\phi,p,t)\equiv u(\lambda,\phi,p,t)-\overline{u}(\phi,p,t). \tag{2.6}$$

By definition $\overline{(a)}=0$, also $\overline{\frac{\partial(a)'}{\partial\lambda}}=0$ for any $a=a(\lambda)$, due to λ being periodic.

Separating each variable into zonal mean and departure terms, taking the zonal average and doing some manipulation gives the Eulerian mean form of the primitive equations:

$$\begin{aligned}\frac{\partial\overline{u}}{\partial t}+\overline{v}\left[\frac{1}{R_e\cos\phi}\frac{\partial}{\partial\phi}(\overline{u}\cos\phi)-f\right]+\overline{\omega}\,\frac{\partial\overline{u}}{\partial p}-\overline{X}\\ =-\frac{1}{R_e\cos^2\phi}\frac{\partial}{\partial\phi}(\overline{v'u'}\cos^2\phi)-\frac{\partial}{\partial p}(\overline{\omega'u'}),\end{aligned} \tag{2.7a}$$

$$\begin{aligned}\frac{\partial\overline{v}}{\partial t}+\frac{\overline{v}}{R_e}\frac{\partial\overline{v}}{\partial\phi}+\overline{\omega}\,\frac{\partial\overline{v}}{\partial p}+\overline{u}\left(f+\frac{\overline{u}\tan\phi}{R_e}\right)+\frac{1}{R_e}\frac{\partial\Phi}{\partial\phi}-\overline{Y}\\ =-\frac{1}{R_e\cos\phi}\frac{\partial}{\partial\phi}(\overline{v'v'}\cos\phi)-\frac{\partial}{\partial p}\left(\overline{\omega'v'}\right)-\frac{\overline{u'u'}\tan\phi}{R_e},\end{aligned} \tag{2.7b}$$

$$\frac{\partial\Phi}{\partial p}=-\frac{R\overline{T}}{p}, \tag{2.7c}$$

$$\frac{1}{R_e\cos\phi}\frac{\partial}{\partial\phi}(\overline{v}\cos\phi)+\frac{\partial\overline{\omega}}{\partial p}=0, \tag{2.7d}$$

$$\frac{\partial\overline{\theta}}{\partial t}+\frac{\overline{v}}{R_e}\frac{\partial\overline{\theta}}{\partial\phi}+\overline{\omega}\frac{\partial\overline{\theta}}{\partial p}-\overline{Q}=-\frac{1}{R_e\cos\phi}\frac{\partial}{\partial\phi}(\overline{v'\theta'}\cos\phi)-\frac{\partial}{\partial p}(\overline{\omega'\theta'}). \tag{2.7e}$$

From these equations it is difficult to anticipate the response of the zonal mean flow to disturbances of the "eddy momentum flux", $\overline{v'u'}$ (the poleward flux of zonal momentum), or "eddy heat flux", $\overline{v'\theta'}$ (the poleward flux of potential temperature), the two most important eddy terms in 2.7. It is also difficult to see which physical properties of the flow can control these eddy fluxes. In the transformed Eulerian mean (TEM) form of these equations the effects of the eddy momentum and eddy heat flux are combined and, in this form, these questions can be addressed. In the next two sections, the TEM equations are derived.

2.2.3 The residual mean meridional circulation

First a residual mean meridional circulation, $(0, \overline{v}^*, \overline{\omega}^*)$, is defined where

$$\overline{v}^* \equiv \overline{v} - \frac{\partial}{\partial p}\left(\frac{\overline{v'\theta'}}{\overline{\theta}_p}\right), \tag{2.8a}$$

$$\overline{\omega}^* \equiv \overline{\omega} + \frac{1}{R_e \cos\phi}\frac{\partial}{\partial \phi}\left(\cos\phi \frac{\overline{v'\theta'}}{\overline{\theta}_p}\right) \tag{2.8b}$$

(Andrews and McIntyre, 1978).

In these equations the effect of the poleward temperature flux, $\overline{v'\theta'}$, has been removed from the mean circulation to form the residual circulation.

The Eulerian mean circulation, $(\overline{v}, \overline{\omega})$, represents the motion averaged over a coordinate system fixed in latitude and height, whereas a Lagrangian mean circulation represents the motion averaged following individual parcels of air. The transformed Eulerian mean circulation, $(\overline{v}^*, \overline{\omega}^*)$, is related to the diabatic circulation—the movement across isentropes associated with radiative heating and cooling (Norton, 2003). It is in qualitative agreement with the Lagrangian mean circulation although, being an Eulerian averaged motion, it does not indicate the chaotic motion of air parcels displaced individually by waves.

Figure 2.2 shows the meridional and vertical components of the Eulerian mean circulation (panels (a) and (b)) and transformed Eulerian mean circulation (panels (c) and (d)) for December. For the vertical velocities (panels (b) and (d)), negative values indicate ascent. The Eulerian mean circulation has a cell with ascent in the tropics, northwards motion aloft and descent in the winter hemisphere mid-latitudes. There is a small cell (reaching up to 50 hPa) of ascent in the tropics, southwards motion aloft and descent in the summer hemisphere mid-latitudes. There is a reverse "Ferrel" cell at high latitudes of the winter hemisphere, with ascent north of 60°, southwards motion aloft and descent in the winter hemisphere mid-latitudes. This does not agree with the single cell per hemisphere Brewer-Dobson circulation which long lived chemical tracers and the Lagrangian mean (parcel following) circulation indicate. The appearance of the Ferrel cell is due to the averaging used in the Eulerian mean calculation—averaging isobaric surfaces around latitude circles. However, the mean flow does not follow latitude circles and when the vertical motion is averaged along contours of the mean flow there is a large cancellation between the ascent near the pole and descent in mid-latitudes (Norton, 2003). The transformed Eulerian mean circulation shows the classic

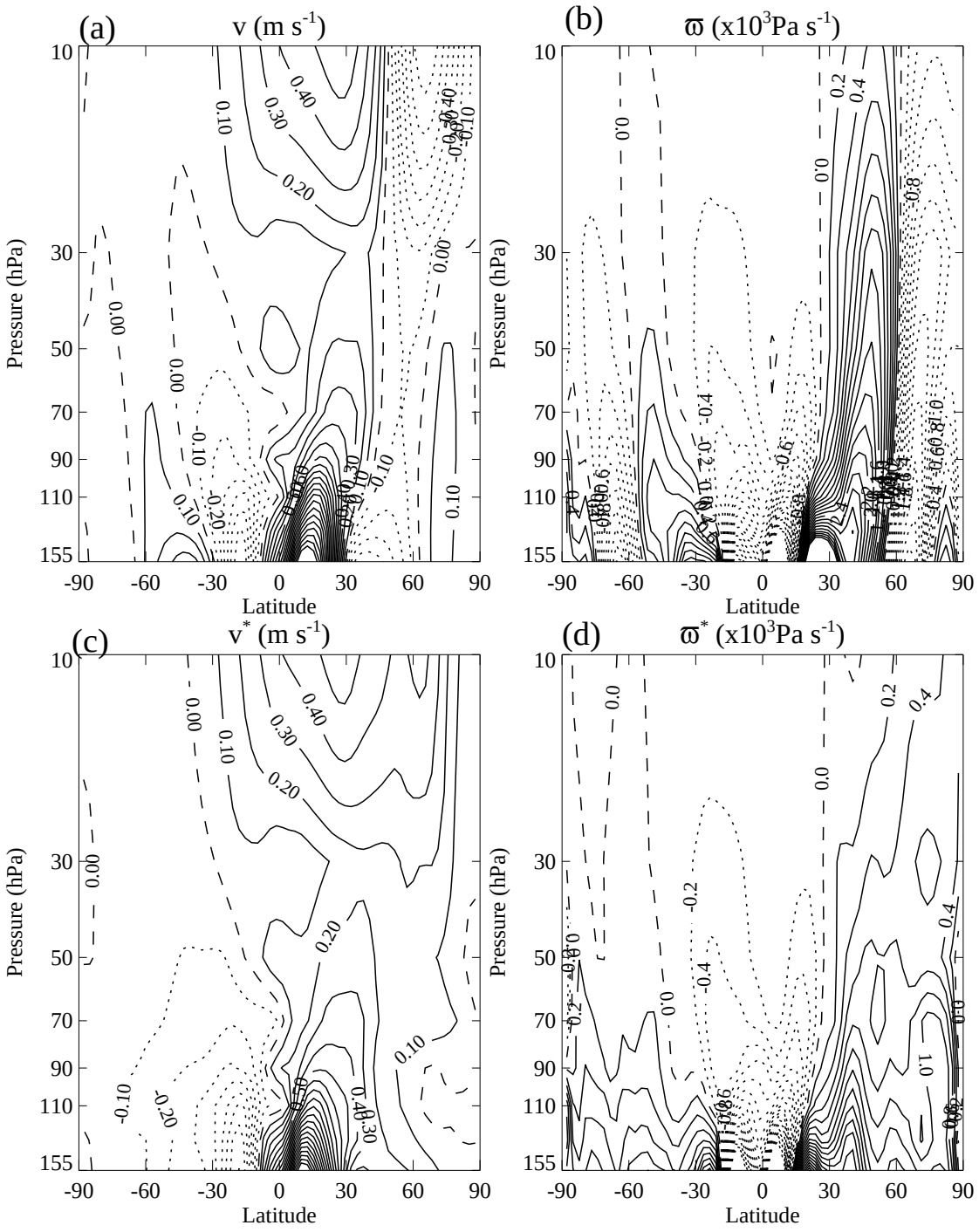

Figure 2.2: 22 year average of mean circulation diagnostics for December. Top row; Eulerian mean circulation (a) $\overline{v}$ and (b) $\overline{\omega}$. Bottom row; transformed Eulerian mean circulation (c) $\overline{v}^*$ and (d) $\overline{\omega}^*$. Solid contours indicate positive values, dashed contours zero and dotted contours negative. The contour interval for the meridional velocities (a) and (c) is $0.1\,\mathrm{m\,s^{-1}}$, the contour interval for the vertical velocities (b) and (d) is $0.2\times10^{-3}\,\mathrm{Pa\,s^{-1}}$. In (b) and (d) negative values indicate ascent.

single cell per hemisphere circulation. For the winter hemisphere there is ascent in the tropics, northwards motion aloft and descent in the winter extra-tropics. For the summer hemisphere the circulation is less strong, reaching only up to 50 hPa, with weak ascent in the tropics, southwards motion aloft and weak descent in the summer extra-tropics. The Ferrel cell of the Eulerian mean circulation induced by the poleward temperature fluxes has been removed from the residual circulation by the transformations in equation 2.8 (James, 1994, section 9.2). The residual mean circulation is stronger in NH winter than SH winter because of the strong wave-driving in the NH winter (Norton, 2003).

2.2.4 The transformed Eulerian mean equations

Substituting equations (2.8) for $(\overline{v}, \overline{\omega})$ in the Eulerian-mean equations (2.7) and rearranging gives the transformed Eulerian mean equations:

$$\frac{\partial \overline{u}}{\partial t} = \overline{v}^* \left(f - \frac{1}{R_e \cos\phi} \frac{\partial}{\partial \phi} \left(\overline{u} \cos\phi \right) \right) - \overline{\omega}^* \frac{\partial \overline{u}}{\partial p} + \frac{1}{R_e \cos\phi} \nabla . \mathbf{F} + \overline{X}, \tag{2.9a}$$

$$\overline{u} \left(f + \frac{\overline{u} \tan\phi}{R_e} \right) + \frac{1}{R_e} \frac{\partial \overline{\Phi}}{\partial \phi} = G, \tag{2.9b}$$

$$\frac{\partial \overline{\Phi}}{\partial p} = -\frac{RT}{p}, \tag{2.9c}$$

$$\frac{1}{R_e \cos\phi} \frac{\partial}{\partial \phi} \left(\overline{v}^* \cos\phi \right) + \frac{\partial \overline{\omega}^*}{\partial p} = 0, \tag{2.9d}$$

$$\frac{\partial \overline{\theta}}{\partial t} = -\frac{\overline{v}^*}{R_e} \frac{\partial \overline{\theta}}{\partial \phi} - \overline{\omega}^* \frac{\partial \overline{\theta}}{\partial p} + \overline{Q} - \frac{\partial}{\partial p} \left(\overline{\theta}_\phi \frac{\overline{v'\theta'}}{R_e \overline{\theta}_p} + \overline{\omega'\theta'} \right). \tag{2.9e}$$

In the zonal momentum equation (2.9a) $\mathbf{F} \equiv \left(0, \mathbf{F}^{(\phi)}, \mathbf{F}^{(p)}\right)$ is the Eliassen-Palm flux (EP flux) where

$$\mathbf{F}^{(\phi)} \equiv R_e \cos\phi \left(\overline{u}_p \frac{\overline{v'\theta'}}{\overline{\theta}_p} - \overline{v'u'} \right), \tag{2.10a}$$

$$\mathbf{F}^{(p)} \equiv R_e \cos\phi \left(\left[f - \frac{1}{R_e \cos\phi} \left(\overline{u} \cos\phi \right)_\phi \right] \frac{\overline{v'\theta'}}{\overline{\theta}_p} - \overline{\omega'u'} \right) \tag{2.10b}$$

and

$$\nabla . \mathbf{F} \equiv \frac{1}{R_e \cos\phi} \frac{\partial}{\partial \phi} \left(\cos\phi \mathbf{F}^{(\phi)} \right) + \frac{\partial \mathbf{F}^{(p)}}{\partial p}. \tag{2.11}$$

In the meridional momentum equation (2.9b) G represents all the terms that

lead to a departure from the gradient-wind balance between $\overline{u}$ and $\overline{\Phi}$ and in most meteorological applications is small. G is defined as

$$\begin{aligned} G \equiv & -\frac{\partial \overline{v}}{\partial t} - \frac{\overline{v}}{R_e}\frac{\partial \overline{v}}{\partial \phi} - \overline{\omega}\frac{\partial \overline{v}}{\partial p} + \overline{Y} \\ & - \frac{1}{R_e \cos\phi}\frac{\partial}{\partial \phi}\left(\overline{v'v'}\cos\phi\right) - \frac{\partial}{\partial p}\left(\overline{\omega'v'}\right) - \frac{\overline{u'u'}\tan\phi}{R_e}. \end{aligned} \tag{2.12}$$

In the thermodynamic equation (2.9e) the eddy fluxes are $w'u'$, the vertical flux of zonal momentum, and $w'\theta'$, the vertical flux of potential temperature. These eddy terms and $-\frac{\overline{v}^*}{R_e}\frac{\partial \overline{\theta}}{\partial p}$ are small compared with the other terms. Other eddy fluxes are in the EP flux and G terms in the horizontal momentum equations.

2.2.5 The Eliassen-Palm flux

The EP flux is a key diagnostic because it characterises some basic physical properties of the flow and eddy disturbances.

For linear, steady, frictionless and adiabatic disturbances about a conservative (to the order of the wave amplitude) mean flow the divergence of the EP flux vanishes, whereas for the same conditions the forcings on the right of the Eulerian Mean equations (2.7a) and (2.7e) are non-zero (Andrews *et al.*, 1987, section 3.5). This is another advantage of using the transformed Eulerian Mean equations over the Eulerian Mean equations. When the EP flux divergence, $\nabla.\mathbf{F}$, is zero the variations of $\overline{v'\theta'}$ in the vertical and of $\overline{v'u'}$ in the horizontal may not be zero but balance each other to give the zero EP flux divergence.

The dependence of $\nabla.\mathbf{F}$ on the physical properties of the waves can be expressed by the wave activity conservation relation, the generalised Eliassen-Palm theorem;

$$\frac{\partial A}{\partial t} + \nabla.\mathbf{F} = D + O(\alpha^3), \tag{2.13}$$

where A and D are mean quadratic functions of disturbance quantities and the $O(\alpha^3)$ term represents nonlinear wave effects, with α as the wave amplitude. The term A is the wave activity density and $\frac{\partial A}{\partial t}$ represents wave-transient effects and vanishes for steady waves. The term D represents the frictional and diabatic effects and vanishes for conservative waves. The EP flux divergence, $\nabla.\mathbf{F}$, thus depends on wave transience and non-conservative wave effects (Andrews *et al.*, 1987, chapter 3). When the waves are conservative, $\nabla.\mathbf{F}$ describes the variation of the wave activity density as disturbances propagate into regions of different density

or potential vorticity gradient (James, 1994). The EP flux can be interpreted as a flux of "EP wave activity" for small amplitude waves on a purely zonal basic flow (Andrews, 1987).

Section 6.5 of James (1994) shows that in the quasi-geostrophic case the EP flux vector is parallel to the local group velocity and, unlike ray tracing, does not rely on any assumptions about the background flow. $\nabla.\mathbf{F}$ in the quasi-geostrophic case also describes the modification of the basic state changes in the poleward flux of potential vorticity.

Figure 2.3 shows a cross-section of EP flux divergence as defined in equation 2.11 for a climatological mean December. Vectors of EP flux are over-plotted. In this style of figure the divergence contours indicate where disturbances are

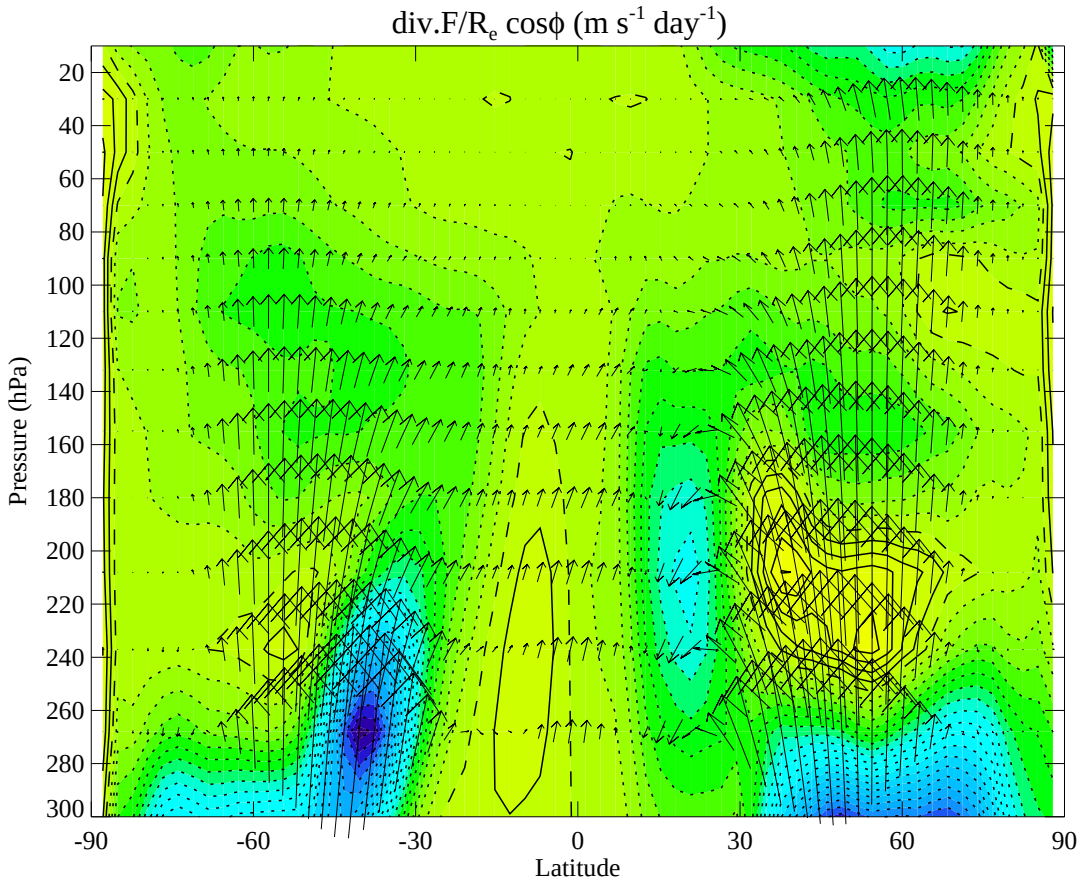

Figure 2.3: 22 year average of Eliassen-Palm flux divergence for December with arrows of Eliassen-Palm flux over-plotted. The contour interval for the EP flux divergence is $0.5\,\mathrm{m\,s^{-1}\,day^{-1}}$. Solid contours indicate divergence (positive $\nabla.\mathbf{F}$), dotted contours indicate convergence.

generated and dissipated and how they interact with the mean flow, while the vectors indicate how disturbances propagate through the atmosphere (Edmon Jr. *et al.*, 1981). Where $\nabla.\mathbf{F} < 0$ (dotted contours) there is wave dissipation whereas where $\nabla.\mathbf{F} > 0$ (solid contours) there is wave generation.

In figure 2.3 there is dissipation or convergence throughout most of the middle atmosphere with some divergence just south of the equator up to 150 hPa, in northern (winter) hemisphere middle latitudes between 240 and 180 hPa at the heart of the NH subtropical jet (see figure 2.1) and near the winter pole in the stratosphere. The convergence is strong in middle latitudes of the southern (summer) hemisphere below 180 hPa and north of 30°N below 240 hPa (i.e. below the the region of convergence). There is also strong convergence in the winter stratosphere, above 40 hPa, which is a region of wave-breaking of planetary scale Rossby waves. Looking at the EP flux vectors, there is upward propagation throughout the middle latitudes, with horizontal propagation at 10°N and between 20 and 30°N, with downwelling between 10 and 20°N below 160 hPa.

In section 4.4 the Eliassen-Palm flux will be considered in more detail to see which of the terms are important for this research. For different waves different eddy terms are important. For example, consider the quasi-geostrophic beta-plane form of the TEM equations and the EP flux. This is discussed in section 3.5 of Andrews *et al.* (1987), section 2 of Andrews (1987) and section 6.5 of James (1994). The terms in $\nabla.\mathbf{F}$ are reduced to those involving horizontal gradients in $\overline{v'u'}$ (from equation 2.10a) and vertical gradients in $\overline{v'\theta'}$ (from equation 2.10b). These are the terms important for Rossby wave propagation. Conversely, the term $\overline{\omega'u'}$ (the vertical transport of zonal momentum) from equation 2.10b is important for gravity waves (section 4.6, Andrews *et al.* (1987)).

2.3 Data processing

Diagnostics available in the ECMWF data set are temperature, zonal and meridional winds and vertical velocity. The terms in the thermodynamic and zonal momentum equations (2.9e and 2.9a) were calculated from these four diagnostics with the exceptions of $\overline{Q}$ and $\overline{X}$. These two terms cannot be calculated from the diagnostics available in the data set and were calculated as residuals from the other terms in the equations, assuming each equation balanced. $\overline{Q}$ is expected to be mainly due to diabatic heating and $\overline{X}$ is expected to be mainly due to the gravity wave drag from the ECMWF model orographic gravity wave scheme.

The terms in the TEM equations were calculated every six hours, then monthly means and an annual cycle (the average of all the Januaries, Februaries etc.) were calculated.

For the transformed Eulerian mean analysis the data have been truncated to T42 resolution and interpolated onto 23 selected levels ranging from 996 hPa to 10 hPa. The top four levels are evenly spaced with 20 hPa increments, at 10, 30, 50 and 70 hPa. The 15 lower levels are unevenly spaced. The levels used can be seen on the right hand side of figure 2.4. After interpolation and before any time meaning each zonally averaged diagnostic has 64 latitudes by 23 levels by 33360 timesteps with file sizes of about 190 MB each. Care was taken to ensure that only essential diagnostics were calculated and stored at this resolution.

Various derivatives were needed for the calculation of some of the terms in the thermodynamic and zonal momentum equations (2.9e and 2.9a).

Latitudinal derivatives of $\overline{\theta}$, $\overline{u}\cos\phi$ and $\cos\phi\mathbf{F}^{(\phi)}$ were required. The horizontal grid used is unequally spaced so that horizontal derivatives must be calculated

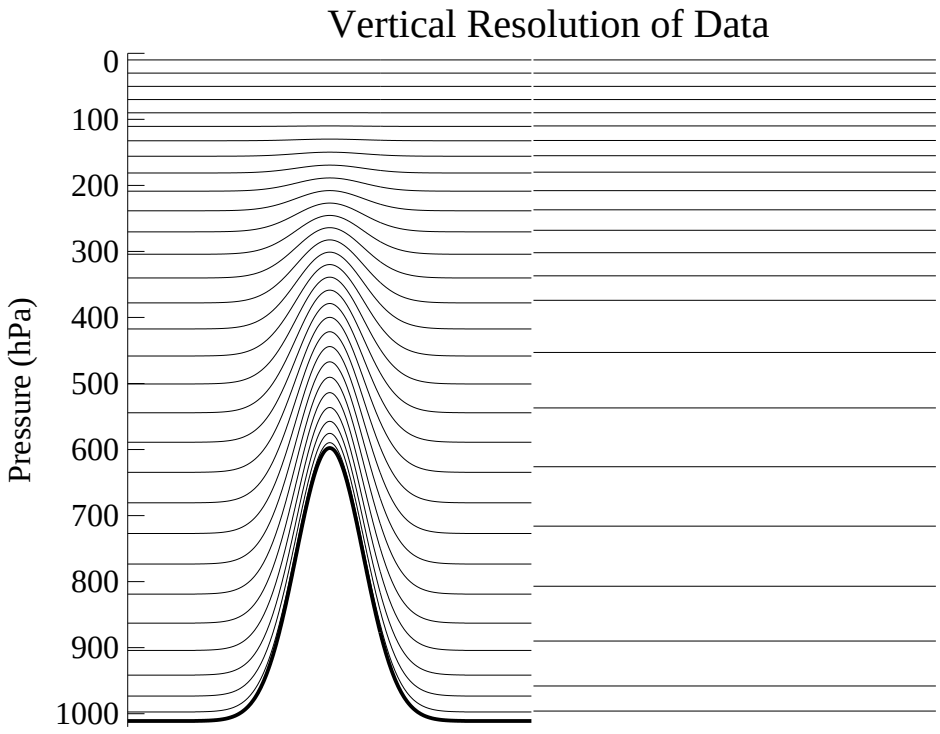

Figure 2.4: The thirty-one level vertical resolution of the ECMWF model including topography (left) and the pressure levels used for the analysis of the ECMWF data (right).

using a finite differencing method for an unequally spaced grid—this is discussed in section 2.3.1.

The two equations include time derivatives of $\overline{u}$ and $\overline{\theta}$. Monthly means were to be calculated from these six-hourly time derivatives. Taking the monthly mean of such a time derivative would result in finding the time difference between the beginning and the end of the month, rather than the mean of the values of the time derivatives over the month. A smoothing to prevent this was required—this is discussed in section 2.3.2.

Vertical derivatives of $\overline{u}$, $\overline{\omega}^*$, $\overline{\theta}$, $\frac{\overline{v'\theta'}}{\overline{\theta}_p}$ and $\mathbf{F}^{(p)}$ were required. Some of the diagnostics to be differentiated with respect to the vertical have large changes in magnitude over the range of atmospheric levels used, whereas others are at similar orders of magnitude over the entire vertical range. This presented a challenge due to potential numerical errors in the differencing—this is discussed in section 2.3.3.

2.3.1 Second order differencing for first order derivatives for unequally spaced points

For equally spaced grid points the equations for calculating the first order derivative, $y'(x)$, using second order differencing are;

$$y'(x_n) \approx \left(-y_{n+2} + 4y_{n+1} - 3y_n\right)/2h, \tag{2.14a}$$

$$y'(x_n) \approx \left(y_{n+1} - y_{n-1}\right)/2h \tag{2.14b}$$

and

$$y'(x_n) \approx \left(y_{n-2} - 4y_{n-1} + 3y_n\right)/2h, \tag{2.14c}$$

for forward, centred and backward differences respectively. The subscripts indicate the grid point of the value and $h = (x_n - x_{n-1})$ is the spacing between the grid points.

For a grid where the points are not equally spaced, such as with the ECMWF data, the equations for calculating the first order derivative using second order differencing were derived using Taylor expansions. These are:

$$y'(x_n) \approx \frac{(x_{n+2} - x_n)(y_{n+1} - y_n)}{(x_{n+1} - x_n)(x_{n+2} - x_{n+1})} - \frac{(x_{n+1} - x_n)(y_{n+2} - y_n)}{(x_{n+2} - x_n)(x_{n+2} - x_{n+1})}, \tag{2.15a}$$

$$y'(x_n) \approx \frac{(x_n - x_{n-1})(y_{n+1} - y_n)}{(x_{n+1} - x_n)(x_{n+1} - x_{n-1})} - \frac{(x_{n+1} - x_n)(y_{n-1} - y_n)}{(x_n - x_{n-1})(x_{n+1} - x_{n-1})} \tag{2.15b}$$

and

$$y'(x_n) \approx \frac{(x_n - x_{n-2})(y_{n-1} - y_n)}{(x_n - x_{n-1})(x_{n-2} - x_{n-1})} - \frac{(x_n - x_{n-1})(y_{n-2} - y_n)}{(x_n - x_{n-2})(x_{n-2} - x_{n-1})} \tag{2.15c}$$

for forward, centred and backward differences respectively. For equal spacing equations 2.15 simply reduce to equations 2.14. The derivation for equations 2.15 can be found in appendix B.

2.3.2 Smoothing and meaning

Finding the monthly mean value of the six-hourly data is surprisingly non-trivial. Two of the terms in the TEM equations are time differentials, so the first attempt to calculate a monthly mean would begin

$$\left\langle \frac{\partial\overline{\theta}}{\partial t} \right\rangle = \frac{1}{n}\left[\frac{\partial\overline{\theta}}{\partial t}^{(1)} + \frac{\partial\overline{\theta}}{\partial t}^{(2)} + \frac{\partial\overline{\theta}}{\partial t}^{(3)} + \frac{\partial\overline{\theta}}{\partial t}^{(4)} \cdots + \frac{\partial\overline{\theta}}{\partial t}^{(n-3)} + \frac{\partial\overline{\theta}}{\partial t}^{(n-2)} + \frac{\partial\overline{\theta}}{\partial t}^{(n-1)} + \frac{\partial\overline{\theta}}{\partial t}^{(n)} \right], \tag{2.16}$$

where angle brackets, $<$ and $>$, indicate a time mean over the number of time points in a month, n. The time domain is equally spaced so the differencing used is as in equations 2.14. Substituting equation 2.14 into equation 2.16 gives

$$\begin{aligned}\left\langle \frac{\partial\overline{\theta}}{\partial t} \right\rangle &= \frac{1}{n}\left[\frac{\left(-\overline{\theta}_3 + 4\overline{\theta}_2 - 3\overline{\theta}_1\right)}{2\delta t} + \frac{\left(\overline{\theta}_3 - \overline{\theta}_1\right)}{2\delta t} + \frac{\left(\overline{\theta}_4 - \overline{\theta}_2\right)}{2\delta t} + \frac{\left(\overline{\theta}_5 - \overline{\theta}_3\right)}{2\delta t} \cdots \right. \\ &\quad \left. + \frac{\left(\overline{\theta}_{n-2} - \overline{\theta}_{n-4}\right)}{2\delta t} + \frac{\left(\overline{\theta}_{n-1} - \overline{\theta}_{n-3}\right)}{2\delta t} + \frac{\left(\overline{\theta}_n - \overline{\theta}_{n-2}\right)}{2\delta t} + \frac{\left(\overline{\theta}_{n-2} - 4\overline{\theta}_{n-1} - 3\overline{\theta}_n\right)}{2\delta t} \right] \\ &= \frac{-4\overline{\theta}_1 + 3\overline{\theta}_2 - \overline{\theta}_3 + \overline{\theta}_{n-2} - 3\overline{\theta}_{n-1} - 2\overline{\theta}_n}{2n\delta t}. \end{aligned} \tag{2.17}$$

It can be seen from equation 2.17 that the result for the time mean of the time differential will depend on the six points at the ends of the month rather than being a true mean of all the points in the month—if any of these six end points is an outlier from the rest of the data then there is a potential for the mean to be biased. To solve this problem a smoothing was used so that the calculation of the mean would include all the data points in the month.

A simple trapezium smoothing was defined such that extended over a period

of 61 days. This is approximately twice the average month length, which is 30.43 days. For this smoothing the weighting is increased linearly to a maximum for the first 15.25 days and decreased linearly to zero for the last 15.25 days, see figure 2.5. The maximum value was normalised such that the integrated weighting was unity.

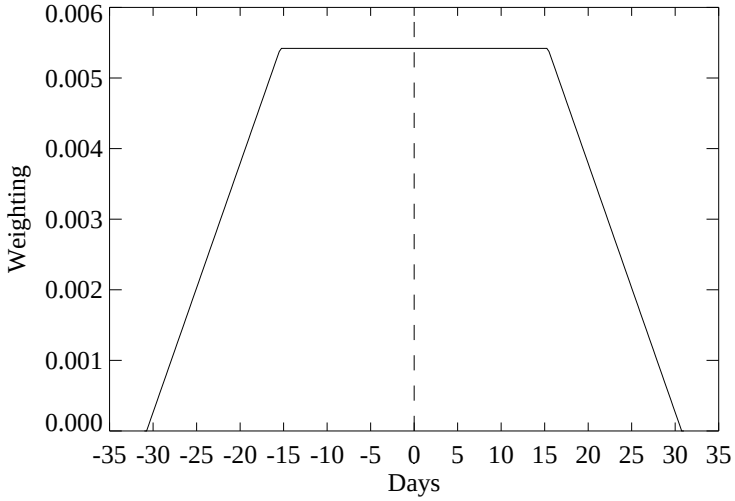

Figure 2.5: The trapezium weighting function used in smoothing the diagnostics.

The data was then smoothed using this weighting function. The weighted data around the centre point of each month was totalled to find a monthly mean.

2.3.3 Methods of calculating vertical derivatives

When calculating a derivative with low resolution data it is important to consider the way the data is changing along the direction of the derivative—derivatives where one variable changes rapidly compared to the other can become inaccurate due to numerical errors. Changing the variable that is involved in the differentiation, such as by taking the natural logarithm, can decrease the errors in the result, e.g.

$$\frac{\partial}{\partial x} \equiv \frac{1}{x}\frac{\partial}{\partial \ln x}. \tag{2.18}$$

For the ECMWF data set the pressure coordinate changes by two orders of magnitude over its range (from 1000 hPa to 10 hPa) but the natural logarithm of pressure will only double over that range. The terms $\overline{\theta}$ and $\overline{u}$ do not change by much over the vertical range so it is more accurate to use differentiation with respect to log-pressure. The terms $\overline{\omega}^*$, $\frac{\overline{v'\theta'}}{\overline{\theta}_p}$ and $\mathbf{F}^{(p)}$ change by orders of magnitude over the vertical range so a differentiation with respect to pressure is more accurate.

2.3.4 Integration of mass continuity equation

In section 3.4.1 the mass continuity equation (2.9d) is rearranged and integrated to find the average vertical velocity across a latitude band:

$$\langle\overline{\omega}^*\rangle(p) = \int_p^{p=0} \frac{-\cos\phi_L}{\int_{-\phi_L}^{\phi_L} R_e \cos\phi d\phi} \left(\overline{v}^*(\phi_L, p) - \overline{v}^*(-\phi_L, p)\right) dp. \tag{2.19}$$

The trapezium rule was used to evaluate the integral. The values of the integrand were found and then used to form the integral, so that as an intermediate step the integrand itself could be examined. The data has finite resolution, so let

$$I_n = \frac{-\cos\phi_L}{\int_{-\phi_L}^{\phi_L} R_e \cos\phi d\phi} \left(\overline{v}_n^*(\phi_L) - \overline{v}_n^*(-\phi_L)\right) \tag{2.20}$$

where, given the values of $\overline{v}^*$ on full model levels (10, 30, 50 hPa etc.), I_n is evaluated on full model levels. Here, the notation of a subscript n for model levels is used. "Half-levels" (20, 40, 60 hPa etc.) are half-way between adjacent model levels and a subscript $n+\frac{1}{2}$ is used to denote these levels. To evaluate $\overline{\omega}^*$ on the $k+\frac{1}{2}$ level, a vertical sum of I_n is done, calculated from the top of the atmosphere downwards,

$$\overline{\omega}^*_{k+\frac{1}{2}} = \sum_{n=1}^{k} I_n \left(p_{n+\frac{1}{2}} - p_{n-\frac{1}{2}}\right). \tag{2.21}$$

with $\overline{\omega}^* = 0$ at $p = 0$. The values of $\overline{\omega}^*$ on full model levels can then be found by averaging the values on the half-levels;

$$\overline{\omega}^*_n = \frac{1}{2}\left(\overline{\omega}^*_{k+\frac{1}{2}} + \overline{\omega}^*_{k-\frac{1}{2}}\right). \tag{2.22}$$

2.3.5 Horizontal wavenumber decomposition

In section 4.4.1 the data is decomposed into various horizontal wavenumbers to examine which length scales are important to the annual cycle in wave-driving. Because the model data is spectral in the horizontal this is simply done by filtering out the wavenumbers not required before converting the data to a Gaussian grid. The wavenumbers selected were wavenumbers one, two, three and all those greater than three.

2.3.6 The Eliassen-Palm flux and eddy flux terms

In section 4.4 the Eliassen-Palm flux is examined in greater detail, examining its northern and southern hemisphere, vertical and horizontal and stationary and transient components. For the stationary and transient components, this requires a small change to the data processing. The eddy fluxes, such as $\overline{v'u'}$, are decomposed to find the stationary and transient components.

Recall from section 2.2, equations 2.5 and 2.6, that the Eulerian zonal mean is denoted by an over-bar, $\overline{u}$, and the departure from the zonal mean is denoted by a prime, u'. Similarly the simple time means used in this section will be denoted by angle-brackets:

$$\langle u(\lambda,\phi,z)\rangle = \frac{1}{t}\int_0^t u(\lambda,\phi,z,t)dt. \tag{2.23}$$

The transient part or departure from the time mean is denoted by an asterisk:

$$u^*(\lambda,\phi,z,t) \equiv u(\lambda,\phi,z,t) - \langle u(\lambda,\phi,z)\rangle\,. \tag{2.24}$$

A stationary eddy is then defined as $<u>'=<u> - \overline{<u>}$. "Eddy" refers to the departure from the zonal mean and "stationary" refers to the time average term. Note that $<\overline{u}>= \overline{<u>}$, $<u'>=<u>'$ and $\overline{u^*} = \overline{u}^*$ because time and zonal meaning commute.

The trapezium smoothing described in section 2.3.2 to solve the problem of biases when finding the time mean of time derivatives cannot be used. It is less important to use it here because time derivative terms are not considered. For part of the theory used in investigating eddy fluxes it is required that $<<x>>=<x>$ (the time mean of the time mean of a set of data being equal to the time mean of that set of data) is true and, though it is true for the simple "top-hat" meaning of the form

$$\langle u(\lambda,\phi,z)\rangle = \frac{1}{t}\sum_0^t u(\lambda,\phi,z,t), \tag{2.25}$$

it is not true for the more complicated trapezium smoothing discussed in section 2.3.2. For the investigation of eddy fluxes the simple "top-hat" meaning defined in equation 2.25 is used.

The eddy momentum flux is the zonal mean of $v'u'$. The time mean of the zonal mean is usually calculated. To investigate $v'u'$ itself (e.g. to examine a latitudinal-longitudinal structure), the zonal meaning is no longer performed but some time meaning is still required. $v'u'$ can be split up into its stationary and transient

components;

$$\begin{aligned} \langle v'u' \rangle &= \big\langle\, (v - \overline{v})\,(u - \overline{u})\,\big\rangle, \\ &= \underset{\text{stationary}}{\langle v' \rangle \langle u' \rangle} + \underset{\text{transient}}{\langle v'^{*} u'^{*} \rangle}\,, \end{aligned} \tag{2.26}$$

provided that $<v<u>>=<v><u>$. Note that $<vu>\neq<v><u>$. See appendix C for a proof of equation 2.26.

The stationary and transient terms for $v'u'$, $v'\theta'$ and $\omega'u'$ were calculated and time-averaged using the simple top-hat meaning as described above. Two meaning periods were used; 30.5 days, which is near to the average month length of 30.43 days, and 10 days. For each meaning period the mean of all 10 or 30.5 day periods where the centre point fell in a January, February etc. were then found to give an annual cycle. In section 2.3 it was noted that for the zonally averaged data, before any time meaning, each diagnostic of 64 latitudes, 23 levels and 33360 timesteps took about 190 MB of disk space. For the stationary and transient term calculations the data is not zonally averaged. Including the extra dimension of 128 longitude points would make a 23 level data file about 24 GB in size, which is not a practical file size either in terms of manipulation or storage. Instead, individual levels were stored in separate files and only selected levels near the tropopause level were considered, these being 50, 70, 90, 110, 132 and 155 hPa.

Stream function

The horizontal winds, u and v, can be divided into their rotational and divergent components. The horizontal velocity field, $\mathbf{v} = (u, v)$, can then be described in terms of two scalar fields, the stream function, ψ, and the velocity potential, χ, (see James, 1994, chapter 8) where

$$\mathbf{v} = \hat{\mathbf{k}} \wedge \nabla\psi + \nabla\chi, \tag{2.27}$$

$$\mathbf{v}_{\psi} = \hat{\mathbf{k}} \wedge \nabla\psi, \tag{2.28}$$

$$\mathbf{v}_{\chi} = \nabla\chi. \tag{2.29}$$

The stream function represents streamlines for the non-divergent flow, with the distance between lines of constant stream function being proportional to the magnitude of the non-divergent velocity. A plot of stream function gives an idea of the spatial distribution of the rotational or non-divergent flow (Holton, 1972,

section 8.3).

The next two chapters look at the results of the TEM study of the ECMWF analysis data. Chapter 3 looks at the annual cycle in temperature in the thermodynamic equation, linking it to wave-driving in the zonal momentum equation. Chapter 4 looks at the Eliassen-Palm flux in greater detail.

Chapter 3

The driving of the annual cycle in temperature in the ECMWF analysis data

3.1 Introduction

This chapter investigates the driving of the annual cycle in the thermodynamic equation (2.9e) by investigating the annual cycle of each of the individual terms in that equation. The mass continuity equation (2.9d) is investigated, linking the thermodynamic equation to the zonal momentum equation (2.9a). Finally the driving of the annual cycle in the zonal momentum equation is investigated. The terms in each of these equations have been calculated from the six hourly ECMWF analysis data discussed in section 2.1, using the data processing methods discussed in section 2.3.

In this research the 90 hPa level of the data set was principally studied. This level is just above the tropical tropopause where there is a large annual cycle in temperatures, see figure 1.2, page 8. In section 3.6 the 70 hPa level is considered and the results compared with those at 90 hPa.

3.2 The annual cycle in the terms of the thermodynamic equation

The thermodynamic equation (2.9e) was investigated to see what drives the changes in potential temperatures over the annual cycle. Figure 3.1 shows the annual

cycle in potential temperature at 90 hPa from 40°N to 40°S. A large annual cycle can be seen between approximately 20°N and 20°S—this has largest amplitude between approximately 10°N and 10°S. The potential temperature at the equator is approximately 10 K warmer in NH summer than NH winter.

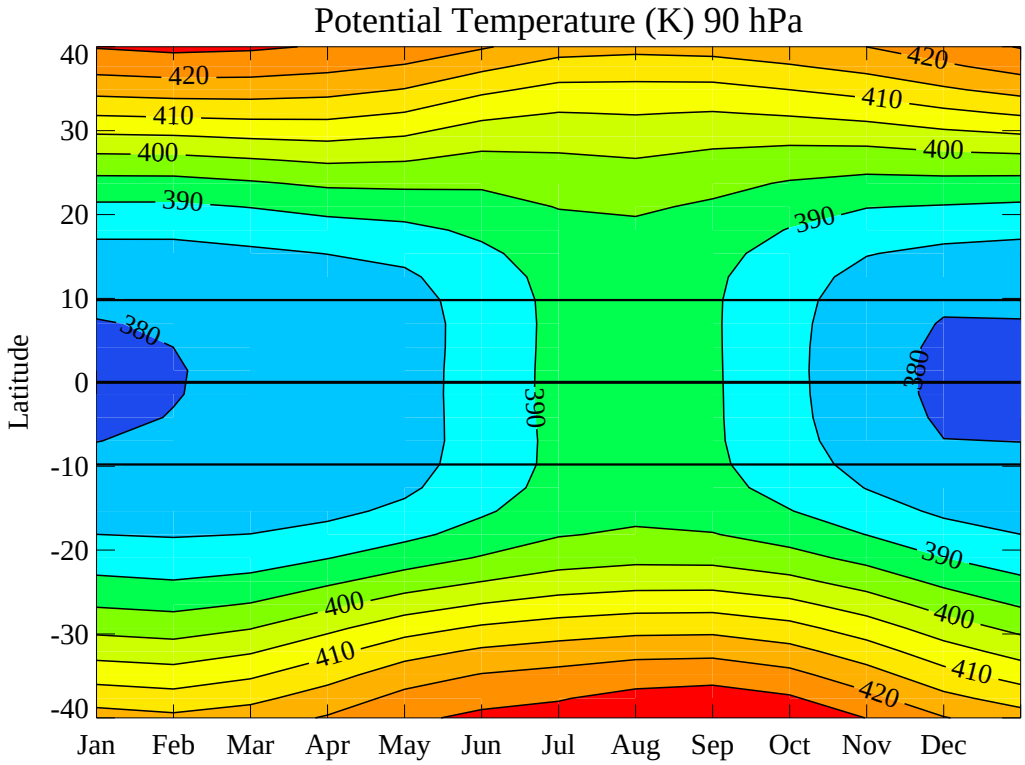

Figure 3.1: Mean annual cycle of the zonal mean potential temperature at 90 hPa. The contour interval is 10 K. Solid black lines indicate 9.8°N, the equator and 9.8°S.

The annual cycle in the rate of change of potential temperature with respect to time, $\frac{\partial\overline{\theta}}{\partial t}$, is shown in figure 3.2. There is a strong warming between 20°N and 20°S from April to July and a strong cooling from August to November. The warming and cooling are strongest between 10°N and 10°S, decreasing in strength from 10° to 20° in both hemispheres. From January to April, between 20°N and 20°S, there is very weak warming. Further south, between about 20°S and 50°S, there is warming starting earlier than the equatorial warming, lasting from February to July, and there is cooling from August to January, finishing later than the equatorial cooling. North of the equatorial warming and cooling, between about 25°N and 50°N, there is warming and cooling of the opposite sense to the equatorial warming and cooling, with cooling from February to July and warming

from August to January.

This research will concentrate on the 10°N to 10°S latitude band because the annual cycle between those latitudes is relatively large for both potential temperature and rate of change of potential temperature. Between 10°N and 10°S the rate of change of potential temperature is nearly constant at a given time for the latitude band, decreasing in magnitude outside that latitude band. Using a wider latitude band would decrease the amplitude of the annual cycle being studied. Some other studies have used wider latitude bands in examining the tropical annual cycle. Randel *et al.* (2002) use 20°N to 20°S and 30°N to 30°S latitude bands to examine upwelling, Yulaeva *et al.* (1994) use 30°N to 30°S to look at temperature and Reid and Gage (1981) use 20°N to 20°S to look at tropopause height. These all include the region where the rate of change of potential temperature is not constant across latitudes. The horizontal spacing of the ECMWF data is such that the nearest grid box to 10° is 9.8°. Reid and Gage (1981) also use 10°N to 10°S for their tropopause height study, noting that the amplitude of the annual cycle varies with latitude.

The adiabatic cooling term, $-\overline{\omega}^* \frac{\partial \overline{\theta}}{\partial p}$, is shown in figure 3.3. There is general adiabatic cooling throughout the tropics (blue-green) between 20°S and 20°N. This extends 10° further north to 30°N in NH summer and 10° further south to 30°S in NH winter, such that the band of cooling spans about 50° in latitude at any time during the year. In the extra-tropics heating (yellow-red) can be seen. There is a strong cooling (dark blue) near the equator in October and November and a warming just north of the equator in June and July. These times correspond with the largest changes in temperature in figure 3.2, occurring just after the minimum and maximum in the equatorial $\frac{\partial \overline{\theta}}{\partial t}$ respectively. In the NH there is a region of strong cooling near the equator in the winter which moves northwards in the summer when it also reaches a maximum.

The residual of the thermodynamic equation, the diabatic heating, $\overline{Q}$, is shown in figure 3.4. This term mainly opposes that of the adiabatic cooling. There is heating throughout the tropics, which moves northwards during NH summer, and cooling in the extra-tropics. In the NH there is a band of stronger heating (orange), which is pushed away from the equator in the summer.

The adiabatic cooling and diabatic heating terms are much larger than the rate of change of potential temperature, reaching $1.4\,\mathrm{K\,day^{-1}}$ values in this region during NH summer, whereas $\frac{\partial \overline{\theta}}{\partial t}$ is an order of magnitude lower at its maximum, reaching only $0.16\,\mathrm{K\,day^{-1}}$. The adiabatic cooling and diabatic heating terms

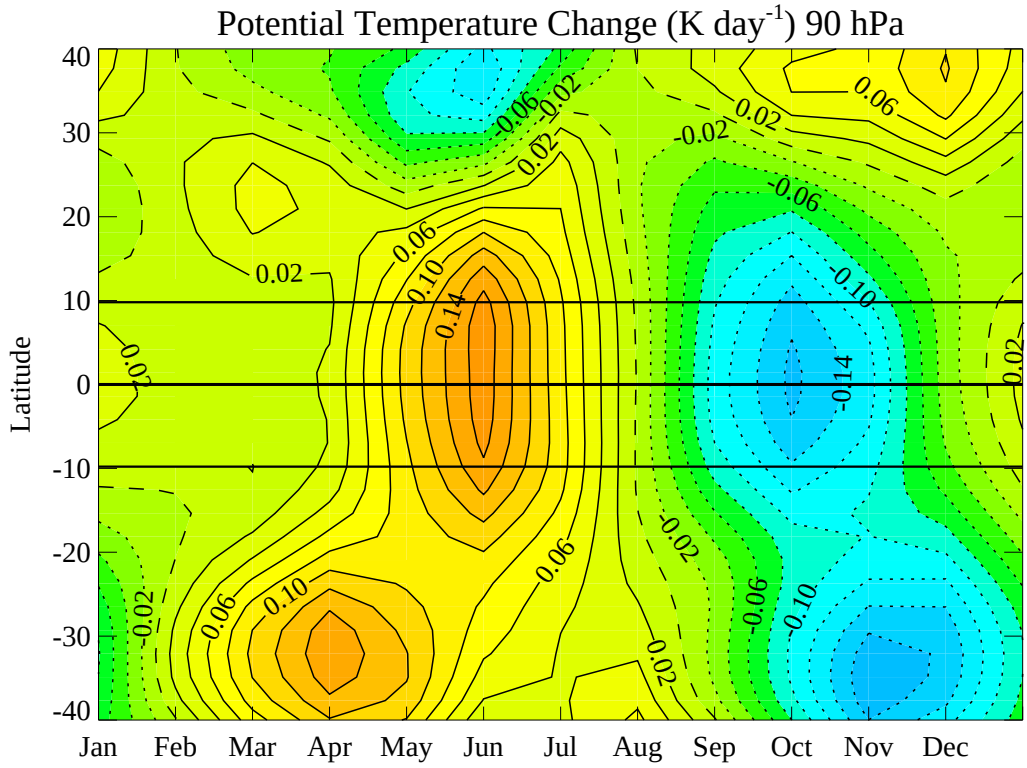

Figure 3.2: Mean annual cycle of the rate of change of zonal mean potential temperature at 90 hPa. The contour interval is 0.02 K day^{-1}. Solid contours indicate positive values (increasing temperatures), dashed contours indicate zero values (no change) and dotted contours indicate negative values (decreasing temperatures). Solid black lines indicate 9.8°N, the equator and 9.8°S.

cancel each other out quite closely. Rosenlof (1995) also shows that the these two terms largely cancel each other out, leaving $\frac{\partial\overline{\theta}}{\partial t}$ as a small residual between them.

The remaining two terms in the thermodynamic equation, $-\frac{\overline{v}^*}{R_e}\frac{\partial\overline{\theta}}{\partial\phi}$ and $-\frac{\partial}{\partial p}\left(\frac{\overline{v'\theta'}\,\overline{\theta}_\phi}{R_e\overline{\theta}_p}+\overline{\omega'\theta'}\right)$, are much smaller than the terms illustrated in this chapter, especially in the tropics and near the tropopause. They do not have a significant effect on the annual cycle in temperatures compared with terms such as diabatic heating (Andrews *et al.*, 1987; Gille *et al.*, 1987; Eluszkiewicz *et al.*, 1996; Randel *et al.*, 2002).

Figure 3.5 shows the annual cycle in potential temperature anomaly (panel (a)) and each of the terms in the thermodynamic equation (panel (b)) averaged across the latitude band 9.8°N to 9.8°S at 90 hPa.

The potential temperature is higher in NH summer than in NH winter (figure 3.5a), increasing between April and August and decreasing between August and

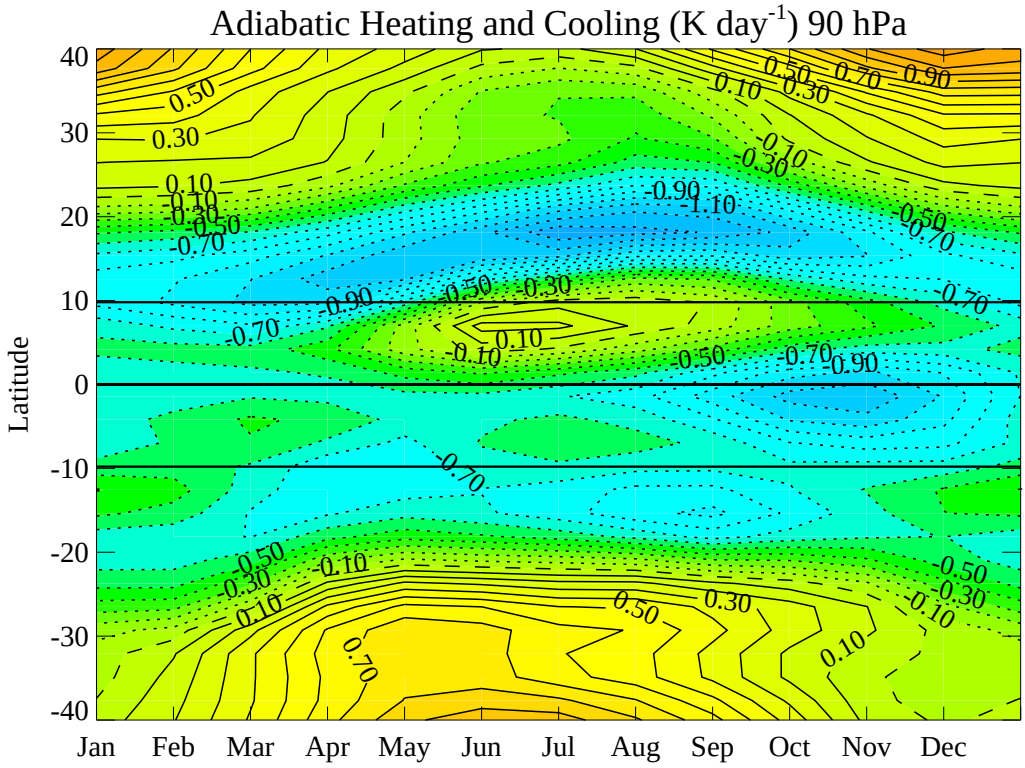

Figure 3.3: Mean annual cycle of the zonal mean adiabatic cooling, $-\overline{\omega}^* \frac{\partial \overline{\theta}}{\partial p}$, at 90 hPa. The contour interval is 0.1 K day^{-1}. Solid contours indicate positive values (heating), dashed contours indicate zero values and dotted contours indicate negative values (cooling). Solid black lines indicate 9.8°N, the equator and 9.8°S.

December (3.5a and $\frac{\partial \overline{\theta}}{\partial t}$, black line in figure 3.5b). The adiabatic heating and cooling term (green line in figure 3.5b) is negative throughout the year so there is always upwelling and cooling. A clear annual cycle can be seen in the adiabatic cooling term with decreased cooling in NH summer. The diabatic heating (orange line in figure 3.5b) is always positive and therefore heating the atmosphere. There is a clear annual cycle in the diabatic heating term, with decreased heating in NH summer.

As the adiabatic cooling decreases between April and June, $\frac{\partial \overline{\theta}}{\partial t}$ responds to the decreased cooling and increases, giving more warming, and the potential temperature increases. The diabatic heating term responds to the change in potential temperature, decreasing its heating rate (i.e. more longwave cooling when the temperature is higher).

The adiabatic cooling reaches a minimum cooling in June and from July the cooling starts to increase again. Responding to this, $\frac{\partial \overline{\theta}}{\partial t}$ then decreases, changing

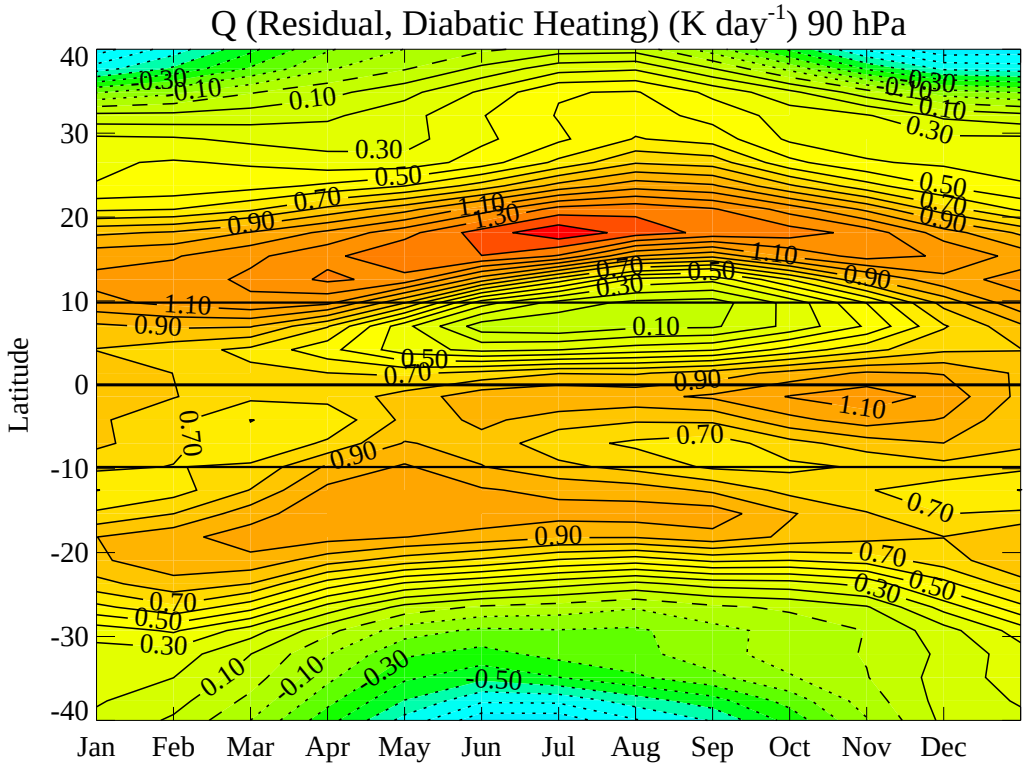

Figure 3.4: Mean annual cycle of the zonal mean residual diabatic heating at 90 hPa. The contour interval is 0.1 K day^{-1}. Solid contours indicate positive values (heating), dashed contours indicate zero values and dotted contours indicate negative values (cooling). Solid black lines indicate 9.8°N, the equator and 9.8°S.

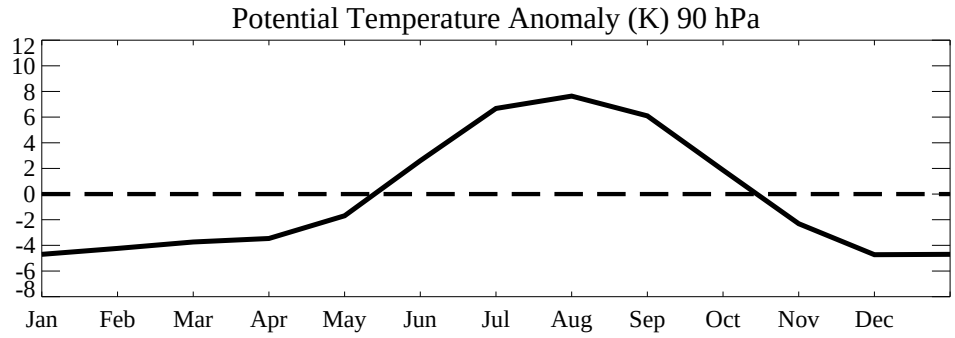

(a) Potential temperature anomaly

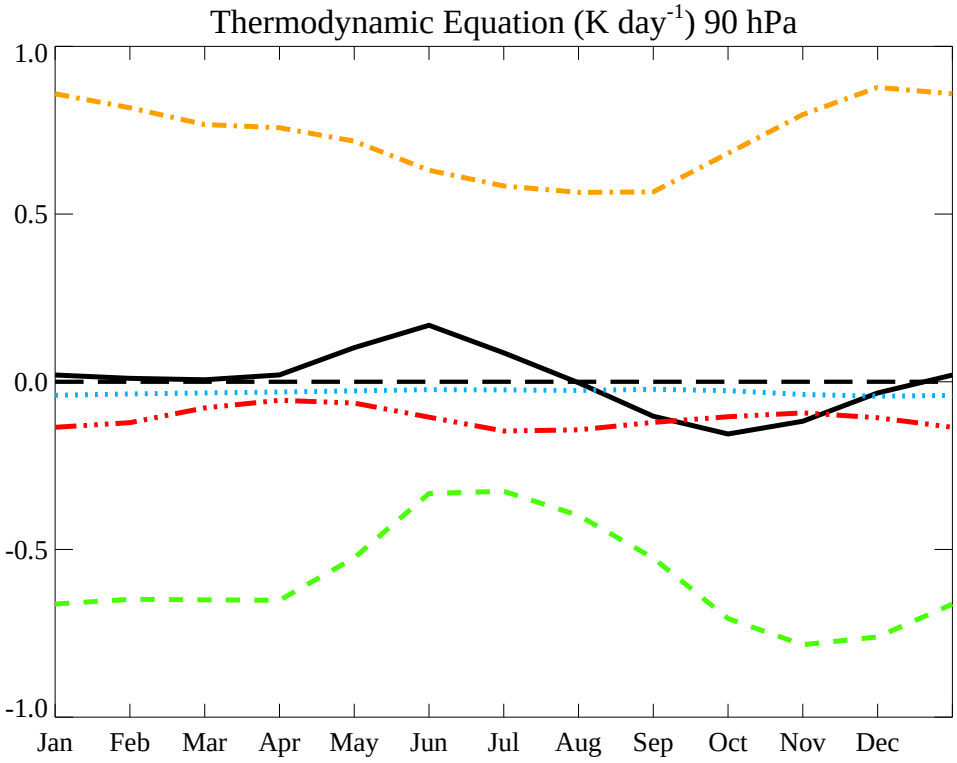

(b) Terms in the thermodynamic equation

Figure 3.5: Mean annual cycle averaged from 9.8°N to 9.8°S at 90 hPa of (a) the potential temperature and (b) the terms in the thermodynamic equation at 90 hPa. In (b) the terms are $\frac{\partial \overline{\theta}}{\partial t}$ (solid black line), $-\frac{\overline{v}^*}{R_e}\frac{\partial \overline{\theta}}{\partial \phi}$ (dotted blue line), $-\overline{\omega}^*\frac{\partial \overline{\theta}}{\partial p}$ (dashed green line), $\overline{Q}$ (dashed and dotted orange line) and $-\frac{\partial}{\partial p}\left(\frac{\overline{v'\theta'}\,\overline{\theta}_\phi}{R_e\overline{\theta}_p}+\overline{\omega'\theta'}\right)$ (dash and three dotted red line).

from positive (increasing potential temperature) to negative (decreasing potential temperature) in August, when there is a maximum potential temperature. As the potential temperature decreases from August onwards the diabatic heating responds by increasing again, from its minimum in September, slightly lagged with respect to the maximum in potential temperature.

In October the adiabatic cooling slows its rate of increase, reaching a maximum cooling in November. The $\frac{\partial\overline{\theta}}{\partial t}$ reaches a minimum in October and increases as the adiabatic cooling decreases. The diabatic heating is still increasing as the temperature is still decreasing and is partly countering the adiabatic cooling, causing $\frac{\partial\overline{\theta}}{\partial t}$ to increase before the adiabatic cooling decreases. When $\frac{\partial\overline{\theta}}{\partial t}$ crosses zero again, in December, the potential temperature reaches a minimum and the diabatic heating reaches a maximum and then begins to decrease. From December to April the adiabatic cooling and $\frac{\partial\overline{\theta}}{\partial t}$ terms remain fairly constant. The $\frac{\partial\overline{\theta}}{\partial t}$ term is slightly positive between December to April and the potential temperature increases slowly, with a corresponding slow decrease in diabatic heating.

This analysis indicates that it is the adiabatic cooling, i.e. vertical motion, which largely drives the annual cycle in the temperatures in this region, with the diabatic heating responding to the temperature changes.

3.3 Simple model for potential temperature

To test the hypothesis that the adiabatic cooling drives the annual in temperatures, a simple one-dimensional model was formed. A simplified version of the thermodynamic equation was used;

$$\frac{\partial\overline{\theta}}{\partial t} + \alpha\overline{\theta} = S \tag{3.1}$$

where α^{-1} is the radiative relaxation timescale and the forcing term is $S = -\overline{\omega}^{*}\frac{\partial\overline{\theta}}{\partial p}$, the adiabatic heating and cooling. Here $\overline{\theta}$ and S have had their time means removed. This model assumes that solar heating does not have any annual variation. This equation has the solution;

$$\theta(t) = e^{-\alpha t}\int_0^t Se^{\alpha t}dt + \frac{e^{-\alpha t}}{e^{\alpha T}-1}\int_0^T Se^{\alpha t}dt \tag{3.2}$$

and is periodic in t with period T (1 year), $\theta(0) = \theta(T)$.

This equation was then forced with the adiabatic cooling data and the result

compared with the potential temperature data. Radiative forcing timescales of 10, 20, 40 and 80 days were used. The results for 90 hPa are shown in figure 3.6. This shows that, for a radiative timescale of 40 days, most of the annual cycle in potential temperature can be explained by adiabatic forcing. The fit is worst from November to January, where (figure 3.5) the diabatic heating is still increasing and counters the adiabatic cooling.

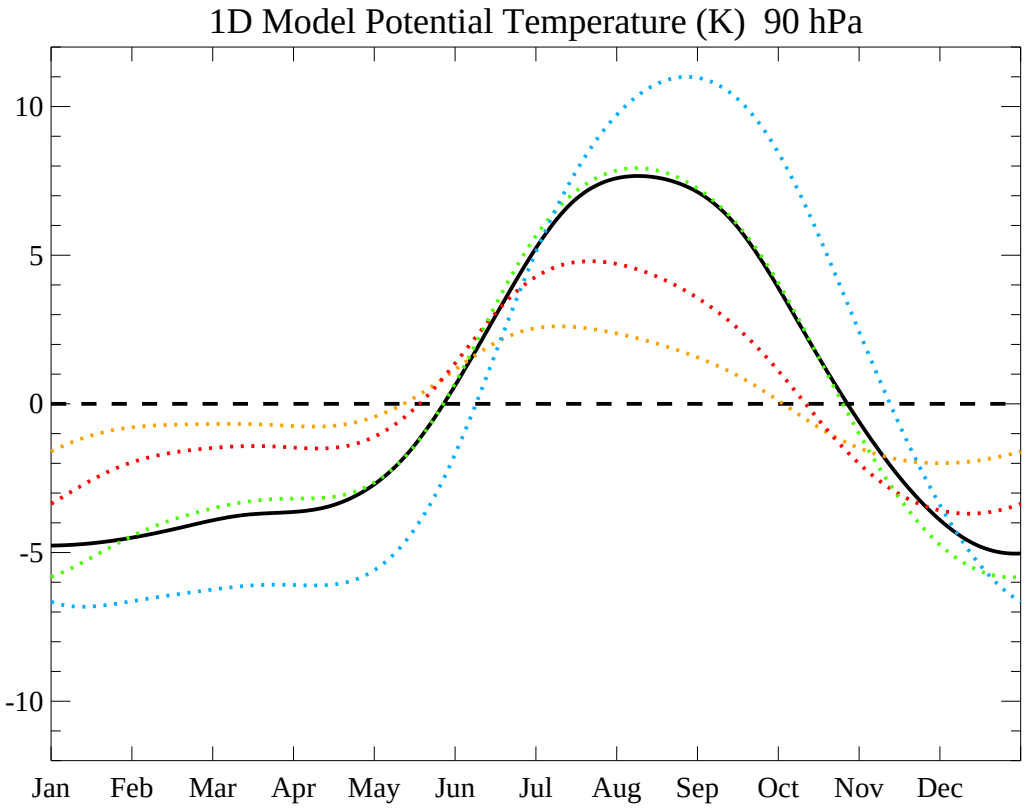

Figure 3.6: 1D model potential temperature at 90 hPa. The solid black line is the ECMWF data potential temperature. The dotted lines show the potential temperatures calculated from the adiabatic cooling for radiative timescales of 10 days (orange), 20 days (red), 40 days (green) and 80 days(blue).

This analysis was done for a number of levels. The results for 70 hPa are shown in figure 3.7. At 110 hPa, the radiative timescale which fits the model is 10 days and at 70 hPa it is 80 days. However the model does not work well at 50 hPa, where ozone may also have a forcing effect. For 110 to 70 hPa there is a rapid increase in radiative timescale with height. Randel *et al.* (2002) use a similar model to look at phase relationships between temperature and vertical velocity using UK Met Office and NCEP analysis data. They are also using a wider latitude band (30°N to 30°S). They find a similar increase in radiative relaxation timescale with

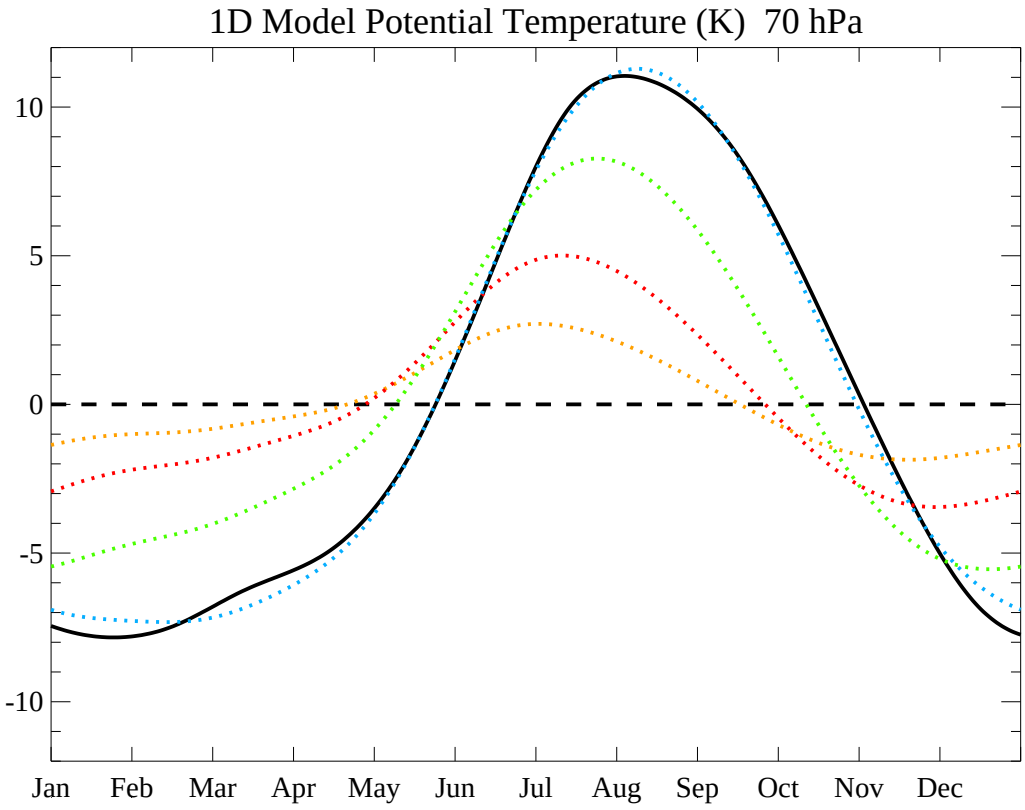

Figure 3.7: 1D model potential temperature at 70 hPa. The solid black line is the ECMWF data potential temperature. The dotted lines show the potential temperatures calculated from the adiabatic cooling for radiative timescales of 10 days (orange), 20 days (red), 40 days (green) and 80 days(blue).

height, although their timescales are longer than those found here. They also find a decrease in radiative relaxation timescale above 70 hPa.

A simple Newtonian cooling model will give long radiative relaxation timescales in the tropical tropopause region, with decreasing timescales in the warmer upper stratosphere (Ramanathan *et al.*, 1983). This is not surprising because these relaxation timescales depend inversely on temperature and there is a temperature minimum in this region. Another reason for the relatively long radiative relaxation timescales in the tropopause region is the near balance between weak long wave cooling by greenhouse gases and weak heating by ozone (Clough and Iacono, 1995; Hood, 2003). Estimates of these heating rates based on longwave heating rate calculations, such as those of Kiehl and Solomon (1986) and Mlynczak *et al.* (1999) also show a maximum in the tropical tropopause region and decreasing timescales above. In the stratosphere, particularly noticeably in the polar stratosphere, the timescales exhibit strong annual cycles and a strong relationship to temperature

(Newman and Rosenfield, 1997). The timescale calculated also depends on the vertical scale of the temperature anomaly assumed in the calculation (Fels, 1982; Bresser *et al.*, 1995), such as that of planetary waves. Using a radiative transfer model, Hartmann *et al.* (2001) produces similar profiles to those of Randel *et al.* (2002). They associate the increase in radiative relaxation timescale in the upper troposphere with the decrease in net cooling near 200 hPa. This is due to the absorption and emission of longwave radiation by water vapour becoming ineffective at the low temperatures in this region.

3.4 Resolving the mean vertical transport near the tropopause

Having established that it is the adiabatic cooling term that drives the potential temperature changes, the next stage is to investigate what is driving the adiabatic cooling term, $-\overline{\omega}^* \frac{\partial \overline{\theta}}{\partial p}$. The vertical component of the residual mean meridional circulation, $\overline{\omega}^*$, is considered.

Figure 3.8 shows the annual cycle in $\overline{\omega}^*$ from 40°N to 40°S at 90 hPa. Note that because pressure units are in use here negative values of $\overline{\omega}^*$ correspond to upwelling, positive values to downwelling. The pattern in $\overline{\omega}^*$ in figure 3.8 is very similar to that of adiabatic cooling in figure 3.3. There is a strong upwelling near the equator in October and November, corresponding to the region of enhanced cooling in figure 3.3. There is also a strong upwelling pushed north of the equator from late January and through NH summer, which follows a region of enhanced cooling. There is a small region of weak downwelling just north of the equator in NH summer, at the same time and in the same location as a region of adiabatic warming (as opposed to reduced adiabatic cooling). The similarity between the figures confirms that the residual vertical velocity is driving the changes in adiabatic cooling. The movement of the tropical band of upwelling towards the summer hemisphere has been previously noted by Rosenlof (1995). Plumb and Eluskiewicz (1999) also noted that, in the annual mean, there was always upwelling within about 20° of the equator, with enhanced upwelling migrating towards the summer hemisphere.

Figure 3.9 shows a vertical cross-section of the residual mean vertical velocity averaged from 9.8°N to 9.8°S. The figure shows only the upper troposphere and stratosphere, from 150 hPa to 10 hPa, i.e. the top of the data set. A clear annual cycle can be seen at most levels, with enhanced upwelling in NH winter and decreased upwelling in NH summer. At 90 hPa the maximum upwelling is

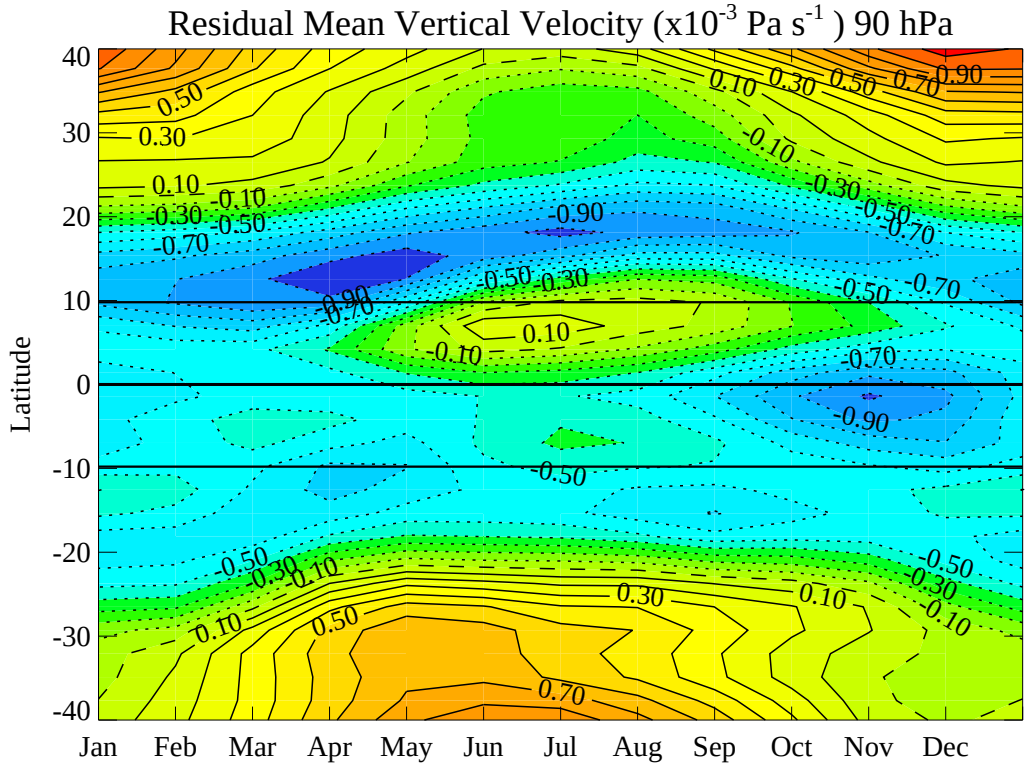

Figure 3.8: Mean annual cycle of the residual mean vertical velocity at 90 hPa. The contour interval is $0.2\times10^{-3}\,\mathrm{Pa\,s^{-1}}$. Solid contours indicate positive values (downwelling), dashed contours indicate zero values and dotted contours indicate negative values (upwelling).

$-0.7\times10^{-3}\,\mathrm{Pa\,s^{-1}}$ and occurs from late November to December and the minimum is $-0.25\times10^{-3}\,\mathrm{Pa\,s^{-1}}$ and occurs from June to August. Figure 3.10 shows the equivalent figure with the annual mean removed from the data. This figure shows only 110 hPa to 10 hPa due to the large decrease in magnitude of the annual cycle with height. The decreased upwelling in NH summer is earlier in the year at higher levels, indicating the possibility of different processes with different annual cycles driving the annual cycle in upwelling in the troposphere and stratosphere respectively.

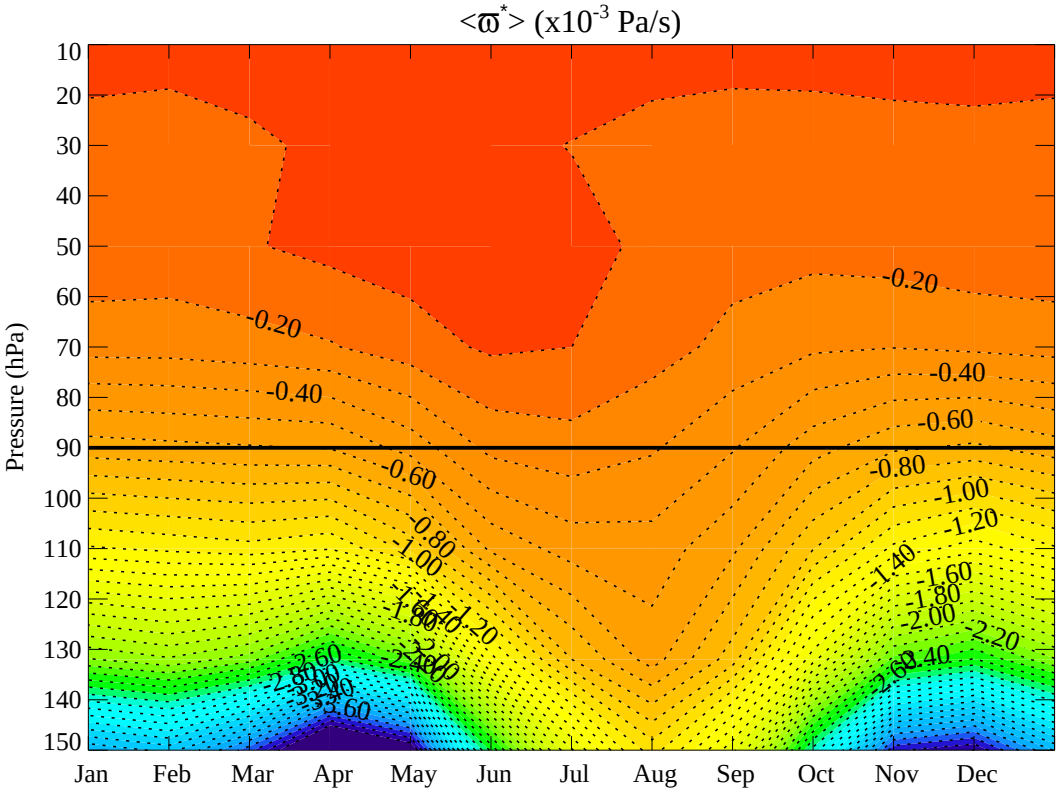

Figure 3.9: Mean annual cycle of the residual mean vertical velocity, $\overline{\omega}^*$, averaged from 9.8°N to 9.8°S. The 90 hPa level is indicated with a solid black line. The contour interval is $0.1\times10^{-3}\,\mathrm{Pa\,s^{-1}}$. Dotted contours indicate negative values (upwelling).

3.4.1 The mass continuity equation

The average vertical velocity across a latitude band from ϕ_L to $-\phi_L$ can be found by integrating the mass continuity equation (2.9d) to give:

$$\langle\overline{\omega}^*\rangle = \frac{-\cos\phi_L}{\int_{-\phi_L}^{\phi_L} R_e\cos\phi d\phi}\int_p^{p=0}\overline{v}^*\left(\phi_L\right)-\overline{v}^*\left(-\phi_L\right)dp. \tag{3.3}$$

Hence the average vertical velocity in a latitude band from ϕ_L to $-\phi_L$ is given by the sum of the net outflow or mass divergence from the horizontal velocities at the edge of the band, $\overline{v}^*(\phi_L)$ and $\overline{v}^*(-\phi_L)$, summed from the top of the atmosphere down to that level, with the upper boundary condition as $\overline{\omega}^*(p=0)=0$. Haynes *et al.* (1991) show that the calculation from the top of the atmosphere downwards ("downward control"), rather than from the bottom of the atmosphere upwards ("upward control"), is the appropriate calculation to do.

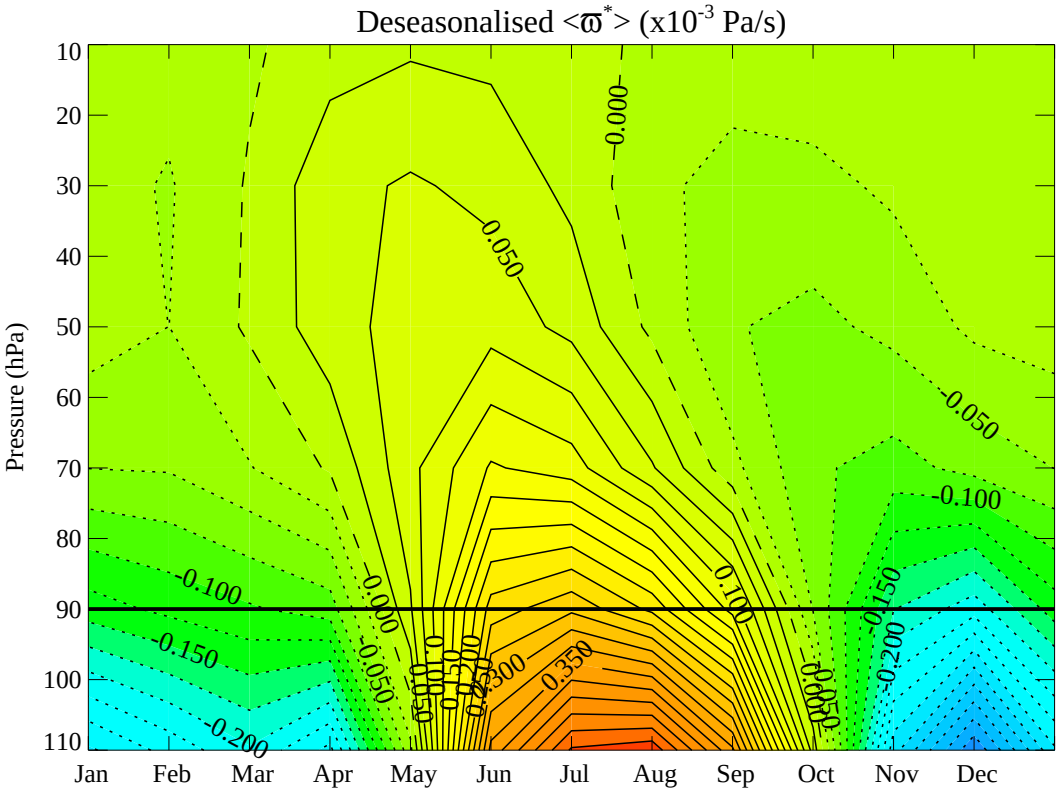

Figure 3.10: Annual cycle of the residual mean vertical velocity, $\overline{\omega}^*$, averaged from 9.8°N to 9.8°S with the annual mean removed. The 90 hPa level is indicated with a solid black line. The contour interval is $0.025\times10^{-3}\,\mathrm{Pa\,s^{-1}}$.

By considering the contributions to the integral from each level, it can be seen which of the upper levels give the most important contributions to the mean upwelling at a particular level. Figure 3.11 illustrates this concept. The outflow from the horizontal velocities at a level drives upwelling from the levels below.

Figure 3.12 shows the annual cycle in the integrand of equation 3.3. The latitude band used for the integration is 9.8°N to 9.8°S so the horizontal velocities used are $\overline{v}^*$ (9.8°) and $\overline{v}^*$ (−9.8°). The figure shows the contributions to the integral for the mean vertical velocity at 90 hPa, showing only the levels down to 90 hPa. Summing these contributions will give the mean vertical velocity between 9.8°N and 9.8°S at 90 hPa.

Figure 3.13 shows the equivalent figure to 3.12 with the annual mean removed. This gives a clearer picture of how the levels in the integrand contribute to the annual cycle in $\overline{\omega}^*$.

The largest variation in the annual cycle in this figure is in the lowest level, at 90 hPa where the integrand is $0.14\times10^{-3}\,\mathrm{Pa\,s^{-1}}$ below the mean in December

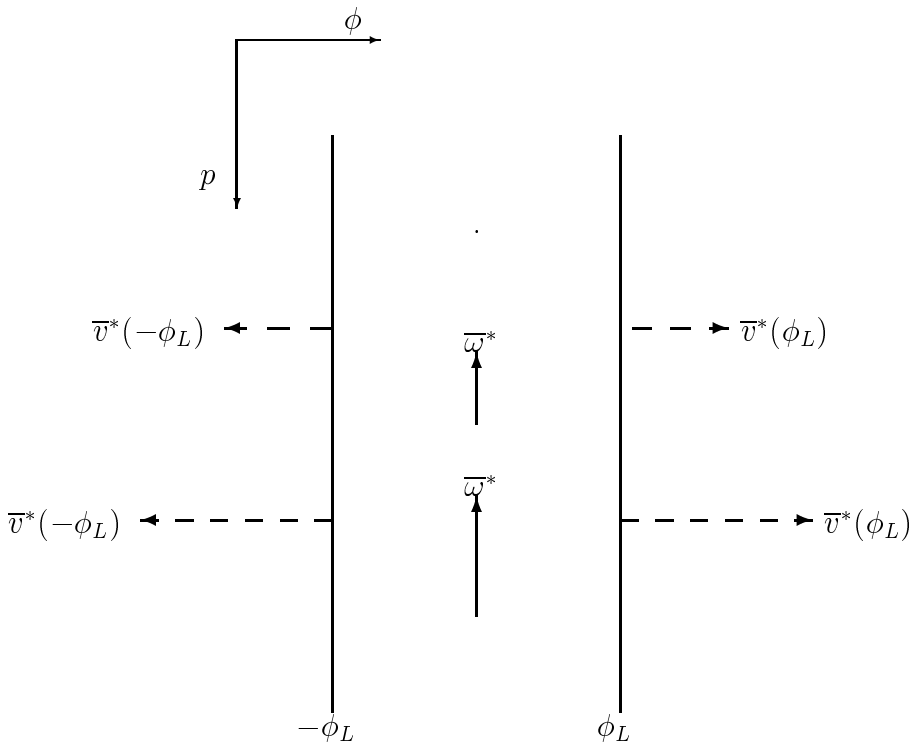

Figure 3.11: Diagram to illustrate the contributions from each level to the integral of the mass continuity equation.

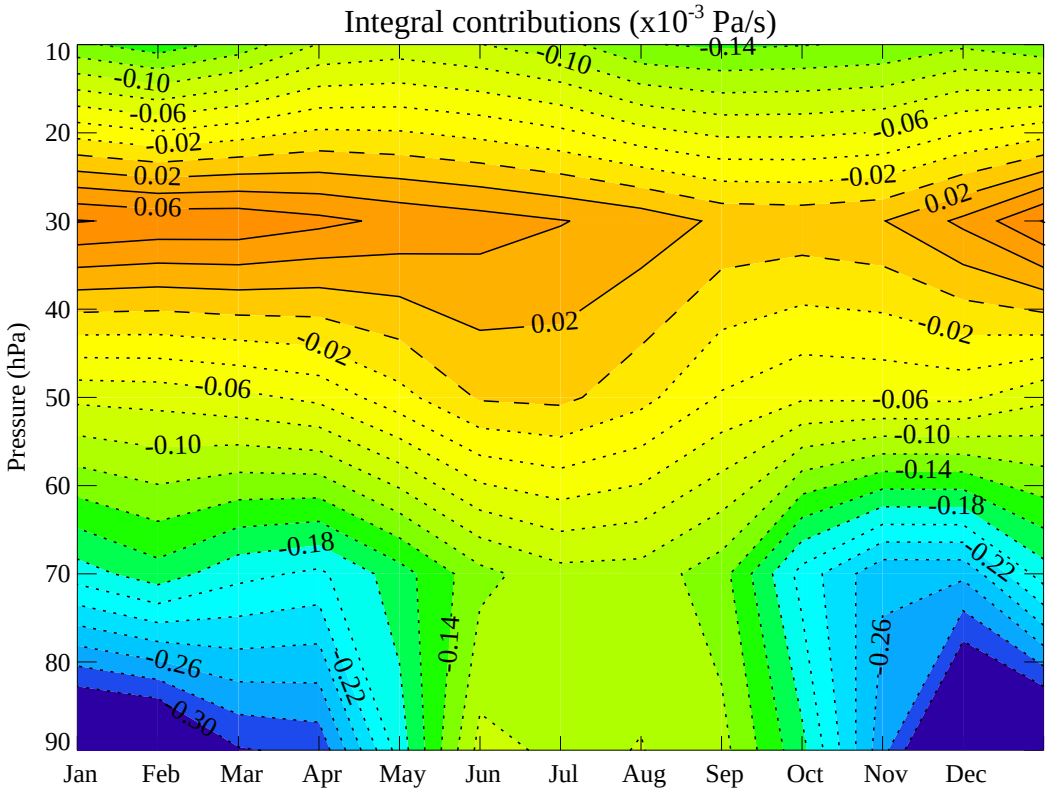

Figure 3.12: Mean annual cycle of the integrand of equation 3.3, taken at the limits 9.8°N and 9.8°S, showing from the top of the atmosphere down to 90 hPa. This is multiplied by the factor in front of the integral sign in equation 3.3 to be comparable with $\overline{\omega}^*$. The contour interval is $0.02\times10^{-3}\,\mathrm{Pa\,s^{-1}}$. Solid contours indicate positive values (downwelling), dashed contours indicate zero values and dotted contours indicate negative values (upwelling).

and $0.13\times10^{-3}\,\mathrm{Pa\,s^{-1}}$ above the mean in June. This has the same timing as the annual cycle in $\overline{\omega}^*$ at this level. The annual cycle at 70 hPa is just under half this magnitude, where the integrand is $0.06\times10^{-3}\,\mathrm{Pa\,s^{-1}}$ below the mean in November and $0.06\times10^{-3}\,\mathrm{Pa\,s^{-1}}$ above the mean in July, again with the same timing as the annual cycle in $\overline{\omega}^*$. Higher levels do not show as large a magnitude in annual cycle, as well as the timing of the annual cycle being slightly earlier. Around 30 hPa the annual cycle is in the opposite sense to that required for driving $\overline{\omega}^*$ at 90 hPa, with the maximum in NH winter and minimum in late NH summer. This could be due to ascending branch of the mean upwelling moving across the equator twice yearly or the data being less accurate at the highest levels. Above 30 hPa there is a small semi-annual cycle.

Therefore most of the annual cycle in $\overline{\omega}^*$ between 9.8°N and 9.8°S at 90 hPa is

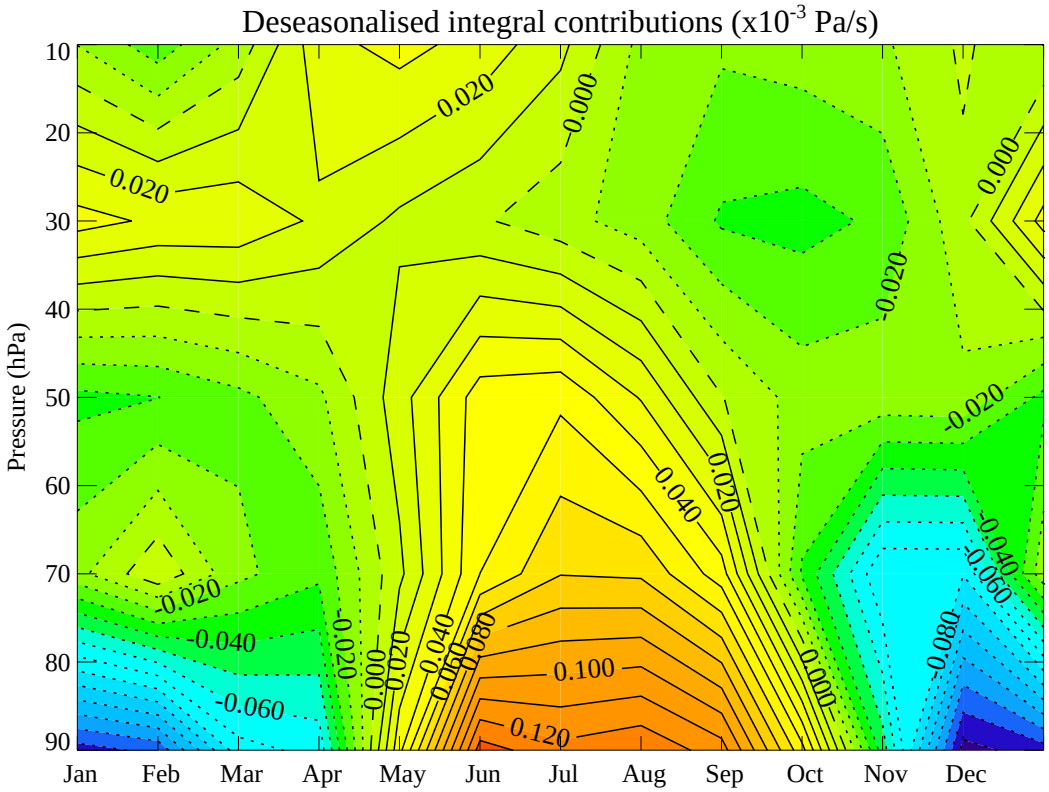

Figure 3.13: Mean annual cycle of the integrand of equation 3.3, taken at the limits 9.8°N and 9.8°S, showing from the top of the atmosphere down to 90 hPa. The annual mean has been removed. The contour interval is 0.01×10^{-3} Pa s^{-1}. Solid contours indicate positive values (downwelling), dashed contours indicate zero values and dotted contours indicate negative values (upwelling).

driven by the horizontal velocities near 90 hPa.

This result cannot be compared with others due to a lack of similar studies. Rosenlof (1995) looked at using a discretised integral of a form of the mass continuity equation to examine what portion of the forcing was from different layers. However she considered the portion of mass flux at 70 hPa which could be accounted for using different upper limits for the integral, which is a very different method to the one employed here.

As a check, figure 3.14 shows $\overline{\omega}^*$ calculated on half model levels from integrating $\overline{v}^*$ at the limits 9.8°N and 9.8°S and figure 3.15 shows this interpolated onto full model levels. These figures are very similar to figure 3.9 which shows $\overline{\omega}^*$ calculated from the definition given by equation 2.8b. The magnitude of the annual cycle at 90 hPa is slightly greater for $\overline{\omega}^*$ calculated by integrating the mass continuity equation, with upwelling reaching lower values in NH summer.

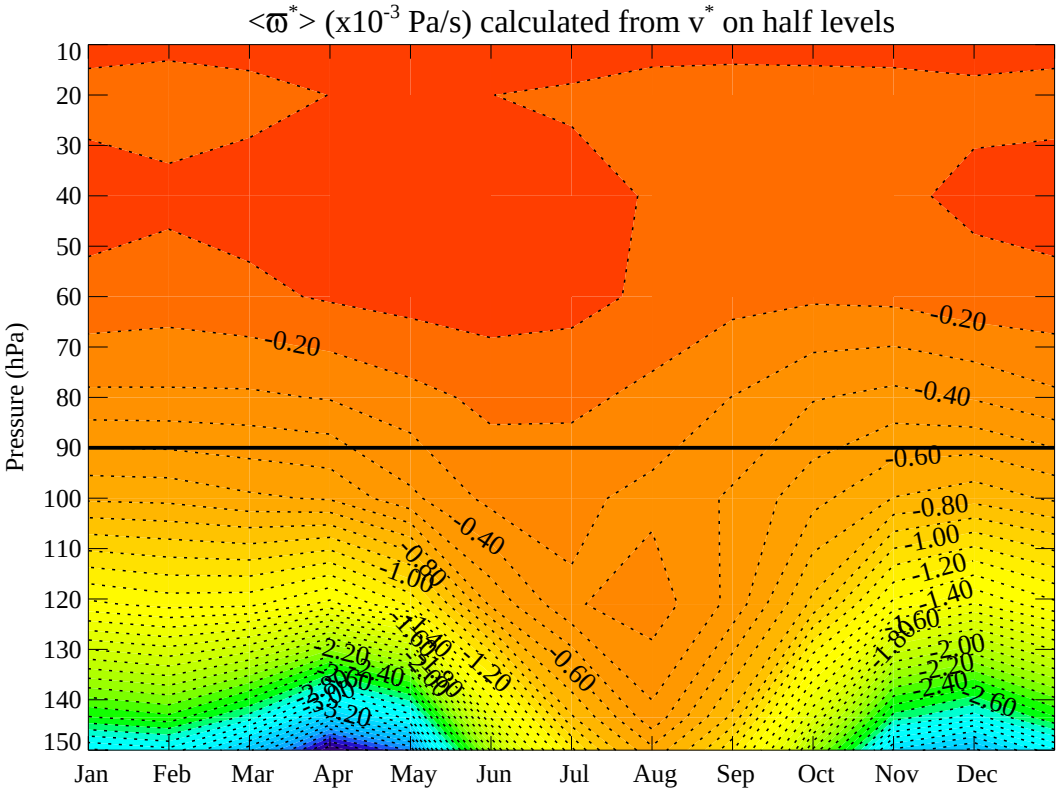

Figure 3.14: Mean annual cycle of the residual mean vertical velocity, $\overline{\omega}^*$, as calculated on half model levels from $\overline{v}^*$ using equation 3.3 with latitude limits 9.8°N and 9.8°S. The 90 hPa level is indicated with a solid black line. The contour interval is $0.1\times10^{-3}\,\mathrm{Pa\,s^{-1}}$. Dotted contours indicate negative values (upwelling).

For comparison, the downward control principle proposed by Haynes *et al.* (1991) uses a stream function to define the residual velocities. Their paper uses the TEM equations in terms of the log-pressure vertical coordinate, z. They write the mass continuity equation as

$$\frac{1}{R_e\cos\phi}\frac{\partial}{\partial\phi}\left(\overline{v}^*\cos\phi\right)+\frac{1}{\rho_0}\frac{\partial}{\partial z}\left(\rho_0\overline{w}^*\right)=0, \tag{3.4}$$

where $\rho_0=\exp\left(-z/H\right)$.

They then define the meridional circulation in terms of a stream function, $\psi(\phi,z)$, such that

$$\overline{v}^*=-\frac{1}{\rho_0\cos\phi}\frac{\partial\psi}{\partial p}, \tag{3.5a}$$

$$\overline{\omega}^*=\frac{1}{R_e\rho_0\cos\phi}\frac{\partial\psi}{\partial\phi}. \tag{3.5b}$$

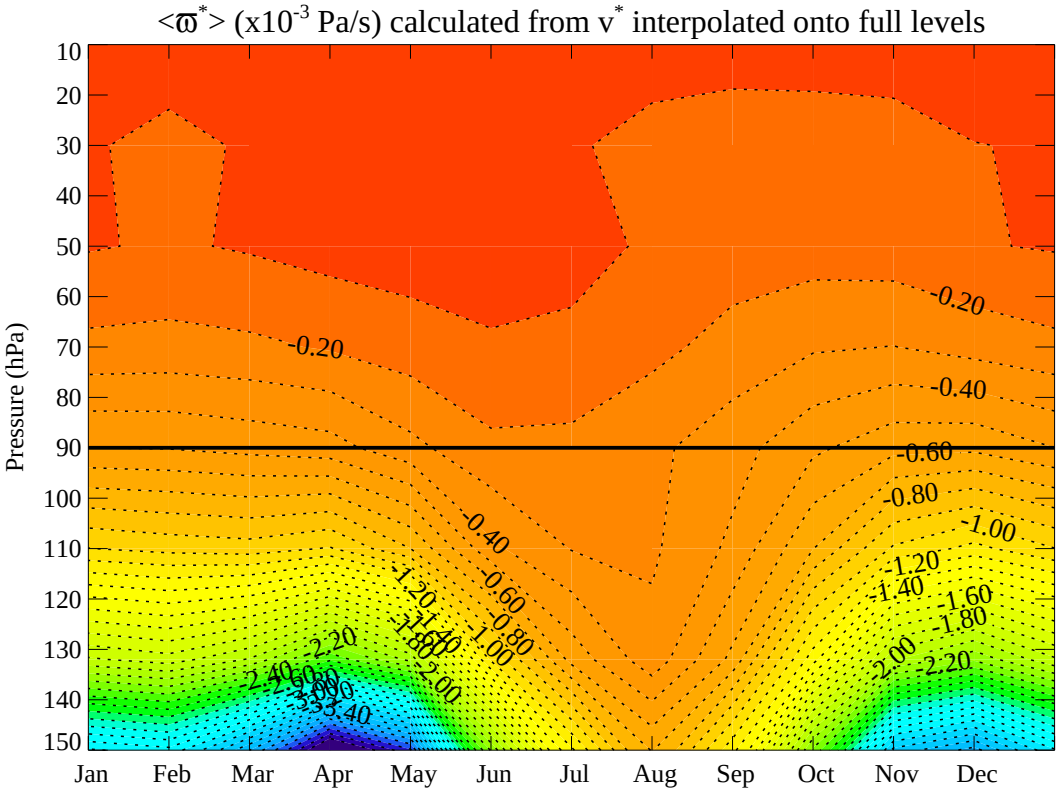

Figure 3.15: Mean annual cycle of the residual mean vertical velocity, $\overline{\omega}^*$, calculated from integrating the mass continuity equation then interpolated onto full model levels. The 90 hPa level is indicated with a solid black line. The contour interval is $0.1\times10^{-3}\,\mathrm{Pa\,s^{-1}}$. Dotted contours indicate negative values (upwelling).

They then rewrite the zonal momentum equation, assuming a steady state atmosphere, to give

$$\frac{\partial(\psi,\overline{m})}{\partial(\phi,z)} = \frac{\partial\psi}{\partial\phi}\frac{\partial\overline{m}}{\partial z} - \frac{\partial\psi}{\partial z}\frac{\partial\overline{m}}{\partial\phi} = \rho_0 R_e^2 \overline{\mathfrak{F}} \cos^2\phi, \tag{3.6}$$

where $\overline{m} = R_e\cos\phi(\overline{u} + R_e\Omega\cos\phi)$, the angular momentum per unit mass, and $\overline{\mathfrak{F}} = \frac{1}{R_e\cos\phi}\nabla.\mathbf{F} + \overline{X}$. The zonal momentum equation is rearranged and integrated to find the stream function:

$$\psi(\phi,z) = \int_z^\infty \left\{ \frac{\rho_0 R_e^2\,\overline{\mathfrak{F}}\cos^2\phi}{\overline{m}_\phi} \right\}_{\phi=\phi(z')} dz', \tag{3.7}$$

where the integration is along a contour of constant angular momentum. Boundary conditions are that $\rho_0\overline{w}^* \dashrightarrow 0$ and $\psi \dashrightarrow 0$ as $z \dashrightarrow \infty$. From this $\overline{w}^*$ can then be calculated from the stream function. In this research $\overline{\omega}^*$ is calculated from $\overline{\omega}$

according to equation 2.8b.

The downward control principle proposed by Haynes *et al.* (1991) breaks down where angular momentum surfaces do not span the atmosphere in the vertical. Rosenlof and Holton (1993) showed that this occurs equatorward of 15°, concluding that downward control is only useful poleward of 15°. They also noted that between 15° and 30° extra care was needed for the calculation due to "significant deviations from a vertically oriented line."

Holton *et al.* (1995) show a generalised form of downward control, where the steady state condition is not used. They show that a forcing in the lower stratospheric extra-tropics can reach sideways across the tropics and into the opposite hemisphere; "non-local control". In the steady state the forcing is entirely downwards, returning to the concept of downward control. In the tropics the timescale to reach a steady state is very long, such that the steady state limit and downward control is useful only in the extra-tropics.

Earlier in this section $\overline{\omega}^*$ calculated directly from $\overline{v}^*$ was shown to be similar to $\overline{\omega}^*$ calculated from the definition given in equation 2.8b, the method used in this research. The assumption of a steady state has not been made and the limitation of angular momentum surfaces spanning the atmosphere in the vertical does not apply. This research is also looking mainly at the balance of terms rather than at using a driving term to calculate the upwelling. The data set used here is the best data set available for the tropical atmosphere. Therefore the calculations used in this research can be done in the tropics, unlike the calculation for downward control of Haynes *et al.* (1991).

3.5 The annual cycle in the terms of the zonal momentum equation

In order to investigate what is driving the changes in the outflow and the horizontal velocities near 90 hPa, the zonal momentum equation (2.9a) is examined. Equation 2.9a rearranges to give:

$$\overline{v}^* \left(f - \frac{1}{R_e \cos\phi} \frac{\partial}{\partial \phi} \left(\overline{u} \cos\phi \right) \right) = \frac{\partial \overline{u}}{\partial t} + \overline{\omega}^* \frac{\partial \overline{u}}{\partial p} - \frac{1}{R_e \cos\phi} \nabla . \mathbf{F} - \overline{X}, \qquad (3.8)$$

which can be written in terms of $\overline{v}^*$ as

$$\overline{v}^* = \frac{1}{\overline{\zeta}_a}\left(\frac{\partial \overline{u}}{\partial t} + \overline{\omega}^*\frac{\partial \overline{u}}{\partial p} - \frac{1}{R_e \cos\phi}\nabla.\mathbf{F} - \overline{X}\right), \tag{3.9}$$

where the absolute vorticity, $\overline{\zeta}_a$, is given by

$$\overline{\zeta}_a = f - \frac{1}{R_e \cos\phi}\frac{\partial}{\partial \phi}\left(\overline{u}\cos\phi\right). \tag{3.10}$$

Figure 3.16 shows the annual cycle of the terms in the zonal momentum equation (3.9) for the latitude band 9.8°N to 9.8°S at 90 hPa. From section 3.4.1 the annual cycle of the outflow from $\overline{v}^*$ at the edges of the latitude band drives the annual cycle in the upwelling of $\overline{\omega}^*$ at that level. Because $\overline{\zeta}_a$ changes sign at the equator it is the difference between $\overline{v}^*$ at 9.8°N and 9.8°S that is required, and hence the difference in the terms at those latitudes for each component of the

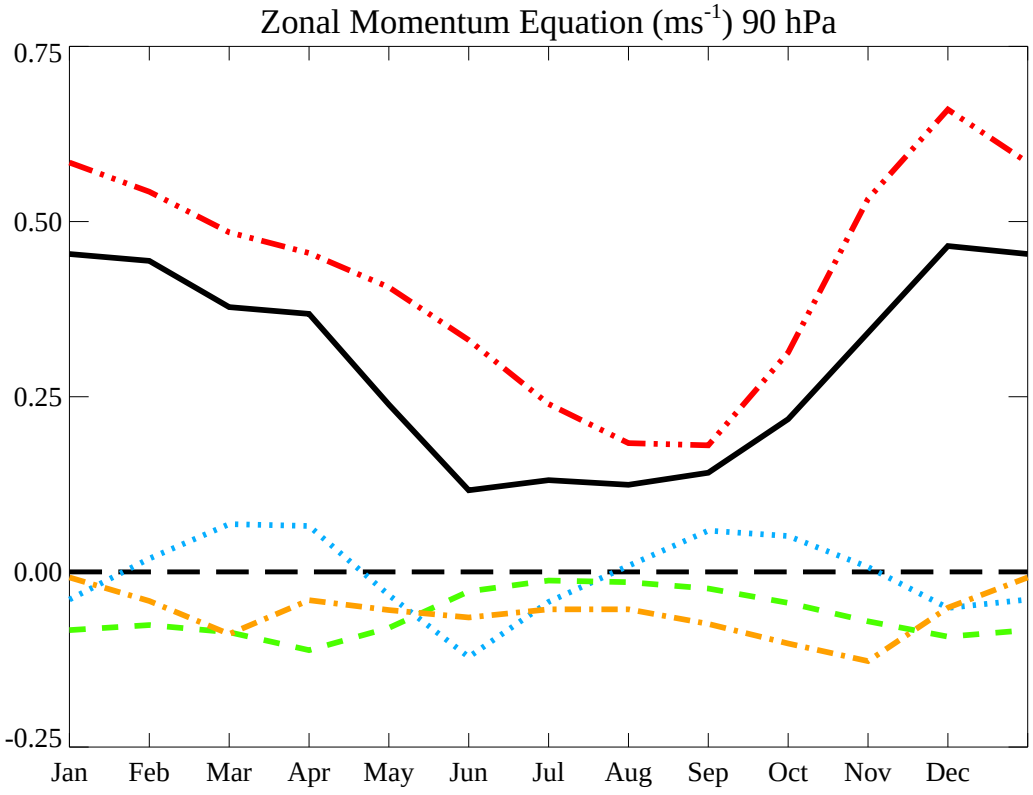

Figure 3.16: Mean annual cycle of the terms in the zonal momentum equation divided by $\overline{\zeta}_a$ (equation 3.9) at 90 hPa, terms at 9.8°N minus terms at 9.8°S. The terms are $\overline{v}^*$ (solid black line), $\frac{1}{\overline{\zeta}_a}\frac{\partial \overline{u}}{\partial t}$ (dotted blue line), $\frac{-\overline{\omega}^*}{\overline{\zeta}_a}\frac{\partial \overline{u}}{\partial p}$ (dashed green line), $\frac{1}{R_e\cos\phi}\frac{\nabla.\mathbf{F}}{\overline{\zeta}_a}$ (dash and three dotted red line) and $\frac{\overline{X}}{\overline{\zeta}_a}$ (dashed and dotted orange line).

zonal momentum equation. The figure shows what is forcing the outflow from the edge of the latitude band at 9.8°N and 9.8°S at 90 hPa.

There is a clear annual cycle in $\overline{v}^*$ (black), which is low in NH summer and higher in NH winter, corresponding with previous annual cycles shown. The strongest driving for this is the EP flux divergence divided by the absolute vorticity (red). There is some contribution to the driving by the rate of change of zonal wind, $\frac{1}{\overline{\zeta}_a}\frac{\partial \overline{u}}{\partial t}$, (blue). Both the EP flux divergence and the rate of change of zonal wind contribute to the decrease in $\overline{v}^*$ between April and June whereas the rate of change of zonal wind opposes the decrease in EP flux divergence between June and September, such that $\overline{v}^*$ barely changes during this time. The rate of change of zonal wind has a semi-annual cycle which Randel *et al.* (2002) attribute to the NH summer monsoon circulation, with a larger variation between April and September than between October and March, but has a mean of near zero over the annual cycle. Randel *et al.* (2002) also show that the majority of the annual cycle in $\overline{\omega}^*$ is due to changes in EP flux divergence and not the rate of change of zonal wind. The remaining terms in the zonal momentum equation, $\frac{-\overline{\omega}^*}{\overline{\zeta}_a}\frac{\partial \overline{u}}{\partial p}$ (green) and the residual non-conservative forcing $\frac{\overline{X}}{\overline{\zeta}_a}$ (orange), are small and negative throughout the year, contributing net inflow to the region, opposing $\overline{v}^*$.

3.6 The 70 hPa level

The main body of this thesis concentrates on the 90 hPa level, being just above the tropical tropopause—the main region of interest. However figure 1.2 shows that the annual cycle in temperature is a maximum at 70 hPa. Section 3.3 showed that adiabatic cooling drives the potential temperature at 70 hPa with a radiative forcing timescale of 80 days–twice that at 90 hPa. Also, in section 3.4.1, it was seen that the annual cycle in the integrand of the integral for $\overline{\omega}^*$ was large at 70 hPa, just under half that at 90 hPa, concluding that the annual cycle in upwelling was driven by levels near 90 hPa (including 70 hPa). The purpose of this section is to have a closer look at 70 hPa in a similar way to that of 90 hPa.

The annual cycle in the rate of change of potential temperature with respect to time, $\frac{\partial \overline{\theta}}{\partial t}$, is shown in figure 3.17 and can be compared with figure 3.2 for 90 hPa. A similar pattern of warming and cooling can be seen in the tropics. At 70 hPa the band of nearly constant rate of change of potential temperature with latitude is wider, reaching to about 15°. Whereas at 90 hPa there is little change in the rate of change of potential temperature between January and April, at 70 hPa there is

a gentle increase. This gradient increases dramatically in April at the same time as for 90 hPa and the peak in warming, decrease and zero line occur at the same time. The peak in cooling is possibly slightly later, in mid-October rather than at the beginning of October and the zero line for changing from cooling to warming occurs slightly later, at the end of December rather than in the middle. There are also a few differences in the timing of changes in warming and cooling in the extratropics.

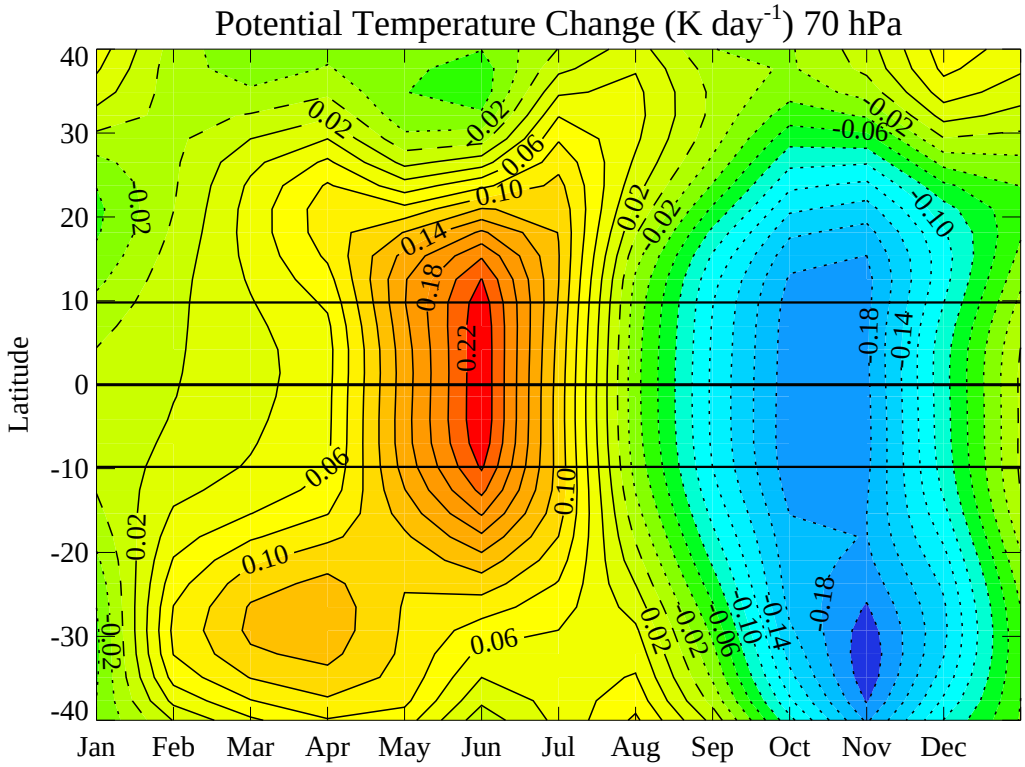

Figure 3.17: Mean annual cycle of the rate of change of zonal mean potential temperature at 70 hPa. The contour interval is $0.02\,\mathrm{K\,day^{-1}}$. Solid contours indicate positive values (increasing temperatures), dashed contours indicate zero values (no change) and dotted contours indicate negative values (decreasing temperatures). Solid black lines indicate 9.8°N, the equator and 9.8°S.

The adiabatic cooling term, $-\overline{\omega}^{*}\frac{\partial\overline{\theta}}{\partial p}$, is shown in figure 3.18, this can be compared with figure 3.3 for 90 hPa. The main features of the two plots are similar. As for 90 hPa there is a strong cooling near the equator in October and November and a warming just north of the equator in June and July corresponding with the extrema in $\frac{\partial\overline{\theta}}{\partial t}$. However the strong cooling in the NH now reaches its maximum in NH spring, rather than summer and the warming in NH summer lasts for longer and penetrates further north, to north of 10°N. Diabatic heating (not shown) is

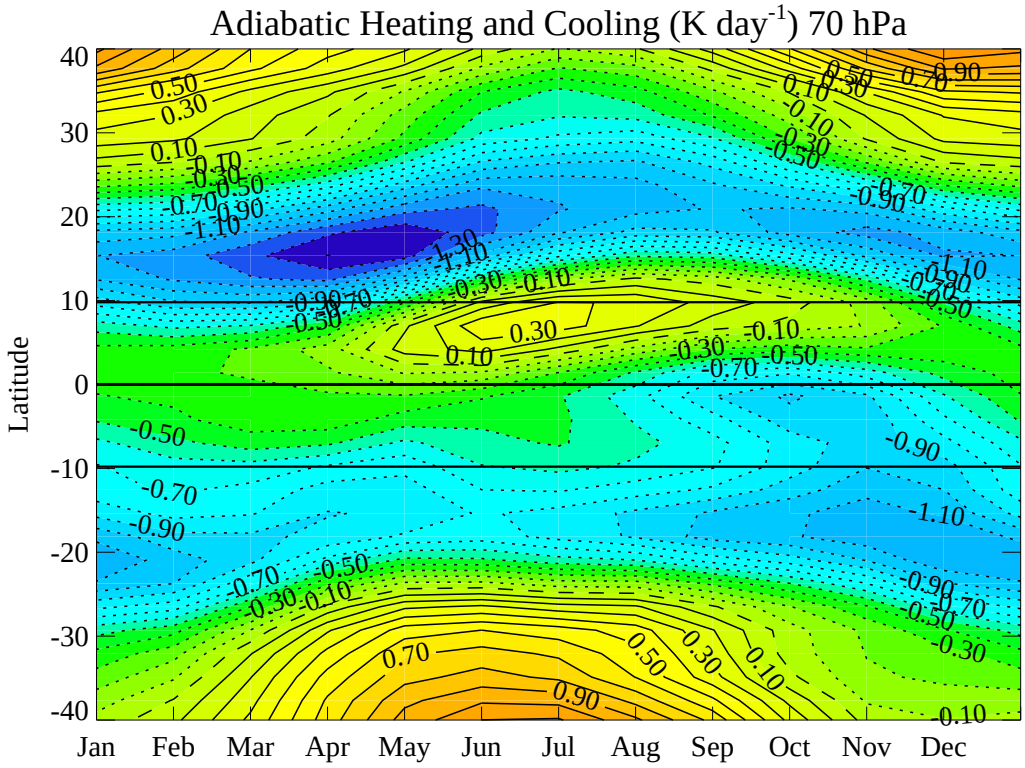

Figure 3.18: Mean annual cycle of the zonal mean adiabatic cooling, $-\overline{\omega}^* \frac{\partial \overline{\theta}}{\partial p}$, at 70 hPa. The contour interval is 0.1 K day^{-1}. Solid contours indicate positive values (heating), dashed contours indicate zero values and dotted contours indicate negative values (cooling). Solid black lines indicate 9.8°N, the equator and 9.8°S.

fairly similar at 70 hPa to that at 90 hPa (figure 3.4) but the minimum in heating near 10°N in NH summer has intensified and is cooling.

Figure 3.19 shows the annual cycle in potential temperature anomaly (panel (a)) and each of the terms in the thermodynamic equation (panel (b)) averaged across the latitude band 9.8°N to 9.8°S at 70 hPa. This can be compared with figure 3.5 for 90 hPa.

The essential process is very similar to that at 90 hPa. From April to August the adiabatic cooling changes, with $\frac{\partial \overline{\theta}}{\partial t}$ responding to these changes and the diabatic heating responding to the changes in potential temperature. As the potential temperature decreases from August onwards the diabatic heating responds by increasing again, this time not lagged with respect to the maximum in potential temperature, which it was at 90 hPa. There is also similar behaviour at the two levels from October to December. Between January and April the adiabatic cooling is not nearly constant, but is slightly increasing and there is a corresponding

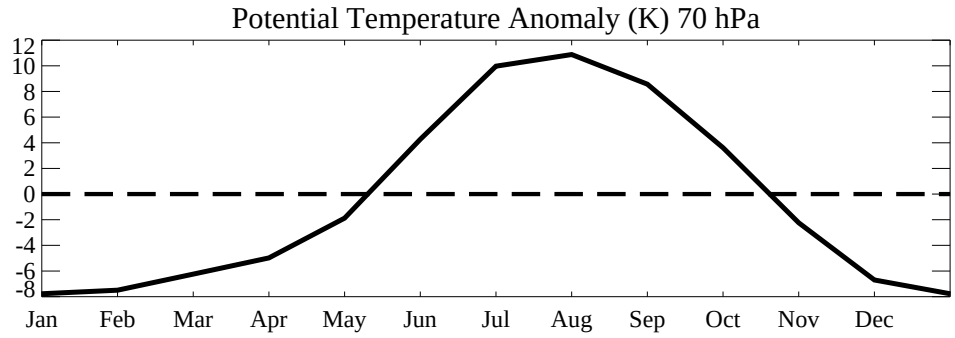

(a) Potential temperature anomaly

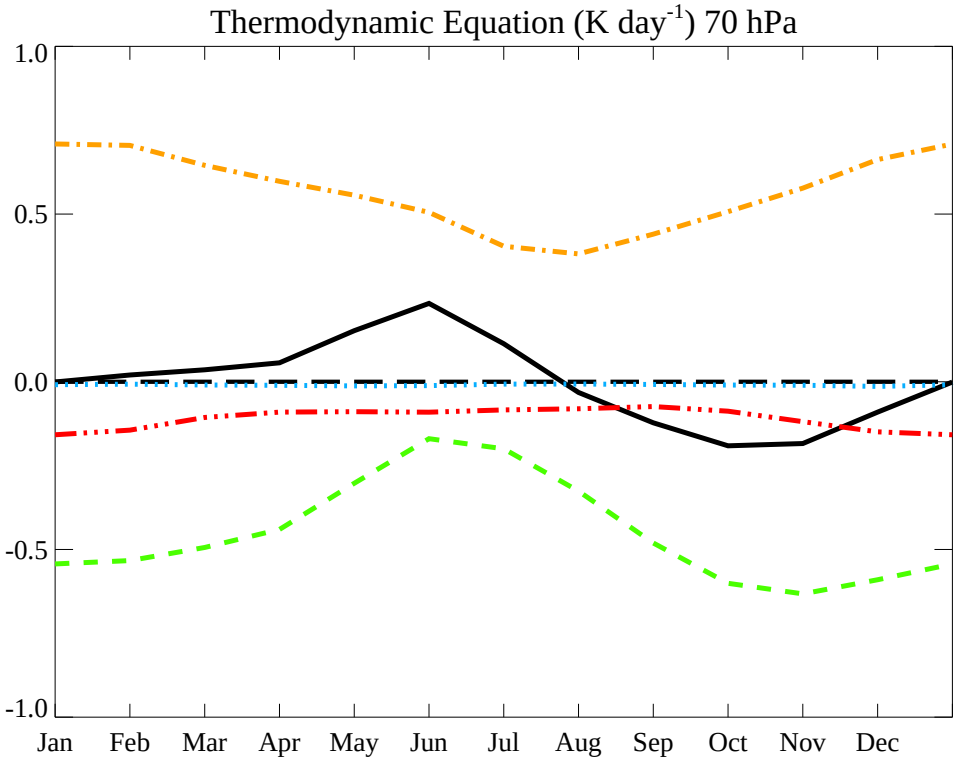

(b) Terms in the thermodynamic equation

Figure 3.19: Mean annual cycle averaged from 9.8°N to 9.8°S at 90 hPa of (a) the potential temperature and (b) the terms in the thermodynamic equation at 70 hPa. In (b) the terms are $\frac{\partial\overline{\theta}}{\partial t}$ (solid black line), $-\frac{\overline{v}^*}{R_e}\frac{\partial\overline{\theta}}{\partial\phi}$ (dotted blue line), $-\overline{\omega}^*\frac{\partial\overline{\theta}}{\partial p}$ (dashed green line), $\overline{Q}$ (dashed and dotted orange line) and $-\frac{\partial}{\partial p}\left(\frac{\overline{v'\theta'}\,\overline{\theta}_\phi}{R_e\overline{\theta}_p}+\overline{\omega'\theta'}\right)$ (dash and three dotted red line).

gradual increase in $\frac{\partial\overline{\theta}}{\partial t}$ during this time, with corresponding changes in temperature and diabatic heating.

In section 3.3 it was shown that adiabatic heating drives the temperature change but with a radiative relaxation timescale twice that of 90 hPa. In section 3.4 it was noted that at 70 hPa the integrand in the integral form of the mass continuity equation had an annual cycle with a magnitude of about half that of 90 hPa.

Figure 3.20 shows the annual cycle of the terms in the zonal momentum equation (3.9) for the latitude band 9.8°N to 9.8°S at 70 hPa. This can be compared with figure 3.16 for 90 hPa. The annual cycle in $\overline{v}^*$ (black) is not as strong at 70 hPa, with some indication of a semi-annual second peak in April. This is mainly driven by the EP flux divergence divided by the absolute vorticity (red). Again, there is some contribution to the driving by the rate of change of zonal wind, $\frac{1}{\overline{\zeta}_a}\frac{\partial\overline{u}}{\partial t}$, (blue) and this has more effect on $\overline{v}^*$ between April and June at 70 hPa than at 90 hPa. The residual non-conservative forcing $\frac{\overline{X}}{\overline{\zeta}_a}$ (orange) also contributes in NH winter and, with rate of change of the zonal wind, gives an indication of a semi-annual cycle in $\overline{v}^*$.

3.7 Summary

Section 3.2 showed that the latitude band 10°N to 10°S is the most appropriate latitude band for this research. It went on to show that the annual cycle in potential temperature at 90 hPa for 9.8°N to 9.8°S is driven by the changes in adiabatic heating and cooling, $-\overline{\omega}^*\frac{\partial\overline{\theta}}{\partial p}$. The diabatic heating residual term, $\overline{Q}$, responds to the changes in potential temperature and opposes the adiabatic heating and cooling. Section 3.3, using a simplified version of the thermodynamic equation, confirmed that the adiabatic heating and cooling term drives the annual cycle in potential temperature at 90 hPa, with a radiative relaxation timescale of 40 days.

Section 3.4.1 showed that the adiabatic heating and cooling term closely follows the residual mean upwelling term, $\overline{\omega}^*$. By mass continuity changes in the upwelling, $\overline{\omega}^*$, in a latitude band are driven by changes in the outflow, $\overline{v}^*$, from the edge of that latitude band at levels above the upwelling. The majority of the annual cycle in the upwelling between 9.8°N and 9.8°S at 90 hPa is driven by changes to the outflow from 9.8°N and 9.8°S near and above 90 hPa. The "near 90 hPa" implies a local control, rather than a non-local downward control.

Section 3.5 then considers the zonal momentum equation, showing that the

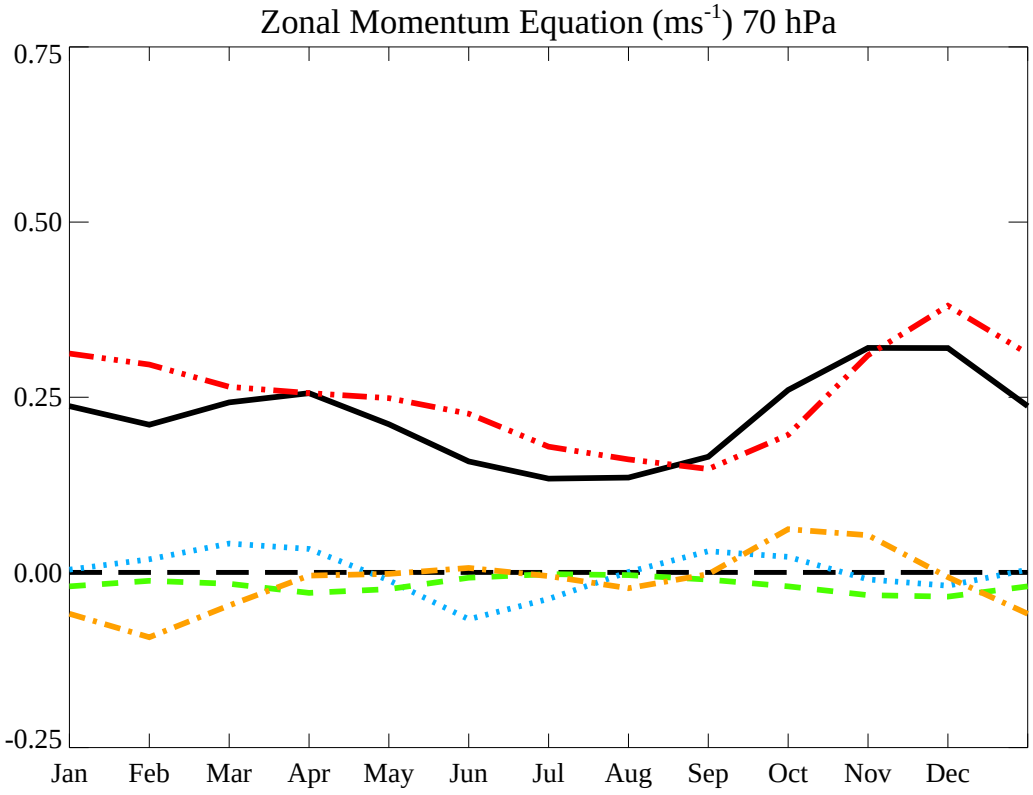

Figure 3.20: Mean annual cycle of the terms in the zonal momentum equation divided by $\overline{\zeta}_a$ (equation 3.9) at 97 hPa, terms at 9.8°N minus terms at 9.8°S. The terms are $\overline{v}^*$ (solid black line), $\frac{1}{\overline{\zeta}_a}\frac{\partial \overline{u}}{\partial t}$ (dotted blue line), $\frac{-\overline{\omega}^*}{\overline{\zeta}_a}\frac{\partial \overline{u}}{\partial p}$ (dashed green line), $\frac{1}{R_e \cos\phi}\frac{\nabla.\mathbf{F}}{\overline{\zeta}_a}$ (dash and three dotted red line) and $\frac{\overline{X}}{\overline{\zeta}_a}$ (dashed and dotted orange line).

outflow, $\overline{v}^*$, from the latitude band, 9.8°N to 9.8°S, is driven by the Eliassen-Palm flux divergence, $\nabla.\mathbf{F}$. This agrees with the results of the downward control principle, that $\overline{\omega}^*$ is driven by EP flux divergence above it.

In section 3.6 the 70 hPa level was examined. This has a larger annual cycle in temperature than 90 hPa. Looking at the terms in the thermodynamic equation this annual cycle is driven by the changes in adiabatic heating and cooling and opposed by diabatic heating. Section 3.3 confirmed that the adiabatic heating and cooling term drives the annual cycle in potential temperature at 70 hPa but with a longer radiative relaxation timescale of 80 days. Randel *et al.* (2002) show an increase in radiative relaxation timescale at heights up to 70 hPa and decrease above. They show a correspondence between the peak in radiative relaxation timescale and the peak in magnitude of annual cycle in temperature. They conclude that the observed annual cycle in temperature is due to the long radiative relaxation timescales coupled with a near constant annual cycle in upwelling

Section 3.4.1 showed that the majority of the annual cycle in the upwelling was driven by outflow near and just above 90 hPa, with a contribution from 70 hPa just under half of that from 90 hPa. Looking at the zonal momentum equation, the annual cycle in $\overline{v}^*$ is smaller than at 90 hPa but is again driven mainly by the EP flux divergence. Although there is a smaller annual cycle in outwelling and upwelling at 70 hPa than 90 hPa, there is a larger annual cycle in temperature due to the much longer radiative relaxation timescales.

The main points of this chapter are:

- The important latitude band is 10°N to 10°S—the nearest grid box to 10° is 9.8°.
- The temperatures are driven by the adiabatic heating and cooling.
- The radiative relaxation timescale for the driving of temperatures by adiabatic heating and cooling is 40 days at 90 hPa.
- The adiabatic heating and cooling is controlled by the upwelling, $\overline{\omega}^*$.
- The upwelling between 9.8°N and 9.8°S at 90 hPa is controlled by the net outflow, $\overline{v}^*$, from 9.8°N and 9.8°S near and above 90 hPa.
- The downward control is local—near and just above 90 hPa.
- The net outflow from 9.8°N and 9.8°S is driven by the Eliassen-Palm flux divergence, $\nabla.\mathbf{F}$, at 9.8°N and 9.8°S.

The next chapter investigates the Eliassen-Palm flux divergence and its components in greater detail.

Chapter 4

The origin of tropical wave-driving in the ECMWF analysis data

4.1 Introduction

In the previous chapter the EP flux divergence was identified as driving the outflow from 9.8°N and 9.8°S near 90 hPa and thus the annual cycle in tropical temperatures at 90 hPa. This chapter investigates the EP flux divergence in order to gain an understanding of the physical origin of the tropical wave-driving. By decomposing the EP flux divergence in different ways, one can determine which processes are important to the annual cycle.

In the rest of this chapter the EP flux divergence is decomposed into the contributions from:

- northern and southern hemispheres,
- horizontal wavenumbers,
- horizontal and vertical components,
- eddy fluxes and stationary and transient components.

4.2 The northern and southern hemisphere contributions to the zonal momentum equation

Figure 4.1 shows the contributions of the different terms in the zonal momentum equation, this time not divided by $\overline{\zeta}_a$ (i.e. equation 3.8), at 9.8°N and 9.8°S at

90 hPa. Panel (a) shows 9.8°N+9.8°S, (b) 9.8°N and (c) 9.8°S.

First of all compare figure 4.1(a), in which the terms are not divided by $\overline{\zeta}_a$, to the equivalent figure in the previous chapter, figure 3.16, in which the terms are divided by $\overline{\zeta}_a$. Because $\overline{\zeta}_a$ changes sign very close to the equator figure 4.1(a) shows the sum of terms at 9.8°N and 9.8°S, rather than the difference. The two figures give essentially the same result; that the outflow, $\overline{v}^*$, from the latitude band is driven by the Eliassen-Palm flux divergence, $\nabla.\mathbf{F}$, although the scaling has changed.

Considering just $\overline{v}^*$ in figure 4.1 panels (a) to (c); the total annual cycle is mainly due to the annual cycle in the NH, the SH opposing this slightly. In the NH (b) it is the EP flux divergence (red line) which is mainly driving the annual cycle in $\overline{v}^*$, although there is some contribution from $\overline{X}$ (orange line). In the SH (c) the annual cycle in $\overline{v}^*$, which opposes the total annual cycle, is mainly coming from $\overline{X}$. This balances out the effect of $\overline{X}$ in the NH, leading to virtually no annual cycle in $\overline{X}$ in the total (a).

4.3 Non-conservative mechanical forcing

The term $\overline{X}$, as previously mentioned in section 2.2.1, is the unspecified zonal component of non-conservative mechanical forcings from the zonal momentum TEM equation (2.9a). It is calculated as a residual by assuming balance in equation 2.9a but is expected to be mainly due to the gravity wave drag from the ECMWF model orographic gravity wave scheme (section 2.3).

Figure 4.2 shows the annual cycle in $\overline{X}$ at 90 hPa. There is a band of positive values of about 20° in width around the equator with negative values surrounding it. This positive band is displaced northwards during NH summer. Consequently there are small annual cycles of opposite senses at 9.8°N and 9.8°S, which sum to produce a net annual cycle near zero in figure 4.1(a). This band follows the same pattern as the climatological mean Inter-Tropical Convergence Zone, see Waliser and Gautier (1993), and may be due to convectively triggered waves. $\overline{X}$ in this band is positive, i.e. eastward, and lies above westward winds so that westward waves are filtered out. In the subtropics $\overline{X}$ is negative i.e. westward waves breaking above the subtropical jets. The minima in $\overline{X}$ near 25°S in SH winter and 35°N in NH winter are due to the wave-breaking over the subtropical jets being stronger during winter.

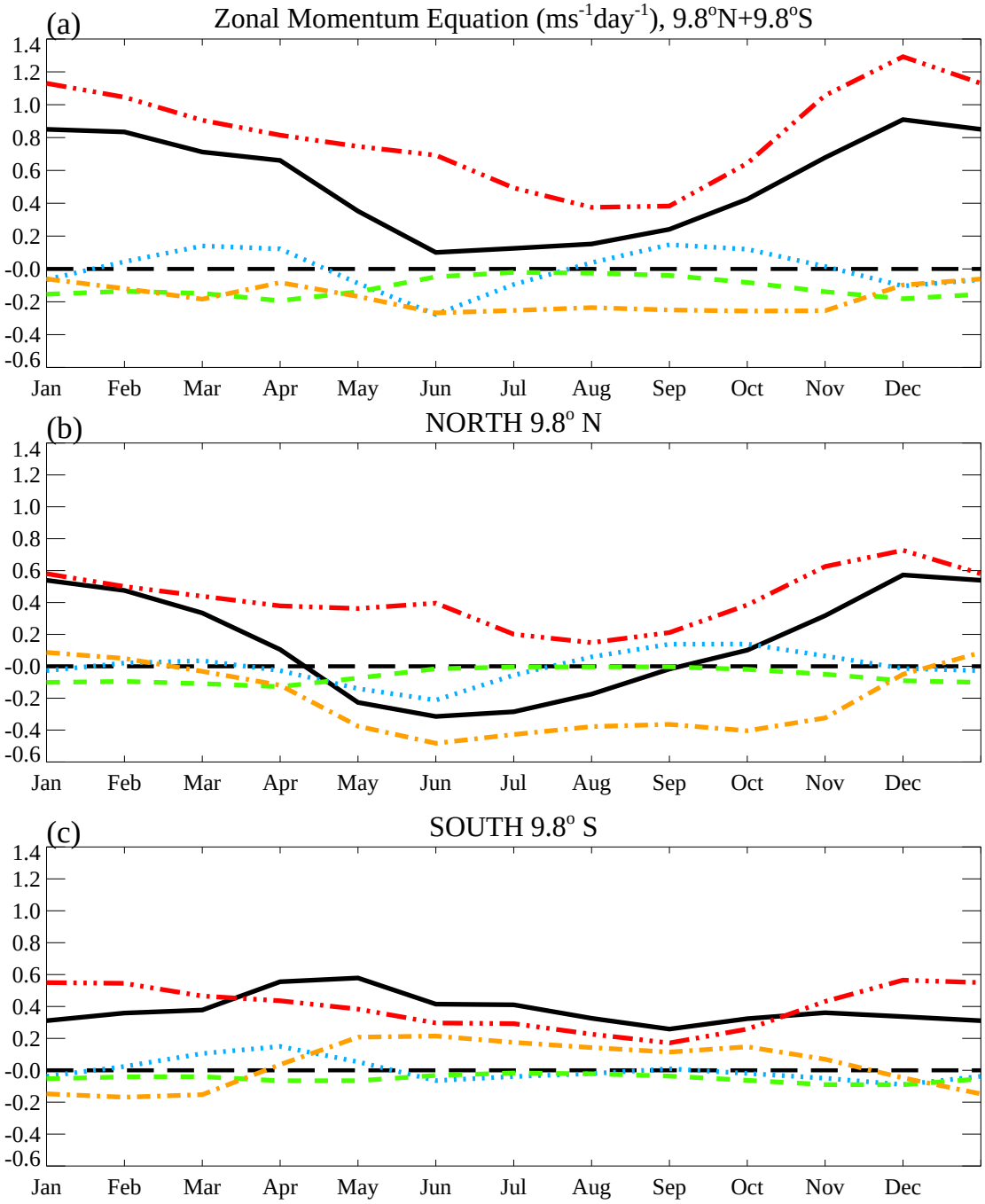

Figure 4.1: Mean annual cycle of the terms in the zonal momentum equation (equation 3.8) at 90 hPa. The plots show terms at (a) 9.8°N plus terms at 9.8°S (as figure 3.16), (b) 9.8°N and (c) 9.8°S. The terms are $\overline{v}^*\overline{\zeta}_a$ (solid black line), $\frac{\partial \overline{u}}{\partial t}$ (dotted blue line), $-\overline{\omega}^*\frac{\partial \overline{u}}{\partial p}$ (dashed green line), $\frac{1}{R_e \cos\phi}\nabla.\mathbf{F}$ (dash and three dotted red line) and $\overline{X}$ (dashed and dotted orange line).

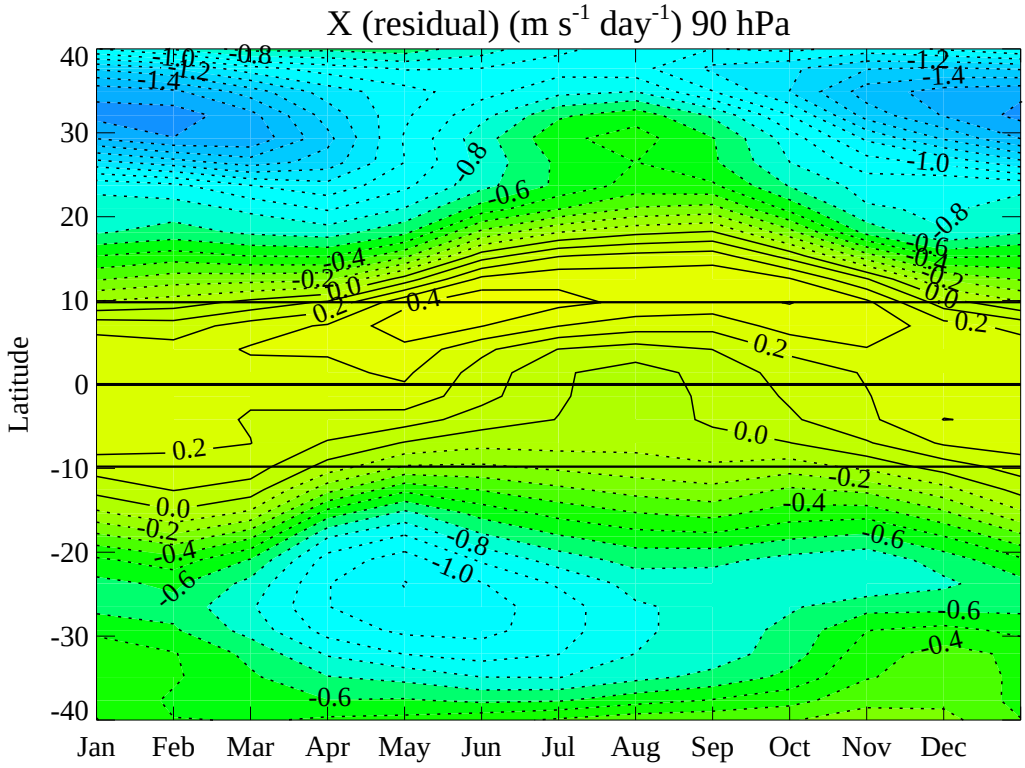

Figure 4.2: Mean annual cycle of $\overline{X}$ at 90 hPa. The contour interval is $2\,\mathrm{m\,s^{-1}\,day^{-1}}$. Solid black lines indicate 9.8°N, the equator and 9.8°S.

4.4 The EP flux divergence

The next step of the investigation is to consider the EP flux divergence, $\nabla.\mathbf{F}$. The EP flux divergence term in equation 2.9a is $\frac{1}{R_e \cos\phi}\nabla.\mathbf{F}$.

Figure 4.3 shows the EP flux divergence, or wave-driving, from 40°N to 40°S at 90 hPa. There is a short period of divergence around the equator in July and August. Contours of constant convergence are pushed away from the equator around this positive region such that, for a given latitude, the convergence is weaker in NH summer than NH winter. There is strong convergence in the extra-tropics (blue regions). There is a minimum in convergence near 30°S between June and September whereas in the NH the plot is noisier with a semi-annual cycle north of 30°N. Considering the 9.8°N to 9.8°S latitude band the convergence decreases from 9.8°N towards the equator and increases again towards 9.8°S throughout the year. In July and August the maximum in divergence is slightly north of the equator whereas in December to April the minimum in convergence is slightly south of the equator. The two extrema of tropical wave-driving are the maximum

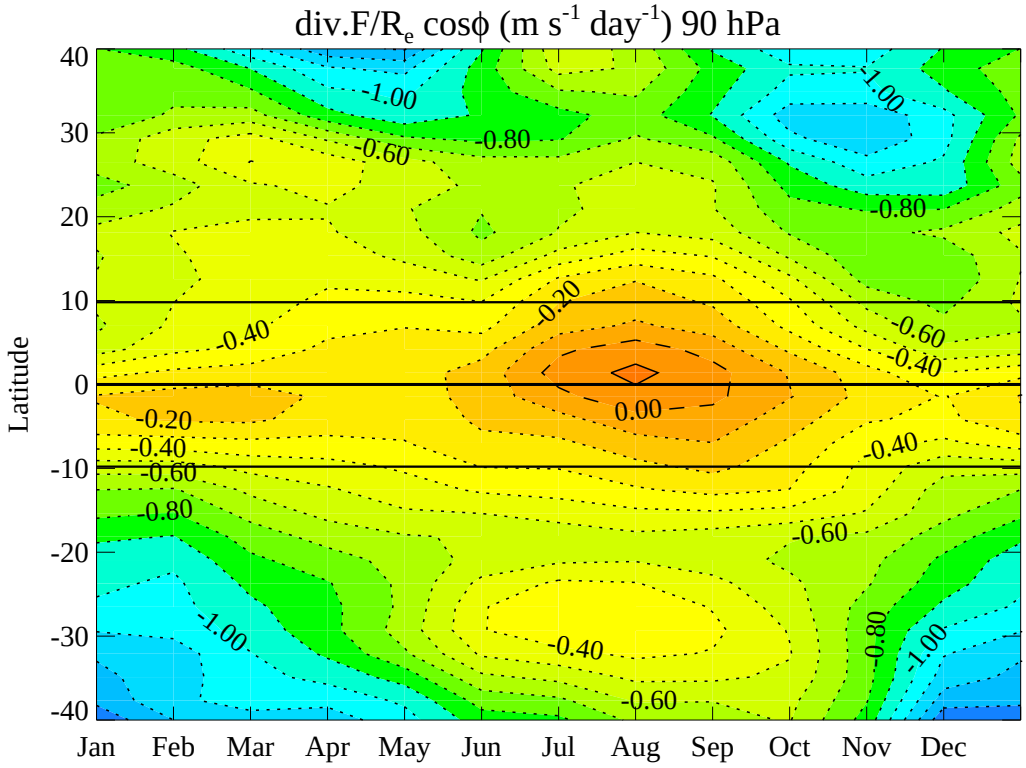

Figure 4.3: Mean annual cycle of the EP flux divergence, $\frac{1}{R_e \cos\phi}\nabla.\mathbf{F}$, at 90 hPa. Solid black lines indicate 9.8°N, 0° and 9.8°S. The contour interval is 0.1 m s^{-1} day^{-1}. Solid contours indicate divergence (positive $\nabla.\mathbf{F}$), dotted contours indicate convergence.

divergence in August and the maximum convergence in December.

4.4.1 Horizontal wavenumber decomposition of EP flux divergence

The decomposition of EP flux divergence into horizontal wavenumbers was performed in order to investigate which scales of waves were contributing to the annual cycle. Low wavenumbers, such as wavenumbers one and two, might indicate Rossby planetary waves, for example. The wavenumbers plotted in this section are the total of all wavenumbers, wavenumbers one, two and greater than or equal to three. These will be referred to as "all-m", "m=1", "m=2" (or "m=1,2" for both wavenumbers one and two) and "m≥3."

Figure 4.4 shows the various wavenumber components for the annual cycle in the EP flux divergence at 90 hPa. Previously it was noted that the wave-driving contours were pushed away from the equator in NH summer due to a region of

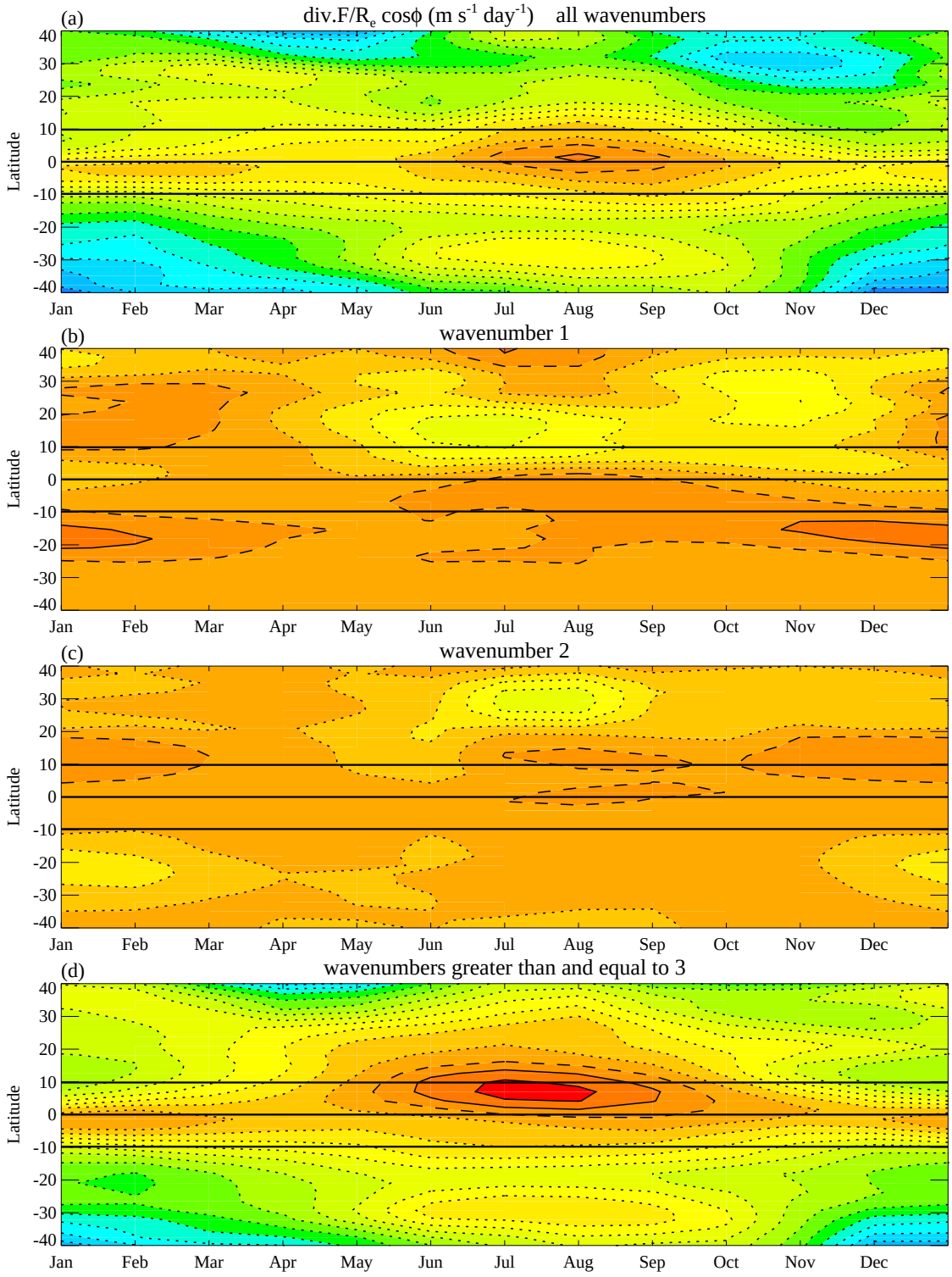

Figure 4.4: Wavenumber components of the annual cycle in the EP flux divergence at 90 hPa. The plots show (a) all-m, (b) m=1, (c) m=2, (d) m≥3. Solid black lines indicate 9.8°N, 0° and 9.8°S. The contour interval is 0.1 m s^{-1} day^{-1}.

divergence near the equator in June and August. It can be seen from figure 4.4 that the majority of the pattern in the total field (panel (a)) is due to m≥3 (panel (d)). However the period of divergence occurs for longer and is further north in m≥3. This has been partially cancelled out in the full field by a region of strong convergence in m=1 (panel (b)). The divergence being further north in m≥3 has the effect of pushing the convergence contours further north in this wavenumber component but also means that the contours in the SH are less distorted, with a less strong annual cycle. Panel (c), showing m=2, has little activity.

Figure 4.5 shows the wavenumber contributions to the EP flux divergence at the edges of the latitude band 9.8°N and 9.8°S (panels (b) and (c) respectively) and their sum (panel (a)). These plots are of EP flux divergence, and not EP flux divergence divided by vorticity, so that the top plot is of the sum of the EP flux divergence at the latitude band edges, not the difference. Also, $\frac{1}{R_e \cos\phi}\nabla.\mathbf{F}$ is multiplied by minus one so that the sign is consistent with figure 3.16 and equation 3.8. This means that negative values now represent divergence and positive values convergence.

Considering the sum of the two hemispheres plot (a) as previously noted there is a clear annual cycle in all-m (solid black line). This is due to m≥3. The m=1 component opposes this annual cycle, with a small contribution to this opposition from m=2. Looking at all-m in the two hemispheres the majority of the annual cycle is from the NH (b) with some contribution from the SH (c). In the NH (b) the behaviour is similar to that of the sum of the two hemispheres (a)—the annual cycle in all-m is mainly due to m≥3 with some opposition from m=1. There is a small "kink" in June, which is due to a combination of m=1 and m=2. In the SH (c) there is a comparatively small annual cycle in all wavenumber components compared with the NH, but again the majority of the annual cycle is from m≥3. In summary:

- The annual cycle in tropical wave-driving is from m≥3 in both the northern and southern hemispheres.
- This annual cycle is opposed by m=1 in the NH.

4.4.2 Horizontal and vertical components of EP flux divergence

This section considers how the annual cycle in tropical wave-driving can be decomposed into contributions from the horizontal and vertical dissipation of waves.

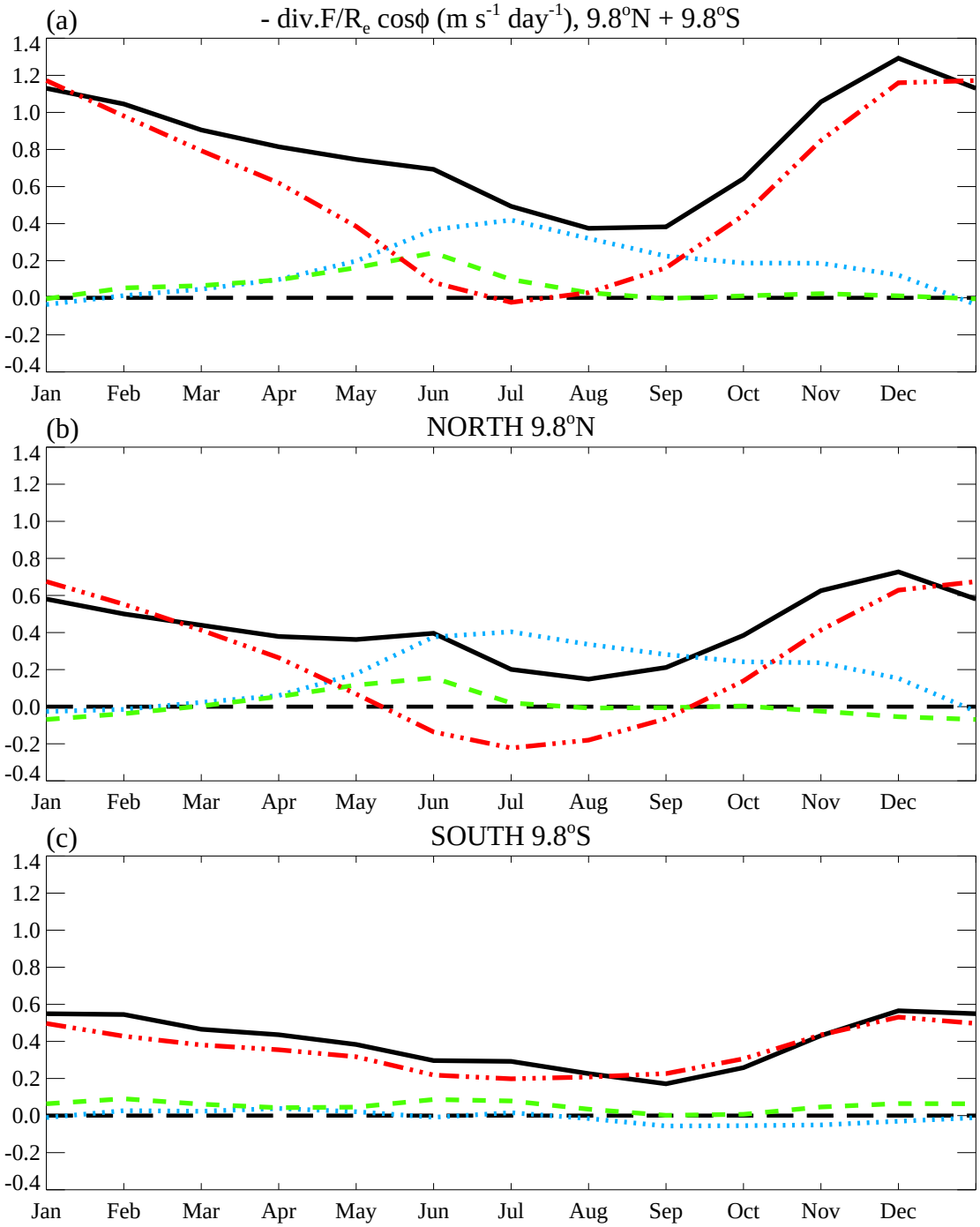

Figure 4.5: Annual cycle of EP flux divergence, divided into wavenumber components and into northern and southern hemisphere contributions. The plots show (a) 9.8°N plus 9.8°S, (b) 9.8°N and (c) 9.8°S. The terms are all-m (solid black line), m=1 (dotted blue line), m=2 (dashed green line), m≥3 (dash and three dotted red line).

This is done by examining the divergence of the horizontal and vertical components of the EP flux.

In equation 3.8 $\frac{1}{R_e \cos\phi}\nabla.\mathbf{F}$ is on the right-hand side of the equation multiplied by minus one. For consistency with previous plots and equations $\frac{-1}{R_e \cos\phi}\nabla.\mathbf{F}$ will be used in this chapter. In the plots the sense of the annual cycle for the required driving of $\overline{v}^*$ is reduced EP flux divergence in NH summer and increased EP flux divergence in NH winter or a "U" shape.

From equations 2.10 and 2.11, the divergence of the horizontal component of the EP flux multiplied by minus one is given by

$$\frac{-1}{R_e \cos\phi}\nabla.\mathbf{F}^{(\phi)} = \frac{-1}{R_e \cos^2\phi}\frac{\partial}{\partial\phi}\left(\cos^2\phi\left[\overline{u}_p\frac{\overline{v'\theta'}}{\overline{\theta}_p} - \overline{v'u'}\right]\right), \tag{4.1}$$

and the divergence of the vertical component is given by

$$\frac{-1}{R_e \cos\phi}\nabla.\mathbf{F}^{(p)} = -\frac{\partial}{\partial p}\left(\left[f - \frac{1}{R_e\cos\phi}\left(\overline{u}\cos\phi\right)_\phi\right]\frac{\overline{v'\theta'}}{\overline{\theta}_p} - \overline{\omega'u'}\right). \tag{4.2}$$

Figure 4.6 shows the annual cycle in the horizontal and vertical components of the EP flux divergence, $\frac{-1}{R_e \cos\phi}\nabla.\mathbf{F}$, at 9.8°N and 9.8°S, and the decomposition of these components into wavenumbers. Wavenumbers one and two have been combined in this figure and will be referred to as m=1,2.

Total $\frac{-1}{R_e \cos\phi}\nabla.\mathbf{F}$ (first column):

Both the NH (d) and SH (g) have annual variations which arise from m≥3. The NH has a strong opposing variation in m=1,2. This causes a semi-annual cycle in all-m. The opposing variation in m=1,2 has a sharp maximum in June, earlier than the July minimum in m≥3. In the SH m≥3 has a minimum from June to September but the small decrease in m=1,2 between August and November causes the minimum in the SH total to occur in September. The minimum in the total $\frac{-1}{R_e \cos\phi}\nabla.\mathbf{F}$ (a) due to the combined effects of m=1,2 and m≥3 from the two hemispheres then occurs in August.

Horizontal and vertical components for 9.8°N+9.8°S (first row):

Both the horizontal (b) and vertical (c) components have annual variations which arise from m≥3. The horizontal component has a strong opposing variation in m=1,2. This causes a semi-annual variation in all-m. The opposing variation in m=1,2 has a sharp maximum in June, earlier than the July minimum in m≥3.

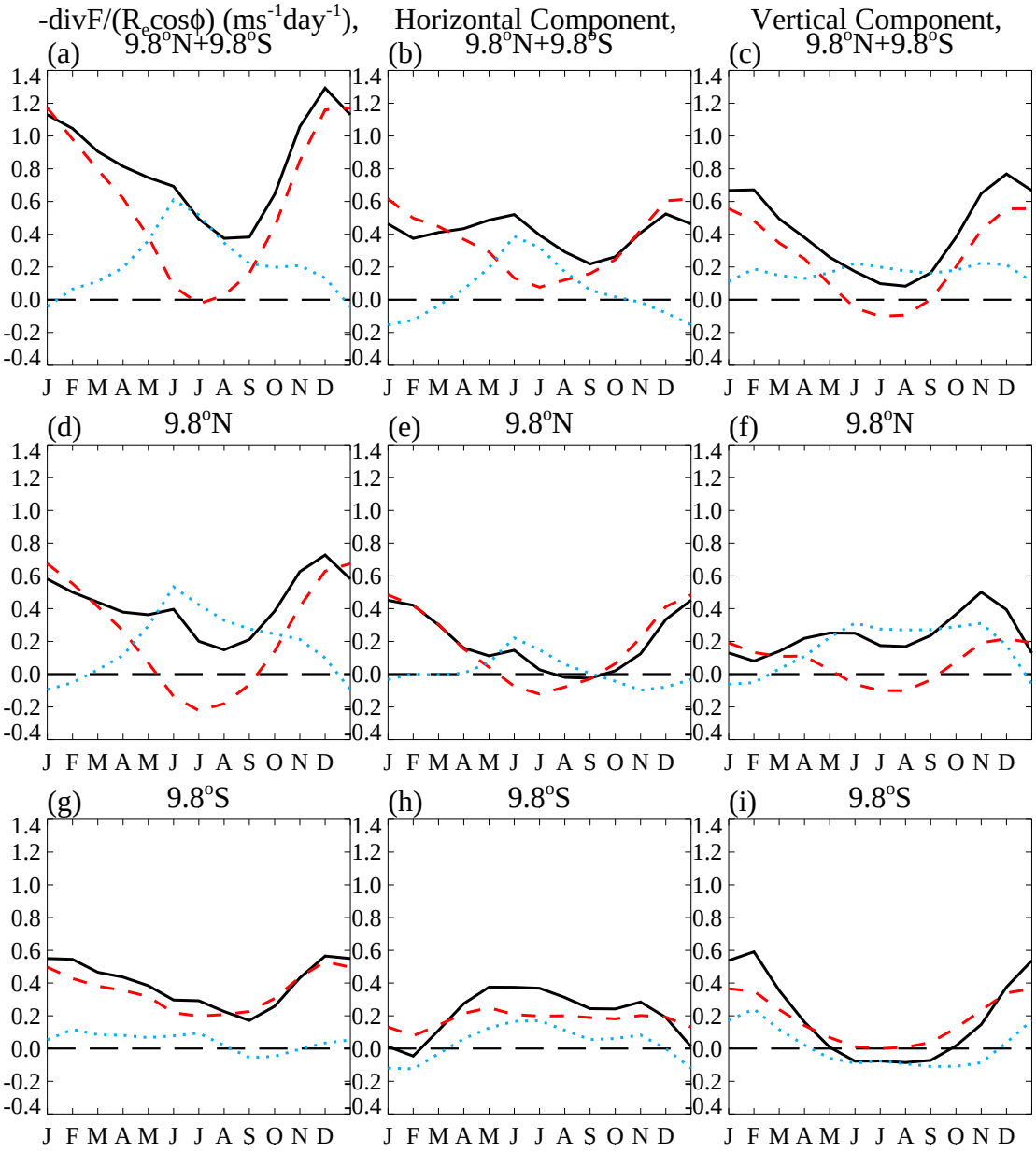

Figure 4.6: Annual cycle in the horizontal and vertical components of the EP flux divergence, $\frac{-1}{R_e \cos\phi}\nabla.\mathbf{F}$. The columns show total, horizontal and vertical components respectively. The rows show 9.8°N+9.8°S, 9.8°N and 9.8°S respectively. The wavenumber components are all-m (solid black line), m=1,2 (dotted blue line) and m≥3 (dashed red line).

9.8°N (middle row):

In the total $\frac{-1}{R_e \cos\phi}\nabla.\mathbf{F}$ (d) and the horizontal (e) and vertical (f) components, m≥3 has an annual variation in the sense required to drive $\overline{v}^*$ and m=1,2 opposes this annual variation. The sharp peak in m=1,2 in June is from the NH and the horizontal component of $\frac{-1}{R_e \cos\phi}\nabla.\mathbf{F}$.

9.8°S (bottom row):

In the horizontal (h) and vertical (i) components respectively the annual variations in m=1,2 and m≥3 are in the same sense. The annual variations in the horizontal and vertical components are opposite to each other, the vertical component being of the sense required to drive $\overline{v}^*$. The total $\frac{-1}{R_e \cos\phi}\nabla.\mathbf{F}$ (g) has a small annual variation in all-m and m≥3 and very little annual variation in m=1,2 due to the horizontal and vertical components cancelling each other out.

Horizontal component (second column):

The annual variation in all-m and m≥3 in the NH (e) is of the sense to drive $\overline{v}^*$. The annual variation in m=1,2 opposes this, with a sharp peak in June causing a small semi-annual effect in all-m in the NH. The annual variation in the SH (h) opposes the annual variation in the NH. This amplifies the small semi-annual effect in all-m for 9.8°N+9.8°S.

Vertical component (third column):

The annual variation in m≥3 in the NH (f) and SH (i) is of the sense to drive $\overline{v}^*$. In the NH this is opposed by m=1,2 giving a small all-m whereas in the SH m=1,2 is of the same sense as m≥3 giving a large all-m. The minimum in NH winter in the vertical component in the NH reduces the maximum in NH winter in the total for the vertical component. In 9.8°N+9.8°S m≥3 has a strong annual variation because it has the same sense in both hemispheres but m=1,2 has only a small annual variation because it is of opposite sense in the two hemispheres.

To summarise:

- Both the NH and SH have annual variations which arise from m≥3.
- The NH has a strong opposing variation in m=1,2. This causes a semi-annual cycle in all-m.
- The SH does not have an opposing variation in m=1,2 because the variations in the horizontal and vertical components cancel.
- The horizontal and vertical components have annual variations which arise from m≥3.
- In the horizontal component in the NH m=1,2 opposes m≥3 whereas in the SH m=1,2 and m≥3 are in the same sense and opposing the annual cycle

required to drive $\overline{v}^*$. The variations in m=1,2 add to give a strong opposing annual cycle for the two hemispheres and thus a semi-annual cycle in the total horizontal component.

- In the vertical component in the NH m=1,2 opposes m≥3 whereas in the SH m=1,2 and m≥3 are in the same sense and of the sense to drive $\overline{v}^*$. The variations in m=1,2 cancel between the two hemispheres.

Both the northern and southern hemispheres are important; the horizontal component of $\frac{-1}{R_e \cos\phi}\nabla.\mathbf{F}$ being important in the NH and the vertical component in the SH.

4.4.3 Eddy terms and stationary and transient decomposition of EP flux divergence

Having identified that both the horizontal and vertical components of the EP flux divergence contribute to driving the annual cycle, but different components are important in the two hemispheres, it is logical to examine the EP flux divergence more closely. Recall equations 4.1 and 4.2; each component is made up of two eddy flux terms. Thus $\frac{-1}{R_e \cos\phi}\nabla.\mathbf{F}$ can be rewritten as the contributions from the horizontal component, $\frac{-1}{R_e \cos\phi}\nabla.\mathbf{F}^{(\phi)}$, from the eddy heat flux, $\overline{v'\theta'}$, and the horizontal eddy momentum flux, $\overline{v'u'}$, and from the vertical component, $\frac{-1}{R_e \cos\phi}\nabla.\mathbf{F}^{(p)}$, from the eddy heat flux and the vertical eddy momentum flux, $\overline{\omega' u'}$:

$$
\begin{aligned}
\frac{-1}{R_e\cos\phi}\nabla.\mathbf{F} = \quad & -\frac{1}{R_e\cos^2\phi}\frac{\partial}{\partial\phi}\left(\cos^{\,2}\phi\,\overline{u}_p\frac{\overline{v'\theta'}}{\overline{\theta}_p}\right) && (\nabla.\mathbf{F}^{(\phi)}\mathrm{i}) \\
& + \quad \frac{1}{R_e\cos^2\phi}\frac{\partial}{\partial\phi}\left(\cos^{\,2}\phi\,\overline{v'u'}\right) && (\nabla.\mathbf{F}^{(\phi)}\mathrm{ii}) \\
& - \frac{\partial}{\partial p}\left(\left[f-\frac{1}{R_e\cos\phi}\left(\overline{u}\cos\phi\right)_\phi\right]\frac{\overline{v'\theta'}}{\overline{\theta}_p}\right) && (\nabla.\mathbf{F}^{(p)}\mathrm{i}) \\
& + \quad \frac{\partial}{\partial p}\left(\overline{\omega' u'}\right). && (\nabla.\mathbf{F}^{(p)}\mathrm{ii}) \qquad (4.3)
\end{aligned}
$$

The eddy heat flux, $\overline{v'\theta'}$, is the correlation between meridional wind perturbations and temperature perturbations or the poleward flux of potential temperature. The horizontal eddy momentum flux, $\overline{v'u'}$, is the correlation between meridional and zonal wind perturbations or the poleward flux of westward flow. Boehm and Lee (2003) suggest that in the tropics this is mainly due to Rossby waves of tropical origin. The vertical eddy momentum flux, $\overline{\omega' u'}$, is the correlation between vertical

and zonal wind perturbations or the vertical flux of westward flow. In the tropics this is mainly due to vertically propagating gravity and Kelvin waves. These fluxes do not act separately to drive changes in $\frac{\partial \overline{u}}{\partial t}$ and $\frac{\partial \overline{\theta}}{\partial t}$ and the residual circulation but in the combination given by the EP flux divergence (Andrews *et al.*, 1987, section 3.5).

Recall from section 2.3.6 equation 2.26:

$$\begin{aligned} \langle v'u' \rangle &= \left\langle (v - \overline{v})(u - \overline{u}) \right\rangle \\ &= \langle v' \rangle \langle u' \rangle + \langle v'^* u'^* \rangle \\ &\quad \text{stationary} \quad \text{transient.} \end{aligned}$$

The stationary and transient components of $v'u'$, $v'\theta'$ and $\omega'u'$ in the form of the components of the EP flux divergence, $\nabla.\mathbf{F}^{(\phi)}$, can then be considered. For example, the $\nabla.\mathbf{F}^{(\phi)}$ii term in equation 4.3 can be rewritten as:

$$\begin{aligned} \frac{1}{R_e \cos^2\phi} \frac{\partial}{\partial \phi} \left(\cos^2\phi \, \overline{v'u'} \right) &= \frac{1}{R_e \cos^2\phi} \frac{\partial}{\partial \phi} \left(\cos^2\phi \, \overline{\langle v' \rangle \langle u' \rangle} \right) \\ &\quad + \frac{1}{R_e \cos^2\phi} \frac{\partial}{\partial \phi} \left(\cos^2\phi \, \overline{\langle v'^* u'^* \rangle} \right). \end{aligned} \tag{4.4}$$

Thus the EP flux divergence can be considered in terms of its stationary and transient components. The stationary component would be due to time mean slowly varying forcing from such things as tropical heating. The transient component would be due to forcing on much shorter timescales, such as Rossby waves breaking into the tropics particularly in the westerly ducts in the east Pacific and Atlantic, and other transient behaviour in the tropics including variability in the monsoons and the Madden-Julian oscillation.

Figure 4.7 shows the EP flux divergence (multiplied by minus one), $\frac{-1}{R_e \cos\phi} \nabla.\mathbf{F}$, decomposed into stationary and transient components (middle and right columns respectively) for the northern and southern hemispheres (middle and bottom rows respectively) and vertical and horizontal components (blue and orange lines respectively). Here the period of time-meaning is 30.5 days.

Total $\frac{-1}{R_e \cos\phi} \nabla.\mathbf{F}$ (first column):

As previously noted when examining figure 4.6 both hemispheres have an annual cycle of the correct sense for driving $\overline{v}^*$. In the NH (panel (d)) this is due to both the horizontal and vertical components whereas in the SH (g) the horizontal component opposes the vertical component and the driving of $\overline{v}^*$. In the NH both the horizontal and vertical components show a semi-annual cycle, with the NH

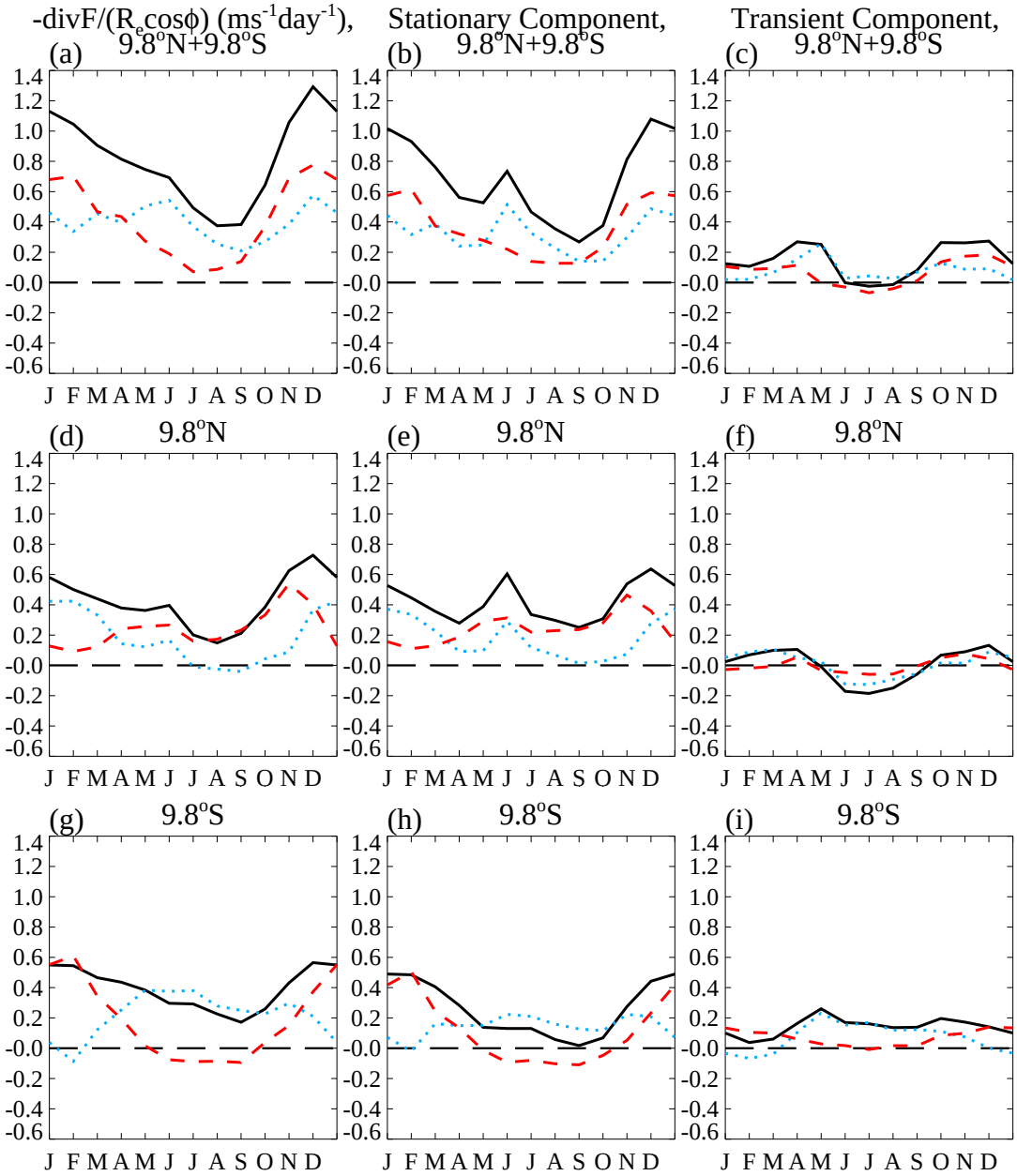

Figure 4.7: Annual cycle in the stationary and transient components of the EP flux divergence, $\frac{-1}{R_e \cos\phi}\nabla.\mathbf{F}$. The columns show total, stationary and transient components respectively. The rows show 9.8°N+9.8°S, 9.8°N and 9.8°S respectively. The horizontal and vertical components are total (solid black line), horizontal (dotted blue line) and vertical (dashed red line). The time-meaning period is 30.5 days.

spring maximum much smaller than the NH winter maximum. In the horizontal component the summer minimum lasts for longer than in the vertical component. The horizontal component NH winter maximum begins two months later than the vertical component NH winter maximum, lasting longer so that when the vertical component has its early NH spring minimum (February) the horizontal component is still at a maximum.

Stationary and transient components for 9.8°N+9.8°S (first row):

The majority of the annual cycle is due to the stationary component (b). This has a semi-annual cycle due to the horizontal component, which has a semi-annual cycle with a sharp maximum in June. In the transient component (c) there is a small semi-annual cycle from both the vertical and horizontal components. The minimum in the transient component from June to August reduces the effect of the sharp maximum in June in the stationary component.

9.8°N (middle row):

Again, the majority of the annual cycle is due to the stationary component (e). This also has a semi-annual cycle. This is due mainly to the horizontal component but there is some contribution from the vertical component. The horizontal component has a sharp maximum in June, which gives a sharp maximum in the total for the stationary component. In NH winter the combination of maxima in January and November in the horizontal and vertical components respectively give a second maximum in the total in December. In the transient component (f) both the horizontal and vertical components have a small semi-annual cycle with a stronger minimum in NH summer than winter. This NH summer minimum reduces the effect of the sharp maximum in June in the stationary component.

9.8°S (bottom row):

The annual cycle in the SH is due to the stationary component (h) with a small opposing annual cycle in the transient component (i). In both stationary and transient components the annual cycle in the correct sense for driving $\overline{v}^*$ is due to the vertical component and opposed by the horizontal component.

Stationary component (second column):

In the stationary component the annual cycle in the sense for driving $\overline{v}^*$ is due to the vertical component in both hemispheres and the horizontal component in the NH. It is opposed by the horizontal component in the SH. The sharp maximum in June is due to the horizontal component from the NH.

Transient component (third column):
In the transient component the semi-annual cycle is due to both horizontal and vertical components in the NH. In the SH the total annual cycle opposes driving of $\overline{v}^*$ and this is due to the horizontal component.

Figure 4.8 shows the EP flux divergence, $\frac{-1}{R_e \cos\phi}\nabla.\mathbf{F}$, further decomposed into the four different eddy terms from equation 4.3 as well as into its stationary and transient components (middle and right columns respectively) for the northern and southern hemispheres (middle and bottom rows respectively).

In all panels of figure 4.8 the $v'\theta'$ term from the horizontal component ($\nabla.\mathbf{F}^{(\phi)}$i) (dotted blue line) is small and does not show a strong annual cycle, so the horizontal component of $\frac{-1}{R_e \cos\phi}\nabla.\mathbf{F}$ is mainly due to the term involving $v'u'$ ($\nabla.\mathbf{F}^{(\phi)}$ii). In the following, the $v'\theta'$ term from the horizontal component will be ignored.

Total $\frac{-1}{R_e \cos\phi}\nabla.\mathbf{F}$ (first column):
The majority of the annual cycle in panels (a) and (d) is clearly from $\omega'u'$ (red line) from the vertical component ($\nabla.\mathbf{F}^{(p)}$ii). This is opposed by $v'\theta'$ (orange line) from the vertical component ($\nabla.\mathbf{F}^{(p)}$i). There is also a contribution from $v'u'$ (green line) from the horizontal component ($\nabla.\mathbf{F}^{(\phi)}$ii). The opposition from $v'\theta'$ is due only to the NH. In the SH (panel (g)) $v'\theta'$ has an annual cycle in the sense for driving $\overline{v}^*$, stronger than that of $\omega'u'$, and this annual cycle is opposed by $v'u'$.

Stationary and transient components for 9.8°N+9.8°S (first row):
The annual cycle in $\omega'u'$ is in the sense to drive $\overline{v}^*$ and is the largest contributer to the annual cycle in both the stationary and transient components. It has a semi-annual cycle with a small decrease in NH winter, a strong minimum in NH summer and maxima in NH spring and autumn. $v'\theta'$ also has the same sense in both the stationary and transient components, opposing the driving of $\overline{v}^*$. This too has a semi-annual cycle with minima in NH spring and autumn and maxima in NH winter and summer. $v'u'$ has a clear semi-annual cycle in the stationary component, with a sharp maximum in June, another maximum in NH winter and minima in NH spring and autumn. In the transient component the semi-annual cycle in $v'u'$ is reversed and has a weaker maximum in NH autumn than spring.

9.8°N (middle row):
$\omega'u'$ has the same sense (the sense to drive $\overline{v}^*$) and is the largest contributer to the annual cycle in both the stationary and transient components. $\omega'u'$ has a semi-annual cycle with maxima in May and November, a strong minimum in July and a weak minimum in February in the stationary component but in the transient component it does not have a semi-annual cycle. $v'\theta'$ also has the same sense in

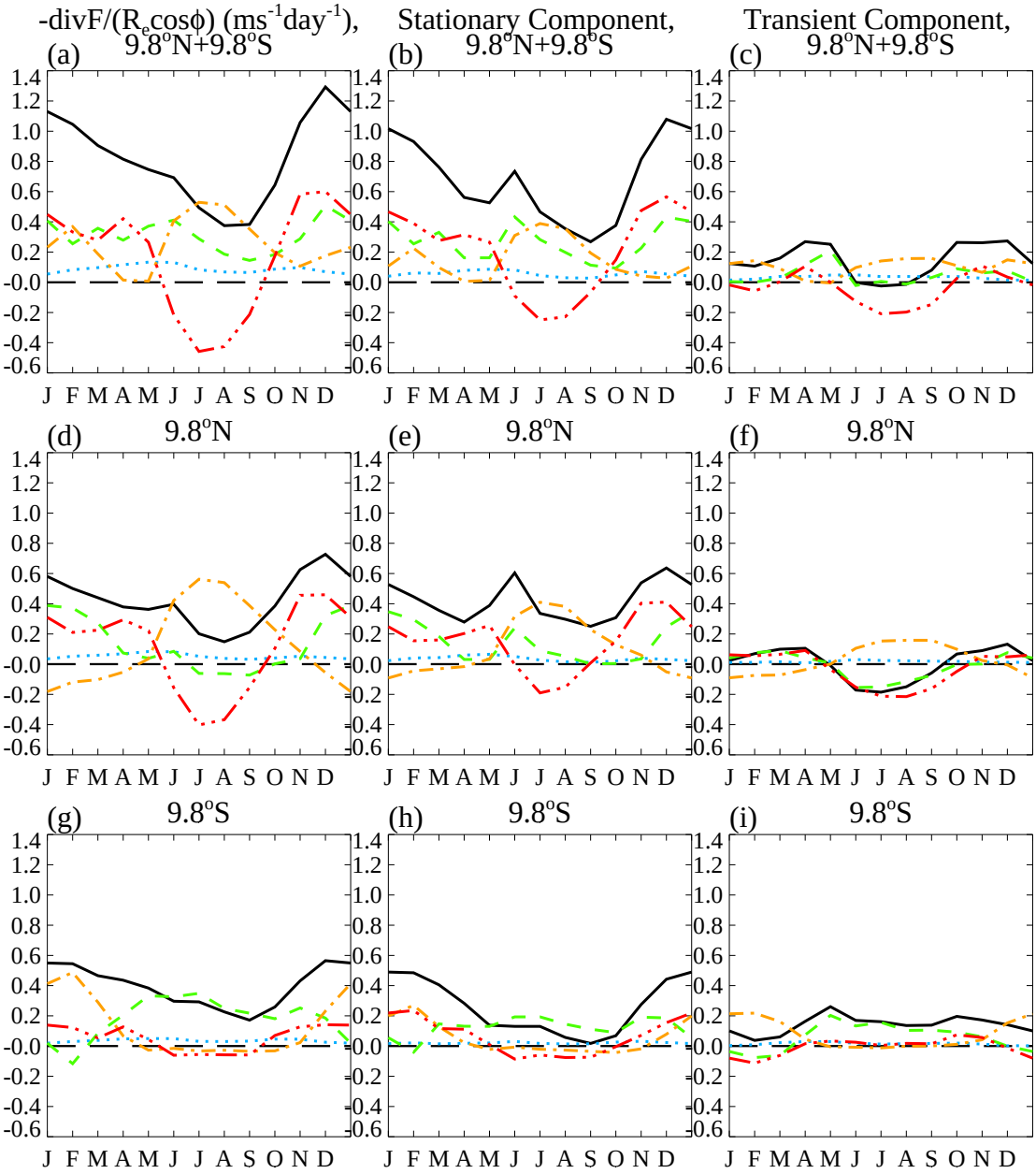

Figure 4.8: Annual cycle in the stationary and transient components of the EP flux divergence, $\frac{-1}{R_e \cos\phi}\nabla.\mathbf{F}$. The columns show total, stationary and transient components respectively. The rows show 9.8°N+9.8°S, 9.8°N and 9.8°S respectively. The eddy components are total (solid black line), $\nabla.\mathbf{F}^{(\phi)}$i $(v'\theta')$ (dotted blue line), $\nabla.\mathbf{F}^{(\phi)}$ii $(v'u')$ (dashed green line), $\nabla.\mathbf{F}^{(p)}$i $(v'\theta')$ (dashed and dotted orange line) and $\nabla.\mathbf{F}^{(p)}$ii $(\omega'u')$ (dash and three dotted red line). The time-meaning period is 30.5 days.

both the stationary and transient components, opposing the driving of $\overline{v}^*$. $v'\theta'$ does not have a semi-annual cycle in either the stationary or transient components. $v'u'$ has a semi-annual cycle in the stationary component, with minima in NH summer and spring, a maximum in NH winter and a small sharp maximum in June. In the transient component $v'u'$ has an annual cycle of the sense to drive $\overline{v}^*$.

9.8°S (bottom row):

In the stationary component the annual cycle is due to $v'\theta'$ and $\omega'u'$ equally and opposed by $v'u'$. In the transient component $v'\theta'$ and $v'u'$ are zero from April to November, with $v'\theta'$ increasing to a maximum in February and $\omega'u'$ decreasing to a minimum in February. The majority of the annual cycle in the transient component is due to $v'u'$, in the sense to oppose the driving of $\overline{v}^*$ and opposed by $v'\theta'$ in NH winter. In panel (g) the annual cycle is mainly due to $v'\theta'$ because $\omega'u'$ in the stationary component is opposed by $\omega'u'$ in the transient component.

It is important to note that the $v'u'$ term in the horizontal component and both the $\omega'u'$ and $v'\theta'$ terms in the horizontal component have contributions to the seasonal behaviour and are important. Traditionally the $\omega'u'$ term would be neglected under quasi-geostrophic scaling and $v'\theta'$ would be neglected because the temperature perturbations in the tropics are small. Boehm and Lee (2003), for example, neglect the vertical component of EP flux divergence, missing out a part of the driving in the zonal momentum equation.

Using a 10 day meaning period gives similar results to the 30.5 day meaning period. Figure 4.9 shows the EP flux divergence, $\frac{-1}{R_e \cos\phi}\nabla.\mathbf{F}$, decomposed into its stationary and transient components for the 10 day meaning period. This figure can be compared with figure 4.7 for the 30.5 day meaning period.

The cycles in all components of $\frac{-1}{R_e \cos\phi}\nabla.\mathbf{F}$ for the 10 day meaning are very similar to the 30.5 day meaning. The timings and magnitudes of maxima and minima in both annual and semi-annual cycles are generally similar. However, comparing panels (e) in the two figures (the stationary component in the NH), the sharp maximum ($0.29\,\mathrm{m\,s^{-1}\,day^{-1}}$) in the horizontal component in June is much less pronounced for the 10 day meaning, with the maximum distributed over June and July (0.23 and $0.22\,\mathrm{m\,s^{-1}\,day^{-1}}$ respectively). This gives a smoother peak in June in both the horizontal component and total stationary $\frac{-1}{R_e \cos\phi}\nabla.\mathbf{F}$ in the sum of the two hemispheres panel (b) and a smoother "kink" in the total $\frac{-1}{R_e \cos\phi}\nabla.\mathbf{F}$ (black line in panel (a)).

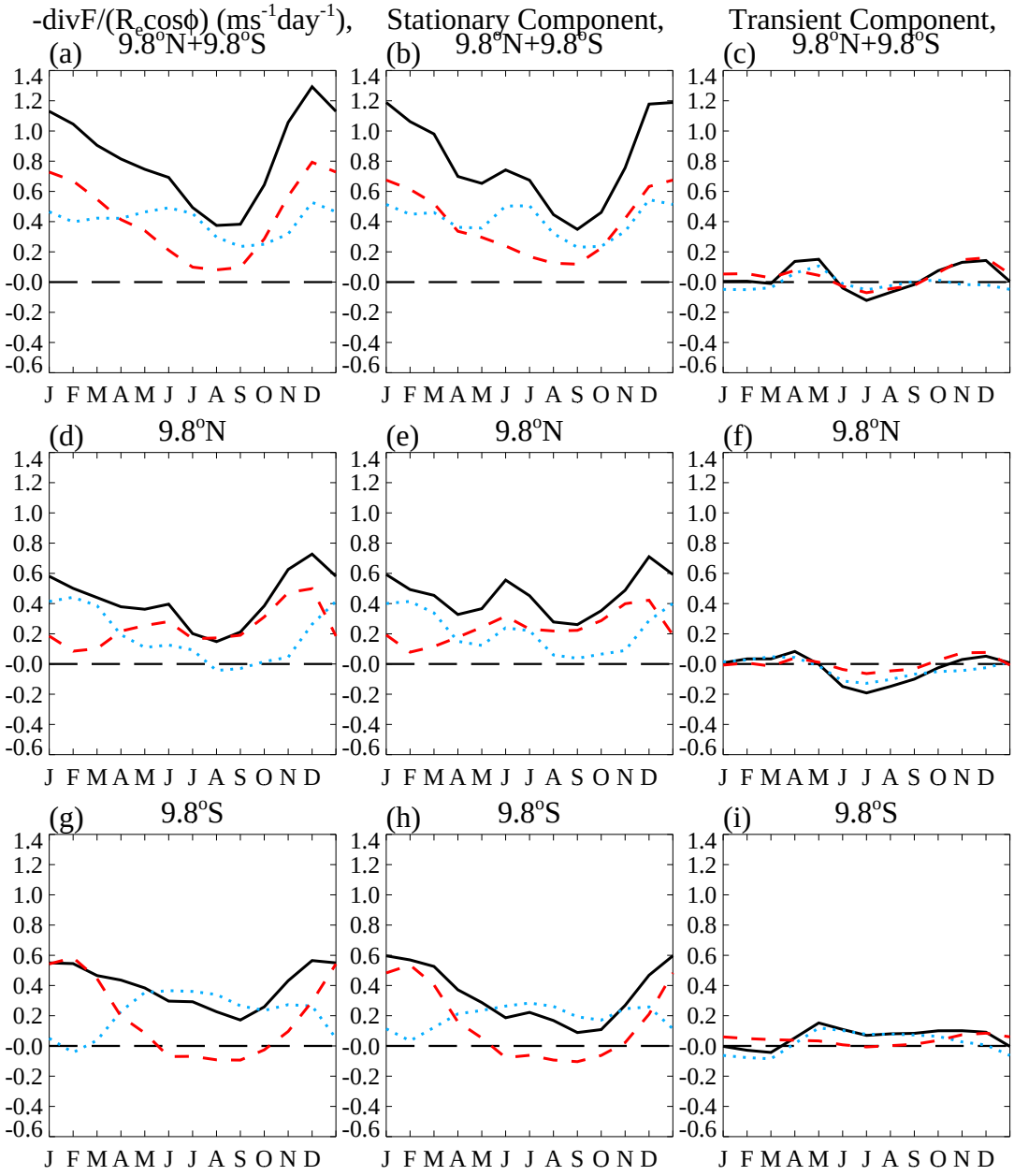

Figure 4.9: Annual cycle in the stationary and transient components of the EP flux divergence, $\frac{-1}{R_e \cos\phi}\nabla.\mathbf{F}$. The columns show total, stationary and transient components respectively. The rows show 9.8°N+9.8°S, 9.8°N and 9.8°S. The horizontal and vertical components are total (solid black line), horizontal (dotted blue line), and vertical (dashed red line). The time-meaning period is 10 days.

Key points are:

- The driving of the annual cycle is mainly from the stationary and not the transient component.
- This is true for both a 30.5 day and a 10 day meaning period.
- The SH contributes a strong annual cycle and the NH has a semi-annual cycle with a main NH winter maximum and secondary NH early summer maximum.
- The $v'u'$ term in the horizontal component and both the $\omega'u'$ and $v'\theta'$ terms in the horizontal component are important.
- $\omega'u'$ gives the main contribution to the annual cycle in the NH with a semi-annual contribution from $v'u'$ increasing the NH winter maximum. The annual cycle is opposed by an annual cycle in $v'\theta'$ from the vertical component.
- $v'\theta'$ from the vertical component gives the main contribution to the annual cycle in the SH with some contribution from $\omega'u'$ and opposition from $v'u'$.
- In August $v'u'$, $v'\theta'$ from the vertical component and $\omega'u'$ are all small at both 10°N and 10°S. In December $v'u'$ and $\omega'u'$ are at or near maximum at 10°N and all three are at or near maximum at 10°S.
- The maximum in the stationary component in June is due to the $v'u'$ component in the horizontal EP flux in the NH. $v'\theta'$ and $\omega'u'$ in the vertical EP flux also contribute to the semi-annual cycle in the NH. This maximum occurs only in June when the meaning period is 30.5 days and in both June and July when the meaning period is 10 days. The transient component, with its minimum in NH summer, decreases the effect of this June maximum in the total EP flux divergence.

4.4.4 Longitudinal source of the wave-driving

Whereas $\nabla.\mathbf{F}$ is a zonally averaged quantity, the contributing eddy terms do not have to be zonally averaged and their longitudinal distributions can be considered. We can define a vector $\mathbf{E} \equiv \left(0, \mathbf{E}^{(\phi)}, \mathbf{E}^{(p)}\right)$ such that

$$\mathbf{E}^{(\phi)} \equiv R_e \cos\phi \left(\overline{u}_p \frac{v'\theta'}{\overline{\theta}_p} - v'u' \right), \tag{4.5a}$$

$$\mathbf{E}^{(p)} \equiv R_e \cos\phi \left(\left[f - \frac{1}{R_e \cos\phi} \left(\overline{u} \cos\phi \right)_\phi \right] \frac{v'\theta'}{\overline{\theta}_p} - \omega'u' \right) \tag{4.5b}$$

and

$$\nabla.\mathbf{E} \equiv \frac{1}{R_e \cos\phi}\frac{\partial}{\partial\phi}\left(\cos\phi \mathbf{E}^{(\phi)}\right) + \frac{\partial \mathbf{E}^{(p)}}{\partial p}. \tag{4.6}$$

Thus $\nabla.\mathbf{F} \sim \nabla.\overline{\mathbf{E}}$. This is an approximation because of the presence of terms such as $\overline{u}$, $\overline{u}_p$ and $\overline{\theta}_p$ in equations (2.10) and (4.5). Previously we considered $\frac{-1}{R_e\cos\phi}\nabla.\mathbf{F}$ for consistency with the zonal momentum plots. Here $\frac{-1}{R_e\cos\phi}\nabla.\mathbf{E}$ will be used and the various components in terms of the four contributing eddy terms will be labelled as follows:

$$\begin{aligned}
\frac{-1}{R_e\cos\phi}\nabla.\mathbf{E} = \quad & -\frac{1}{R_e\cos^2\phi}\frac{\partial}{\partial\phi}\left(\cos^{\,2}\phi\,\overline{u}_p\frac{v'\theta'}{\overline{\theta}_p}\right) && (\nabla.\mathbf{E}^{(\phi)}\mathrm{i}) \\
& + \frac{1}{R_e\cos^2\phi}\frac{\partial}{\partial\phi}\left(\cos^{\,2}\phi\, v'u'\right) && (\nabla.\mathbf{E}^{(\phi)}\mathrm{ii}) \\
& - \frac{\partial}{\partial p}\left(\left[f - \frac{1}{R_e\cos\phi}\left(\overline{u}\cos\phi\right)_\phi\right]\frac{v'\theta'}{\overline{\theta}_p}\right) && (\nabla.\mathbf{E}^{(p)}\mathrm{i}) \\
& + \frac{\partial}{\partial p}\left(\omega'u'\right). && (\nabla.\mathbf{E}^{(p)}\mathrm{ii})
\end{aligned} \tag{4.7}$$

Figures 4.10 and 4.11 show the geographical distribution of $\frac{-1}{R_e\cos\phi}\nabla.\mathbf{E}$ as calculated from the separate eddy terms for December and August respectively. The total, stationary and transient components are shown in panels (a), (b) and (c) respectively.

Looking at the total $\frac{-1}{R_e\cos\phi}\nabla.\mathbf{E}$, panel (a) in both figures, in the deep tropics between 10°N and 10°S; in August there is some eddy activity over east Africa, the northern Indian ocean and south Asia, between about 30°E and 150°E. In December there is more eddy activity than in August with eddy activity at most longitudes, especially over the Pacific and Atlantic oceans. There is also more eddy activity outside this latitude band in December than August. Comparing panel (a) with panels (b) and (c) in the two figures, the majority of the eddy activity in each figure is due to the stationary component (panel (b)). There is more eddy activity in the transient component in December than August, but in both cases it is much less than in the stationary component.

Figures 4.12 and 4.13 show the geographical distribution of the stationary component of the horizontal components of $\frac{-1}{R_e\cos\phi}\nabla.\mathbf{E}$ for December and August respectively. The term in $v'\theta'$ ($\nabla.\mathbf{E}^{(\phi)}$i) is shown in panel (a) and the term in $v'u'$ ($\nabla.\mathbf{E}^{(\phi)}$ii) is shown in panel (b). Figures 4.14 and 4.15 show the geographical distribution of the stationary component of the vertical components of $\frac{-1}{R_e\cos\phi}\nabla.\mathbf{E}$

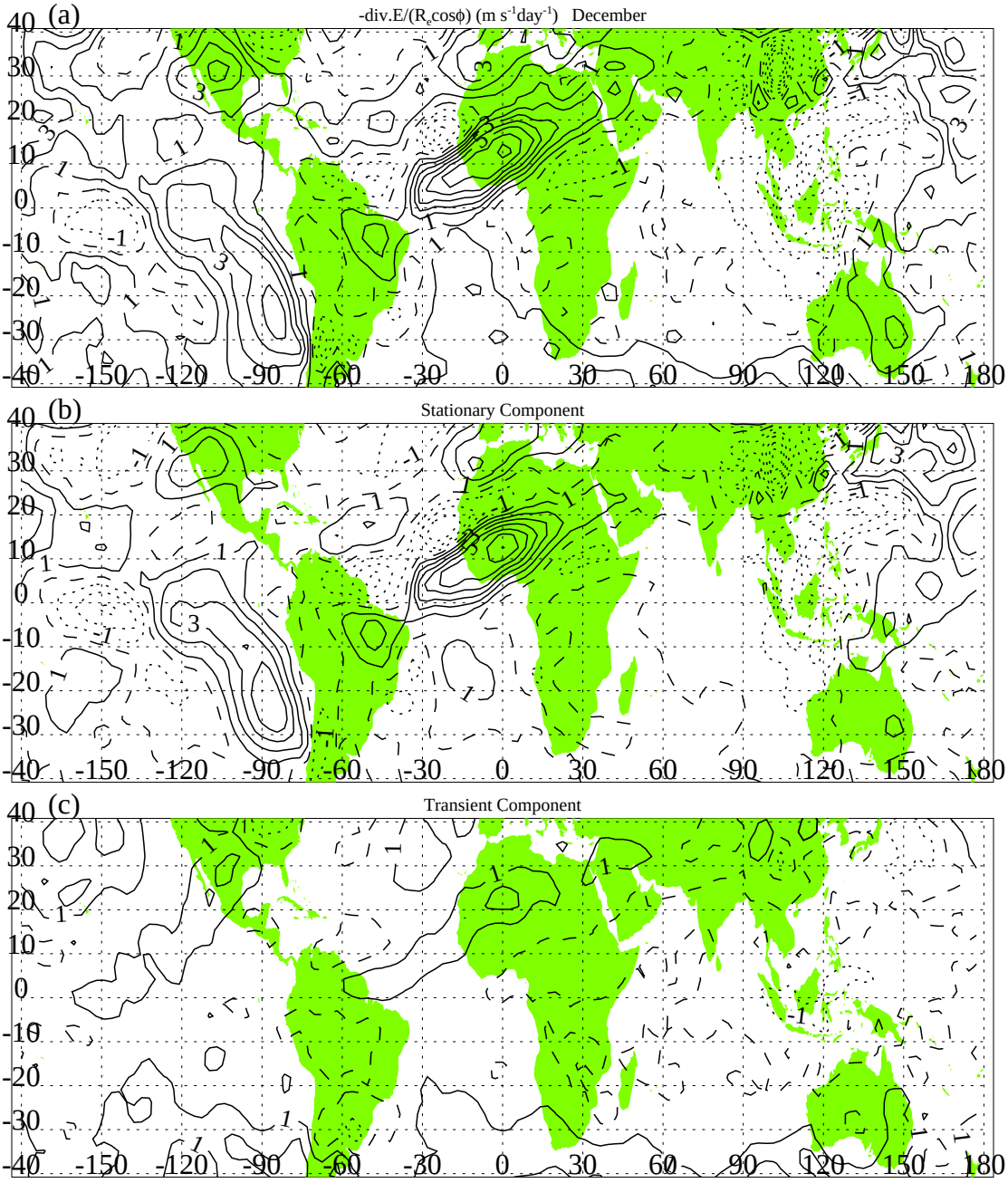

Figure 4.10: Geographical distribution of $\frac{-1}{R_e \cos\phi}\nabla.\mathbf{E}$ for December. Panel (a) shows the total $\frac{-1}{R_e \cos\phi}\nabla.\mathbf{E}$, (b) the stationary component and (c) the transient component. The contour interval is $1.0\,\mathrm{m\,s^{-1}\,day^{-1}}$. All longitudes are plotted, for the latitude band 40°N to 40°S. A map of the continents is also shown.

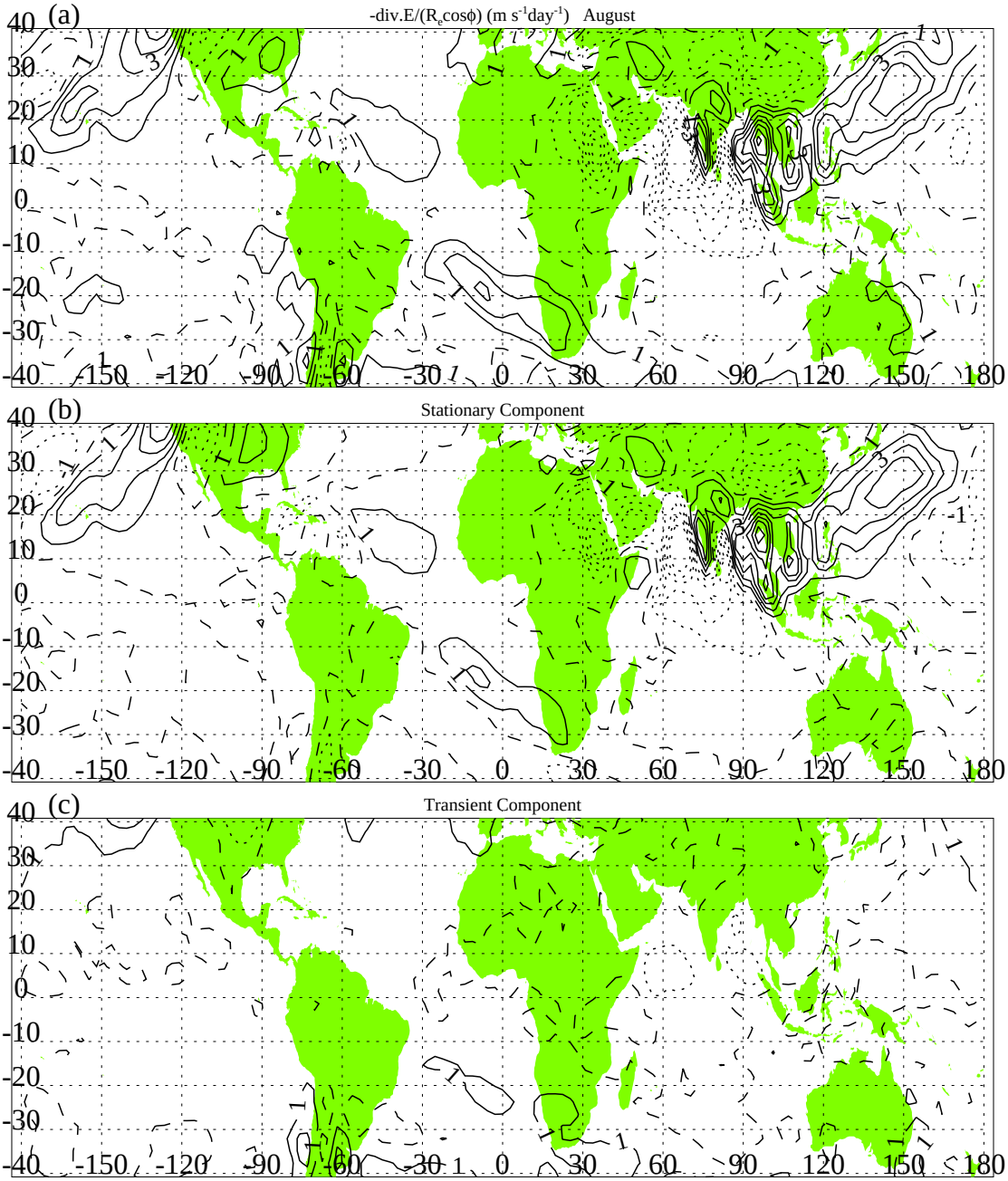

Figure 4.11: Geographical distribution of $\frac{-1}{R_e \cos\phi}\nabla.\mathbf{E}$ for August. Panel (a) shows the total $\frac{-1}{R_e \cos\phi}\nabla.\mathbf{E}$, (b) the stationary component and (c) the transient component. The contour interval is $1.0\,\mathrm{m\,s^{-1}\,day^{-1}}$. All longitudes are plotted, for the latitude band 40°N to 40°S. A map of the continents is also shown.

for December and August respectively. The term in $v'\theta'$ ($\nabla.\mathbf{E}^{(p)}$i) is shown in panel (a) and the term in $\omega'u'$ ($\nabla.\mathbf{E}^{(p)}$ii) is shown in panel (b). These should be compared with panel (b) in figures 4.10 and 4.11.

There is very little eddy activity in $v'\theta'$ ($\nabla.\mathbf{E}^{(\phi)}$i) in either December (figure 4.12a) or August (figure 4.13a). From here onwards, unless otherwise specified, it should be assumed that mention of $v'\theta'$ is referring to that of the vertical component, $\nabla.\mathbf{E}^{(p)}$i.

Contributions to eddy activity in December:

Comparing figures 4.10b, 4.12 and 4.14 it can be seen that the majority of the eddy activity in the 10° latitude band in the total stationary component (4.10b) is due to $v'u'$ (figure 4.12b) with some contribution from $\omega'u'$ (figure 4.14b). $v'u'$ has a banded structure of positive and negative regions of $\frac{-1}{R_e \cos\phi}\nabla.\mathbf{E}$ between 60°W and 30°E in the NH, which can be seen in the total stationary component. This pattern could be due to a combination of stationary planetary waves generated in the tropics propagating outwards and stationary planetary generated in the extra-tropics propagating inwards (Boehm and Lee, 2003). The positive region over the south-east Pacific is due to $v'u'$ between 10°N and 10°S and $v'\theta'$ (figure 4.14a) below 10°S. The negative region over south Asia and Indonesia is due to $v'u'$ between 10°N and 10°S and $v'\theta'$ (figure 4.14a) above 10°N. The positive region over the equatorial west Pacific is primarily due to $\omega'u'$ (figure 4.14b).

Contributions to eddy activity in August:

Comparing figures 4.11b, 4.13 and 4.13 it can be seen that the eddy activity over east Africa, India and south Asia in the total stationary component (4.11b) is due to $v'u'$ (figure 4.13b) and $\omega'u'$ (figure 4.15b). Outside the 10° latitude band $v'\theta'$ (figure 4.15a) contributes to the regions of convergence (positive values of $\frac{-1}{R_e \cos\phi}\nabla.\mathbf{E}$) over Asia and the north-west Pacific and the north-east Pacific. The divergence over north Africa and the Middle East in $v'\theta'$ cancels with the convergence in $v'u'$ (figure 4.13b).

Annual cycle in $v'u'$ ($\nabla.\mathbf{E}^{(\phi)}$ii):

Consider figures 4.12b and 4.13b. There is a lot more eddy activity in December than in August between 40°N and 40°S. In December at 10°N, although there is a lot of cancellation between positive and negative regions, figure 4.8e shows that there is a positive zonal mean. In August at 10°N there is much less eddy activity than 10°N in December. This eddy activity cancels to give a near zero but positive zonal mean. In both August and December there is less eddy activity at 10°S than 10°N with some cancellation between positive and negative regions giving small

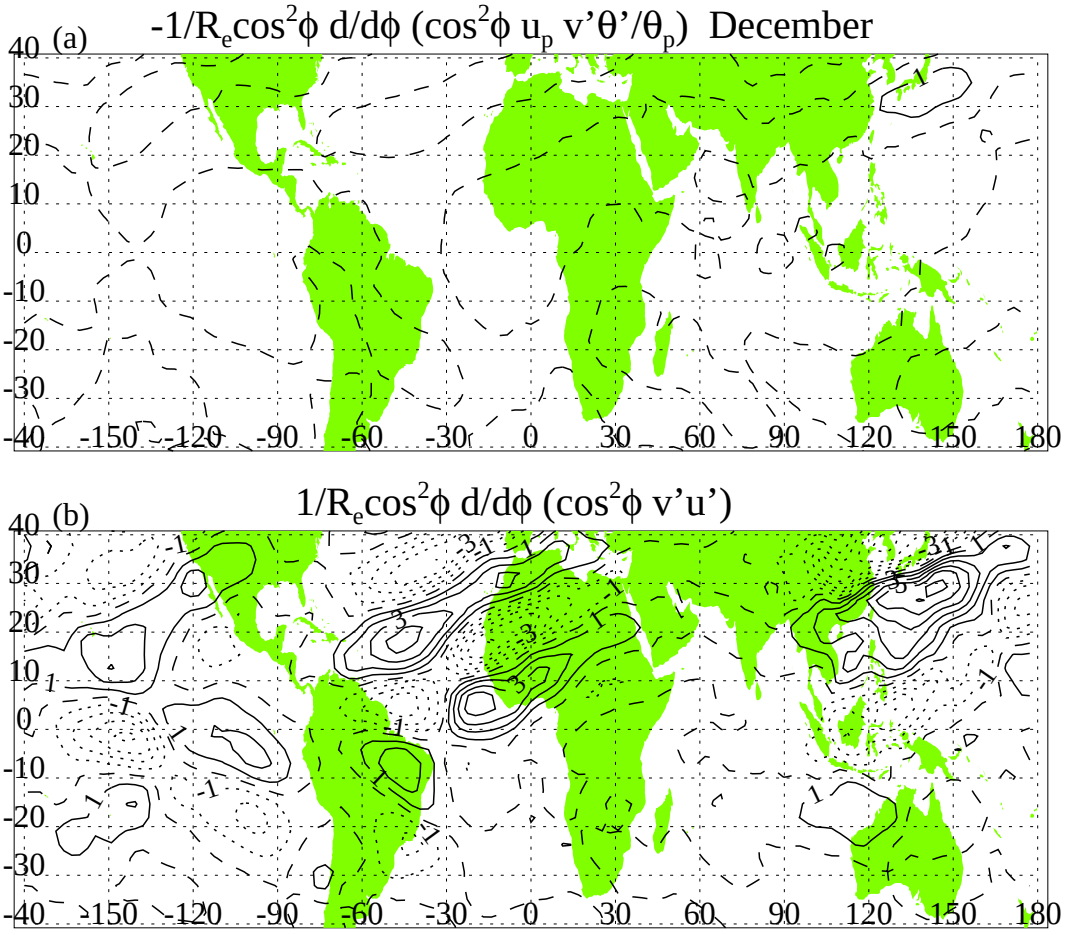

Figure 4.12: Geographical distribution of the stationary component of the horizontal components of $\frac{-1}{R_e \cos\phi}\nabla.\mathbf{E}$ for December. Panel (a) shows the term in $v'\theta'$ ($\nabla.\mathbf{E}^{(\phi)}$i) and (b) shows the term in $v'u'$ ($\nabla.\mathbf{E}^{(\phi)}$ii). The contour interval is $1.0\,\mathrm{m\,s^{-1}\,day^{-1}}$. All longitudes are plotted, for the latitude band 40°N to 40°S. A map of the continents is also shown.

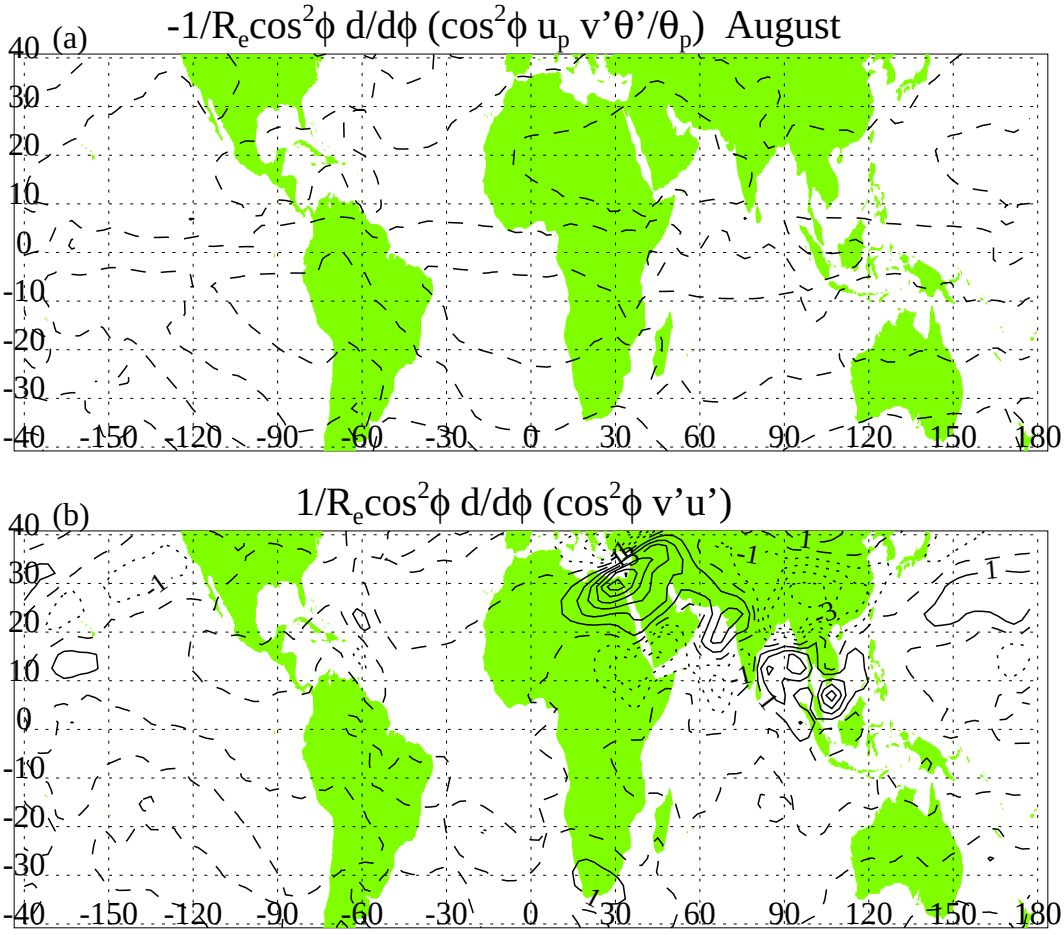

Figure 4.13: Geographical distribution of the stationary component of the horizontal components of $\frac{-1}{R_e \cos\phi}\nabla.\mathbf{E}$ for August. Panel (a) shows the term in $v'\theta'$ ($\nabla.\mathbf{E}^{(\phi)}$i) and (b) shows the term in $v'u'$ ($\nabla.\mathbf{E}^{(\phi)}$ii). The contour interval is $1.0\,\mathrm{m\,s^{-1}\,day^{-1}}$. All longitudes are plotted, for the latitude band 40°N to 40°S. A map of the continents is also shown.

positive zonal means (figure 4.8h).

Annual cycle in $v'\theta'$ ($\nabla.\mathbf{E}^{(p)}$i):

Consider figures 4.14a and 4.15a. There is very little eddy activity in either December or August between 10°N and 10°S. Between 40°N and 40°S there is more eddy activity in December than August. In December the 10° latitude bands cut across the edges of contours surrounding maxima and minima centred between 15° and 30°. At 10°N these positive and negative regions give a small negative zonal mean (figure 4.8e) and at 10°S they give a small positive zonal mean (figure 4.8h). In August the 10°N latitude band cuts across the region of convergence over eastern Asia and the north-west Pacific, giving a larger positive zonal mean than in December. At 10°S the zonal mean is close to zero. In the NH there is some cancellation between $v'\theta'$ and $v'u'$.

Annual cycle in $\omega'u'$ ($\nabla.\mathbf{E}^{(p)}$ii):

Consider figures 4.14b and 4.15b. In December the majority of eddy activity is between 20°N and 10°S with some eddy activity above 20°N, over Asia and the north-west Pacific. In August the eddy activity is confined to between 30°E, 120°E, 30°N and 10°S. In December at both 10°N and 10°S, the zonal mean is positive with small negative regions to cancel out the stronger positive regions (see also figure 4.8e and h). The zonal mean at 10°S is smaller than that at 10°N. In August at 10°S the negative regions outweigh the positive regions to give a net negative zonal mean whereas at 10°S there is much less eddy activity and a small net negative zonal mean.

To understand the changes in eddy contributions between December and August figure 4.16 shows the stream function, ψ, at 90 hPa for December and August. In August the flow is mostly zonal and westward in the tropics. In the region of the Asian monsoon, which occurs over east Africa, India and Asia in the summer, the stream function shows the upward extension of the monsoon anticyclone (Ramanathan, 1958; James, 1994; Dunkerton, 1995). There is also a minor anticyclone associated with monsoon over Mexico but this is well away from the tropics. Figure 4.16a shows that in December anticyclones associated with the monsoon are present over South America, west Africa and north-east Australia. These circulations are nearly symmetrical about the equator. In the tropics the flow is westward over Indonesia and the Indian Ocean and eastward over the Pacific and Atlantic oceans. There is northward and southward flow between the monsoon circulations. The monsoon anticyclones at this time of year can be thought of as the Rossby modes of the Gill solution for localised heating near

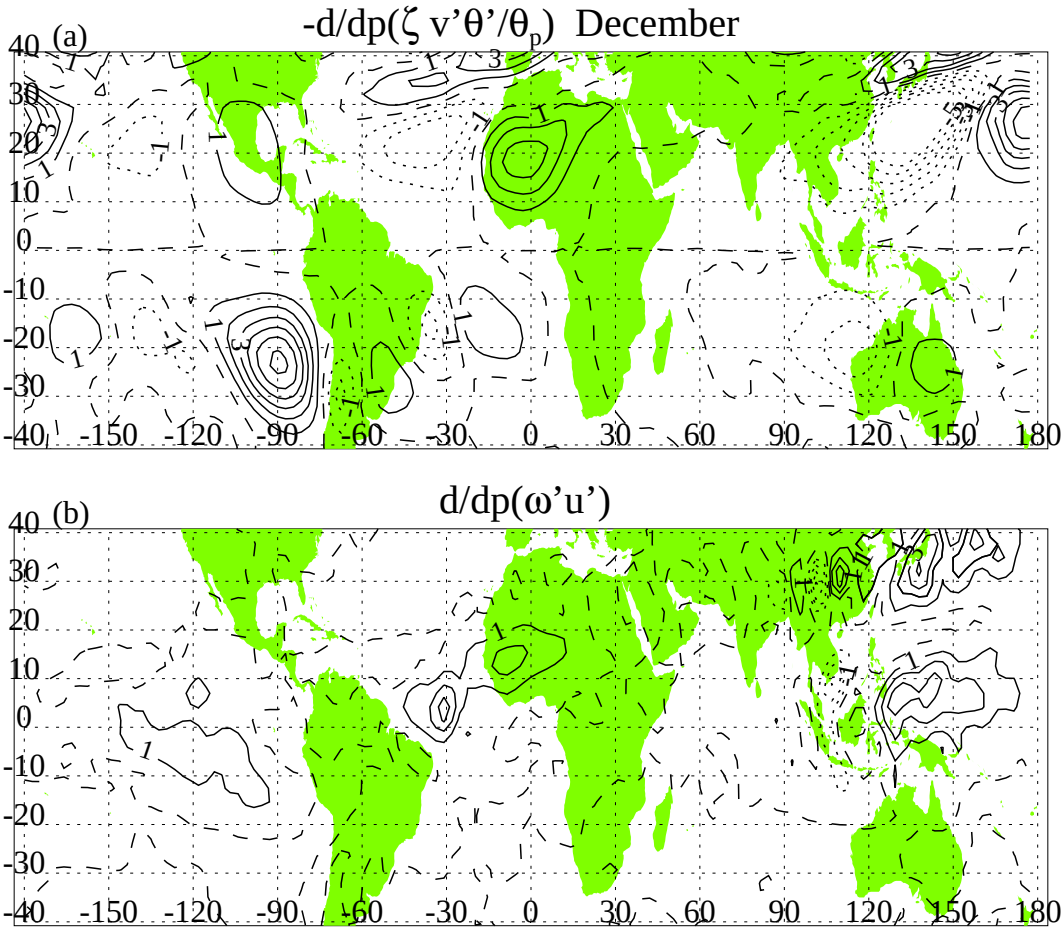

Figure 4.14: Geographical distribution of the stationary component of the vertical components of $\frac{-1}{R_e \cos\phi}\nabla.\mathbf{E}$ for December. Panel (a) shows the term in $v'\theta'$ ($\nabla.\mathbf{E}^{(p)}$i) and (b) shows the term in $\omega' u'$ ($\nabla.\mathbf{E}^{(p)}$ii). The contour interval is $1.0\,\mathrm{m\,s^{-1}\,day^{-1}}$. All longitudes are plotted, for the latitude band 40°N to 40°S. A map of the continents is also shown.

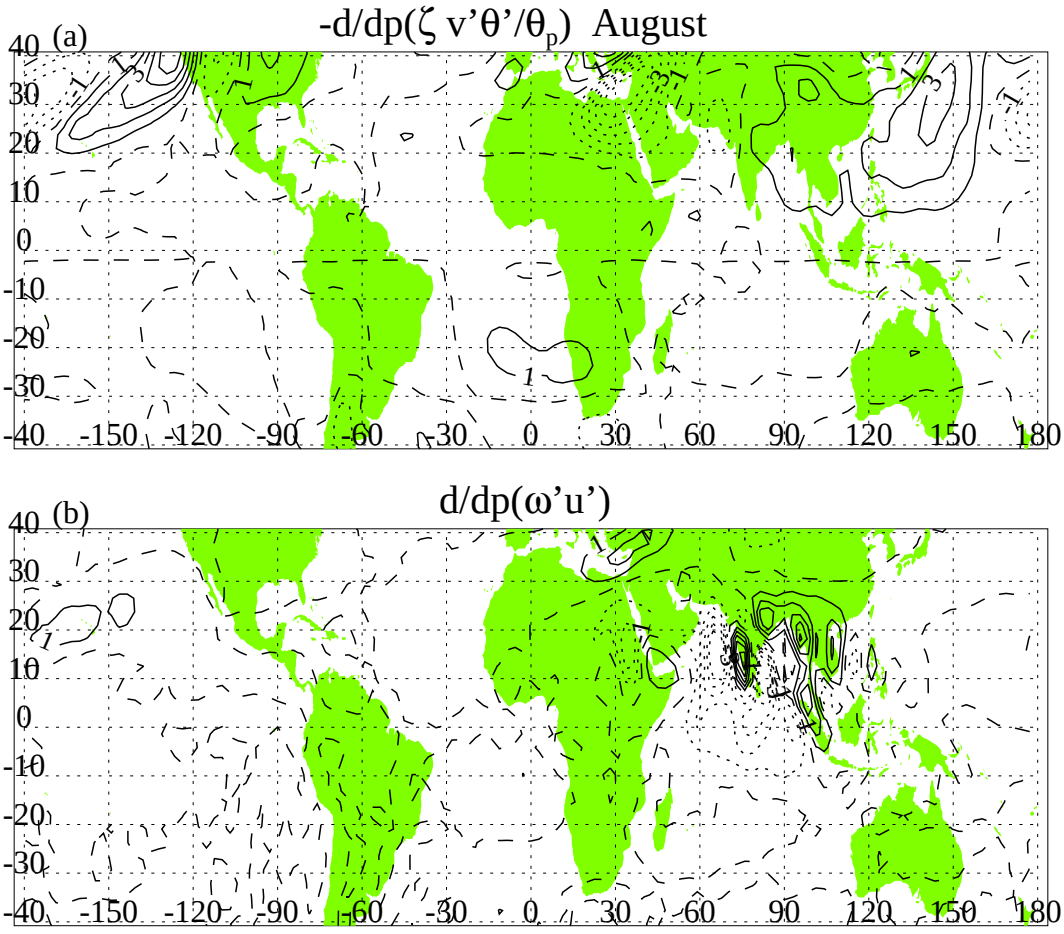

Figure 4.15: Geographical distribution of the stationary component of the vertical components of $\frac{-1}{R_e \cos\phi}\nabla.\mathbf{E}$ for August. Panel (a) shows the term in $v'\theta'$ ($\nabla.\mathbf{E}^{(p)}$i) and (b) shows the term in $\omega' u'$ ($\nabla.\mathbf{E}^{(p)}$ii). The contour interval is $1.0\,\mathrm{m\,s^{-1}\,day^{-1}}$. All longitudes are plotted, for the latitude band 40°N to 40°S. A map of the continents is also shown.

the equator (Gill, 1980; James, 1994). In December the monsoon anticyclones are much more symmetrical about the equator and occur over more longitudes than in August. The Gill solution shows that, when there is heating which is symmetrical about the equator, a Kelvin wave propagates eastward and planetary waves propagate westward from the forcing region. When the heating is off the equator, it can be decomposed into a part which is symmetric about the equator and a part which is antisymmetric. To the east of the heating only the symmetric part has any effect. To the west of the heating an asymmetry in the anticyclones north and south of the heating develops. The anticyclone in the hemisphere to which the heating is displaced dominates (James, 1994). The Asian monsoon in NH summer has a strong anticyclone centred near India and the circulation is of the form of the asymmetric form of the Gill solution.

In December the eddy terms $v'u'$ (figure 4.12b) and $v'\theta'$ (figure 4.14a) show eddy activity near each of the anticyclones associated with the monsoon circulations shown in the stream function (figure 4.16a), $\omega'u'$ (figure 4.14b) also has eddy activity near these anticyclones, to a lesser extent. Similarly in August the eddy terms $v'u'$ (figure 4.13b) and $v'\theta'$ (figure 4.15a) have eddy activity near each of the anticyclones associated with monsoon circulations shown in the stream function (figure 4.16a), $\omega'u'$ (figure 4.15b) also has eddy activity near these anticyclones, to a lesser extent. The main eddy activity for all these eddy terms is near the monsoon anticyclones or where there is significant meridional motion.

Figure 4.17 shows the geographical distribution of the perturbation from the zonal mean residual mean vertical velocity, ω', for December and August. In December there is a pattern of enhanced upwelling and downwelling in the regions of the monsoon circulations noted in the previous paragraph. In August there is strongly enhanced upwelling near the monsoon circulation noted in the August stream function.

Figure 4.18 shows the geographical distribution of the perturbation from the zonal mean potential temperature, θ', for December and August. In December temperatures are generally greater than the zonal mean between 150°W and 90°E, with enhanced temperatures either side of the equator at 120°W and 30°W. Temperatures are below the zonal mean between 120°E and 150°W, with decreased temperatures either side of the equator at 150°E. Within the 10° latitude band temperatures are up to 7 K above the zonal mean and down to 7.9 K below it. In August there is a small region of temperatures below the zonal mean pushing into the region above the zonal mean at the equator from 120°W to

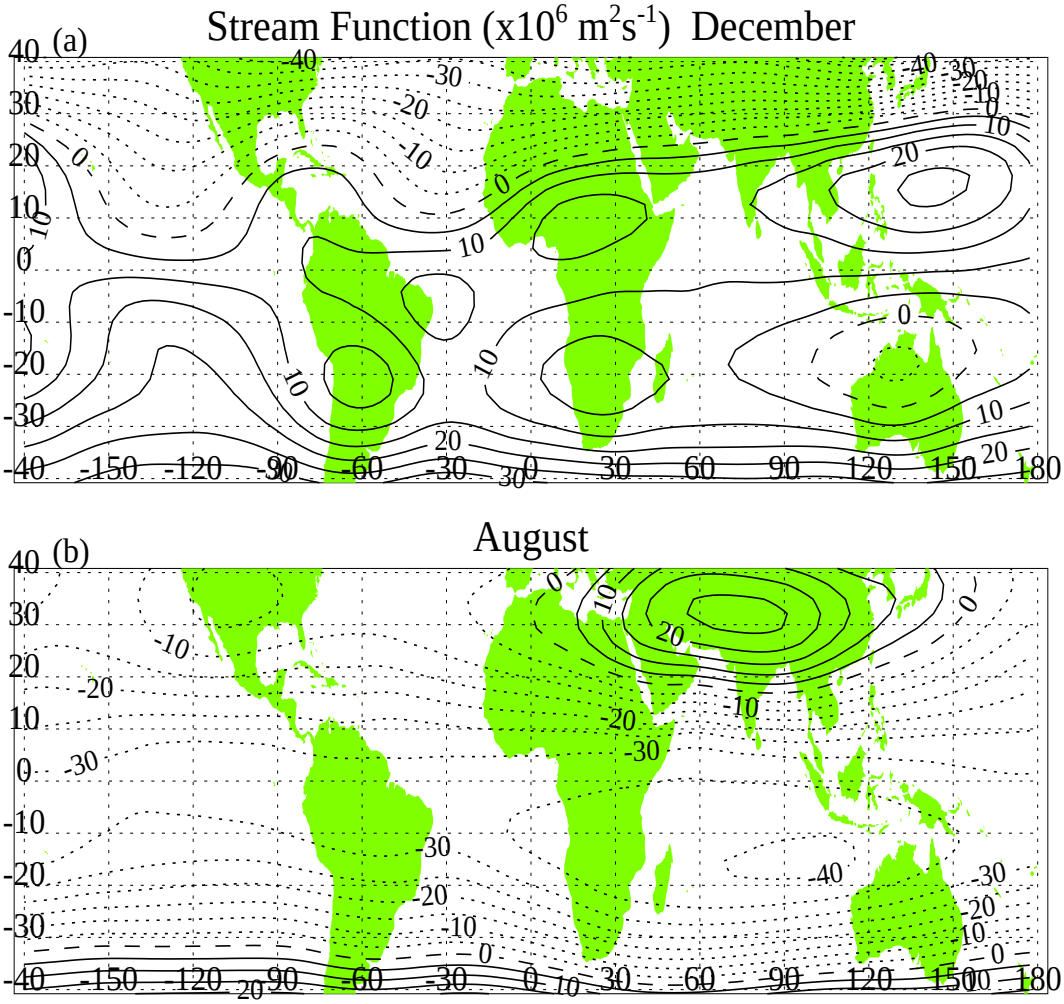

Figure 4.16: Geographical distribution of the stream function for (a) December and (b) August. The contour interval is 5×10^6 m^{2}s^{-1}. All longitudes are plotted, for the latitude band 40°N to 40°S. A map of the continents is also shown.

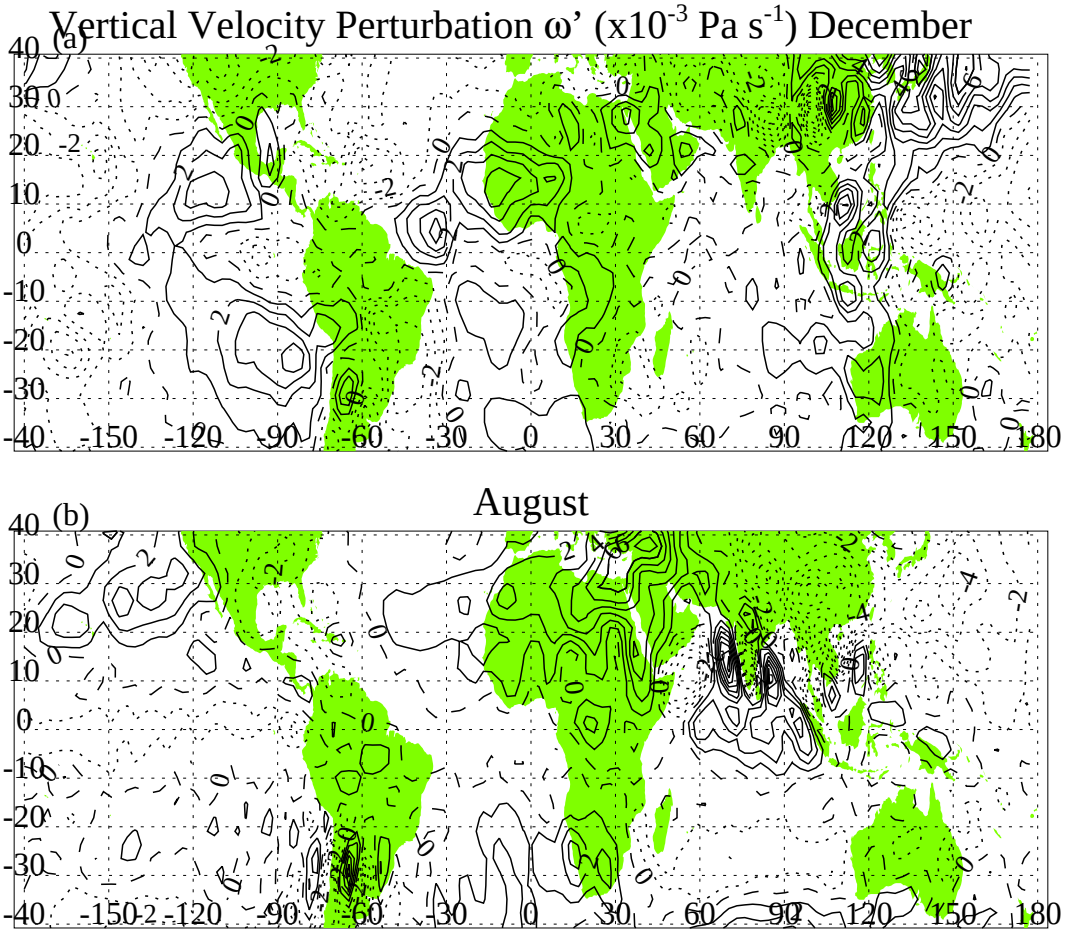

Figure 4.17: Geographical distribution of the perturbation from the zonal mean residual mean vertical velocity, ω', for (a) December and (b) August. The contour interval is $0.5\times10^{-3}\,\mathrm{Pa\,s^{-1}}$. Negative values indicate enhanced upwelling with respect to the zonal mean. All longitudes are plotted, for the latitude band 40°N to 40°S. A map of the continents is also shown.

70°W. There are also enhanced temperatures above the zonal mean around the equator between 60°E and 100°E. Within the 10° latitude band temperatures are up to 5.3 K above the zonal mean and 4.8 K below it. Although the variation in temperatures in December is greater the zonal mean temperature is less than that of August (section 3.2). In December the temperature perturbations are nearly symmetrical about the equator, with maxima and minima pairs near the locations of the monsoons, whereas in August the temperature distribution is much less symmetrical.

Figure 4.19 shows the geographical distribution of the perturbation from the zonal mean meridional velocity, v', for December and August. In December there are clear pairs of maxima of northwards and southwards flow either side of the equator in the regions of the monsoon circulations. In August the main northwards and southwards flow is in the monsoon region over south Asia.

In section 4.4.3, looking at the stationary and transient components of the eddy terms of $\nabla.\mathbf{F}$, there was a sharp maximum noted in June in $v'u'$ (figure 4.8e). Figure 4.20 shows the geographical distribution of the stationary component of $\frac{-1}{R_e \cos\phi}\nabla.\mathbf{E}$ from $v'u'$ for June. As well as the region of eddy activity seen in August (figure 4.13) over east Africa and Asia there is an additional region of convergence and divergence over South America and the Atlantic. This gives an extra positive region between 60°W and 20°W at 10°N, which gives a greater positive zonal mean. This is not present in July and is smaller and cancelled out by a slightly stronger negative region between 30°E and 60°E in May. Figure 4.21 shows the stream function for June which is similar to that of August (figure 4.16b) except that there is some meridional flow over the Atlantic in the same region as the extra eddy activity in the eddy momentum flux noted in figure 4.20. The monsoon circulation in June also has greater zonal extent than in August.

In examining the longitudinal source of wave-driving, the results of this section show:

- The main differences between December and August are the presence of additional monsoon anticyclones in December and the movement of the Asian monsoon off the equator in August. These anticyclones are shown in the stream function and the main changes in eddy activity between the eddy flux terms are in the regions of these anticyclones.
- The majority of the eddy activity in the geographical distribution of $\frac{-1}{R_e \cos\phi}\nabla.\mathbf{E}$ is from the stationary component.
- There is little contribution from $v'\theta'$ ($\nabla.\mathbf{E}^{(\phi)}$i).

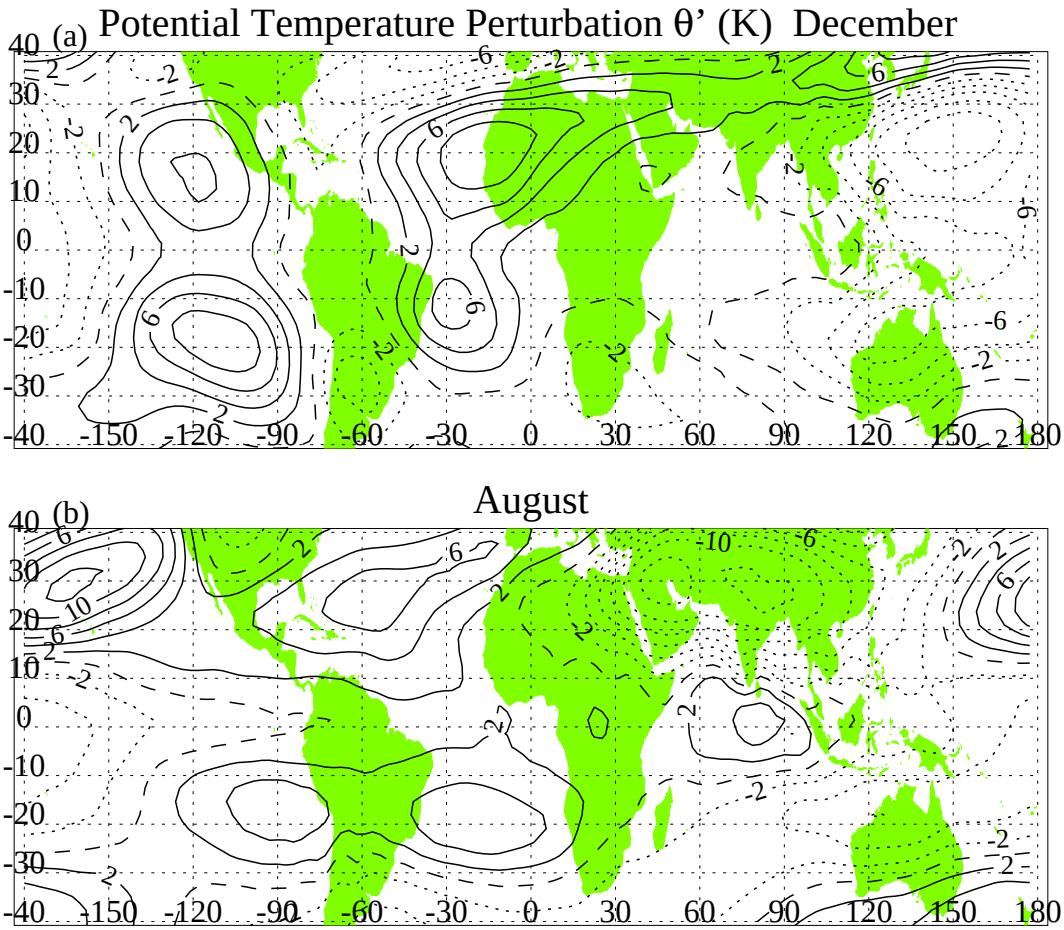

Figure 4.18: Geographical distribution of the perturbation from the zonal mean potential temperature, θ', for (a) December and (b) August. The contour interval is 2 K. All longitudes are plotted, for the latitude band 40°N to 40°S. A map of the continents is also shown.

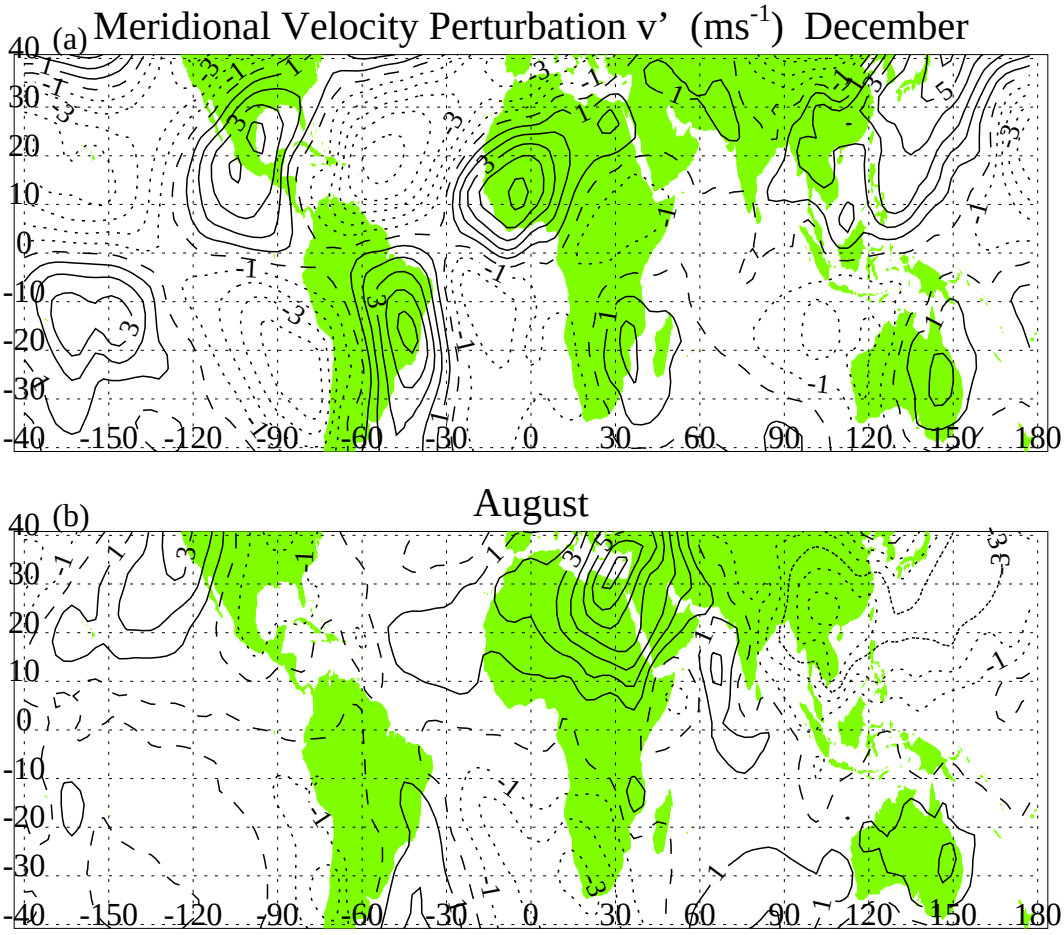

Figure 4.19: Geographical distribution of the perturbation from the zonal mean meridional velocity, v', for (a) December and (b) August. The contour interval is $0.5\,\mathrm{m\,s^{-1}}$. All longitudes are plotted, for the latitude band 40°N to 40°S. A map of the continents is also shown.

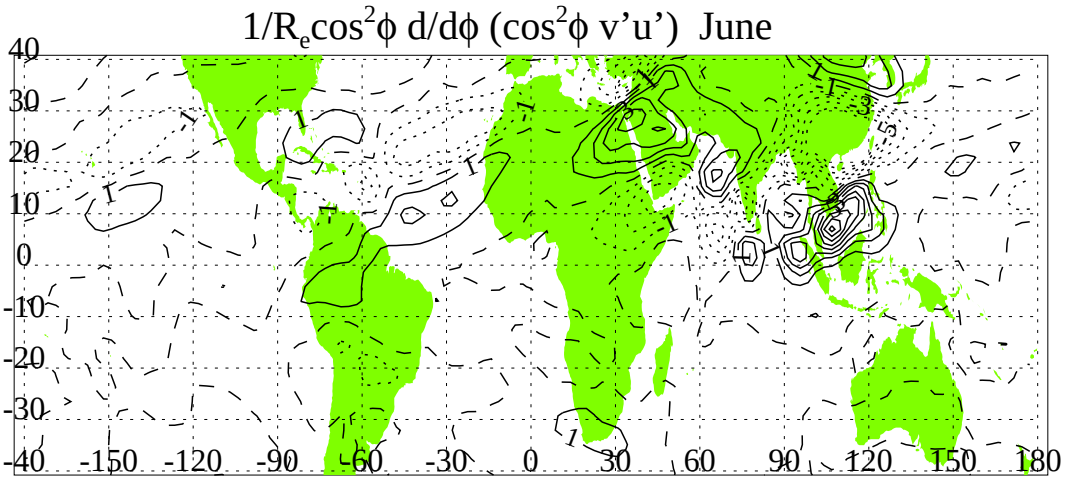

Figure 4.20: Geographical distribution of the stationary component of the horizontal eddy term $v'u'$ ($\nabla.\mathbf{E}^{(\phi)}$ii) of $\frac{-1}{R_e \cos\phi}\nabla.\mathbf{E}$ for June. The contour interval is 1.0 m s^{-1} day^{-1}. All longitudes are plotted, for the latitude band 40°N to 40°S. A map of the continents is also shown.

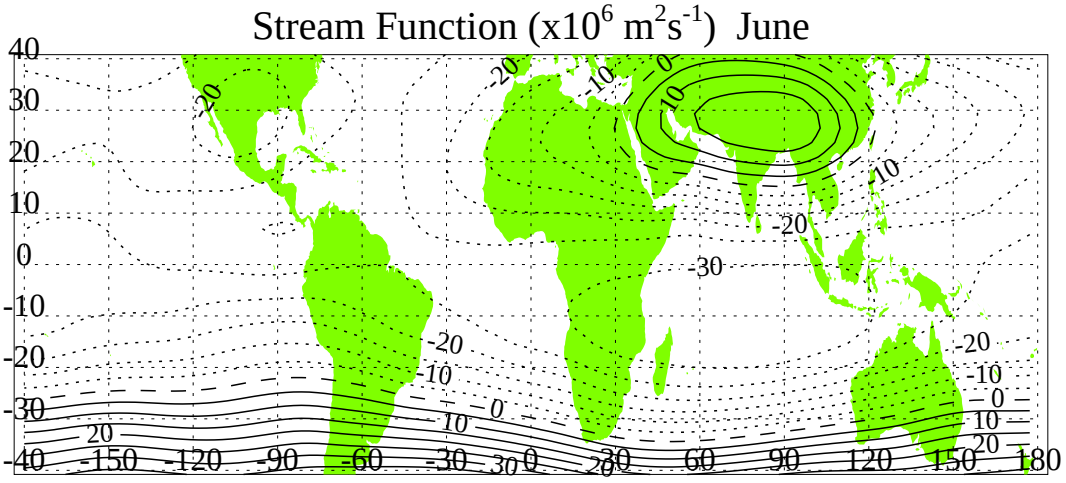

Figure 4.21: Geographical distribution of the stream function for June. The contour interval is 5×10^6m^{2}s^{-1}. All longitudes are plotted, for the latitude band 40°N to 40°S. A map of the continents is also shown.

- The component $v'u'$ ($\nabla.\mathbf{E}^{(\phi)}$ii) contributes to most of the eddy activity within the 10° latitude band as well as to some of the eddy activity outside this latitude band. In December there is eddy activity throughout the 10° latitude band, particularly in the same regions as the upward extensions of the monsoon anticyclones are seen in the stream function. In August the eddy activity is over southern Asia, where a monsoon anticyclone can be seen in the stream function.
- The majority of the eddy activity in $v'\theta'$ ($\nabla.\mathbf{E}^{(p)}$i) is outside the 10° latitude band. In December more of the eddy activity reaches lower latitudes than in August. In December and August the majority of the eddy activity is near to regions where there is a monsoon anticyclone.
- The component $\omega'u'$ ($\nabla.\mathbf{E}^{(p)}$ii) contributes to some of the eddy activity within the 10° latitude band near the regions of monsoon anticyclones in December and August.
- In June there is extra eddy activity in $v'u'$ over the Atlantic, with the Asian monsoon reaching further westward to this region. This is not present in May or July. This causes the semi-annual cycle seen in the horizontal component.

4.5 Summary

EP flux divergence has two main extrema in its annual cycle, in December and August. In December contours of EP flux are closer to the equator, giving higher EP flux at 10°; in August they are pushed out from the equator, giving lower EP flux at 10° (figure 4.3).

In section 4.4.1 the EP flux divergence was decomposed into horizontal wavenumbers and it was found that the majority of the annual cycle was due to wavenumbers greater than or equal to three, rather than longer wavelength planetary waves. The annual cycle for the edges of the latitude band 10°N to 10°S was also due more to the NH component than to the SH component.

The EP flux was then further decomposed into vertical and horizontal components (section 4.4.2). This showed that both the vertical and horizontal components were important and both the northern and southern hemispheres were important. In the SH the annual cycles in the vertical and horizontal components mostly cancel each other out for wavenumbers one and two. For wavenumbers greater than or equal to three the horizontal component partially cancels the vertical component, giving a small residual annual cycle. In the NH wavenumbers

one and two partially cancel the annual cycle in wavenumbers greater than or equal to three. This gives a semi-annual cycle in the horizontal component.

Section 4.4.3 showed that the EP flux can be considered in terms of the individual eddy fluxes, which can be decomposed into stationary and transient components. If these are not zonally averaged their geographical distribution can be studied to give an idea of which longitudes contribute to the annual cycle (section 4.4.4). The stationary component is the significant component, the driving is therefore a longer timescale, slower effect. The transient component gives only a small contribution to the annual cycle, but does reduce the effect of the semi-annual cycle secondary maximum in June.

The annual cycle in EP flux divergence is due to a combination of $v'u'$ in the horizontal component and $\omega'u'$ and $v'\theta'$ in the vertical component. The $v'\theta'$ term in the horizontal component is not important. The $\omega'u'$ and $v'\theta'$ terms in the vertical component oppose each other in the NH but complement each other in the SH. In the NH $v'u'$ provides a semi-annual cycle, enhancing the annual cycle in NH winter but adding a secondary maximum in June. In the SH $v'u'$ opposes the annual cycle in the vertical component. August is a time when all three of these terms are small in both hemispheres, whereas in December all the terms are near maximum except for $v'\theta'$ from the vertical component in the NH.

An important difference between August and December is the position and number of the monsoon anticyclones. In December monsoon anticyclones can be seen over South America, west Africa, and north-west Australia. In August there is only the south Asian monsoon anticyclone which is pushed well off the equator. This potentially has important implications for the EP flux distribution and wave driving in the lower tropical stratosphere. It is hypothesised that in December the various monsoon anticyclones mean that there is much more EP flux divergence and convergence. The EP flux divergence plots from the separate eddy fluxes all have enhanced eddy activity (regions of convergence and divergence) near the monsoon anticyclones. In each eddy flux term there is a lot of cancellation between these regions when calculating the zonal mean, but in December there is a greater net EP flux divergence.

In June there is additional eddy activity in $v'u'$ as the Asian monsoon anticyclone has a greater westward extent, reaching the Atlantic Ocean. This is not present in July. This gives an early summer maximum in the horizontal component of EP flux divergence, and a semi-annual contribution to the signal.

In December the monsoon anticyclones are nearly symmetrical about the equa-

tor and spread out covering most longitudes. The associated anticyclone penetrates up into the tropical lower stratosphere (Dunkerton, 1995) where it dissipates to give a non-zero contribution to the EP flux divergence. This drives outwelling from the tropical lower stratosphere. In August the monsoon anticyclone covers less of the globe and is centred off the equator, in the NH. Consequently there is less wave dissipation in the stratosphere, giving a smaller contribution to the EP flux divergence. The change in EP flux divergence over the year modulates the outwelling from the tropical lower stratosphere which, by local downward control, modulates the amount of tropical upwelling and thus adiabatic heating and cooling. This in turn causes changes in the zonal mean potential temperature.

Further understanding of the links between the heat-induced tropical circulations and their influence on tropical lower stratospheric temperatures could be gained by considering the solutions given by Gill (1980). In that study it was shown a tropical Rossby wave (which is akin to the upper-level monsoon anticyclones) is forced to the west of the heating region, while a Kelvin wave is forced to the east of the heating region. Both these waves could vertically propagate into the stratosphere and produce fluxes of $v'u'$ (from the Rossby wave) and $\omega'u'$ (from the Kelvin wave). It would be possible to study the dissipation of the Rossby and Kelvin waves in a non-linear mechanistic model where the EP fluxes could be compared to the results of this chapter. Since this chapter shows that both the divergence of $v'u'$ and $\omega'u'$ are important, this may imply that both the Rossby and Kelvin waves play a role in the annual cycle.

Chapter 5

Methodology for the transformed Eulerian mean study of the Unified Model data

In the previous chapters the ECMWF analysis data was studied. This chapter will begin with describing the shortcomings of the ECMWF data set and explaining why data from a general circulation model (GCM) such as the Unified Model (UM) will be useful. In section 5.4 the Unified Model will be described and section 5.6 will describe the processing of the UM data. The main methodology will be as follows:

- Set up and run the Unified Model to produce an equivalent data set to that of the ECMWF analysis data.
- Form a mean annual cycle in potential temperatures from the Unified Model data.
- Analyse the balance of the terms in the TEM thermodynamic equation to find what is driving the temperature changes over the annual cycle.
- Analyse the TEM mass continuity equation to find where the net outflow from the tropics is producing a cycle in tropical vertical ascent.
- Analyse the balance of the terms in the TEM momentum equation to find what forces are driving mass outflow from the tropics.
- Compare the results with those of the ECMWF analysis data.

In chapter 6 the results of this analysis will be described and compared with the results from the ECMWF analysis data.

5.1 Shortcomings of the ECMWF data

Many aspects of a re-analysis data set such as the ECMWF data set are dependent on the assimilating forecast model and its physics. There have been various changes to the ECMWF model which have affected, amongst other things, the humidity fields. These changes included changing the way humidity is represented in the model and changing the way the assimilation of observational data was done (Simmons *et al.*, 1999). Each of these changes may have had an effect on the residual mean circulation in the model. It was mentioned in section 2.1.2 that the implementation of 4D-Var is known to have affected the stratospheric residual mean circulation, $(0, \overline{v}^*, \overline{\omega}^*)$. A comparison of the ERA-15 data set and the ERA-15 plus the operational analyses data set, used in the previous chapters, is shown in the next section.

5.2 Comparison of ERA-15 and ERA-15 plus operational analyses

This section compares the 22 years of ERA-15 plus operational analyses (December 1978–October 2001) used in chapters 3 and 4 with data from just the ERA-15 period (December 1978–February 1994) in order to see if the results are affected by the changes in the model after the ERA-15 period.

Figure 5.1 shows the residual mean vertical velocity, $\overline{\omega}^*$, for (panel (a)) the 22 years of the ECMWF analysis data used and (panel (b)) the ERA-15 period. The plots for the two data periods are very similar in general shape. Near 90 hPa in the tropics differences are generally less than 10%. In other areas differences are greater, especially in the mid-latitudes and near the poles.

Figure 5.2 shows the annual cycle in potential temperature anomaly (panel (a)) and each of the terms in the thermodynamic equation (panel (b)) averaged across the latitude band 9.8°N to 9.8°S at 90 hPa for ERA-15. Figure 3.5 is the equivalent for the entire 22 year data set. The result is essentially the same for the two periods with changes in potential temperature of the same magnitude at the same time of year. The adiabatic cooling has a similar cycle in ERA-15, although with a greater decrease in cooling in NH summer. $\frac{\partial \overline{\theta}}{\partial t}$ responds to the adiabatic cooling and the diabatic heating responds to the change in potential temperature, although decreasing its heating effect by less in NH summer.

Figure 5.3 shows the annual cycle of the terms in the zonal momentum equation

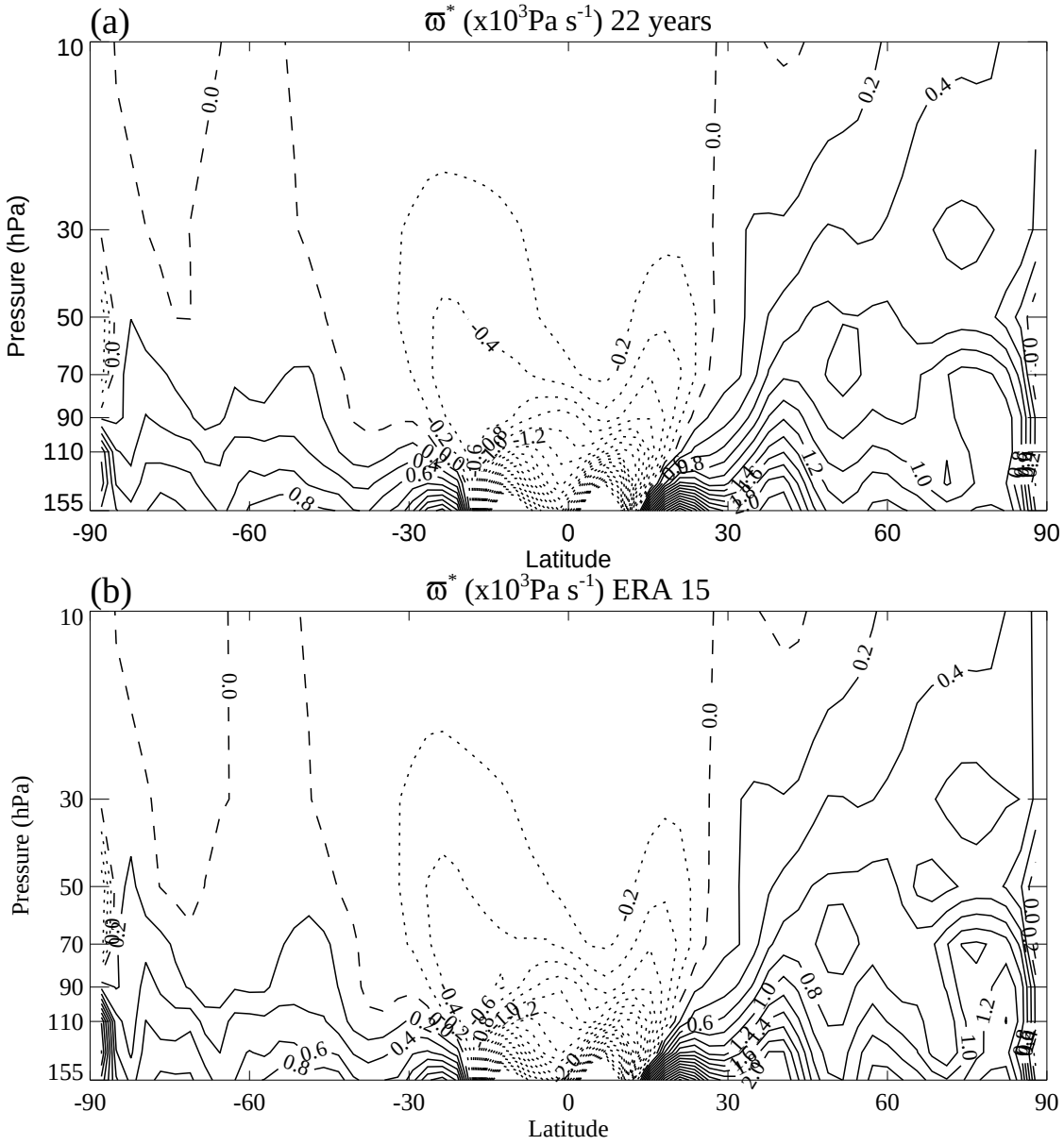

Figure 5.1: $\overline{\varpi}^*$ for December (a) 22 year average (entire ECMWF analysis data period) (b) ERA-15 period average. Solid contours indicate positive values (descent), dashed contours zero and dotted contours negative (ascent). The contour interval is $0.2\times10^{-3}\,\mathrm{Pa\,s^{-1}}$.

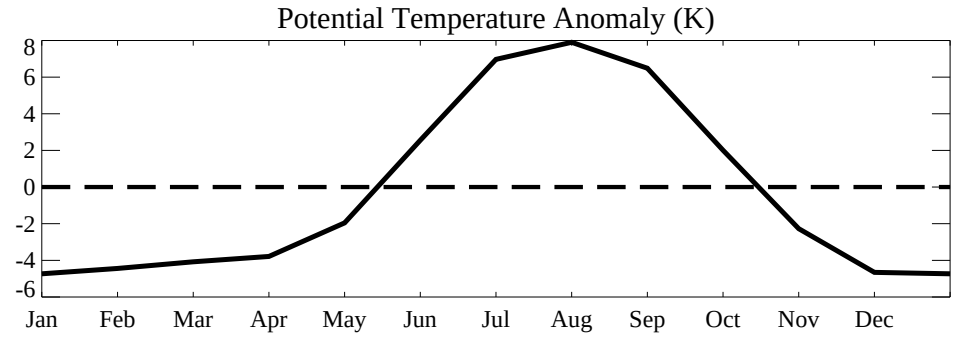

(a) Potential temperature anomaly

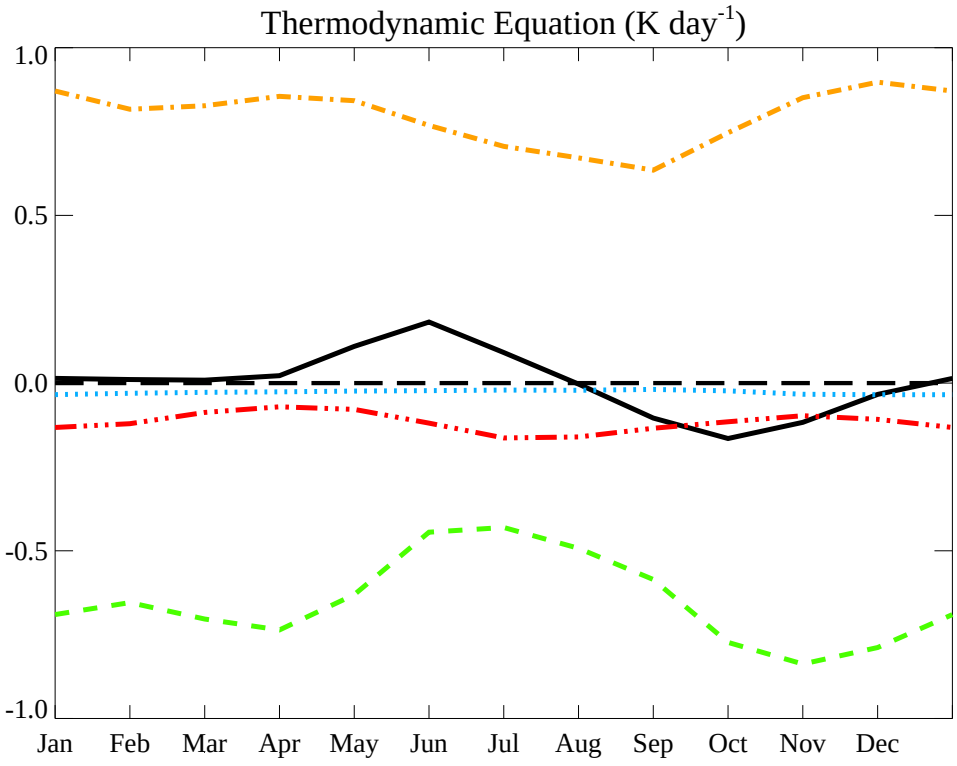

(b) Terms in the thermodynamic equation

Figure 5.2: Mean annual cycle averaged from 9.8°N to 9.8°S at 90 hPa of (a) the potential temperature and (b) the terms in the thermodynamic equation at 90 hPa for ERA-15 data. In (b) the terms are $\frac{\partial\overline{\theta}}{\partial t}$ (solid black line), $-\frac{\overline{v}^*}{R_e}\frac{\partial\overline{\theta}}{\partial\phi}$ (dotted blue line), $-\overline{\omega}^*\frac{\partial\overline{\theta}}{\partial p}$ (dashed green line), $\overline{Q}$ (dashed and dotted orange line) and $-\frac{\partial}{\partial p}\left(\frac{\overline{v'\theta'}\,\overline{\theta}_\phi}{R_e\overline{\theta}_p}+\overline{\omega'\theta'}\right)$ (dash and three dotted red line).

(3.9) for the latitude band 9.8°N to 9.8°S at 90 hPa. Figure 3.16 is the equivalent for the 22 year data set. Again the result is essentially the same for the two periods. The annual cycle in $\overline{v}^*$ is driven by the EP flux divergence. The rate of change of zonal wind has a semi-annual cycle which contributes to and opposes the driving of $\overline{v}^*$ at the same times of year as for the 22 year data set.

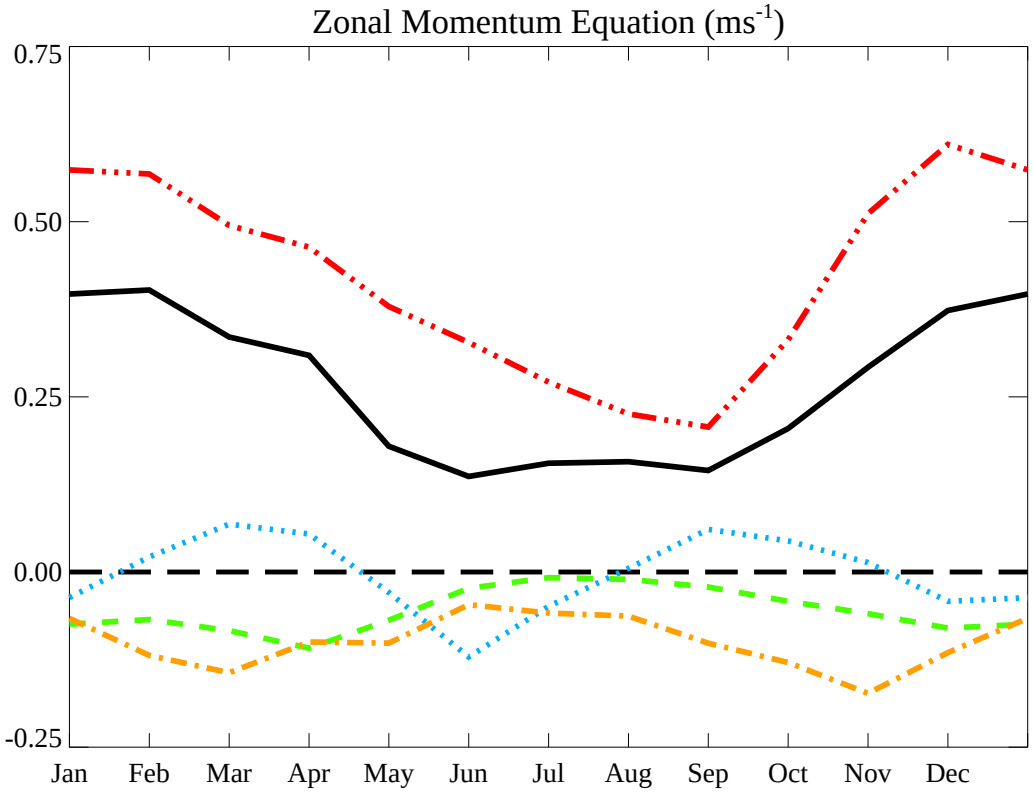

Figure 5.3: Mean annual cycle of the terms in the zonal momentum equation divided by $\overline{\zeta}_a$ (equation 3.9) at 90 hPa for ERA-15 data, terms at 9.8°N minus terms at 9.8°S. This is the difference between the terms at 9.8°N and 9.8°S at 90 hPa. The terms are $\overline{v}^*$ (solid black line), $\frac{1}{\overline{\zeta}_a}\frac{\partial \overline{u}}{\partial t}$ (dotted blue line), $\frac{-\overline{\omega}^*}{\overline{\zeta}_a}\frac{\partial \overline{u}}{\partial p}$ (dashed green line), $\frac{1}{R_e \cos\phi}\frac{\nabla.\mathbf{F}}{\overline{\zeta}_a}$ (dash and three dotted red line) and $\frac{\overline{X}}{\overline{\zeta}_a}$ (dashed and dotted orange line).

These figures show that there have been small changes in the residual mean circulation between the ERA-15 and subsequent operational analyses which will have affected model balance. However the changes have not affected the results of this research.

5.3 Assimilated observational data and model data

Because the ECMWF data set has been produced by assimilating mixed resolution, unevenly spaced, observational data into a model and using the model to produce data on a regular grid the data will not necessarily represent a balanced state of the atmosphere. There is a large variation in the accuracy and types of observations in different regions and this is not obvious in the analysed data. Model biases may dominate variables which have not been directly observed. The model forces the variables within it towards the values which would give a balanced model simulation, thus the result may not be the same as either a balanced atmosphere or a balanced model, but somewhere in between. As mentioned in the previous section the residual mean circulation has also changed slightly between ERA-15 and the operational analyses. It is possible that the residual mean circulation in the analysis fields from the ECMWF model is not self-consistent or balanced such that there may be extra fictitious terms in the TEM equations. Equation 5.1 illustrates the possibility of an added term $\overline{A}$ in the zonal momentum equation;

$$\frac{\partial \overline{u}}{\partial t} = \overline{v}^* \left(f - \frac{1}{R_e \cos\phi} \frac{\partial}{\partial \phi} \left(\overline{u} \cos\phi \right) \right) - \overline{\omega}^* \frac{\partial \overline{u}}{\partial p} + \frac{1}{R_e \cos\phi} \nabla . \mathbf{F} + \overline{X} + \overline{A}. \qquad (5.1)$$

This term, $\overline{A}$, represents a perturbation due to the analysis scheme and it may provide some of the driving of the residual mean circulation in the analysis fields. Thus the residual "$\overline{X}$" in chapters 2 to 4 will actually be representing $\overline{X} + \overline{A}$.

In contrast to assimilated data a model run with specified initial and boundary conditions should be in a balanced state, such that the residual mean circulation will be self-consistent and without the fictitious term $\overline{A}$ in equation 5.1. It will, however, be less close to the real world than assimilated data. The use of a GCM should give a balanced data set with a balanced residual mean circulation. Using a different GCM than that used for assimilating the data will also mean the use of a different set of compromises where models cannot absolutely represent the real world. Because a specific model integration can be set up for the research any output diagnostics available which would be useful for the research can be selected. Diagnostics expected to give more information about $\overline{X}$ and $\overline{Q}$ were selected for this research.

5.4 The Unified Model

The model used is the UK Met Office Unified Model, HadAM3 (Cullen, 1993; Pope *et al.*, 2001). This is a GCM which has been developed for the dual purpose of climate modelling and weather forecasting.

General circulation models are complicated three-dimensional numerical models based on sets of equations which govern the time evolution of the atmosphere. The primitive equations are used. These are the momentum, mass continuity and thermodynamic equations. To solve these equations numerically in a reasonable length of time with the computer resources currently available approximations and assumptions are made. Most GCMs use the hydrostatic form of the primitive equations, equations 2.2 given in chapter 2. These equations assume that vertical accelerations are small and that vertical length scales are much smaller than horizontal length scales (the "shallow-atmosphere" approximation). Some terms are neglected including the Coriolis terms involving $2\Omega\cos\phi$ from the momentum equation. However White and Bromley (1995) showed that this latter approximation is not always valid, especially in synoptic-scale motions in the tropical atmosphere. They produced a set of equations which include the Coriolis terms involving $2\Omega\cos\phi$ and which still conserve energy, angular momentum and potential vorticity.

5.4.1 Model equations

The UM uses a similar set of equations to White and Bromley (1995) but with a different vertical coordinate. The vertical coordinate used is $\eta = \eta(p, p_*)$ where p_* is the surface pressure, $\eta(0, p_*) = 0$ and $\eta(p_*, p_*) = 1$ (Cullen *et al.*, 1993). Because the shallow atmosphere approximation has been abandoned, the "pseudo-radius" (r_s) is defined. This is the sum of the mean radius of the Earth and the height above the Earth's surface:

$$r_s(p) = R_e + \int_p^{p_1} \frac{RT_r(p)}{gp} dp, \tag{5.2}$$

where $T_r(p)$ is a reference temperature profile representing the horizontally averaged balanced state of the atmosphere and p_1 is a reference pressure (White and Bromley, 1995). This gives a vertical velocity defined as

$$\tilde{w} = \frac{Dr_s}{Dt} = -\frac{RT_r(p)\omega}{gp}. \tag{5.3}$$

The model equations are then given by:

$$\frac{Du}{Dt} - \left(2\Omega + \frac{u}{r_s \cos\phi}\right)(v \sin\phi - \tilde{w}\cos\phi) + \frac{1}{r_s \cos\phi}\left(\frac{\partial\Phi}{\partial\lambda} + \frac{R}{p}\left(T_v + \mu T_r\right)\frac{\partial p}{\partial\lambda}\right) = F_u, \tag{5.4a}$$

$$\frac{Dv}{Dt} + \left(2\Omega + \frac{u}{r_s \cos\phi}\right)u \sin\phi - 2\Omega \sin\lambda \cos\phi\tilde{w} + \frac{v}{r_s}\tilde{w} + \frac{1}{r_s}\left(\frac{\partial\Phi}{\partial\phi} + \frac{R\left(T + \mu T_r\right)}{p}\frac{\partial p}{\partial\phi}\right) = F_v, \tag{5.4b}$$

$$\frac{\partial\Phi}{\partial\eta} = -\frac{R\left(T_v + \mu T_r\right)}{p}\frac{\partial p}{\partial\eta}, \tag{5.4c}$$

$$\frac{\partial}{\partial\eta}\left(r_s^2\frac{\partial p}{\partial t}\right) + \frac{1}{\cos\phi}\frac{\partial}{\partial\lambda}\left(u r_s \frac{\partial p}{\partial\eta}\right) + \frac{\partial}{\partial\phi}\left(v r_s \cos\phi\frac{\partial p}{\partial\eta}\right) + \frac{\partial}{\partial\eta}\left(\dot{\eta} r_s \frac{\partial p}{\partial\eta}\right) = 0, \tag{5.4d}$$

$$\frac{D\theta_L}{Dt} - \frac{1}{\pi c_p T} + \left(L_c q_c^{(L)} + \left(L_c + L_f\right) q_c^{(F)}\right)\frac{RT\omega}{c_p p} = F_\theta, \tag{5.4e}$$

$$\frac{Dq_T}{Dt} = F_q, \tag{5.4f}$$

(after White and Bromley (1995) and Cullen *et al.* (1993)).

Equations 5.4a and 5.4b are the horizontal momentum equations, 5.4c expresses hydrostatic balance, 5.4d expresses mass continuity and 5.4e is the thermodynamic equation. An additional equation, 5.4f, represents the continuity of water vapour. In equations 5.4a and 5.4b F_u and F_v represent sources and sinks of momentum. In equation 5.4e F_θ represents sources and sinks of heat and in equation 5.4f F_q represents sources and sinks of water vapour.

The material derivative, $\frac{D}{Dt}$, is defined as

$$\frac{D}{Dt} \equiv \frac{\partial}{\partial t} + \frac{u}{r_s \cos\phi}\frac{\partial}{\partial\lambda} + \frac{v}{r_s}\frac{\partial}{\partial\phi} + \dot{\eta}\frac{\partial}{\partial\eta} \tag{5.5}$$

and μ, found in equations 5.4a to 5.4c, is defined as

$$\mu = \frac{2\Omega u r_s \cos\phi + u^2 + v^2}{r_s g}. \tag{5.6}$$

Two new thermodynamic variables are defined. θ_L is the liquid water potential temperature where

$$\theta_L = \theta - \frac{L_c q_c^{(L)} + (L_c + L_f)\, q_c^{(F)}}{c_p \Pi} \tag{5.7}$$

and $\Pi = \left(\frac{p}{100000}\right)^{\kappa}$ (where p is in Pascals) and L_c and L_f are the latents heats of condensation and fusion. Also, q is the atmospheric specific humidity with $q_c^{(L)}$ and $q_c^{(F)}$ as the cloud liquid and ice water contents respectively and $\kappa = (c_p - c_v)/c_p$. The total water content is given by q_T where

$$q_T = q + q_c^{(L)} + q_c^{(F)}. \tag{5.8}$$

These equations also use a "virtual" temperature, T_v which is defined as

$$T_v = T(1 + (\epsilon^{-1} - 1)q) \tag{5.9}$$

where ϵ is the ratio of the molecular weight of water to the molecular weight of dry air.

In equations 5.4a and 5.4b the Coriolis term, $2\Omega\tilde{w}\cos\phi$, is included, with the smaller terms $\frac{u\tilde{w}}{r_s}$ and $\frac{v\tilde{w}}{r_s}$ included for conservation (White and Bromley, 1995). The $-2\Omega u\cos\phi$ term is retained in μ to conserve energy when the Coriolis term is retained. The last terms on the left hand side of these equations, involving $\frac{\partial p}{\partial \lambda}$ and $\frac{\partial p}{\partial \phi}$, are due to the use of the η vertical coordinate rather than pressure.

5.4.2 Model integration

The UM was used in the set-up which was designed for the Atmospheric Model Inter-comparison Project (AMIP) second phase (AMIP-II). AMIP is an ongoing international project to compare atmospheric models and determine any systematic errors under a set of realistic and nearly identical conditions and for the same time period. The background and formulation of AMIP-I is described in Gates (1992). The model results for AMIP-I were compared with a subset of the ECMWF ERA-15 re-analysis data (see Gates *et al.* (1999)) so that the relative behaviours of models and re-analysis data is well known. AMIP-II is a continuation of AMIP-I but with an improved experimental design and with a wider range of variables and processes under investigation as well as an investigation into how the AMIP models have improved. It is expected that AMIP-II will become a benchmark reference for atmospheric models. Because the AMIP-II model set-up is well defined and understood in the atmospheric community and will later be rigorously compared

with a range of other atmospheric models and re-analysis data, such as the ERA-40 project, it is a good set-up to use for this research.

The basic set-up of the Unified Model for AMIP-II is described in AMIP UKMO documentation (2002), although key points will be repeated here. The model is HadAM3 version 4.5. This research uses the thirty level version of the model, rather than the nineteen level version described in AMIP UKMO documentation (2002). Different diagnostics to the standard AMIP-II diagnostic output are used for this research, although the standard AMIP-II diagnostics are available from a parallel integration.

The model uses a regular grid-point horizontal numerical representation, the Arakawa staggered "B" grid. The horizontal resolution is a longitude-latitude grid of 96 by 73 grid points, or 2.5° by 3.75°. This is about 417 km by 278 km at the equator and about 295 km by 278 km at 45° of latitude. It is comparable to the T42 spectral resolution. This is twice as coarse as the ECMWF analysis data used. There are thirty hybrid unevenly spaced model levels in the vertical, from the surface to 5 hPa. The top three levels are pure pressure levels, the lowest five levels are are sigma levels. The vertical resolution in the troposphere is about 2 km. The vertical resolution of the model is shown in figure 5.4. Compare this to the equivalent ECMWF resolution shown in figure 2.4. For this research the UM data was interpolated onto the same pressure levels as for the ECMWF data. Due to data storage limitations only the top 16 pressure levels were stored.

The model was run from December 1978 to March 1996 which, at 17 years and 3 months, is 5 years and 8 months shorter than the ECMWF data used.

5.4.3 Model diagnostics

Instead of the standard diagnostics used for AMIP-II, diagnostics were chosen to be most useful to this research. So that the data processing was as similar as possible to that for the ECMWF analysis data diagnostics were output every six hours, at 00:00, 06:00, 12:00 and 18:00 UTC. This however does mean that very high-frequency transients may be excluded from the EP flux diagnostics and the momentum equation. The basic diagnostics chosen were T, u, v and ω on pressure levels; these are the diagnostics which were also available in the ECMWF analysis data. Eddy terms $u'v'$, $v'T'$, $\omega'T'$ and $\omega'u'$ were output to ease the calculation of the EP flux diagnostics. These diagnostics were interpolated from model levels to pressure levels within the model and were output as zonal means. Additional diagnostics, not available from the ECMWF analysis data, are discussed in the

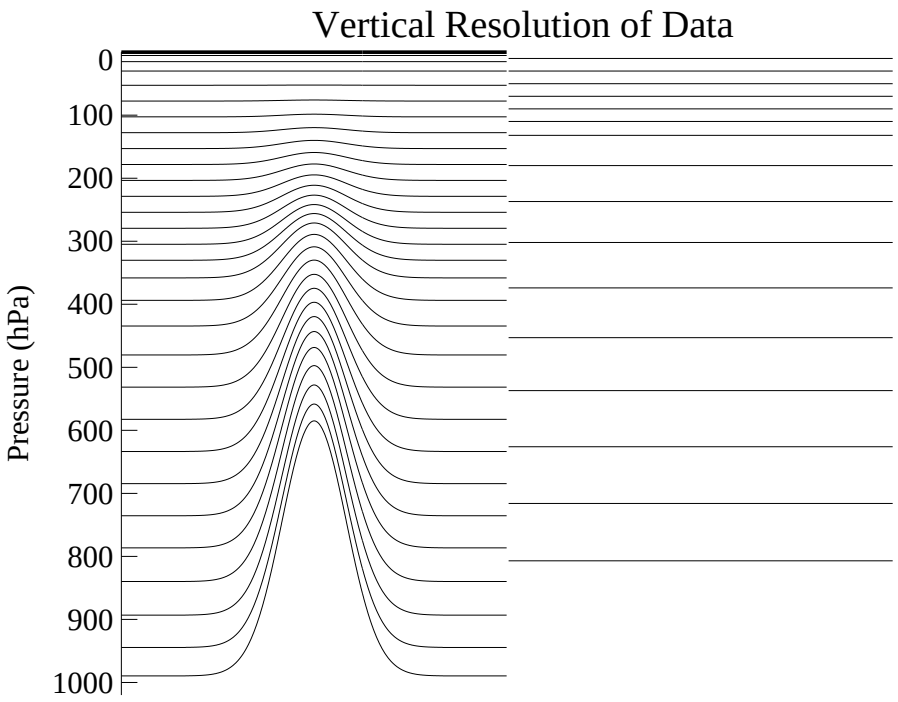

Figure 5.4: The thirty level vertical resolution of the UM including topography (left) and the pressure levels used for the analysis of the UM data (right).

following sections. Other diagnostics are available from parallel AMIP-II runs, such as horizontal velocities and convective rain. These are available on the full latitude-longitude grid on model levels. The horizontal velocities, u and v, were interpolated onto pressure levels for calculation of the stream function.

Radiation diagnostics and parametrisation scheme

The diabatic heating, $\overline{Q}$, in the thermodynamic equation (2.9e), will be mainly due to shortwave (SW) and longwave (LW) heating. However, it may also include some other small terms such as thermal conduction (Andrews *et al.*, 1987, page 115) and heating due to processes such as condensation. Both of these may occur in the assimilated data and the latter is parametrized in the UM.

Two radiation diagnostics were chosen for investigation of $\overline{Q}$, namely shortwave heating rates from solar radiation and longwave heating rates from absorbed and re-emitted long and shortwave radiation by the Earth's surface, clouds and atmospheric gases. These diagnostics are available on model (η) levels from the UM and are then interpolated onto the pressure levels required for the TEM calculation

for comparison with the ECMWF data. These diagnostics can be substituted directly in place of $\overline{Q}$ in the thermodynamic equation because they are heating rates and the equation describes the forcing of the rate of change of temperature by different rates of change of heating.

The radiation scheme is as described in Pope *et al.* (2000) and references therein. The parametrisation includes the effects of various atmospheric gases, aerosols and clouds due to absorption, re-emission and scattering.

It is also possible that convection and clouds can reach up to the tropopause in this model simulation, such that there may be other heating from cloud processes such as latent heat from condensation.

Gravity wave drag diagnostics and parametrisation scheme

The unspecified non-conservative mechanical forcing, $\overline{X}$, in the zonal momentum equation (2.9a) may include such things as friction and driving due to gravity wave drag (GWD) or convective momentum flux. All these may occur in the assimilated data and the latter are parametrized in the UM.

Various gravity wave drag diagnostics were chosen, namely the horizontal accelerations from saturated stress, hydraulic jump and trapped lee waves. These should give more information about $\overline{X}$ in the zonal momentum equation.

The GWD diagnostics are available on model (η) levels from the UM and are then interpolated onto the pressure levels required for the TEM calculation for comparison with the ECMWF data. This interpolation is done before summing the different GWD diagnostics in order to get a total GWD forcing because of the large changes in surface pressure over orography (Webster, 2002). These diagnostics can be substituted directly in place of $\overline{X}$ in the zonal momentum equation because they are accelerations due to the GWD and the equation describes the forcing of the rate of change of zonal velocity (or zonal acceleration) in terms of different accelerations.

The gravity wave drag scheme uses anisotropic orography with low-level breaking such that the orographic gravity wave drag is proportional to the vertical divergence of the wave stress:

$$\frac{\partial \mathbf{u}_{\mathrm{GWD}}}{\partial t} = -\frac{1}{\rho}\frac{\partial \tau}{\partial z} \tag{5.10}$$

where τ is the wave stress and ρ is the atmospheric density profile.

The hydrostatic hydraulic jump diagnostic represents the effect of low level,

non-linear wave-breaking effects which occur at low Froude numbers. On the downwind, downwards slope of a mountain ridge strong winds occur beneath well-mixed layers of air. This gives a hydraulic-jump type response (Peltier and Clark, 1979).

Another low level contribution to gravity wave drag is the breaking of non-hydrostatic trapped lee waves. Lee waves can occur on the lee or downwind side of a mountain ridge under certain physical conditions. The width of the mountain ridge must be such that the air flows over rather than around the mountain. The wind speed is also important. Whether lee waves arise is governed by a parameter known as the Scorer parameter. Lee waves may become trapped when the Scorer parameter has two distinct values at two distinct levels with high values low down and low values high up, such that the higher level cannot form waves. The vertically propagating waves reflect off the interface between the two levels giving downwardly propagating gravity waves. These reflect off the ground and back off the interface, producing a train of lee waves. These can be seen visually when clouds form in a regular pattern downwind of mountain ranges. They are most common in mid-latitudes.

Above the hydraulic jump and for waves at higher Froude numbers saturated stress is parametrised. Wind stress is carried upwards by vertically propagating waves. If the amount of stress carried up from below is greater than a critical value then the wave becomes unstable and partially breaks, causing wave drag, see equation 5.10. This is represented by the saturated stress diagnostic.

At 90 hPa the gravity wave drag is expected to be mainly from saturated stress with a possible small contribution from hydraulic jump and no contribution from trapped lee waves (Webster, 2002; Gregory *et al.*, 1998). Figure 5.5 shows vertical cross-sections of the zonal mean gravity wave drag from (a) trapped lee waves, (b) hydraulic jump and (c) saturated stress for December for the UM data. Trapped lee waves mainly contribute below 600 hPa in the NH mid-latitudes with some contribution in the SH. Hydraulic jump has a strong contribution in the NH mid-latitudes up to 250 hPa and smaller contributions at lower levels in the rest of the NH and in SH polar regions. Saturated stress has a strong contribution throughout the NH with some contribution at low levels in the SH polar regions. Saturated stress is the only component with significant contributions above 200 hPa and these are mainly in NH and SH mid-latitudes. None of the components has a strong contribution in the tropical upper troposphere and lower stratosphere. These figures are similar to those shown in Gregory *et al.* (1998). Gregory *et al.* (1998)

also indicate that gravity wave drag is largest during NH winter.

The gravity wave drag scheme and calculations for the various GWD diagnostics are described more fully in Gregory *et al.* (1998).

These diagnostics may not include all possible contributions to $\overline{X}$. Gregory *et al.* (1998) note that other sources of gravity waves such as deep convection penetrating through the tropopause may play a role in providing gravity wave activity in the stratosphere. Gravity waves due to convection are not represented in these model diagnostics but may be important, especially in the tropical tropopause region. The convection scheme in this model incorporates convective momentum drag (Gregory *et al.*, 1997). This is parametrized at all levels, so that convective momentum drag may be significant at 90 hPa. In Gregory *et al.* (1997) it is certainly shown to occur near the tropical tropopause. Unfortunately, a diagnostic representing this drag was not output from the model for this model integration. Also, because the data is six-hourly, the effects of high-frequency transients are not included in the EP flux diagnostics and may be present in $\overline{X}$.

5.5 Differences between the ECMWF and UM data sets

The main differences between the ECMWF and the UM data sets are indicated in table 5.1.

5.6 Data processing

The majority of the data processing for the UM data was as described for the ECMWF analysis data in section 2.3. The main differences are described here.

The radiation and gravity wave drag diagnostics were interpolated from model levels onto the required pressure levels. The pressure of each model level was calculated from the surface pressure, p_*, and "a" and "b" coefficients for each grid point and timestep according to the relation $p = a + bp_*$. The data were then interpolated to the required pressure levels.

The various terms in the zonal momentum and thermodynamic equations (2.9a and 2.9e) were then calculated but with the diabatic heating given by

$$\overline{Q} = \overline{Q}_{LW} + \overline{Q}_{SW} + \overline{Q}_{\text{Residual}}, \tag{5.11}$$

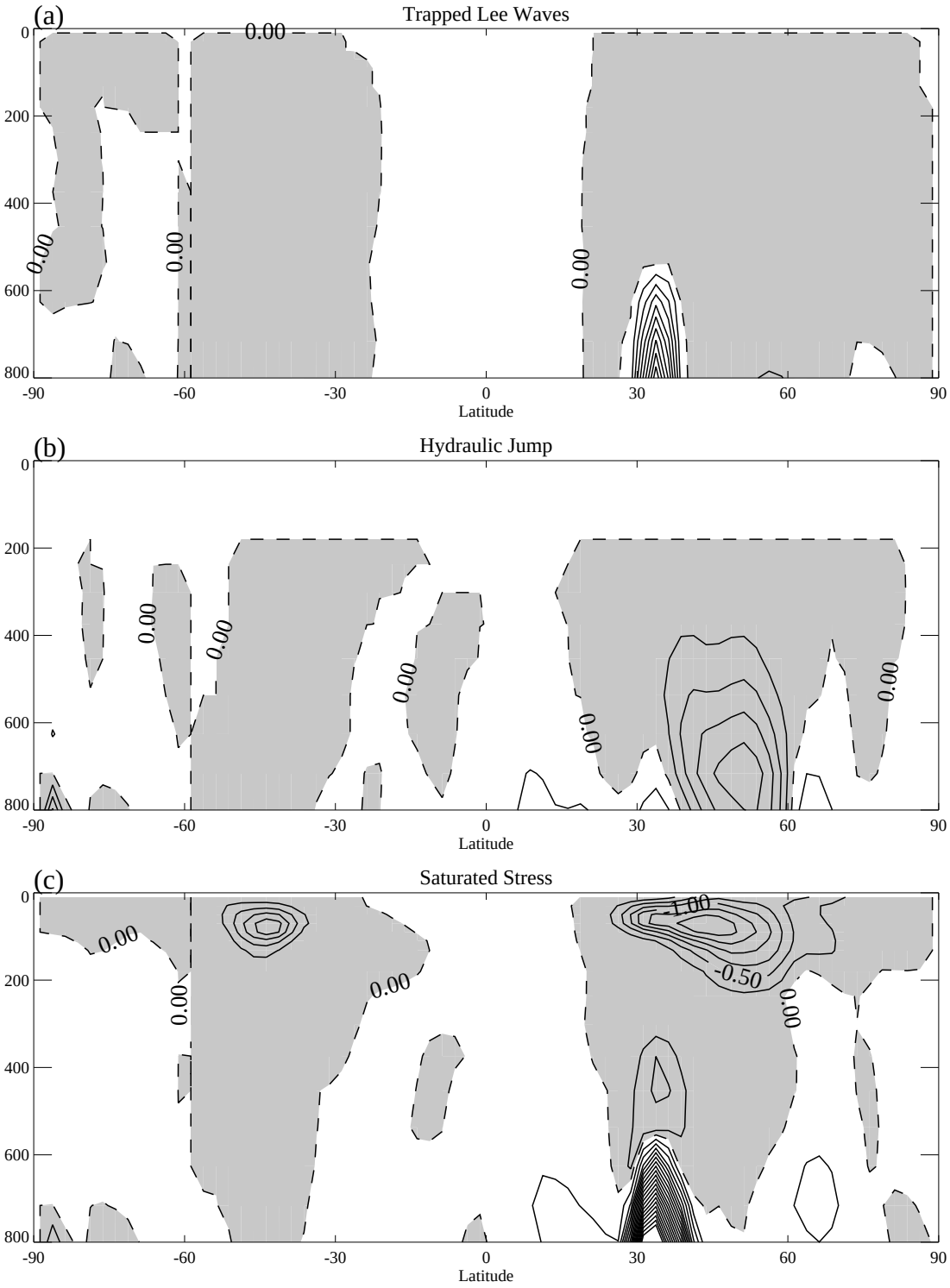

Figure 5.5: Gravity wave drag diagnostics for December for (a) trapped lee waves, (b) hydraulic jump and (c) saturated stress. The contour interval is $0.25\,\mathrm{m\,s^{-1}\,day^{-1}}$. Negative regions are shaded.

	ECMWF	UM
Data	Assimilated (representation of observations, circulation not necessarily in balance)	Modelled (balanced circulation, not necessarily like real world)
Resolution	Spectral	Gridpoint
Horizontal	T106 Spectral or N80 Gaussian 1.125° or ∼125 km	Arakawa B $3.75° \times 2.7°$ or $\sim 420 \times 280$ km
Advection	Semi-Lagrangian	Eulerian
Vertical	31 levels, bottom 3 pure "sigma", top 5 pure pressure	30 levels, bottom 5 pure "sigma", top 3 pure pressure
Data Period	December 1978 to October 2001 (22 years 11 months)	December 1978 to March 1996 (17 years 3 months)
Key Diagnostics	T, u, v, ω	T, u, v, ω, LW & SW heating rates, GWD diagnostics

Table 5.1: Table comparing the main points of the ECMWF and UM data sets.

where the subscripts LW and SW stand for the contributions from longwave and shortwave heating rates respectively. The term $\overline{Q}_{\text{Residual}}$ allows for not all of $\overline{Q}$ being from the longwave and shortwave radiation but from such things as latent heat from condensation in clouds not included in the output diagnostics.
The non-conservative mechanical forcing was given by

$$\overline{X} = \overline{X}_{\text{GWD}} + \overline{X}_{\text{Residual}} \tag{5.12a}$$

and

$$\overline{X}_{\text{GWD}} = \overline{X}_{\text{GWD Lee Waves}} + \overline{X}_{\text{GWD Hydraulic Jump}} + \overline{X}_{\text{GWD Saturated Stress}}, \tag{5.12b}$$

where the subscript GWD stands for gravity wave drag. In equation 5.12a $\overline{X}_{\text{GWD}}$ represents the total of the GWD diagnostics as given in equation 5.12b. This summation is performed before the interpolation onto pressure levels due to the large variation in surface pressure over orography, which is important when considering gravity waves (Webster, 2002). The term $\overline{X}_{\text{Residual}}$ allows for not all of $\overline{X}$ being from the available gravity wave drag diagnostics, such as convective momentum drag and any high-frequency transients not included in EP flux divergence.

Chapter 6

The driving of the annual cycle in temperature in the Unified Model data

6.1 Introduction

This chapter investigates the driving of the annual cycle in the thermodynamic equation (2.9e) by investigating the annual cycle of each of the individual terms in that equation. The mass continuity equation (2.9d) is investigated, linking the thermodynamic equation to the zonal momentum equation. The driving of the annual cycle in the zonal momentum equation (2.9a) is then investigated. Finally, the EP flux divergence is studied in greater detail. The terms in each of the TEM equations have been calculated from the six hourly UM data discussed in section 5.4 using the data processing techniques discussed in sections 2.3 and 5.6. As in chapter 3 the 90 hPa level is investigated. The results are compared with those of chapter 3 and 4.

6.2 The annual cycle in the terms of the thermodynamic equation

The thermodynamic equation (2.9e) is investigated to see what drives the changes in potential temperatures over the annual cycle. Figure 6.1 shows the annual cycle in potential temperature at 90 hPa between 40°N and 40°S. A large annual cycle can be seen between approximately 20°N and 20°S, this is stronger between

approximately 10°N and 10°S. The potential temperature at the equator is approximately 10 K warmer in NH summer than winter. In comparison to the ECMWF data (figure 3.1) the UM is about 5 K warmer throughout the year between 20°N and 20°S, the annual cycle has similar magnitude but the minimum occurs about one month later.

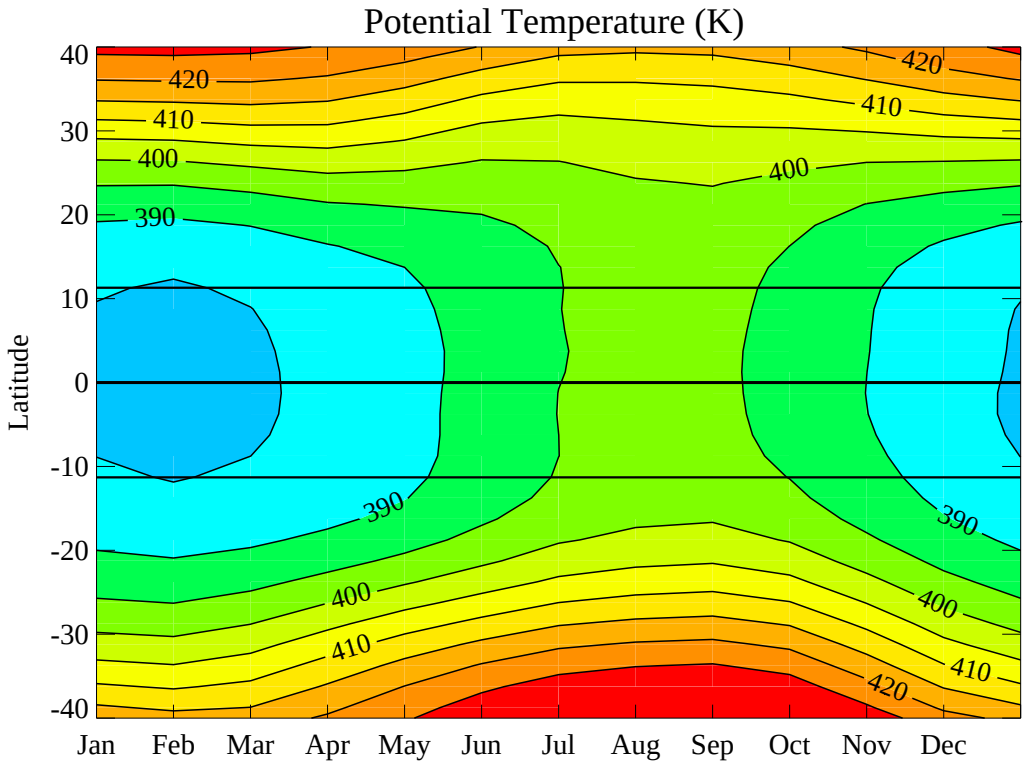

Figure 6.1: Mean annual cycle of the zonal mean potential temperature at 90 hPa. The contour interval is 5 K. Solid black lines indicate 11.3°N, the equator and 11.3°S.

The annual cycle in the rate of change of potential temperature with respect to time, $\frac{\partial \overline{\theta}}{\partial t}$, is shown in figure 6.2. There is warming between 20°N and 20°S from February to August and cooling from August to February. The warming is strongest in June and the cooling strongest in October between 10°N and 10°S. South of 20°S there is a warming which is stronger earlier than the equatorial warming, strongest from March to May, and a strong cooling from October to December, weakening later than the equatorial cooling. North of 20°N there is warming and cooling of the opposite sense to the equatorial warming and cooling, with cooling from February to August and warming from August to February. In comparison to the ECMWF data, figure 3.2, the equatorial warming and cooling

rates are much less strong at the peaks, reaching only 0.12 K day^{-1} and -0.1 K day^{-1} compared with 0.16 K day^{-1} and -0.16 K day^{-1}. The increase in the warming occurs gradually over a longer period whereas the warming in the ECMWF data remains low between January and April. The cooling also occurs over a longer period, finishing in February rather than mid-December. From April to October the rate of change of potential temperature is nearly constant at a given time for the 10°N to 10°S latitude band, changing in magnitude outside that latitude band. This is similar behaviour to the ECMWF data but for a shorter period (in the ECMWF data this occurs from April to December). The horizontal spacing of the UM data is such that the nearest grid boxes to 10° are 8.75° and 11.25°. The latitude chosen as the limit of the band used for calculations with this data is 11.25°.

The adiabatic cooling term, $-\overline{\omega}^*\overline{\theta}_p$, is shown in figure 6.3. There is general adiabatic cooling throughout the tropics (blue-green) between 20°S and 30°N. This extends further north to above 40°N in NH summer and further south to

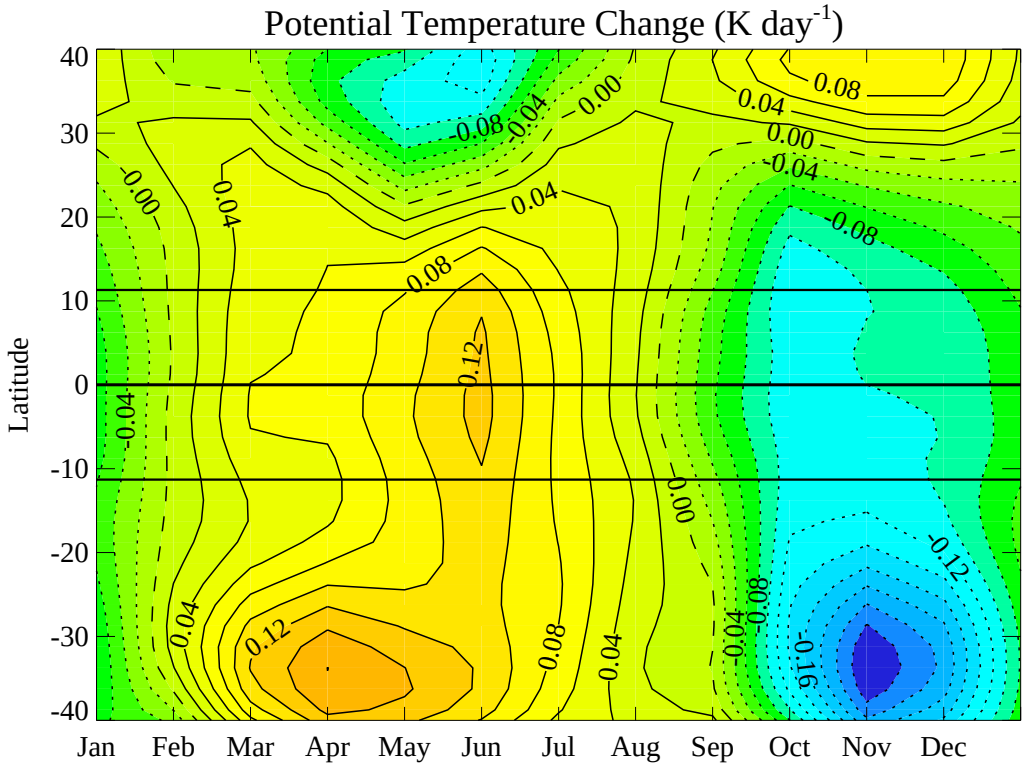

Figure 6.2: Mean annual cycle of the rate of change of zonal mean potential temperature at 90 hPa. The contour interval is 0.02 K day^{-1}. Solid contours indicate positive values (increasing temperatures), dashed contours indicate zero values (no change) and dotted contours indicate negative values (decreasing temperatures). Solid black lines indicate 11.3°N, the equator and 11.3°S.

below 40°S in NH winter such that the band of cooling spans over 60° of latitude throughout the year, wider than in the ECMWF data (figure 3.3). In the extra-tropics heating (yellow-red) can be seen. There is a strong cooling (dark blue) near the equator in December and January and a warming just north of the equator in June and July. These times correspond with large changes in the temperature in figure 3.2, occurring just after the minimum and maximum in the equatorial $\frac{\partial\overline{\theta}}{\partial t}$, as for the ECMWF data. In the NH there is a region of strong cooling near the equator in the winter. This branches out, with one branch moving northwards around the warming in the summer and the other remaining near the equator. This is slightly different to the ECMWF data, which has a strong cooling moving northwards in the summer with a maximum in August. The northern branch in the UM data is noisier and has weakened by August. There is also a distinct band of stronger cooling along the equator in the UM data whereas in the ECMWF data there is generally stronger cooling between 0° and 20°S.

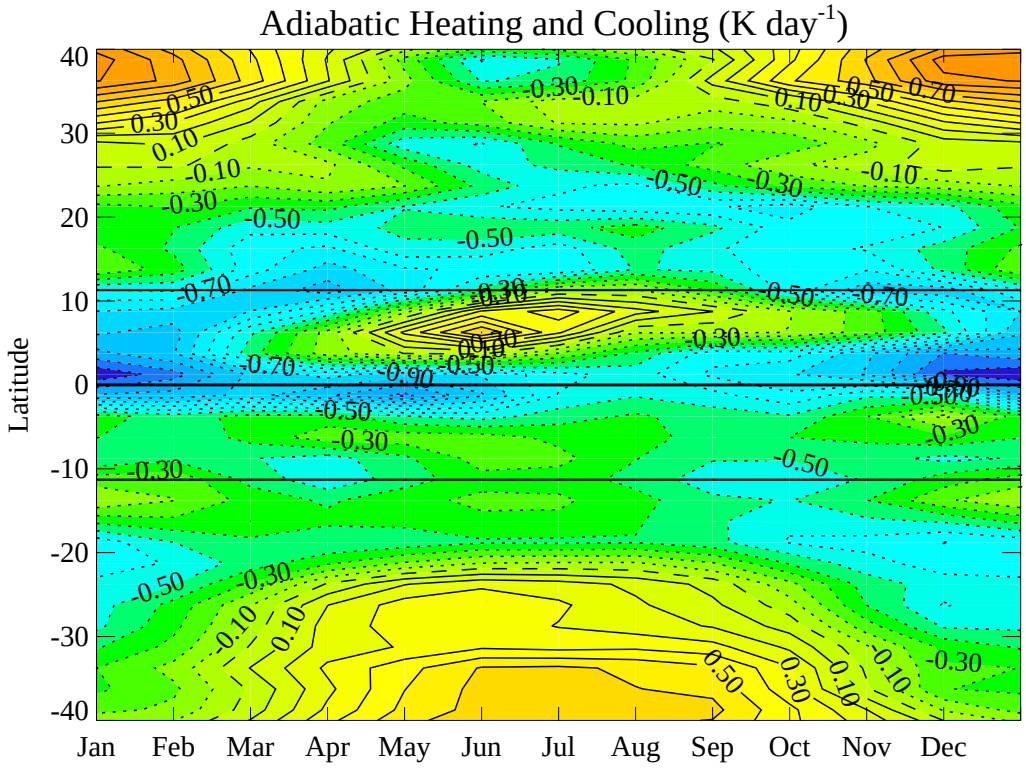

Figure 6.3: Mean annual cycle of the zonal mean adiabatic cooling, $-\overline{\omega}^*\overline{\theta}_p$, at 90 hPa. The contour interval is 0.1 K day^{-1}. Solid contours indicate positive values (heating), dashed contours indicate zero values and dotted contours indicate negative values (cooling). Solid black lines indicate 11.3°N, the equator and 11.3°S.

Figures 6.4 and 6.5 show the annual cycle in the components of $\overline{Q}$ (equation 5.11) at 90 hPa. Longwave and shortwave heating rates are shown in figures 6.4 (a) and (b) respectively, the residual is shown in figure 6.5 (a) and the sum of these in 6.5 (b).

The LW heating (figure 6.4a) has heating between about 30°N and 30°S, this band moving slightly northwards during NH summer. In the extra-tropics there is cooling. Within 20° of the equator, there is a maximum (up to 0.5 K day^{-1}) in LW heating during NH winter, from November to February, and a minimum (down to 0.3 K day^{-1}) in late NH summer, from July to September. This is centred slightly south of the equator. The SW heating (figure 6.4b) is always heating at 90 hPa, ranging between 0.2 and 0.5 K day^{-1} between 40°N and 40°S. This is a much smaller range than for LW heating, which varies between -1.0 and +0.6 K day^{-1} in the same region. There is a decrease in SW heating south of the equator between April and September and a similar decrease north of the equator between October and February—two anti-phase small annual variations.

The residual $\overline{Q}$ (figure 6.5a) is a fairly noisy diagnostic at 90 hPa. In the SH there is mostly cooling whereas in the NH there is a mixture of heating and cooling. Between 10°N and the equator there is an annual cycle with cooling from March to December decreasing to an extremum of -1.3 K day^{-1} in June and heating from December to February increasing to extremum of 0.7 K day^{-1} in January.

The total $\overline{Q}$ is shown in figure 6.5 (b). This can be compared with the ECMWF residual $\overline{Q}$ of figure 3.4. As for the ECMWF data there is heating throughout the tropics, which moves northwards during NH summer, with cooling in the extra-tropics. The northwards movement is about two months later in the UM data but the southwards movement is near the same time as in the ECMWF data. This band of heating is due to the LW heating. In the ECMWF data there is a region of decreased heating just south of 10°N in NH summer; in the UM data the corresponding region is slightly earlier and is cooling rather than just decreased heating. This cooling is from the strongly cooling region in the residual field. In the ECMWF data a band of increased heating in the NH was noted, pushed away from the equator in NH summer. This is also present in the UM data but it is less strong and, unlike the ECMWF data, does not reach a maximum strength in NH summer.

As for the ECMWF data the adiabatic cooling and diabatic heating total terms are a lot larger than the rate of change of potential temperature. They also cancel each other out quite closely. The remaining terms in the thermodynamic equation

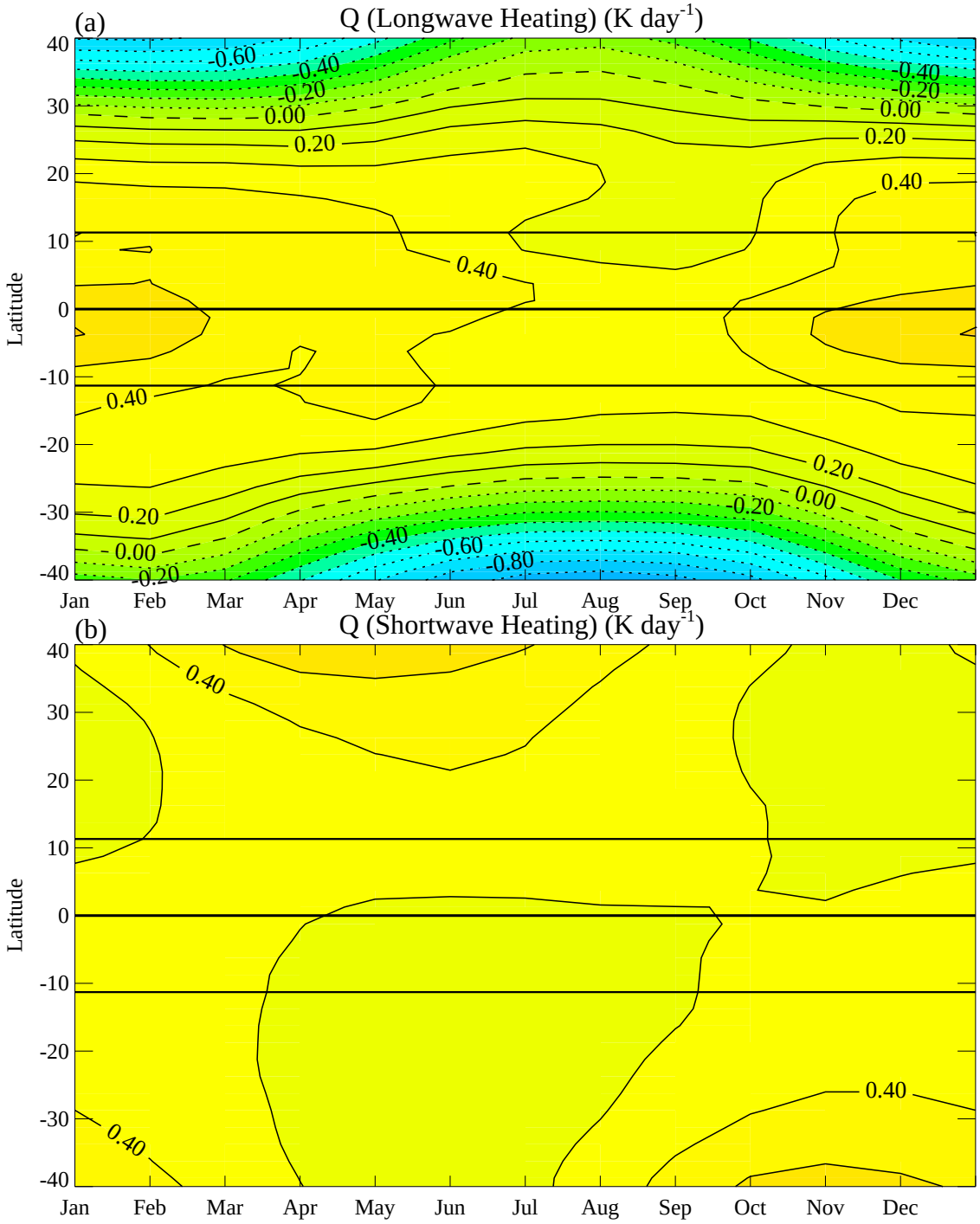

Figure 6.4: Mean annual cycle of the zonal mean diabatic heating at 90 hPa for (a) longwave heating rates and (b) shortwave heating rates. The contour interval is 0.1 K day^{-1}. Solid contours indicate positive values (heating), dashed contours indicate zero values and dotted contours indicate negative values (cooling). Solid black lines indicate 11.3°N, the equator and 11.3°S.

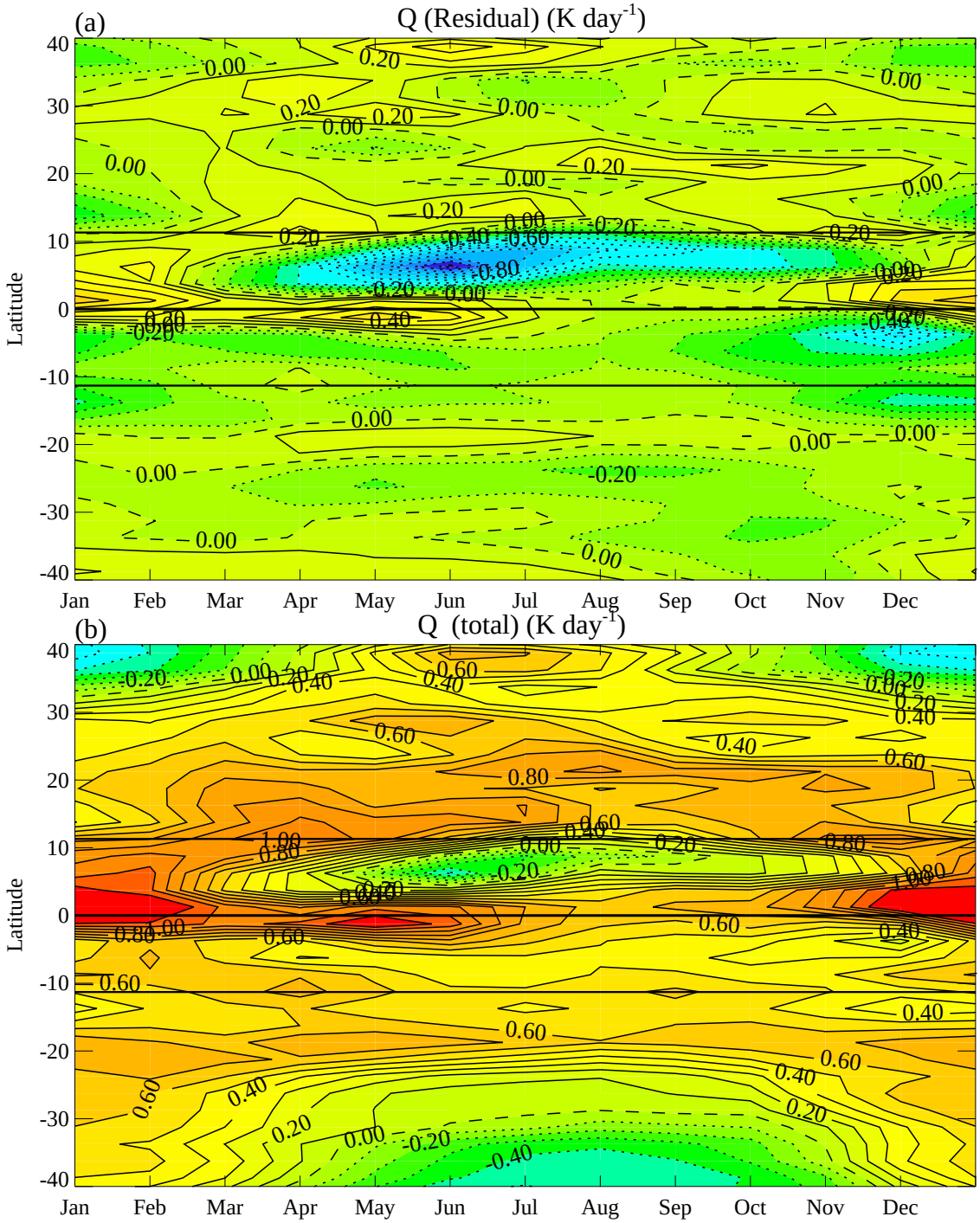

Figure 6.5: Mean annual cycle of the zonal mean diabatic heating at 90 hPa for (a) the residual and (b) the total of longwave heating, shortwave heating and the residual. The contour interval is 0.1 K day^{-1}. Solid contours indicate positive values (heating), dashed contours indicate zero values and dotted contours indicate negative values (cooling). Solid black lines indicate 11.3°N, the equator and 11.3°S.

are much smaller than those illustrated here and do not have a significant effect on the annual cycle in temperature.

Figure 6.6 shows the annual cycle in potential temperature anomaly (panel (a)) and each of the terms in the thermodynamic equation (panel (b)) averaged across the latitude band 11.3°N to 11.3°S at 90 hPa.

The potential temperature is higher in NH summer than in NH winter (figure 6.6a), increasing between February and August and decreasing between September and January (6.6a and $\frac{\partial\overline{\theta}}{\partial t}$, black lines in figure 6.6b). The adiabatic heating and cooling term (green line in figure 6.6b) is negative throughout the year so there is always upwelling and cooling. A clear annual cycle can be seen in the adiabatic cooling term with decreased cooling in NH summer. The diabatic heating (orange line) is always positive and therefore heating the atmosphere. There is a clear annual cycle in the diabatic heating term, with decreased heating in NH summer.

As the adiabatic cooling decreases between January and June $\frac{\partial\overline{\theta}}{\partial t}$ responds to the decreased cooling and increases. The potential temperature increases in response. The diabatic heating responds to the change in potential temperature, decreasing its heating rate. The adiabatic cooling reaches a minimum cooling in June and, from July, the cooling starts to increase again. $\frac{\partial\overline{\theta}}{\partial t}$ decreases, changing sign in August, where there is a maximum potential temperature. As the potential temperature decreases the diabatic heating responds. In October $\frac{\partial\overline{\theta}}{\partial t}$ reaches a minimum and begins to increase. The potential temperature is still decreasing and so the diabatic heating is still increasing, counteracting the adiabatic cooling. When $\frac{\partial\overline{\theta}}{\partial t}$ crosses zero in February the potential temperature reaches a minimum and the diabatic heating reaches a maximum and starts to decrease.

This figure is generally the same as for the ECMWF data (figure 3.5). In the UM data the potential temperature increases less rapidly in NH spring than in the ECMWF data but for longer, increasing from February rather than from April. In the rate of change of potential temperature the maximum and minimum are at the same times and the NH summer change in sign is only half a month later in the UM data, the main difference being the gradual increase from February rather than the near zero values between February and April in the ECMWF data. Similarly the adiabatic heating has a more gentle gradient in the UM data in NH spring, increasing over the whole period rather than the sharp increase in April. The diabatic heating has a greater range over the annual cycle with a minimum of $0.4\,\mathrm{K\,day^{-1}}$ in July compared with the ECMWF minimum of $0.55\,\mathrm{K\,day^{-1}}$ in September. It begins to increase before the maximum in potential temperature

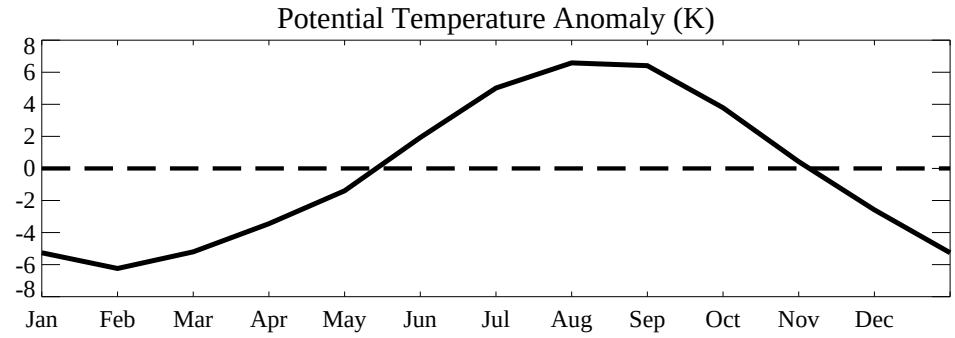

(a) Potential temperature anomaly

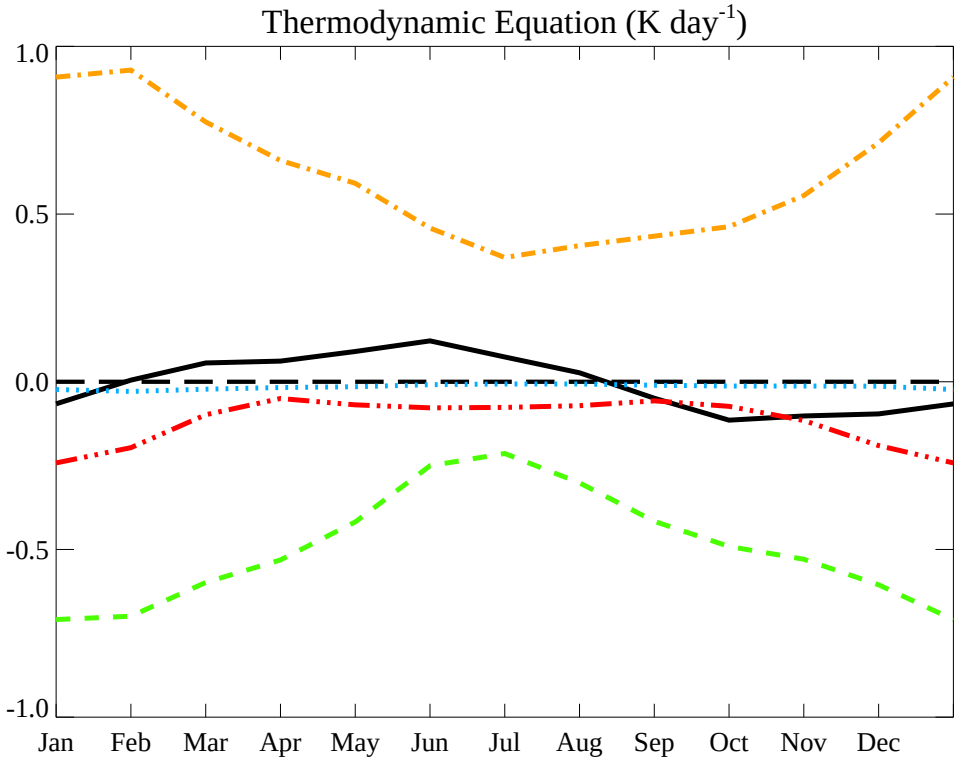

(b) Terms in the thermodynamic equation

Figure 6.6: Mean annual cycle averaged from 11.3°N to 11.3°S at 90 hPa of (a) the potential temperature and (b) the terms in the thermodynamic equation at 90 hPa. In (b) the terms are $\frac{\partial \overline{\theta}}{\partial t}$ (solid black line), $-\frac{\overline{v}^*}{R_e}\frac{\partial \overline{\theta}}{\partial p}$ (dotted blue line), $-\overline{\omega}^*\frac{\partial \overline{\theta}}{\partial p}$ (dashed green line), $\overline{Q}_{\text{total}}$ (dashed and dotted orange line) and $-\frac{\partial}{\partial p}\left(\frac{\overline{v'\theta'}\,\overline{\theta}_\phi}{R_e\overline{\theta}_p}+\overline{\omega'\theta'}\right)$ (dash and three dotted red line).

but lagged with respect to the minimum in adiabatic heating and cooling.

Figure 6.7 shows the decomposition of $\overline{Q}$ into LW heating, SW heating and the residual averaged from 11.3°N to 11.3°S. The annual cycle is composed mainly of the residual term with some contribution from the LW heating. The LW heating has its minimum in September, when the potential temperature of figure 6.6a is a maximum, whereas it is the residual which has its minimum in July. The LW heating is responding closely to the changes in potential temperature.

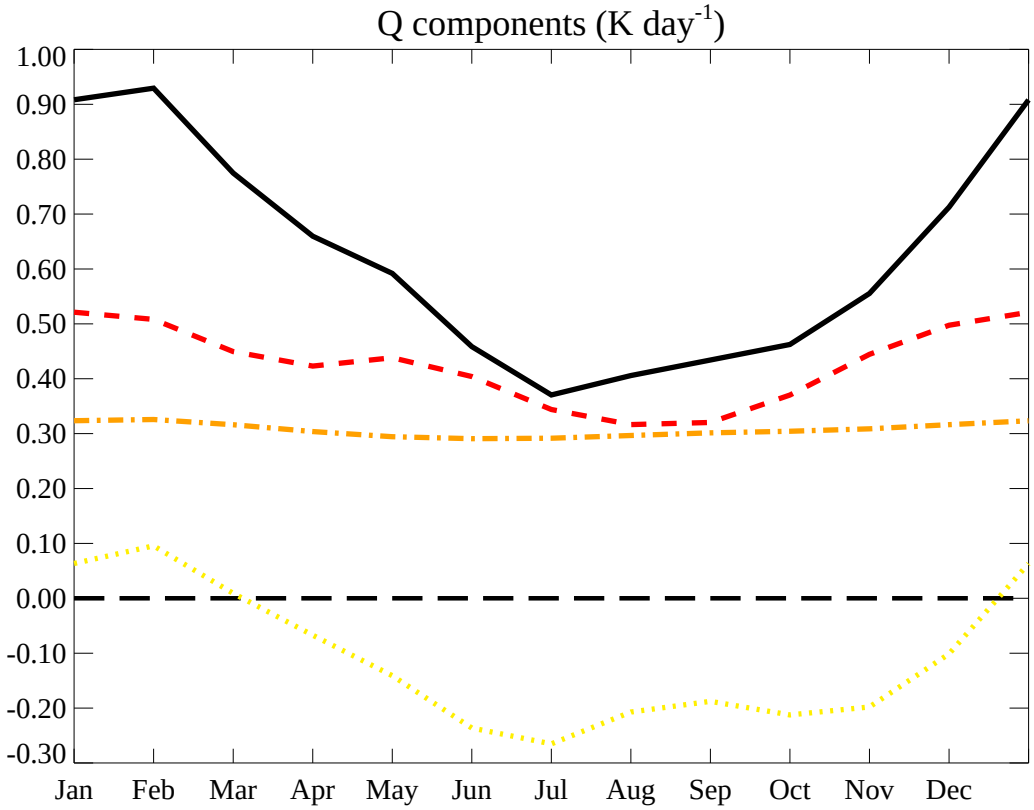

Figure 6.7: Mean annual cycle averaged from 11.3°N to 11.3°S at 90 hPa of the terms in $\overline{Q}$ (equation 5.11). The lines are total $\overline{Q}$ (solid black line), $\overline{Q}_{\mathrm{LW}}$ (dashed red line), $\overline{Q}_{\mathrm{SW}}$ (dashed and dotted orange line) and $\overline{Q}_{\mathrm{residual}}$ (dotted yellow line).

As for the ECMWF data the adiabatic cooling is driving the annual cycle in temperatures in this region. The LW heating is responding to the temperature changes.

6.3 Resolving the mean vertical transport near the tropopause

Next the vertical component of the residual mean meridional circulation, $\overline{\omega}^*$, is considered.

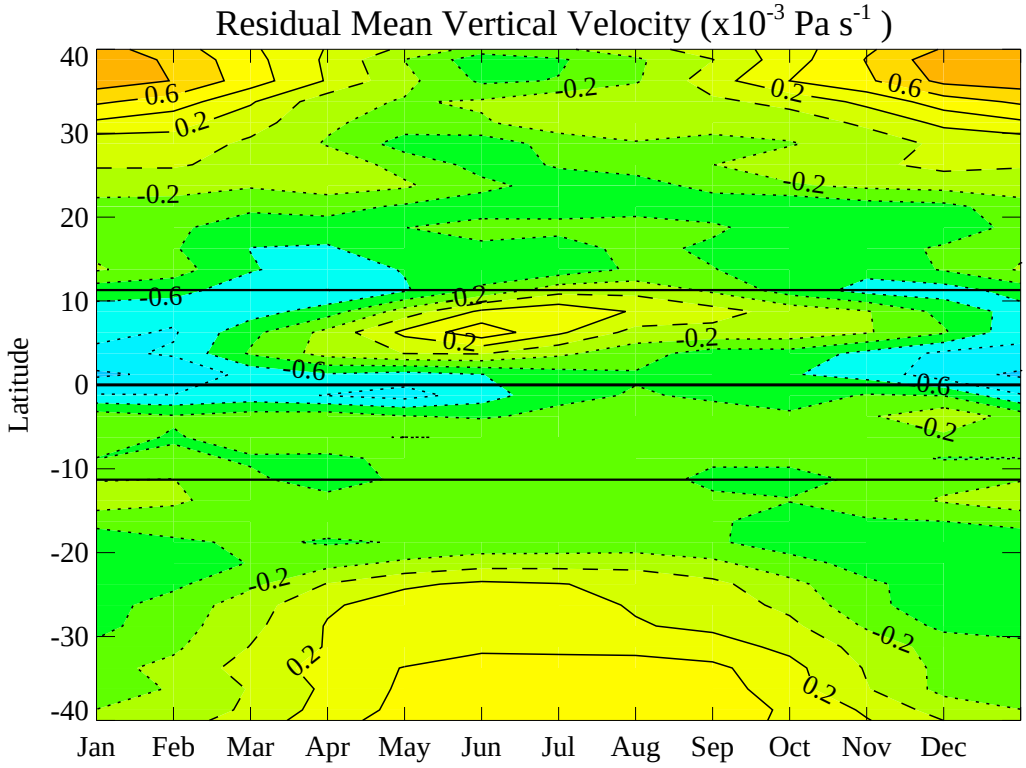

Figure 6.8: Mean annual cycle of the residual mean vertical velocity at 90 hPa. The contour interval is $0.2\times10^{-3}\,\mathrm{Pa\,s^{-1}}$. Solid contours indicate positive values (downwelling), dashed contours indicate zero values and dotted contours indicate negative values (upwelling).

Figure 6.8 shows the annual cycle in $\overline{\omega}^*$ from 40°N to 40°S at 90 hPa. Note that, because pressure units are in use here, negative values of $\overline{\omega}^*$ correspond to upwelling, positive values to downwelling. The general pattern of $\overline{\omega}^*$ is similar to that of the adiabatic cooling in figure 6.3, especially in the extra-tropics, but the similarities between these two figures are not as clear as between the equivalent figures for the ECMWF data ($\overline{\omega}^*$ in figure 3.8 compared with adiabatic cooling in figure 3.3). In the tropics there is a region of downwelling just north of the equator in NH summer, corresponding to warming in the adiabatic heating and cooling. There is enhanced upwelling in the tropics, especially in NH winter,

corresponding to the regions of enhanced cooling. The contours of upwelling follow similar patterns to the contours of cooling, especially in the tropics in the NH; compare especially the contours in $\overline{\omega}^*$ with the blue coloured regions in the adiabatic heating and cooling plot. It is the residual vertical velocity which is driving the changes in adiabatic cooling.

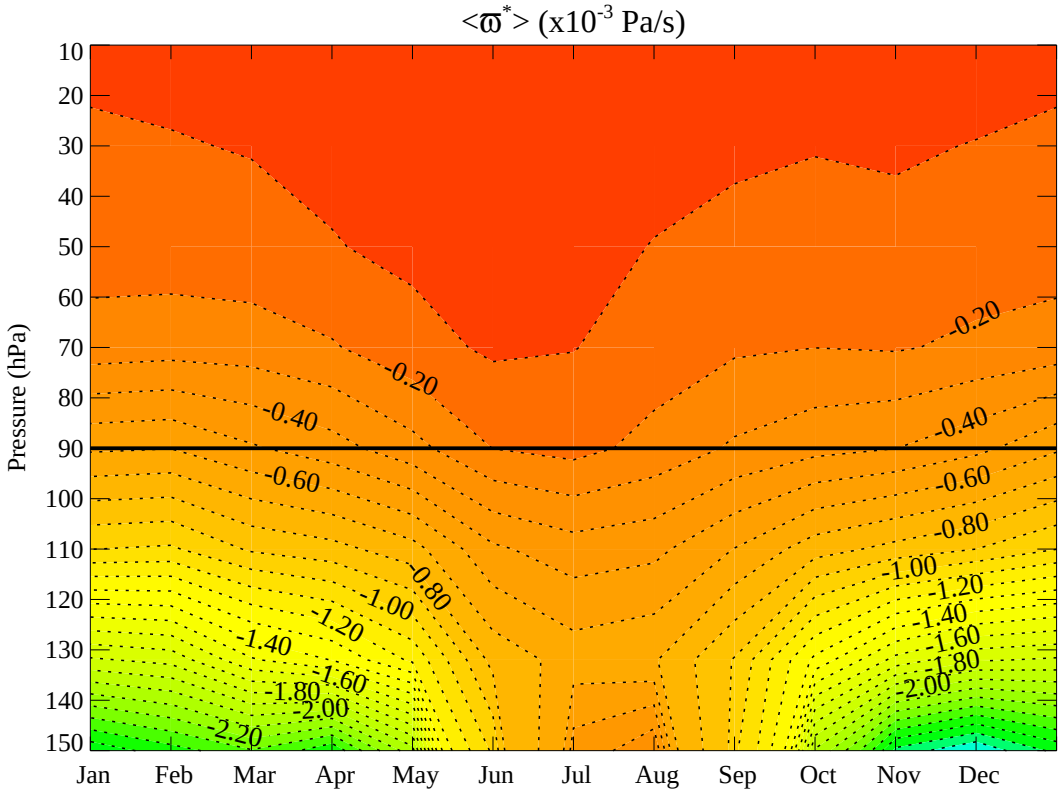

Figure 6.9: Mean annual cycle of the residual mean vertical velocity, $\overline{\omega}^*$, averaged from 11.3°N to 11.3°S. The 90 hPa level is indicated with a solid black line. The contour interval is 0.1×10^{-3} Pa s^{-1}. Dotted contours indicate negative values (upwelling).

Figure 6.9 shows a vertical cross-section of the residual mean vertical velocity, averaged from 11.3°N to 11.3°S. The figure shows only the upper troposphere and stratosphere, from 150 hPa to 10 hPa, i.e. the top of the data set. A clear annual cycle can be seen at most levels, with enhanced upwelling in NH winter and decreased upwelling in NH summer. At 90 hPa the maximum upwelling is -0.6×10^{-3} Pa s^{-1} and occurs from December to January and the minimum is -0.2×10^{-3} Pa s^{-1} from June to late July. Figure 6.10 shows the equivalent figure with the annual mean removed from the data. This figure shows only 110 hPa to 10 hPa due to the large decrease in magnitude of the annual cycle with height.

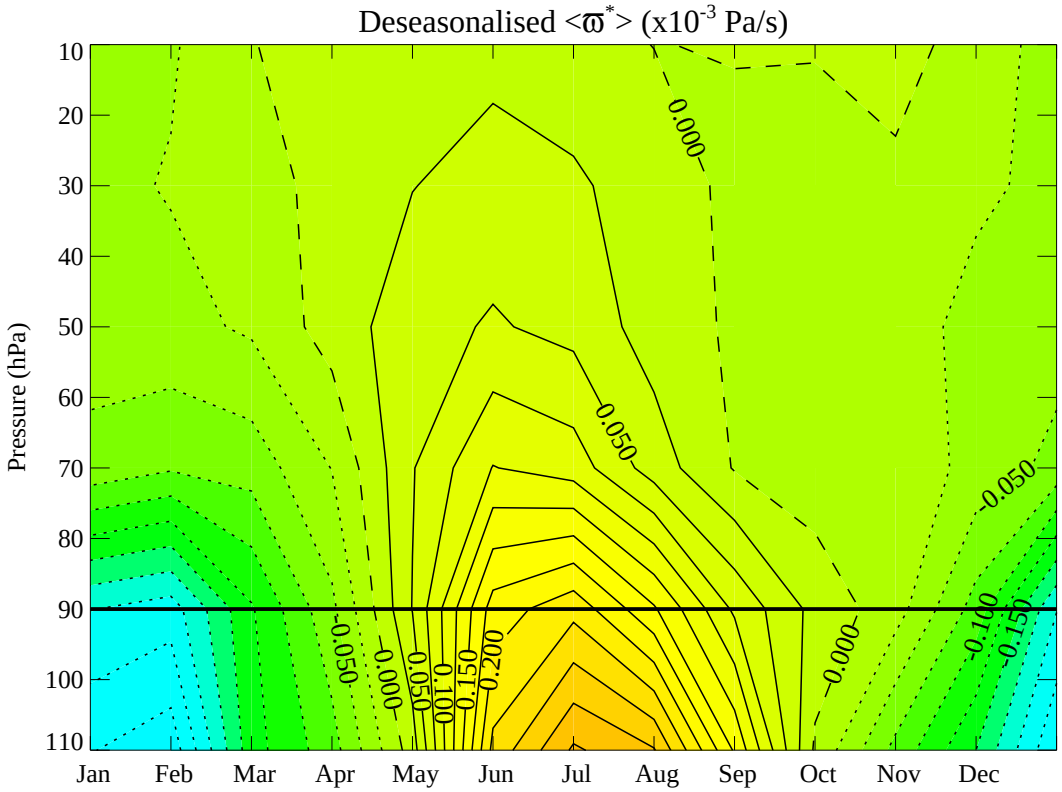

Figure 6.10: Annual cycle of the residual mean vertical velocity, $\overline{\omega}^*$, averaged from 11.3°N to 11.3°Swith the annual mean removed. The 90 hPa level is indicated with a solid black line. The contour interval is $0.025\times10^{-3}\,\mathrm{Pa\,s^{-1}}$.

In the ECMWF data, figure 3.9, it was noted that the decreased upwelling in NH summer occurs earlier in the year at higher levels. This is also true in the UM data but is less pronounced. In the ECMWF data the minimum upwelling (maximum value) is in late July at 110 hPa and in June at 60 hPa. In the UM data the minimum is at the beginning of July at 110 hPa and again in June at 60 hPa. The maximum upwelling (minimum value) in the UM data at 90 hPa occurs slightly later and has a slightly lower value than in the ECMWF data ($-0.6\times10^{-3}\,\mathrm{Pa\,s^{-1}}$ compared with $-0.7\times10^{-3}\,\mathrm{Pa\,s^{-1}}$), the minimum is at a similar time to the ECMWF data and also has a slightly lower value ($-0.2\times10^{-3}\,\mathrm{Pa\,s^{-1}}$ compared with $-0.25\times10^{-3}\,\mathrm{Pa\,s^{-1}}$); the range of the annual cycle at 90 hPa is slightly smaller than in the ECMWF data.

6.3.1 The mass continuity equation

In section 3.4.1 it was shown how the average vertical velocity across a latitude band could be found by integrating the mass continuity equation. Figure 6.11 shows the annual cycle in the integrand of equation 3.3 for the UM data, with the annual mean removed. The latitude band used for the integration is from 11.3°N to 11.3°S.

The largest variation in the annual cycle in this figure is in the lowest level, at 90 hPa where the integrand is $0.11\times10^{-3}\,\mathrm{Pa\,s^{-1}}$ below the mean in January and $0.10\times10^{-3}\,\mathrm{Pa\,s^{-1}}$ above the mean in July. This is the same timing as for the annual cycle in $\overline{\omega}^*$ at 90 hPa. The annual cycle at 70 hPa is just under half this magnitude, where the integrand is $0.4\times10^{-3}\,\mathrm{Pa\,s^{-1}}$ below the mean in March and $0.5\times10^{-3}\,\mathrm{Pa\,s^{-1}}$ above the mean in July, again with the same timing as the annual cycle in $\overline{\omega}^*$. Higher levels do not show as large a magnitude in annual cycle. Above 30 hPa there is a small semi-annual cycle.

Comparing this with the ECMWF data, figure 3.13, the annual cycle in the integral is less strong and timed slightly earlier. However in both the UM and ECMWF data the timing of the annual cycle in the integrand at 90 hPa corresponds with the annual cycle in $\overline{\omega}^*$ at 90 hPa for that data set. Also, the magnitude of the annual cycle at 70 hPa is just under half that at 90 hPa for each data set. Between 60 and 30 hPa the two data sets behave quite differently; the UM data has a very small annual cycle whereas the ECMWF data has changed sign and has a strong annual cycle out of phase with the 90 hPa cycle. Above 30 hPa both data sets show a semi-annual cycle with similar timings.

As for the ECMWF data the UM data show that most of the annual cycle in $\overline{\omega}^*$ between 9.8°N and 9.8°S at 90 hPa is driven by the horizontal velocities near 90 hPa.

Figure 6.12 shows $\overline{\omega}^*$ calculated on half model levels from integrating $\overline{v}^*$ at the limits 11.3°N and 11.3°S. Figure 6.13 shows this interpolated onto full model levels. These figures are very similar to figure 6.9 which shows $\overline{\omega}^*$ calculated from the definition given by equation 2.8b.

These can be compared with the ECMWF data (figures 3.14, 3.15 and 3.9.) In the ECMWF data, the magnitude of the annual cycle at 90 hPa is slightly greater for $\overline{\omega}^*$ calculated by integrating the mass continuity equation whereas in the UM data the opposite is true.

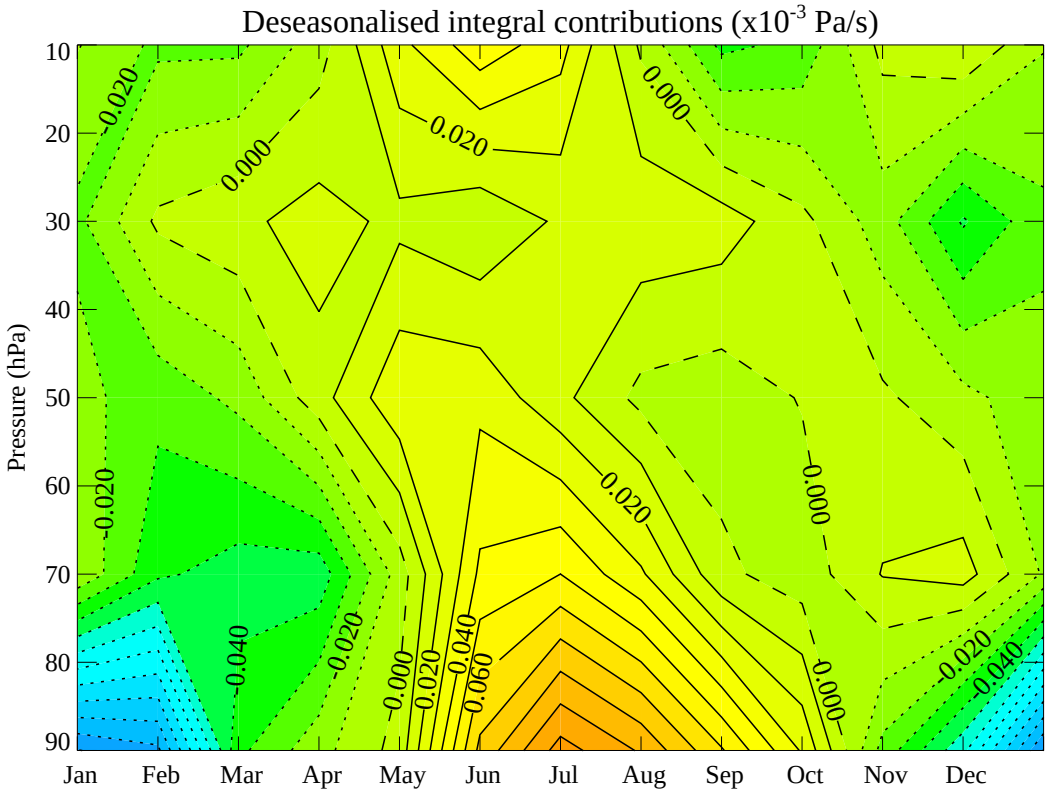

Figure 6.11: Mean annual cycle of the integrand of equation 3.3, taken at the limits 11.3°N and 11.3°S, showing from the top of the atmosphere down to 90 hPa. This is multiplied by the factor in front of the integral sign in equation 3.3 to be comparable with $\overline{\omega}^*$. The contour interval is $0.01\times10^{-3}\,\mathrm{Pa\,s^{-1}}$. Solid contours indicate positive values (downwelling), dashed contours indicate zero values and dotted contours indicate negative values (upwelling).

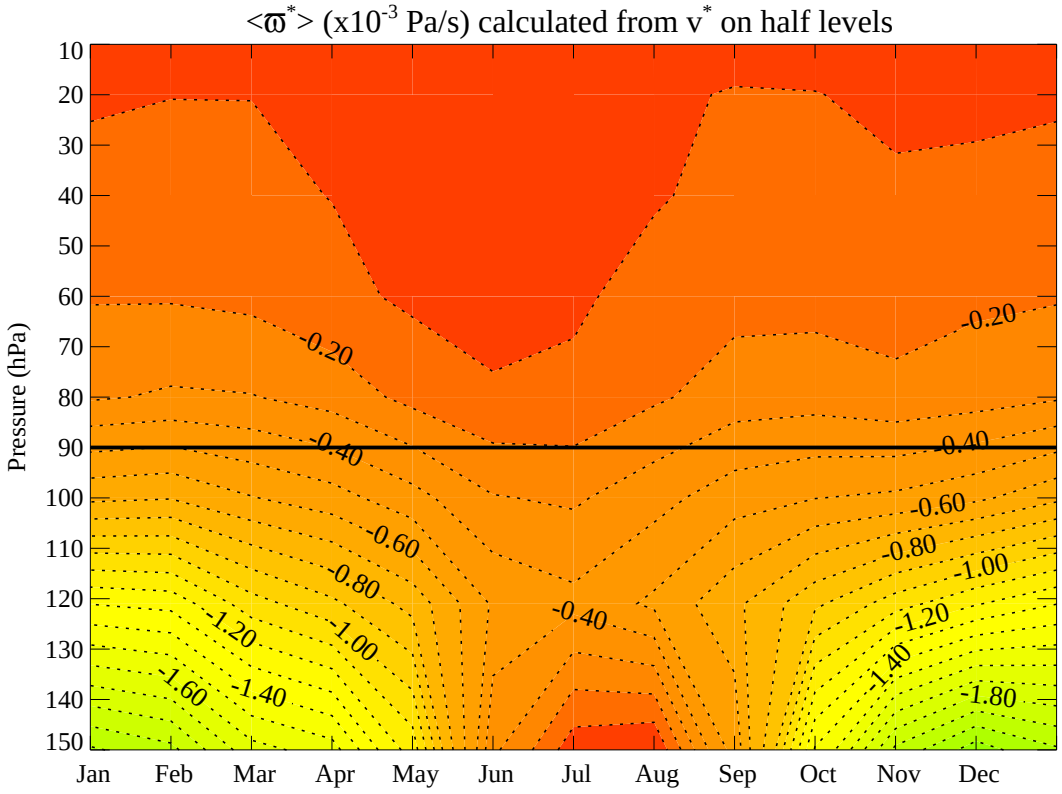

Figure 6.12: Mean annual cycle of the residual mean vertical velocity, $\overline{\omega}^*$, as calculated from $\overline{v}^*$ using equation 3.3 with latitude limits 11.3°N and 11.3°S. The 90 hPa level is indicated with a solid black line. The contour interval is $0.1\times10^{-3}\,\mathrm{Pa\,s^{-1}}$. Dotted contours indicate negative values (upwelling).

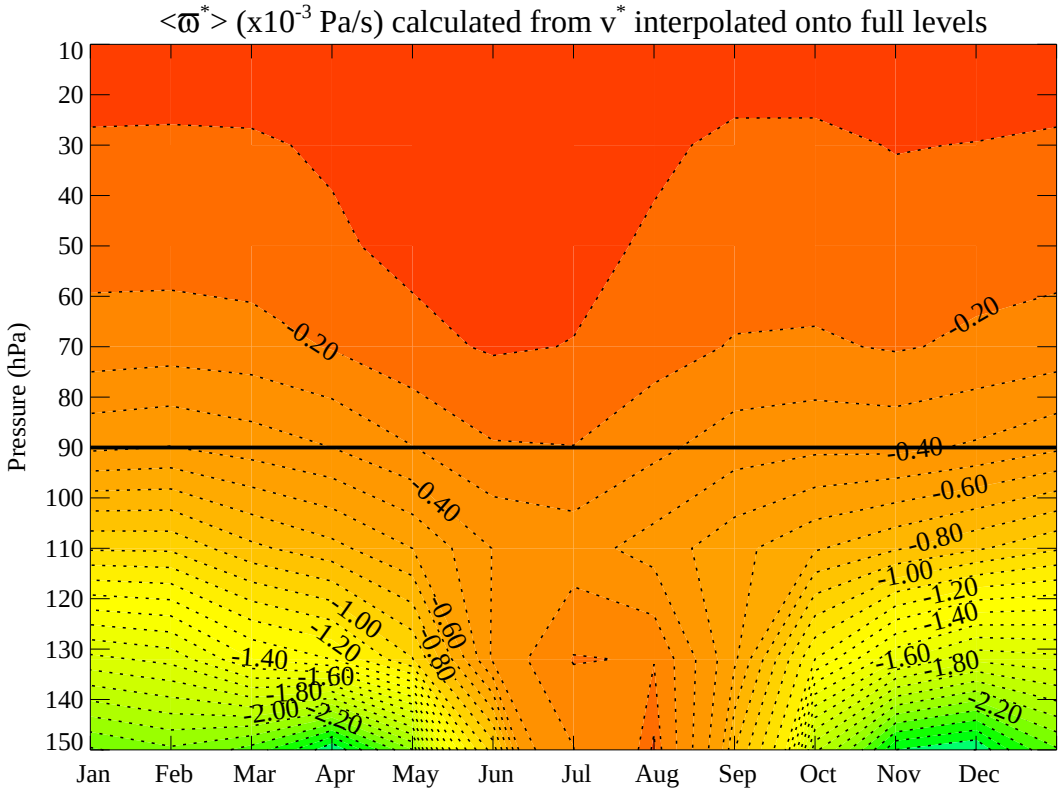

Figure 6.13: Mean annual cycle of the residual mean vertical velocity, $\overline{\omega}^*$, as calculated from $\overline{v}^*$ using equation 3.3 with latitude limits 11.3°N and 11.3°S. The 90 hPa level is indicated with a solid black line. The contour interval is $0.1\times10^{-3}\,\mathrm{Pa\,s^{-1}}$. Dotted contours indicate negative values (upwelling).

6.4 The annual cycle in the terms of the zonal momentum equation

Figure 6.14 shows the annual cycle of the terms in the zonal momentum equation (3.9) for the latitude band 11.3°N to 11.3°S at 90 hPa. The figure shows what is forcing the outflow from the edge of the latitude band at 11.3°N and 11.3°S at 90 hPa. This figure can be compared with figure 3.16 for the ECMWF data.

There is a clear annual cycle in $\overline{v}^*$ (black) which is low in NH summer and higher in NH winter, corresponding with previous annual cycles shown. The main driving for this is from the EP flux divergence (red) with some contribution from $\frac{\overline{X}_{\text{Residual}}}{\overline{\zeta}_a}$ (yellow). The rate of change of zonal wind (blue) has a semi-annual cycle with a larger variation between April and September than between October and March, as for the ECMWF data. The remaining terms are small.

The annual cycle in $\overline{v}^*$ is smaller in the UM data than in the ECMWF data but in both cases is driven by the EP flux divergence.

6.5 The northern and southern hemisphere contributions to the zonal momentum equation

Figure 6.15 shows the contribution of the different terms in the zonal momentum equation, this time not divided by $\overline{\zeta}_a$ (i.e. equation 3.8) at 11.3°N and 11.3°S at 90 hPa. Panel (a) shows 11.3°N+11.3°S, (b) 11.3°N and (c) 11.3°S. This can be compared with figure 4.1 for the ECMWF data. As in chapter 4 the terms in this figure have not been divided by $\overline{\zeta}_a$ so 6.15(a) shows the sum of terms at 11.3°N and 11.3°S, rather than the difference.

Considering just $\overline{v}^*$ in figures 6.15(a) to (c) the total annual cycle is mainly due to the annual cycle in the NH, with a small opposition from the SH. A similar pattern was seen in the ECMWF data. In the NH (b) it appears to be the $\overline{X}_{\text{Residual}}$ which is driving the annual cycle, opposed by the EP flux divergence. In the ECMWF data the annual cycle was driven by the EP flux divergence with some contribution from $\overline{X}$. In the SH (c) the annual cycle in $\overline{v}^*$ is mainly coming from the EP flux divergence and is opposed by $\overline{X}_{\text{Residual}}$. This gives a very small annual cycle in $\overline{v}^*$ with the maximum and minimum later than in the total $\overline{v}^*$. In the ECMWF data the EP flux divergence was of the sense to drive the annual cycle in the total $\overline{v}^*$ but was opposed by $\overline{X}$ to give a $\overline{v}^*$ of the opposite sense. The

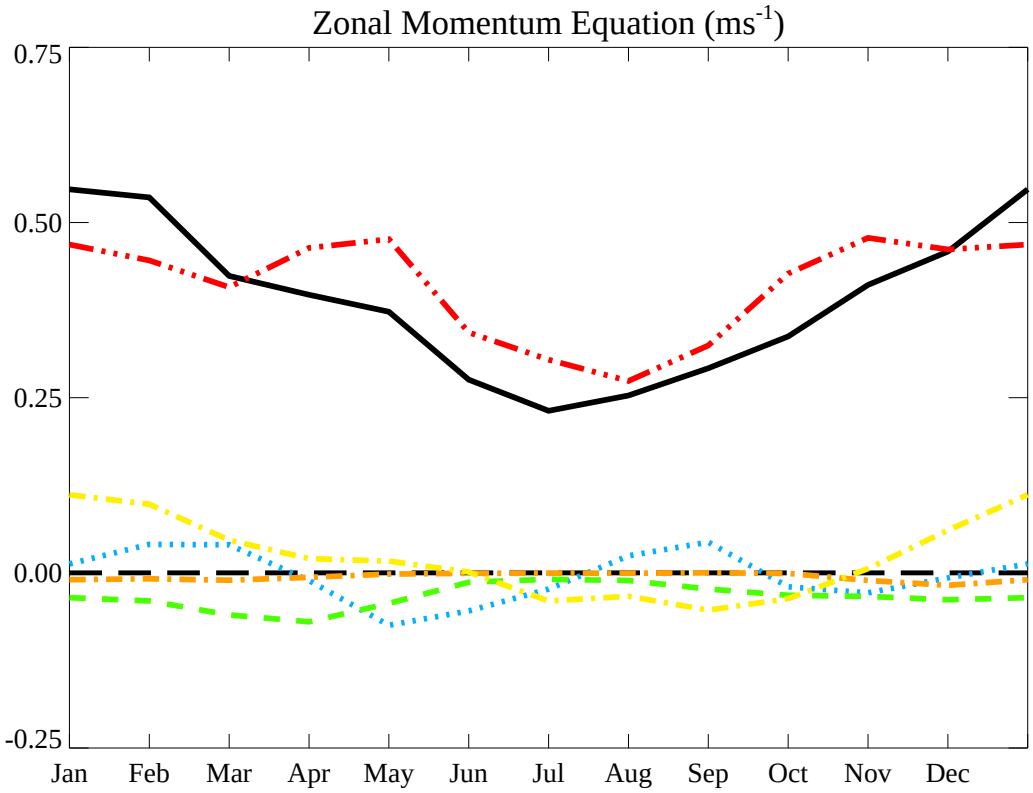

Figure 6.14: Mean annual cycle of the terms in the zonal momentum equation divided by $\overline{\zeta}_a$ (equation 3.9) at 90 hPa, terms at 11.3°N minus terms at 11.3°S. This is the difference between the terms at 11.3°N and 11.3°S at 90 hPa. The terms are $\overline{v}^*$ (solid black line), $\frac{1}{\overline{\zeta}_a}\frac{\partial \overline{u}}{\partial t}$ (dotted blue line), $\frac{-\overline{\omega}^*}{\overline{\zeta}_a}\frac{\partial \overline{u}}{\partial p}$ (dashed green line), $\frac{1}{R_e \cos\phi}\frac{\nabla.\mathbf{F}}{\overline{\zeta}_a}$ (dash and three dotted red line), $\frac{\overline{X}_{\mathrm{GWD}}}{\overline{\zeta}_a}$ (dashed and dotted orange line) and $\frac{\overline{X}_{\mathrm{Residual}}}{\overline{\zeta}_a}$ (dashed and dotted yellow line).

annual cycles in $\overline{X}_{\mathrm{Residual}}$ from the two hemispheres oppose each other to give a small annual cycle in the total (a), as for the ECMWF data. Whereas in the ECMWF data the EP flux divergence in both hemispheres was of the sense to drive $\overline{v}^*$, summing to give a bigger annual cycle of that sense, in the UM data the two hemispheres oppose each other, giving a small residual cycle in the total.

6.6 Components of non-conservative mechanical forcing

Figure 6.16 shows the annual cycle in (a) gravity wave drag from saturated stress, (b) $\overline{X}_{\mathrm{Residual}}$ and (c) the total $\overline{X}$ as in equation 5.12. The residual $\overline{X}$ from the

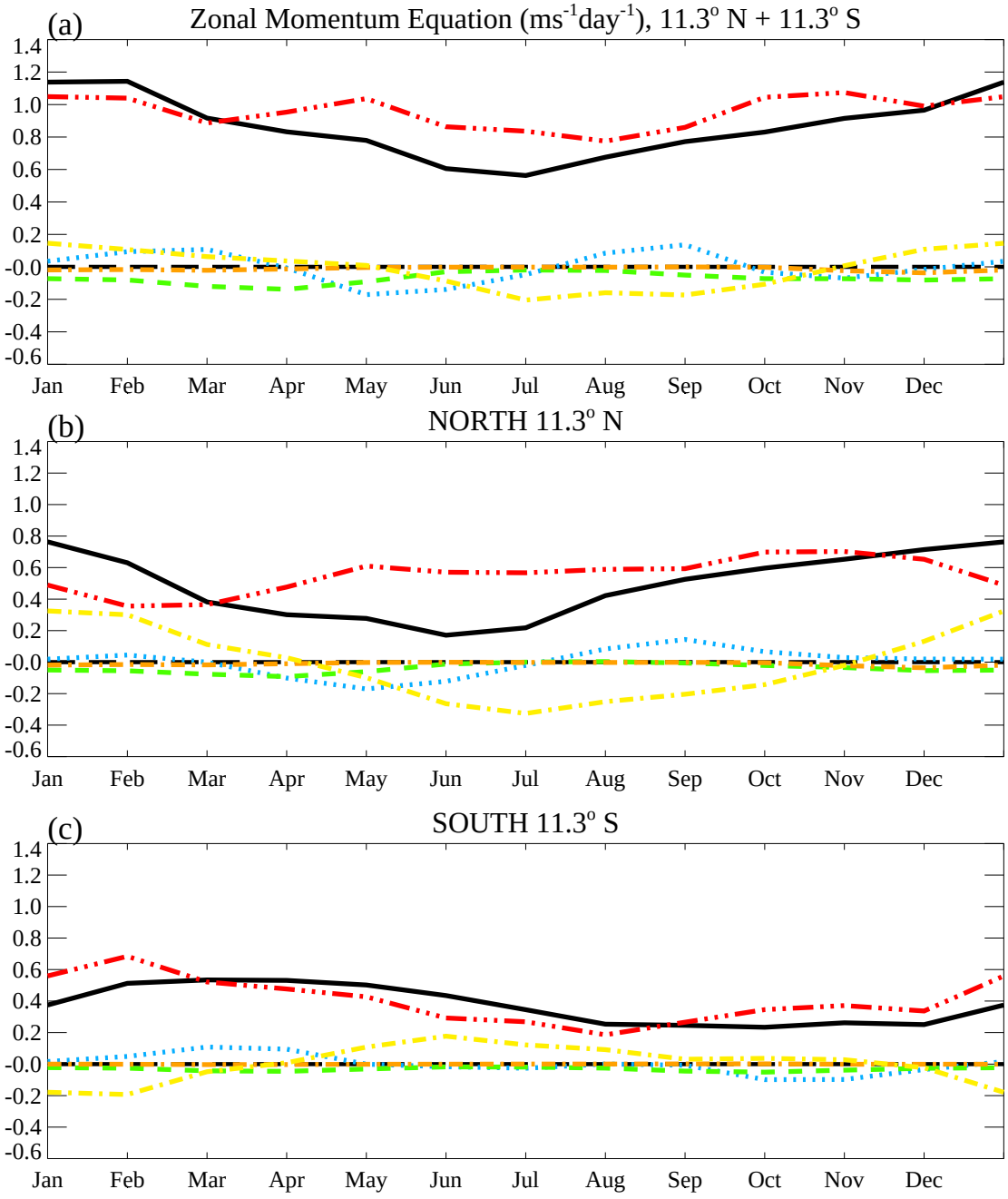

Figure 6.15: Mean annual cycle of the terms in the zonal momentum equation (equation 3.8) at 90 hPa. The plots show terms at (a) 11.3°N plus terms at 11.3°S (as figure 6.14), (b) 11.3°N and (c) 11.3°S. The terms are $\overline{v}^*\overline{\zeta}_a$ (solid black line), $\frac{\partial \overline{u}}{\partial t}$ (dotted blue line), $-\overline{\omega}^*\frac{\partial \overline{u}}{\partial p}$ (dashed green line), $\frac{1}{R_e \cos\phi}\nabla.\mathbf{F}$ (dash and three dotted red line), $\overline{X}_{\mathrm{GWD}}$ (dashed and dotted orange line) and $\overline{X}_{\mathrm{Residual}}$ (dashed and dotted yellow line).

ECMWF data was shown in figure 4.2.

The gravity wave drag (GWD) at 90 hPa, from the diagnostics available, is nearly all due to saturated stress, as shown in section 5.4.3. Looking at the saturated stress (figure 6.16a) there is a band of positive GWD of about 20° in width around the equator with negative GWD surrounding it. This positive band is displaced northwards during NH summer. This has a similar pattern to that in the ECMWF data. However, the positive GWD within the tropics has a very small magnitude, less than $0.1\,\mathrm{m\,s^{-1}\,day^{-1}}$, and the 11.3° latitudes are within this band. Subsequently there is very little of an annual cycle at 11.3° due to the GWD diagnostics.

The residual $\overline{X}$ (figure 6.16b) has strong positive values in the tropics and negative values in the northern hemisphere in NH winter and just south of the equator in NH summer. At 11.3°N $\overline{X}_{\mathrm{Residual}}$ has negative values in NH winter and positive values in NH summer, at 11.3°S the cycle is in the opposite sense. It is this residual term which contributes to the majority of the annual cycle in $\overline{X}$ at these latitudes. Gregory *et al.* (1997), demonstrating the parametrisation used in this model set up, showed a positive acceleration due to convective momentum drag in the centre of the ITCZ just below 100 hPa, with negative accelerations either side. This is similar to the pattern seen here, though $\overline{X}_{\mathrm{Residual}}$ does not quite reach negative values south of the ITCZ in figure 6.16b.

The total $\overline{X}$ (c) has a similar pattern to that of the ECMWF $\overline{X}$ but with an additional positive region in the SH in NH winter. There is also a maximum just south of the equator in NH winter which is not seen in the $\overline{X}$ in the ECMWF data.

In section 4.3 it was commented that the positive tropical band in $\overline{X}$ follows the same pattern as the Inter-Tropical Convergence Zone (ITCZ). Figure 6.17 shows the convective rainfall which is a proxy for the ITCZ. This shows the distinctive northwards movement of tropical convection during NH summer and southwards movement during SH summer. There is a corresponding northwards and southwards movement in the residual $\overline{X}$ in figure 6.16b. This, combined with comparisons to Gregory *et al.* (1997) previously mentioned, means that $\overline{X}_{\mathrm{Residual}}$ is likely to be convective momentum drag due to convectively triggered waves.

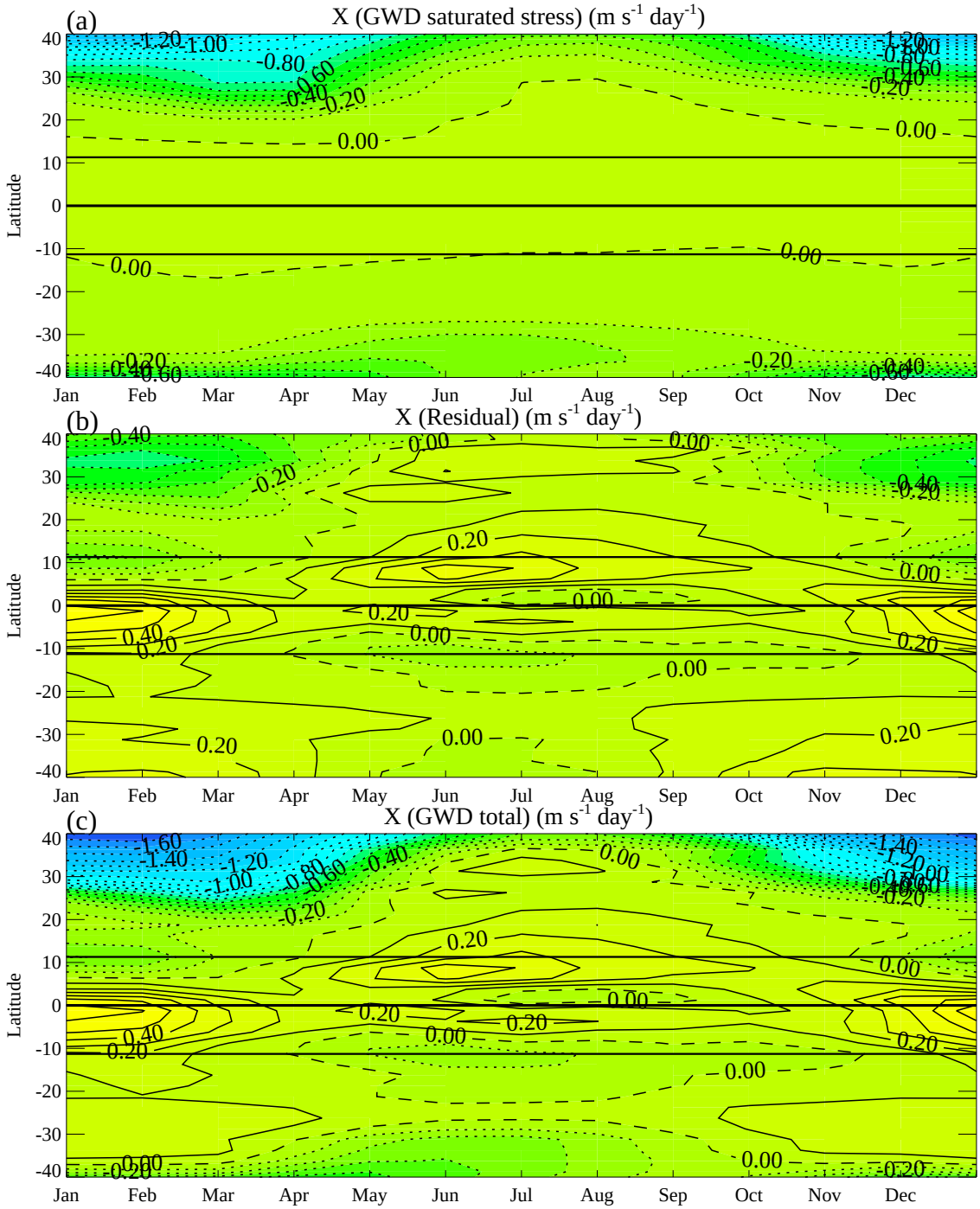

Figure 6.16: Mean annual cycle of the main components of $\overline{X}$ at 90 hPa. (a) shows the contribution from saturated stress, (b) the residual and (c) the sum of all components (including trapped lee waves and hydraulic jump). The contour interval is $0.1\,\mathrm{m\,s^{-1}\,day^{-1}}$. Solid black lines indicate 11.3°N, the equator and 11.3°S.

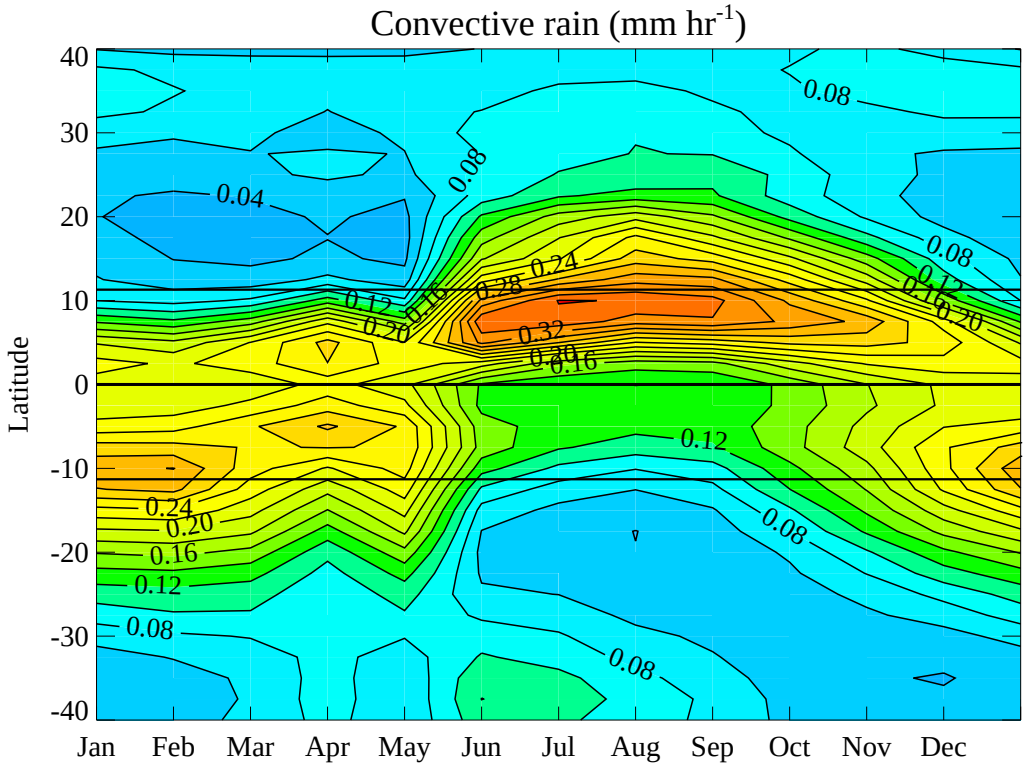

Figure 6.17: Mean annual cycle of the convective rainfall. The contour interval is $0.02\,\mathrm{mm\,hr^{-1}}$. Solid black lines indicate 11.3°N, the equator and 11.3°S.

6.7 EP flux divergence

Figure 6.18 shows the EP flux divergence from 40°N to 40°S at 90 hPa. Figure 4.3 was the equivalent plot for the ECMWF data.

There is a short period of minimum convergence (maximum values) around the equator from June to August. In the ECMWF data divergence is seen in this period—the maximum values are greater, to the extent that there is a change of sign. Contours of constant convergence are pushed away from the equator around this positive region. These extend further south than north giving an annual cycle in convergence at 11.3°S, with more convergence in NH winter than NH summer. The pattern in NH spring is rather different to the ECMWF data. The band of minimum convergence is further north causing an annual cycle of the opposite sense at 11.3°N, with less convergence in NH winter than NH summer.

There is a maximum in convergence near 30°N between April and July and another near 35°N in October giving a semi-annual cycle at these latitudes. In the ECMWF data there is a semi-annual cycle slightly further north. In the SH there

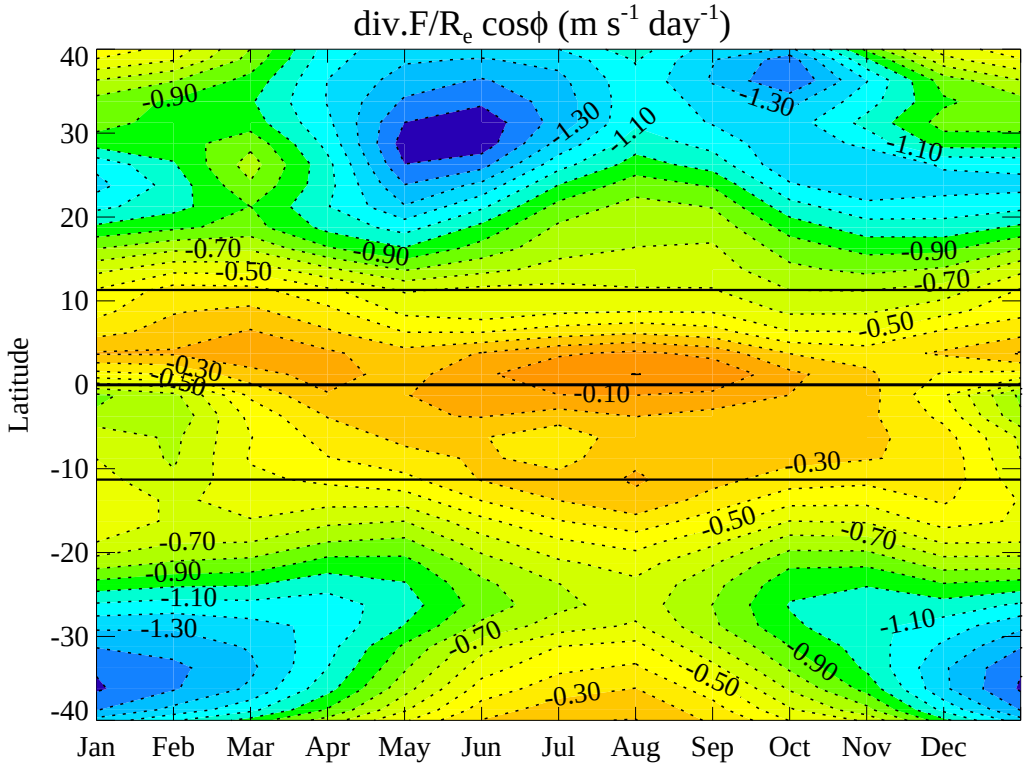

Figure 6.18: Mean annual cycle of the EP flux divergence, $\frac{1}{R_e \cos\phi}\nabla.\mathbf{F}$, at 90 hPa. Solid black lines indicate 11.3°N, 0° and 11.3°S. The contour interval is 0.1 m s^{-1} day^{-1}. Solid contours indicate divergence (positive $\nabla.\mathbf{F}$), dotted contours indicate convergence.

is a maximum convergence in NH winter and a minimum in NH summer as for the ECMWF data, although the minimum occurs for much less time and is slightly further south.

The EP flux divergence can be decomposed into contributions from the northern and southern hemispheres and into contributions from the horizontal and vertical components. Figure 6.19 shows the annual cycle in the horizontal and vertical components of the EP flux divergence at 11.3°N and 11.3°S. The equivalent figure for the ECMWF data is figure 4.6 (black solid lines only). Note that the sense of the annual cycle for the required driving of $\overline{v}^*$ is reduced EP flux divergence in NH summer and increased EP flux divergence in NH winter or a "U" shape in the plots.

Total $\frac{-1}{R_e \cos\phi}\nabla.\mathbf{F}$ (first column)

The NH has an annual cycle in the opposite sense to that for driving $\overline{v}^*$ and in the opposite sense to that of the ECMWF data, while the SH has an annual cycle in the correct sense for driving $\overline{v}^*$ and in the same sense to that of the ECMWF data. This gives a small, noisy annual cycle in the total $\frac{-1}{R_e \cos\phi}\nabla.\mathbf{F}$. There is also a strong semi-annual cycle, with a second maximum in May.

Horizontal and vertical components for 11.3°N+11.3°S (first row)

The horizontal component has a maximum in May and a minimum in June, with a smaller maximum in December and minimum in February. This is similar to the horizontal component in the ECMWF data. The vertical component has a minimum in April, partially cancelling out the maximum in May of the horizontal component. In the ECMWF data the vertical component has a much stronger annual cycle in the sense for driving $\overline{v}^*$.

11.3°N (middle row)

In the NH it is the horizontal component which has an annual cycle in the sense to drive $\overline{v}^*$. This is stronger than in the ECMWF data. The vertical component also has a stronger annual cycle than in the ECMWF data and, as for the ECMWF data, this is in the opposite sense to that required to drive $\overline{v}^*$. Unlike the ECMWF data the vertical component's opposing cycle is stronger than its horizontal component to give a total annual cycle (d) in the opposite sense than required for driving $\overline{v}^*$.

11.3°S (bottom row)

In the SH it is the vertical component which has an annual cycle in the sense to drive $\overline{v}^*$. This is stronger than in the ECMWF data. The horizontal component has an annual cycle in the opposite sense to that required to drive $\overline{v}^*$, as in the

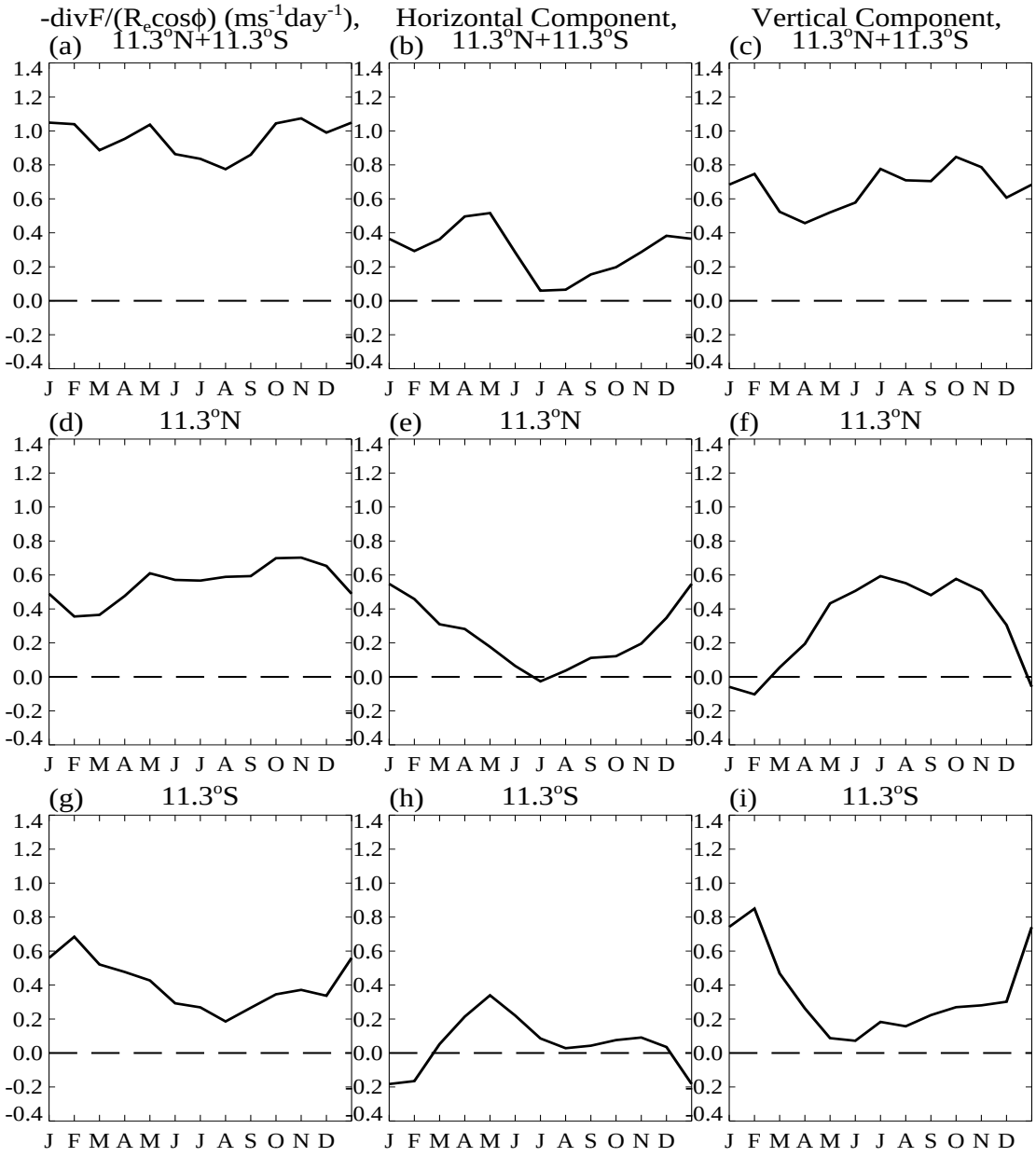

Figure 6.19: Annual cycle in the horizontal and vertical components of the EP flux divergence, $\frac{-1}{R_e \cos\phi}\nabla.\mathbf{F}$. The columns show total, horizontal and vertical components respectively. The rows show 11.3°N+11.3°S, 11.3°N and 11.3°S respectively.

ECMWF data. There is also a sharp peak in May in the horizontal component, not present in the ECMWF data. The horizontal and vertical components sum to give an annual cycle in the correct sense for driving $\overline{v}^*$, as in the ECMWF data.

Horizontal component (second column)

The annual variation in the horizontal component in the NH is of the sense to drive $\overline{v}^*$, with the SH opposing this. The peak in May in the SH contributes to the semi-annual cycle seen in (b). In the ECMWF data, the semi-annual cycle appeared more strongly in the NH.

Vertical component (third column)

There is a strong annual variation in the NH which opposes the driving of $\overline{v}^*$. In the SH the annual variation is equally strong and is of the sense required to drive $\overline{v}^*$. These sum to give a very small, noisy annual cycle in the sense to drive $\overline{v}^*$.

The balance of terms in the vertical component give an opposite result for the sum of the hemispheres in the vertical to that of the ECMWF data, with the NH dominating rather than the SH. The NH vertical component also dominates the NH horizontal component. This gives a small, noisy annual cycle in the total EP flux divergence.

6.7.1 Eddy terms decomposition of EP flux divergence

Again, the EP flux divergence is examined more closely, in terms of the eddy fluxes as in equation 4.3. Figure 6.20 shows the EP flux divergence, $\frac{-1}{R_e \cos\phi}\nabla.\mathbf{F}$, decomposed into the four eddy terms for the northern and southern hemispheres. This can be compared with the first column of figure 4.8 for the ECMWF data.

As for the ECMWF data, in all panels of figure 6.20, $v'\theta'$ from the horizontal component ($\nabla.\mathbf{F}^{(\phi)}$i) (dotted blue line) is small and does not show a strong annual cycle, so the horizontal component of $\frac{-1}{R_e \cos\phi}\nabla.\mathbf{F}$ is mainly due to the term involving $v'u'$ ($\nabla.\mathbf{F}^{(\phi)}$ii). In the following the $v'\theta'$ term from the horizontal component will be ignored.

In panel (a) it can be seen that the terms which are in the sense to drive $\overline{v}^*$ are $\omega'u'$ (red line) from the vertical component ($\nabla.\mathbf{F}^{(p)}$ii) and $v'u'$ (green line) from the horizontal component ($\nabla.\mathbf{F}^{(\phi)}$ii). This is partially cancelled by $v'\theta'$ (orange line) from the vertical component ($\nabla.\mathbf{F}^{(p)}$i). In the ECMWF data the annual cycle in $\omega'u'$ is about $1\,\mathrm{m\,s^{-1}\,day^{-1}}$ peak to peak whereas the annual cycle in $v'u'$ is about $0.4\,\mathrm{m\,s^{-1}\,day^{-1}}$. This is partially cancelled by an annual cycle of about $0.6\,\mathrm{m\,s^{-1}\,day^{-1}}$ in $v'\theta'$. However in the UM data the annual cycle in $\omega'u'$ is only $0.6\,\mathrm{m\,s^{-1}\,day^{-1}}$, with the annual cycle in $v'u'$ about $0.5\,\mathrm{m\,s^{-1}\,day^{-1}}$. The opposing

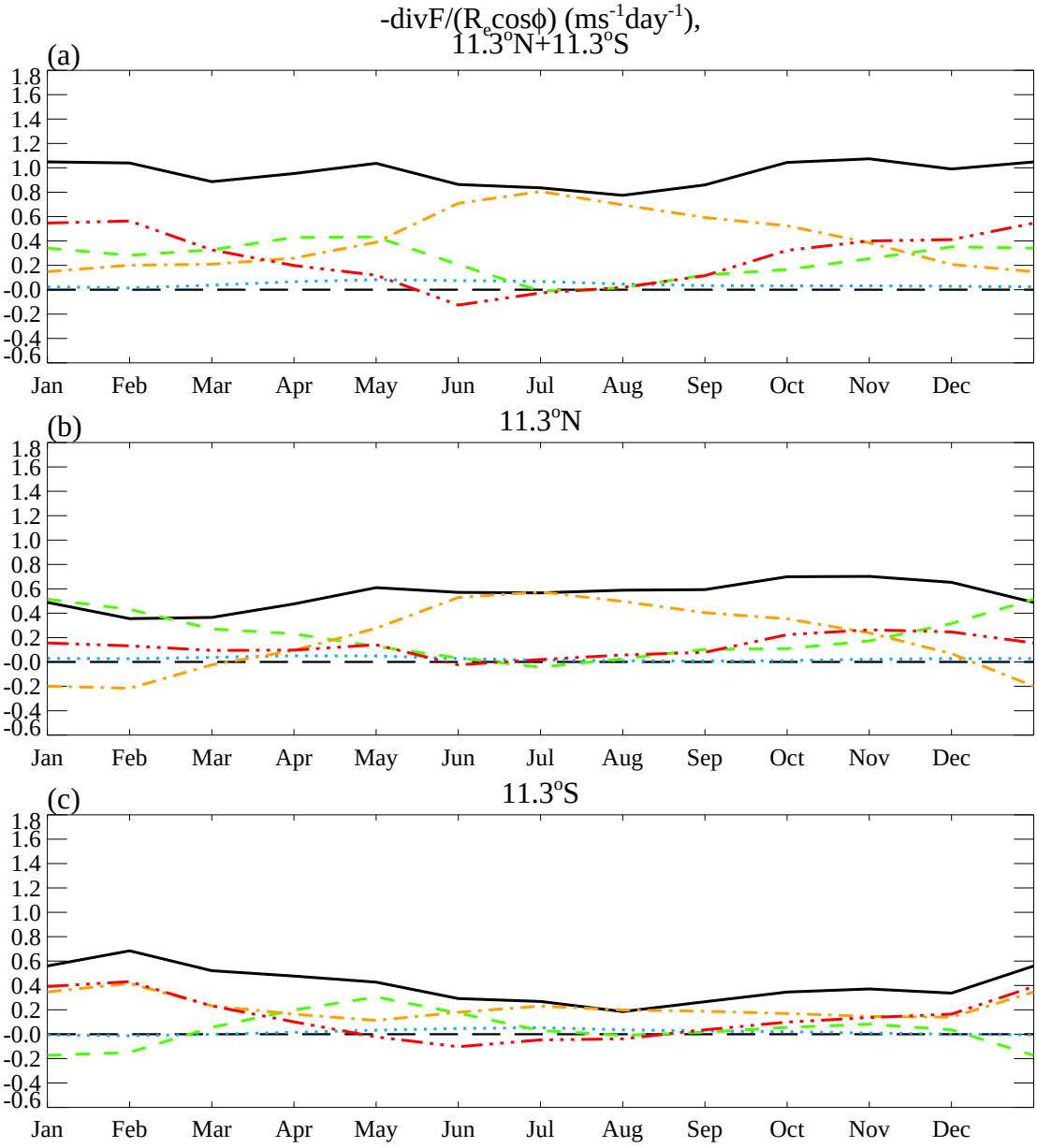

Figure 6.20: Annual cycle in the northern and southern hemisphere components of the EP flux divergence, $\frac{-1}{R_e \cos\phi} \nabla.\mathbf{F}$, showing the contributions from each of the eddy flux terms. The plots show terms at (a) 11.3°N+11.3°S, (b) 11.3°N and (c) 11.3°S respectively. The eddy components are total (solid black line), $\nabla.\mathbf{F}^{(\phi)}$i $(v'\theta')$ (dotted blue line), $\nabla.\mathbf{F}^{(\phi)}$ii $(v'u')$ (dashed green line), $\nabla.\mathbf{F}^{(p)}$i $(v'\theta')$ (dashed and dotted orange line) and $\nabla.\mathbf{F}^{(p)}$ii $(\omega'u')$ (dash and three dotted red line). The time-meaning period is 30.5 days.

annual cycle in $v'\theta'$ is $0.6\,\mathrm{m\,s^{-1}\,day^{-1}}$.

In the northern hemisphere (panel (b)) the majority of the annual cycle in the sense to drive $\overline{v}^*$ is from $v'u'$ and $\omega'u'$ has only a very small annual cycle. The annual cycle in $v'\theta'$ partially cancels this annual cycle, giving a residual $\frac{-1}{R_e \cos\phi}\nabla.\mathbf{F}$ with a small annual cycle opposing the driving of $\overline{v}^*$. Compared with the ECMWF data each eddy term has the same sense of annual cycle but the magnitudes of the annual cycle are different, with the annual cycle in $\omega'u'$ much smaller.

In the southern hemisphere (panel (c)) the annual cycles in $v'\theta'$ and $\omega'u'$ are of the sense to drive $\overline{v}^*$, partially cancelled by $v'u'$. Again the annual cycles are of the same sense as for the ECMWF data but the magnitudes of the annual cycles and the balance in the terms are different, producing a much smaller annual cycle in $\frac{-1}{R_e \cos\phi}\nabla.\mathbf{F}$. The semi-annual cycle seen in the horizontal component in figure 6.19 is due to the $v'u'$ term in this hemisphere.

To summarise:

- The NH annual cycle arises from the horizontal component of $\frac{-1}{R_e \cos\phi}\nabla.\mathbf{F}$ opposed by the vertical component. In the vertical the annual cycle in $v'\theta'$ is partially cancelled by $\omega'u'$.
- The SH annual cycle arises from the vertical component of $\frac{-1}{R_e \cos\phi}\nabla.\mathbf{F}$ opposed by the horizontal component. In the vertical the annual cycles in $v'\theta'$ and $\omega'u'$ are in the same sense.
- The two hemispheres partially cancel each other's annual cycles.
- The two hemispheres and horizontal and vertical components and eddy term components have annual cycles in the same senses as for the ECMWF data but of different strengths, so that the sums give differing results.
- The annual cycle in $\omega'u'$ is much smaller in the UM data than in the ECMWF data whereas the other eddy terms have similar magnitudes.

Both the northern and southern hemispheres are important, the horizontal component of $\frac{-1}{R_e \cos\phi}\nabla.\mathbf{F}$ being important in the NH and the vertical component in the SH.

6.8 Stream function

Although longitudinal information for the eddy contributions to the EP flux for December and August is not available for the UM data because this information was not output from the model due to disk-space limitations, the stream function

can be plotted. This is shown in figure 6.21 and can be compared with figure 4.16 for the ECMWF data.

The flow is mostly zonal and westward in the tropics in August, as for the ECMWF data. The upward extension of the Asian monsoon anticyclone can be seen over east Africa, India and Asia, as can the corresponding circulation over the Indian ocean and the anticyclone over Mexico. The circulations over Asia and the Indian ocean are displaced polewards compared with the ECMWF data. There is also some southwards flow over the east Pacific whereas the flow was zonal and westwards in this region in the ECMWF data.

In December there are anticyclones associated with the monsoons over South America, west Africa and north-east Australia. These anticyclones are nearly symmetrical about the equator, as for the ECMWF data. However the details of the stream function are different. The zero line in the northern hemisphere is further north in the western hemisphere; the furthest south it reaches is 20°N over the Atlantic. In the ECMWF data this line reaches 5°N over the Pacific and 10°N over the Atlantic. Over southern Mexico, there is a closed contour around which there is a circulation, whereas in the ECMWF data the stream function only showed an increase, the contours deviating around this region. Over the south-east Pacific the northwards deviation in the stream function contours seen in the ECMWF data is not present in the UM data, with the South American and Australian anticyclones reaching further into this region. The circulations are displaced eastwards and polewards compared with the ECMWF data. There is also more zonal flow in the tropics, especially in the southern hemisphere.

In August there is less zonal flow in the tropics than in the ECMWF data. In December there is more zonal flow in the tropics than in the ECMWF data. The anticyclones have greater longitudinal extent and are displaced westwards and polewards. As a result the tropical flow is more similar between December and August in the UM data than in the ECWMF data.

6.9 A wider latitude band

The displacement of the anticyclone circulations polewards in the stream function suggests that a wider latitude band might be interesting to consider. Looking again at the EP flux divergence, figure 6.18, it can be seen that moving further north, say to 16°N, might improve the results. Although there is a smaller annual cycle at 16.3°N than 11.3°N ($0.31\,\mathrm{m\,s^{-1}\,day^{-1}}$ compared with $0.35\,\mathrm{m\,s^{-1}\,day^{-1}}$ peak to

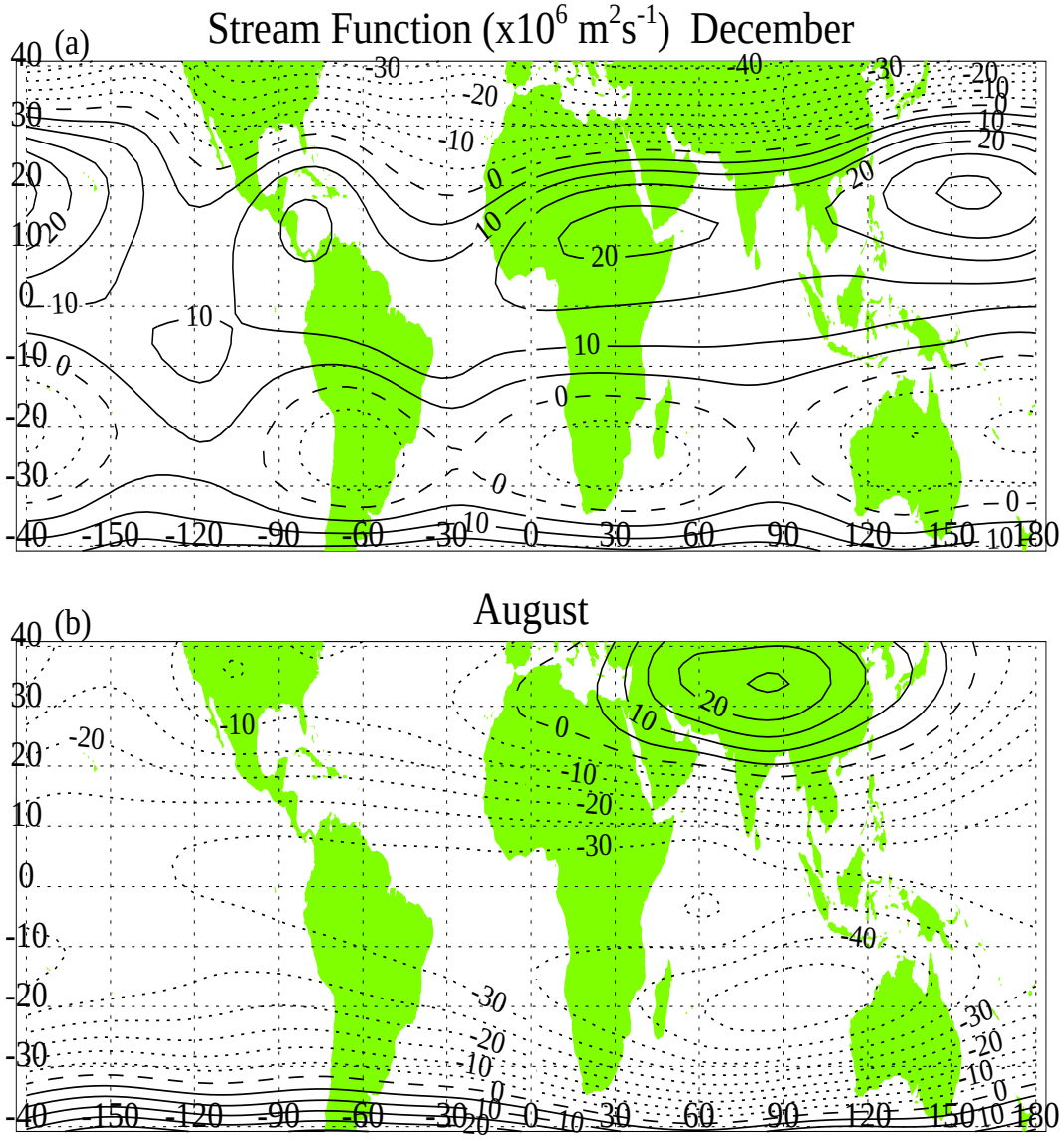

Figure 6.21: Geographical distribution of the stream function for (a) December and (b) August. The contour interval is 5×10^{-6} m^{2}s^{-1}. All longitudes are plotted, for the latitude band 40°N to 40°S. A map of the continents is also shown.

peak) it is of the right sense to drive $\overline{v}^*$, with greater divergence in NH winter than summer. At 11.3°N it was of the opposite sense. In the SH, the annual cycle is of the same sense at 16.3°S as at 11.3°S, but with a smaller annual cycle ($0.36\,\mathrm{m\,s^{-1}\,day^{-1}}$ compared with $0.50\,\mathrm{m\,s^{-1}\,day^{-1}}$ peak to peak). Using 16.3°N (which is the nearest grid point to 16°) might give more similar results to the ECMWF analysis. Looking at $\overline{X}_{\mathrm{Residual}}$ in figure 6.16 there may also be reduced annual cycles in both hemispheres at 16°, so reduced opposition to the driving of $\overline{v}^*$.

Figure 6.22 shows the contribution of the different terms in the zonal momentum equation at 16.3°N and 16.3°S at 90 hPa. Panel (a) shows 16.3°N+16.3°S, (b) 16.3°N and (c) 16.3°S. This can be compared with figure 4.1 for the ECMWF data and figure 6.15 for 11.3° for the UM data.

The annual cycle in $\overline{v}^*$ is mainly due to the EP flux divergence. There are small contributions from $\overline{X}$ and $\frac{\partial \overline{u}}{\partial t}$. There is a semi-annual cycle in EP flux divergence due to the NH, with a maximum in May as well as NH winter. This is opposed by a minimum in $\frac{\partial \overline{u}}{\partial t}$. In the ECMWF data there is a minimum in $\frac{\partial \overline{u}}{\partial t}$ in June which decreases $\overline{v}^*$ and reduces the effect of a small maximum in the NH EP flux divergence in June. The annual cycle in $\overline{v}^*$ follows that of the EP flux divergence more closely for 16.3° than for 11.3°.

Figure 6.23 shows the EP flux divergence decomposed into contributions from the northern and southern hemispheres and into contributions from the horizontal and vertical components. The equivalent figure for the ECMWF data is figure 4.6 (black solid lines only) and for the UM data at 11.3° is figure 6.19. Note that the sense of the annual cycle for the required driving of $\overline{v}^*$ is reduced EP flux divergence in NH summer and increased EP flux divergence in NH winter or a "U" shape in the plots.

Horizontal and vertical components for 11.3°N+11.3°S (first row)

Both panels (b) and (c) have strong annual cycles but these are of opposite sense and with different timing of their NH summer minimum and maximum respectively. This gives a semi-annual cycle, with maxima in May and October and the expected minimum in NH summer. In the ECMWF data the vertical component has a much stronger annual cycle in the sense for driving $\overline{v}^*$. In the UM data at 11.3° the horizontal and vertical components did not have such a clear annual cycle.

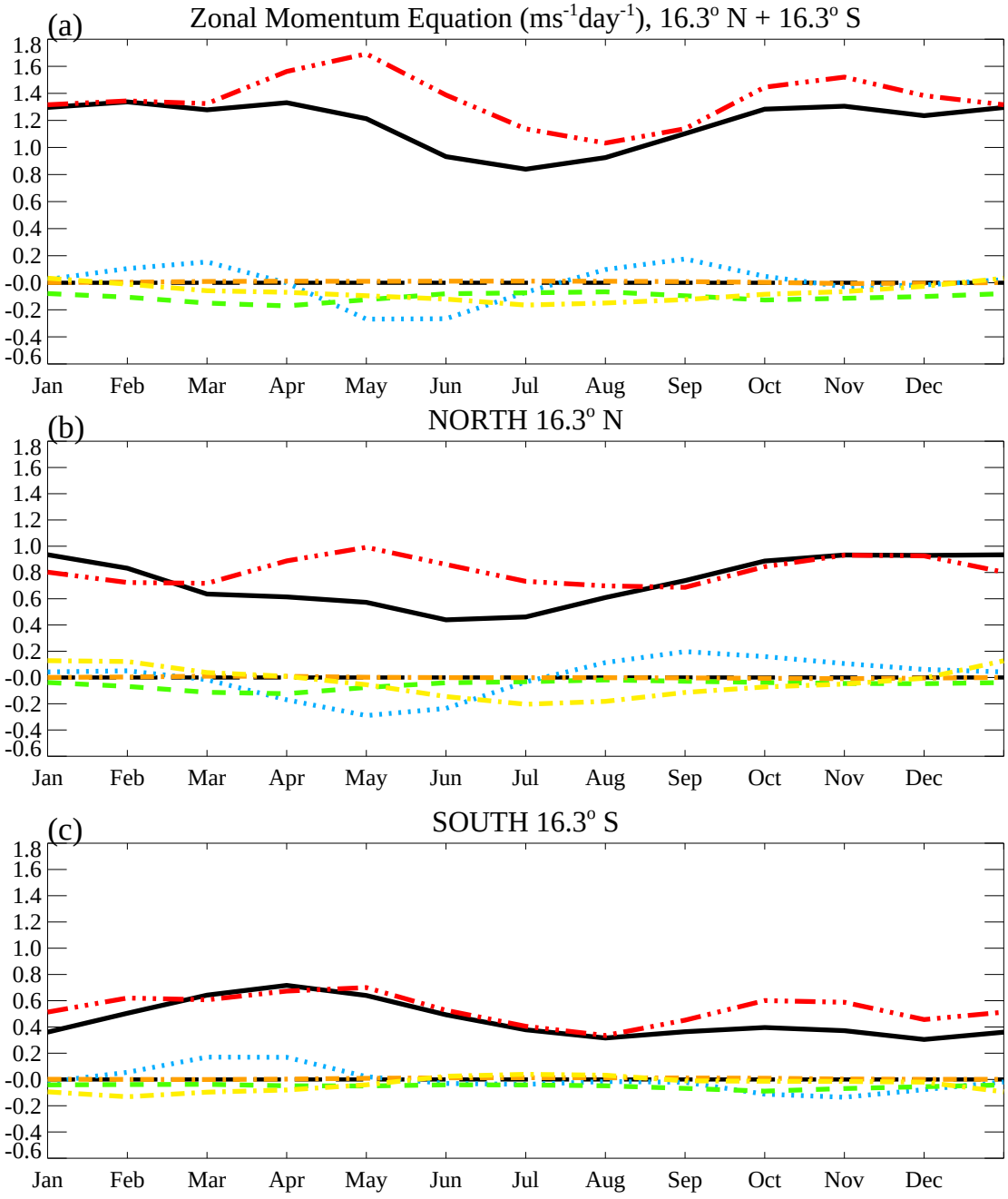

Figure 6.22: Mean annual cycle of the terms in the zonal momentum equation (equation 3.8) at 90 hPa. The plots show terms at (a) 16.3°N plus terms at 16.3°S (as figure 6.14), (b) 16.3°N and (c) 16.3°S. The terms are $\overline{v}^*\overline{\zeta}_a$ (solid black line), $\frac{\partial \overline{u}}{\partial t}$ (dotted blue line), $-\overline{\omega}^*\frac{\partial \overline{u}}{\partial p}$ (dashed green line), $\frac{1}{R_e \cos\phi}\nabla.\mathbf{F}$ (dash and three dotted red line), $\overline{X}_{\mathrm{GWD}}$ (dashed and dotted orange line) and $\overline{X}_{\mathrm{Residual}}$ (dashed and dotted yellow line).

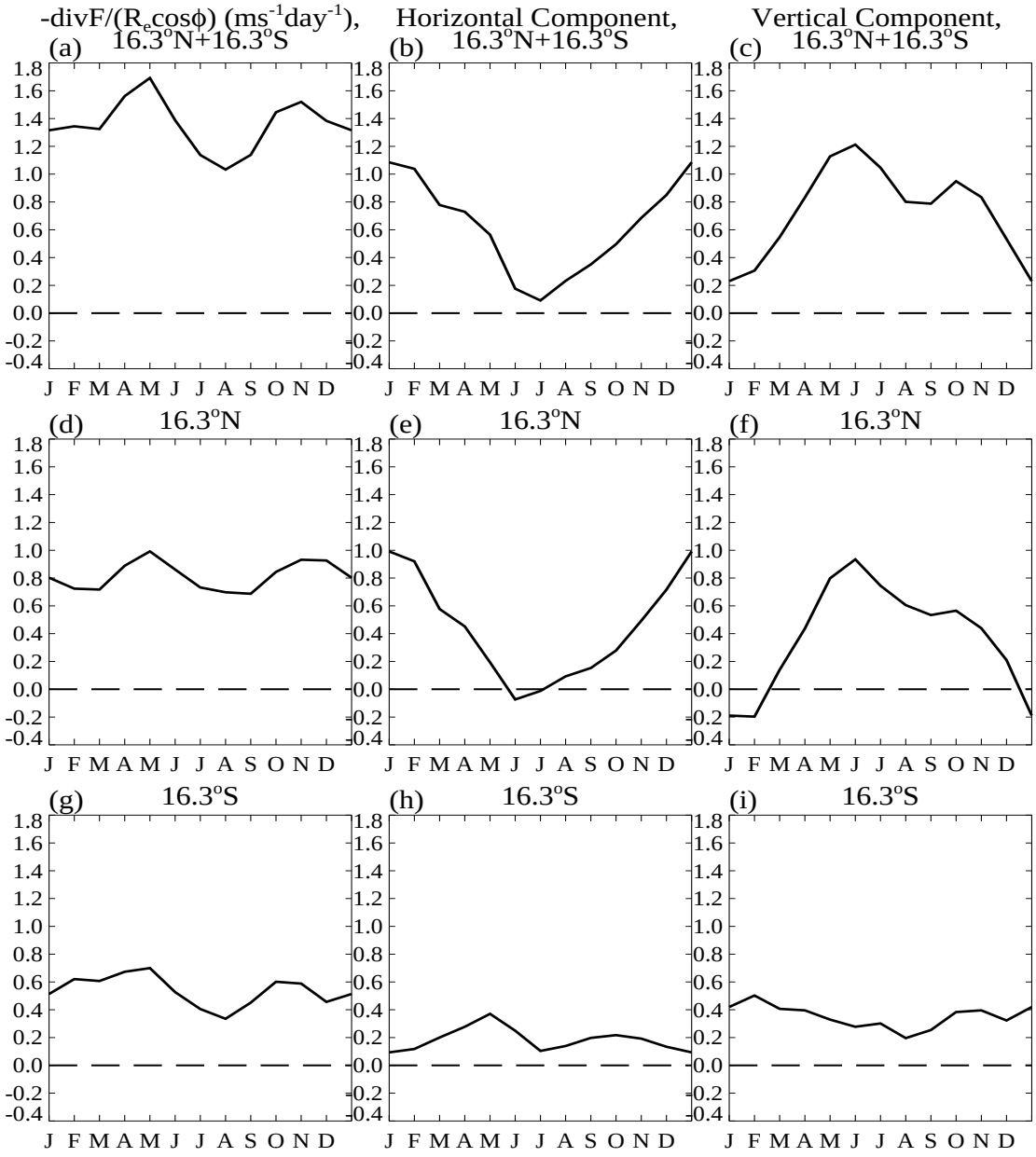

Figure 6.23: Annual cycle in the horizontal and vertical components of the EP flux divergence, $\frac{-1}{R_e \cos\phi}\nabla.\mathbf{F}$. The columns show total, horizontal and vertical components respectively. The rows show 16.3°N+16.3°S, 16.3°N and 16.3°S respectively.

11.3°N (middle row)

In the NH it is the horizontal component which has an annual cycle in the sense to drive $\overline{v}^*$. This is stronger than in the ECMWF data. The vertical component also has a stronger annual cycle than in the ECMWF data and, as for the ECMWF data, this is in the opposite sense to that required to drive $\overline{v}^*$. This gives a semi-annual cycle in the total EP flux divergence, panel (d). Panels (e) and (f) are very similar in the two UM plots but for 16.3° the annual cycle is larger.

11.3°S (bottom row)

In the SH it is the vertical component which has an annual cycle in the sense to drive $\overline{v}^*$. This is weaker than in the ECMWF data unlike for 11.3° which had a stronger annual cycle than the ECMWF data. The horizontal component has an annual cycle in the opposite sense to that required to drive $\overline{v}^*$, as in the ECMWF data and 11.3° UM data. There is also a sharp peak in May in the horizontal component, not present in the ECMWF data but seen at 11.3°. The horizontal and vertical components sum to give an annual cycle in the correct sense for driving $\overline{v}^*$, as in the ECMWF data, but the annual cycle is weaker than in the ECMWF data and at 11.3° in the UM data.

Horizontal component (second column)

The annual variation in the horizontal component in the NH is of the sense to drive $\overline{v}^*$, with the SH opposing this, as for the ECMWF data and at 11.3° in the UM data. There is a peak in May in the SH, also seen at 11.3°S. In the ECMWF data the semi-annual cycle appeared more strongly in the NH.

Vertical component (third column)

There is a strong annual variation in the NH which opposes the driving of $\overline{v}^*$. In the SH the annual variation is weaker (whereas it was equally strong as the NH for 11.3°) and is of the sense required to drive $\overline{v}^*$. These sum to give an annual cycle opposing the driving of $\overline{v}^*$.

As for 11.3°the NH vertical component dominates over the SH vertical component. However, the NH horizontal component is stronger at 16.3° so that the total NH component (panel (d)) does not oppose the driving of $\overline{v}^*$, but has a semi-annual cycle. The annual cycle in the total EP flux divergence is less noisy and stronger than for 11.3°.

Figure 6.24 shows the EP flux divergence decomposed into the four eddy flux terms. This can be compared with panel (a) of figure 4.8 for the ECMWF data and panel (a) of figure 6.20 for 11.3°.

Again, $v'\theta'$ from the horizontal component ($\nabla.\mathbf{F}^{(\phi)}$i) (dotted blue line) is small

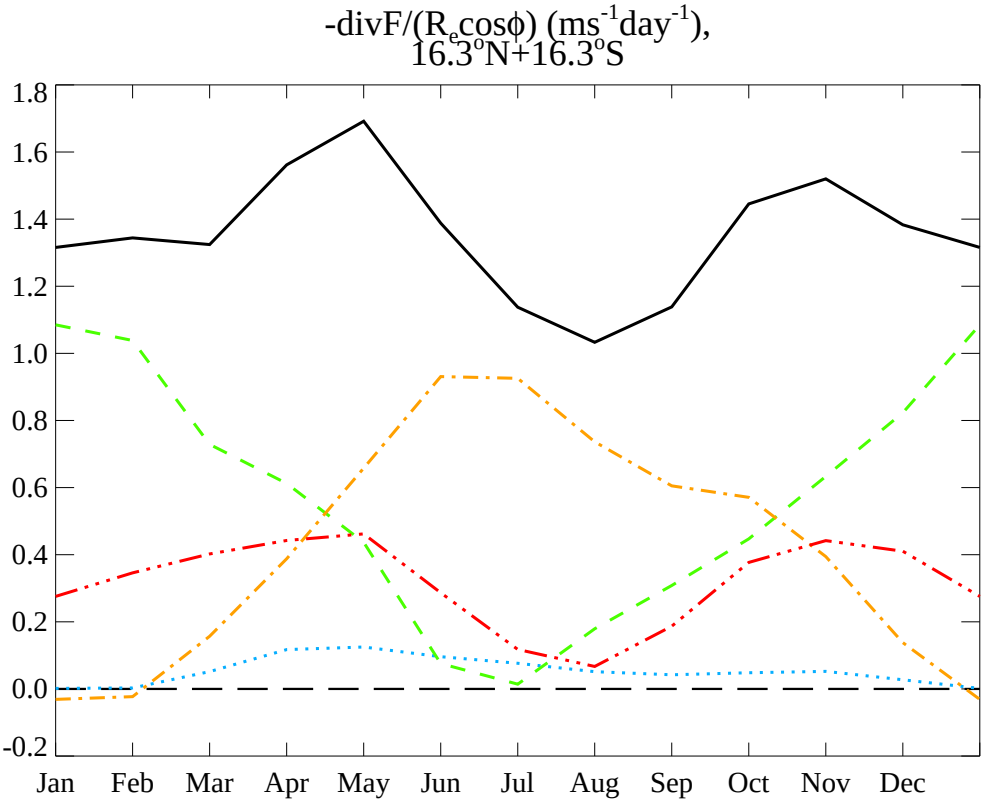

Figure 6.24: Annual cycle in the eddy flux terms contributing to the EP flux divergence, $\frac{-1}{R_e \cos\phi}\nabla.\mathbf{F}$ at 16.3°N+16.3°S. The eddy components are total (solid black line), $\nabla.\mathbf{F}^{(\phi)}$i $(v'\theta')$ (dotted blue line), $\nabla.\mathbf{F}^{(\phi)}$ii $(v'u')$ (dashed green line), $\nabla.\mathbf{F}^{(p)}$i $(v'\theta')$ (dashed and dotted orange line) and $\nabla.\mathbf{F}^{(p)}$ii $(\omega'u')$ (dash and three dotted red line). The time-meaning period is 30.5 days.

and does not show a strong annual cycle so the horizontal component of $\frac{-1}{R_e \cos\phi}\nabla.\mathbf{F}$ is mainly due to the term involving $v'u'$ ($\nabla.\mathbf{F}^{(\phi)}$ii). The terms of the sense to drive $\overline{v}^*$ are $\omega'u'$ (red line) from the vertical component ($\nabla.\mathbf{F}^{(p)}$ii) and $v'u'$ (green line) from the horizontal component ($\nabla.\mathbf{F}^{(\phi)}$ii). This is partially cancelled by $v'\theta'$ (orange line) from the vertical component ($\nabla.\mathbf{F}^{(p)}$i). The relative strengths of the vertical components, with $\omega'u'$ not decreasing below zero in NH summer, contribute to the annual cycle opposing $\overline{v}^*$ seen in figure 6.23.

The two peaks in May and November are due to the semi-annual cycle in $\omega'u'$. This semi-annual cycle was seen in the ECMWF data but not at 11.3° in the UM data. The decomposition into eddy flux terms at this latitude gives a much more similar result to the ECMWF data than at 11.3°. One possible reason for this is the much lower resolution of the UM data compared with the ECMWF data. Another cause may be the difficulty the Unified Model has in simulating the monsoon, including the timing of monsoon onset, the patterns and the strength of the seasonal cycle. For example, the west African monsoon penetrates too far north and arrives too early in HadAM3 (Slingo *et al.*, 2003), which is the model version used for the AMIP-II simulations.

6.10 Summary

Section 6.2 showed that, as in the ECMWF data, the strongest annual cycle in temperature and rate of change of temperature was in the latitude band 10°N to 10°S. The latitude band 11.3°N to 11.3°S was then used to analyse the TEM equations.

The annual cycle in potential temperature at 90 hPa for 11.3°N to 11.3°S is driven by the changes in adiabatic heating and cooling, $-\overline{\omega}^*\frac{\partial\overline{\theta}}{\partial p}$. The changes in potential temperature are responded to and opposed by $\overline{Q}$, the diabatic heating residual term. This is similar to the ECMWF data, although the changes are more gradual in the UM data than in the ECMWF data. The annual cycle in $\overline{Q}$ is mainly due to the residual, with LW radiation responding closely to the changes in potential temperature.

Section 6.3 showed that the adiabatic heating and cooling, $-\overline{\omega}^*\frac{\partial\overline{\theta}}{\partial p}$, is similar to the residual mean upwelling, $\overline{\omega}^*$, although not as close a similarity as for the ECMWF data. Section 6.3.1 shows that, by mass continuity, changes in the upwelling, $\overline{\omega}^*$, in a latitude band are driven by changes in the outflow, $\overline{v}^*$, from the edge of that latitude band above the upwelling. The majority of the annual

cycle in the upwelling between 11.3°N and 11.3°S at 90 hPa is driven by changes to the outflow from 11.3°N and 11.3°S near 90 hPa. The "near 90 hPa" implies local downward control, not non-local control. This result is the same as for the ECMWF data.

Section 6.4 considers the zonal momentum equation. As for the ECMWF data the outflow from the latitude band, $\overline{v}^*$, is driven by the Eliassen-Palm flux divergence, $\nabla.\mathbf{F}$. There is a small contribution from the residual $\overline{X}$. Section 6.5 then considers the contribution to this driving from the two hemispheres. The section shows that in the NH $\overline{X}_{\text{Residual}}$ is driving the annual cycle in $\overline{v}^*$ opposed by the EP flux divergence, whereas in the SH it is the EP flux divergence which is driving $\overline{v}^*$, opposed by $\overline{X}_{\text{Residual}}$. $\overline{X}_{\text{Residual}}$ cancels out when the two hemispheres are considered together. Section 6.6 investigates $\overline{X}$, showing that at 90 hPa it is composed mainly of $\overline{X}_{\text{Residual}}$ in the tropics and from the saturated stress component of gravity wave drag in the extra-tropics. It was shown that $\overline{X}_{\text{Residual}}$ corresponds to the ITCZ and is probably due to convectively triggered waves from the convective momentum drag parametrization. The parametrization has been shown to cause accelerations at 100 hPa (Gregory *et al.*, 1997) and is not capped in this model but is available at all model levels.

The EP flux divergence is studied in section 6.7; this shows that there are some similarities with the ECMWF data and some differences. The shape of the EP flux divergence at 90 hPa in the tropics is important for the annual cycle at the edges of a chosen latitude band. The EP flux divergence is decomposed into northern and southern hemispheres, vertical and horizontal components and eddy terms. The two hemispheres, horizontal and vertical components and individual eddy terms each have annual cycles in the same senses as for the ECMWF data but of different strengths, so that the sums give differing results. This is important in the NH because the resultant sense of the annual cycle is opposite to that of the ECMWF data and opposes driving of $\overline{v}^*$. The decomposition into eddy terms shows that the UM has a much smaller annual cycle in the $\omega' u'$ term in the vertical component of EP flux divergence than the ECMWF data.

In section 6.8 the stream function was studied. As for the ECMWF data, the main differences between August and December are due to the position and number of the monsoon anticyclones, with mainly zonal flow in the tropics in August and increased meridional flow in December. The strength of the stream function in different hemispheres for the two months is also different between the two data sets. There is more zonal flow in the tropics in December than in the

ECWMF data. This gives less variation over the year in the tropics, leading to a smaller annual cycle in $\nabla.\mathbf{F}$. In the UM data the anticyclones are further away from the equator than in the ECMWF data, suggesting that a wider latitude band may be of interest.

In section 6.9 a wider latitude band, 16.3°, is studied. This gives closer results to the ECMWF data but there are still a number of differences. The sense of the vertical component of the EP flux divergence is different because the NH component has a larger annual cycle than the SH component. The relative strengths of the vertical components of the eddy fluxes, with $\omega' u'$ not decreasing below zero in NH summer, contribute to the annual cycle opposing $\overline{v}^*$ seen in figure 6.23.

The problems with the driving of the annual cycle in horizontal motion could be due to the lower resolution and the problems in correctly simulation the monsoons by Unified Model.

The main conclusions of this chapter are:

- Although it appears that the important latitude band is 10°N to 10°S, where the potential temperature change is greatest, a wider latitude band has more similar results to the ECMWF data when looking at $\nabla.\mathbf{F}$.
- The temperatures are driven by the adiabatic heating and cooling.
- The adiabatic heating and cooling is controlled by the upwelling, $\overline{\omega}^*$.
- The upwelling between 11.3°N and 11.3°S at 90 hPa is controlled by the net outflow, $\overline{v}^*$, from 11.3°N and 11.3°S near 90 hPa.
- The downward control is local—near 90 hPa.
- The net outflow from 11.3°N and 11.3°S is mostly driven by the Eliassen-Palm flux divergence, $\nabla.\mathbf{F}$ across the latitude band.
- The net outflow from 16.3°N and 16.3°S is driven by the Eliassen-Palm flux divergence, $\nabla.\mathbf{F}$ across the latitude band in a way more similar to the ECMWF data than for 11.3°.
- As for the ECMWF data, the annual cycle of EP flux divergence in the NH in the sense to drive $\overline{v}^*$ arises from the horizontal component and in the SH annual cycle arises from the vertical component. However the two hemispheres partially cancel each other's annual cycles.
- The components due to the two hemispheres, the horizontal and vertical components and the eddy components of EP flux divergence have annual cycles in the same senses as for the ECMWF data but of different strengths, so that the sums give differing results.

- The eddy term $\omega' u'$ in the vertical component of EP flux divergence has a much smaller annual cycle in the UM data.
- The stream function for the UM data shows anticyclones above the main monsoon regions, varying in position and number over the year. The anticyclones are less close to the equator in the UM data. In December the tropical flow is more zonal in nature than in the ECMWF data.

Chapter 7

Discussion and conclusions

The importance of the annual cycle in temperatures in the tropical lower stratosphere was identified in chapter 1. Theories as to how this cycle is driven have been put forward by a number of authors during the last half century (including Reed and Vlcek, 1969; Reid and Gage, 1981; Gray and Dunkerton, 1990; Haynes *et al.*, 1991; Yulaeva *et al.*, 1994; Holton *et al.*, 1995; Rosenlof, 1995; Randel *et al.*, 2002). However these authors do not fully explain what drives the annual cycle in tropical tropopause temperatures. The aim of this research was to further investigate the annual cycle in tropical tropopause temperatures using the transformed Eulerian mean equations. Two different data sets were analysed; assimilated observational data from ECMWF and model data from the Met Office Unified Model. These two data sets were treated in as similar a way as possible.

In section 1.5 some key questions were identified:

- What is driving the annual cycle in temperature?
- What is driving the annual cycle in the strength of the tropical upwelling?
- Where do the important wave dissipation regions lie?
- Which are the important waves?

These questions will be discussed in the following sections. The driving of the annual cycle in temperature will be discussed in section 7.2, the driving of the annual cycle in tropical upwelling will be discussed in section 7.3, and the details of the waves will be discussed in section 7.4.

7.1 The latitudes and level used for this study

The latitude band 10°N to 10°S was chosen as the most appropriate latitude band for the analysis of the ECMWF data (section 3.2). For the UM data 10°N to 10°S is a reasonable latitude band to choose based on the distribution of $\frac{\partial\overline{\theta}}{\partial t}$ (section 6.2). In both the ECMWF and UM data the annual cycle in potential temperature and in $\frac{\partial\overline{\theta}}{\partial t}$ is largest between these latitudes. The contours of $\frac{\partial\overline{\theta}}{\partial t}$ are also nearly straight and symmetrical about the equator between those latitudes, decreasing outside this latitude band especially at the maximum and minimum in $\frac{\partial\overline{\theta}}{\partial t}$. This latitude band is also well within the tropical region where the adiabatic heating and cooling term is mainly negative (cooling) at 90 hPa and the vertical velocities are mainly upwelling. A wider latitude band for the UM data, 16°N to 16°S, was shown to give closer results to the ECMWF data latitude band of 10°N to 10°S (section 6.9). This could be due to the poorer horizontal resolution of the model or poorer simulation of the monsoons.

In other research other, wider latitude bands were used. Reid and Gage (1981), for example, used 20°N to 20°S to look at convection and tropopause height in both observational and model data.

The downward control principle proposed by Haynes *et al.* (1991) breaks down where angular momentum surfaces do not span the atmosphere in the vertical. Rosenlof and Holton (1993) showed that this occurs equatorward of 15°, concluding that downward control is only useful poleward of 15°. They also noted that between 15° and 30° extra care was needed for the calculation due to "significant deviations from a vertically oriented line" in the angular momentum surfaces. These calculations were based on the assumption that the atmosphere is in a steady state. Holton *et al.* (1995) showed that for a simple stratospheric forcing control was directly downward in the steady state but that when a transient forcing was used the pumping action due to this forcing extended sideways as well as downwards, and could reach further into the tropics. In this research the assumption that the atmosphere is in a steady state has not been made and the calculation method does not require angular momentum surfaces to span the vertical. Therefore this limitation does not affect the choice of latitudes used here.

Randel *et al.* (2002) used 20°N to 20°S and 30°N to 30°S latitude bands. They perform a similar calculation to the downward control calculations of Haynes *et al.* (1991) and Rosenlof and Holton (1993) but do not include the vertical eddy momentum flux, $\omega'u'$, in their EP flux calculation, nor do they include $\overline{X}$ in their forcing terms. They state that the latitude band must be chosen

sufficiently far from the equator that the vorticity is not too small. They also note a practical limitation in obtaining observational estimates of $\nabla.\mathbf{F}$. They conclude that latitude bands of at least 20°N to 20°S give a reasonable result.

However Reid and Gage (1981) used the 10°N to 10°S latitude band in their study of convection and tropopause height, noting that the shape and amplitude of the annual cycle in tropopause height changes with latitude. Rosenlof (1995) used 10°N to 10°S to look at the thermodynamic equation in the lower stratosphere.

Within the 10° latitude band used in this research the contours of the rate of change of potential temperature are nearly constant across the latitude band for any given time. Outside this latitude band the rate of change of potential temperature decreases for a given time, giving a smaller amplitude annual cycle.

The 90 hPa level is chosen because it is the level available in the ECMWF data set nearest to the cold point tropopause and with the greatest annual cycle in potential temperature. Many other studies (Reid and Gage, 1985; Holton, 1990; Rosenlof and Holton, 1993; Randel *et al.*, 2002, for example) have used 100 hPa because, as noted in section 1.2, it is an appropriate level commonly available from observations and models. The 70 hPa is also looked at it, in the ECMWF data, because the largest annual cycle in temperature is at that level and it also has a large contribution to the annual cycle in upwelling at 90 hPa.

7.2 The driving of the annual cycle in temperature

The various terms in the thermodynamic equation (2.9e) were calculated and compared. In both the ECMWF and UM data (see sections 3.2 and 6.2 respectively) the dominant terms in the equation are the adiabatic cooling and the diabatic heating terms. The adiabatic cooling drives the potential temperature changes and the diabatic heating responds to the temperature changes, opposing the adiabatic cooling. In the UM data the diabatic heating response is in the longwave heating and the residual diabatic heating, and not in the shortwave heating. At 70 hPa (section 3.6) in the ECMWF data the result is the same.

Rosenlof (1995) showed plots of latitudinal weighted averages from 10°N to 10°S of terms in the thermodynamic equation at 70 and 10 hPa from two years of assimilated observations. The rate of change of temperature she showed was small compared with the diabatic heating and adiabatic cooling, which mainly cancelled each other out. This is similar to the results presented in this thesis.

In her results the radiative heating dominates and drives the temperature change at 10 hPa and the adiabatic cooling dominates at 70 hPa. She concludes that at 70 hPa the annual cycle in temperature is related to the annual cycle in upwelling, with which the results of this thesis agree.

A simple one-dimensional model was used to test the theory that the adiabatic cooling drives the temperatures. The results are shown in section 3.3. At 90 hPa the adiabatic cooling was shown to drive the annual cycle in temperature with a radiative relaxation timescale of 40 days, and at 70 hPa with a radiative relaxation timescale of 80 days. At 50 hPa and above the model does not work and other processes must dominate. These relaxation timescales are shorter than those in Randel *et al.* (2002) but have a similar vertical profile.

7.3 The driving of the annual cycle in tropical upwelling

The adiabatic heating and cooling was identified as the driving term in the thermodynamic equation and hence the annual cycle in temperatures. Adiabatic heating and cooling and changes in upwelling were then investigated in more detail (sections 3.4 and 6.3). The tropical upwelling shows a similar pattern to that of the adiabatic heating and cooling, with little contribution to the annual cycle from the vertical gradient of potential temperature. The similarity between the adiabatic cooling and upwelling is greater in the ECMWF data than the UM data. The mass continuity equation (2.9d) was rearranged to find the average vertical velocity across a latitude band due to the horizontal mass divergence at the edges of that latitude band (equation 3.3). This was then examined level by level, to determine which levels were significant in driving the upwelling at 90 hPa.

In both data sets the majority of the annual cycle in the upwelling at 90 hPa between 10°N and 10°S was due to the annual cycle in the mass divergence near to 90 hPa, with little contribution from levels above 70 hPa. The timing of the annual cycle higher up is earlier than at the tropopause and in the upper troposphere and there is a semi-annual cycle in the integrand in the stratosphere. This suggests that there are different processes dominating in the stratosphere and troposphere and that for the annual cycle 90 hPa it is the in-situ processes associated with the tropospheric processes, not stratospheric processes, which are important.

The zonal momentum equation (2.9a) was rearranged to identify the driving term for the outflow, $\overline{v}^*$ (equation 3.9). For the ECMWF data (section 3.5) the

driving term was shown to be the Eliassen-Palm flux divergence term. For the UM data (sections 6.4 and 6.9) the main driving term was again the Eliassen-Palm flux divergence, with some contribution from the residual $\overline{X}$ term at 11.3°.

The downward control and non-local control calculations of Haynes *et al.* (1991); Rosenlof and Holton (1993); Holton *et al.* (1995) and Randel *et al.* (2002) use driving of the zonal momentum equation by wave forcings to calculate the upwelling. Rosenlof and Holton (1993) showed that gravity wave drag was significant as a part of the downward control calculation only in limited regions, namely in the NH near 100 hPa between 30°N and 40°N and above 10 hPa between 30°N and 80°N. Randel *et al.* (2002) also neglect $\overline{X}$ in their calculation of upwelling from the zonal momentum equation. A number of authors (Gray and Dunkerton, 1990; Yulaeva *et al.*, 1994; Holton *et al.*, 1995; Plumb and Eluskiewicz, 1999) have shown that, in the steady state, wave induced forcing in the extra-tropics is insufficient to drive the observed annual cycle in upwelling in the tropics. When the timescale of the wave drag is comparable to the radiative relaxation timescale, tropical upwelling can be driven by extratropical wave driving (Holton *et al.*, 1995). Thus on shorter timescales than the annual cycle considered here the stratospheric wave driving can reach into the tropics.

The relative contributions to the driving of $\overline{v}^*$ from the two hemispheres were investigated. For the ECMWF data (section 4.2) the total annual cycle for both hemispheres is due to the NH and partially cancelled by the SH. This annual cycle is driven by $\nabla.\mathbf{F}$ in both hemispheres. However in the SH the residual $\overline{X}$ opposes $\nabla.\mathbf{F}$, causing the annual cycle in $\overline{v}^*$ to be in the opposite sense. The annual cycles in $\overline{X}$ in the NH and SH mostly cancel, to give a small annual cycle in the total $\overline{X}$ of the correct sense to drive the annual cycle seen in $\overline{v}^*$ but a much smaller annual cycle than that of $\nabla.\mathbf{F}$. For the UM data (sections 6.5 and 6.9) the total annual cycle for both hemispheres is due to the NH and partially cancelled by the SH. At 11.3°N $\overline{X}_{\text{Residual}}$ dominates and is partially cancelled by $\nabla.\mathbf{F}$. At 11.3°S $\nabla.\mathbf{F}$ dominates. The annual cycles in $\overline{X}_{\text{Residual}}$ in the NH and SH at 11.3° mostly cancel, to give a small annual cycle in the total $\overline{X}_{\text{Residual}}$ of the sense to drive $\overline{v}^*$ but smaller than the annual cycle in $\nabla.\mathbf{F}$. For the 16.3° latitude band the driving of $\overline{v}^*$ is similar to that of the ECMWF data—$\overline{X}_{\text{Residual}}$ has a much smaller annual cycle than for 11.3°.

7.4 The wave-driving

The Eliassen-Palm flux divergence was further studied to answer the two questions "Where do the important wave dissipation regions lie?" and "Which are the important waves?" For the ECMWF data the results are given in chapter 4 whereas for the UM data the results are given in sections 6.7 and 6.9.

As for the zonal momentum equation the contributions to $\nabla.\mathbf{F}$ from the two hemispheres were studied. The EP flux divergence was decomposed into vertical and horizontal components for both data sets and into horizontal wavenumber for the ECMWF data set.

For the ECMWF data set it was found that the majority of the annual cycle in both hemispheres and for the horizontal and vertical components was due to wavenumbers greater than or equal to three, rather than longer wavelength planetary waves. In the NH, for both the horizontal and vertical components, the annual cycle is opposed by wavenumbers one and two giving a semi-annual cycle in the total of all wavenumbers. In the SH the variations in wavenumbers one and two for the horizontal and vertical components cancel. In the horizontal component in the SH the wavenumber components are of the same sense and oppose the annual cycle required to drive $\overline{v}^*$. In the vertical component the wavenumber components are of the same sense and are of the sense required to drive $\overline{v}^*$. The NH annual cycle is in the sense to drive $\overline{v}^*$ and is due to the horizontal component of $\nabla.\mathbf{F}$, partially cancelled by the vertical component. The SH annual cycle is in the sense to drive $\overline{v}^*$ and is due to the vertical component of $\nabla.\mathbf{F}$, partially cancelled by the horizontal component.

For the UM data at 11.3°N the annual cycle is small and of the sense opposing driving $\overline{v}^*$ and at 16.3°N it has a semi-annual cycle with the summer months of the sense for driving $\overline{v}^*$. The horizontal component has an annual cycle of the sense to drive $\overline{v}^*$ and is opposed by the vertical component, as for the ECMWF data. In the SH the vertical component has an annual cycle of the sense to drive $\overline{v}^*$ and is partially cancelled by the horizontal component, as for the ECMWF data, giving a small annual cycle of the sense to drive $\overline{v}^*$. For both the latitude bands this gives a small residual semi-annual cycle in the total $\nabla.\mathbf{F}$ but 16.3° has a stronger annual cycle of the sense to drive $\overline{v}^*$.

For both data sets both the northern and southern hemispheres are important, the horizontal component of $\nabla.\mathbf{F}$ being important for driving $\overline{v}^*$ in the NH and the vertical component in the SH.

The EP flux divergence was then decomposed into the contributing eddy terms

of the horizontal and vertical components for both data sets and into the stationary and transient components of those eddy terms for the ECMWF data set.

In the ECMWF data it was seen that the annual cycle in $\nabla.\mathbf{F}$ is due to the stationary components of the waves. The transient components, for both 10 day and 30.5 day meaning periods, have little contribution. Variations on seasonal timescales could include those due to wave driving from the stratosphere or wave breaking from the troposphere such as from the monsoon. It was shown in sections 3.4.1 and 6.3.1 that at 90 hPa it was wave breaking in situ, aligned with tropospheric process and not stratospheric process, which dominated. However, on subseasonal timescales rather than the annual cycle we are considering here, the stratosphere can be important because the transient response can reach further into the tropics (Holton *et al.*, 1995; Plumb and Eluskiewicz, 1999).

In the NH the main contribution to the annual cycle in $\nabla.\mathbf{F}$ is from the vertical eddy momentum flux, $\omega'u'$, with a smaller contribution from the horizontal eddy momentum flux, $v'u'$, and some opposition to the annual cycle from the eddy heat flux, $v'\theta'$, from the vertical component of $\nabla.\mathbf{F}$. In the SH the main contribution to the annual cycle is from the eddy heat flux, $v'\theta'$, with some contribution from the vertical eddy momentum flux, $\omega'u'$, and opposition from the horizontal eddy momentum flux, $v'u'$. The NH dominates so that in the total $\nabla.\mathbf{F}$ the main contribution to the annual cycle is also from the vertical eddy momentum flux, $\omega'u'$, with a smaller contribution from the horizontal eddy momentum flux, $v'u'$, and some opposition to the annual cycle from the eddy heat flux, $v'\theta'$.

Planetary wave activity is known to be different between the NH and SH. These waves are generated from zonal asymmetries of topography and diabatic heating and the topography in the two hemispheres is very different (Iwasaki, 1992). He suggested that this difference might cause the seasonal variation in tropical upwelling and temperatures. Rosenlof (1995) showed that the seasonal cycle in tropical lower stratospheric mass flux was due to the northern hemisphere, suggesting that asymmetries of momentum deposition by planetary waves in the stratosphere between the two hemispheres could drive the seasonal cycle in tropical upwelling.

Randel *et al.* (2002) estimate tropical upwelling from the zonal mean momentum budget in a similar manner to that described in section 3.4. They use UKMO analyses and do not include an extra term, X, to represent unresolved forces. They consider mean ascent over latitude bands $\pm 20°$ and $\pm 30°$, wider bands than examined in this thesis. They compare results with vertical velocities

calculated from a radiative heating calculation. The annual cycle in ascent rates for $\pm 30°$ agrees reasonably well between the two methods of calculation, however for $\pm 20°$ the annual cycle in the vertical velocities calculated from heating rates is significantly smaller than that calculated from the momentum balance. They put this difference down to uncertainties in radiative heating rates, EP flux divergence and neglect of X.

Randel *et al.* (2002) do not examine the contributions to the momentum balance from different levels, they only consider a vertical integral up to the top of the analysis domain. In their introduction they imply that "the large-scale stratospheric circulation exerts a strong influence on the tropical lower stratosphere". However they do not demonstrate this for the annual cycle. There are no published works which examines the vertical contributions to tropical upwelling as has been performed in this thesis.

One finding of Randel *et al.* (2002) (which this thesis also finds) is that the time tendency term, $\frac{\partial \overline{u}}{\partial t}$, contributes to the annual cycle during June and July. They attribute this to the Northern hemisphere summer monsoon circulation. Therefore they already suggest the monsoon is important in driving the annual cycle in the tropical lower stratosphere. This thesis makes this case even stronger by indicating the monsoon is also important in the wave driving.

The numerical experiments of Plumb and Eluskiewicz (1999) indicate that to get mean ascent in the tropics the wave driving must be close to the equator, e.g. near 12°. This is difficult to achieve with breaking extratropical planetary waves. Boehm and Lee (2003) examine the possibility that Rossby waves forced by tropical convection could provide the wave drag. They examine the distribution of eddy momentum flux convergence in NCEP reanalysis, particularly near the top of tropical heating convection at 12–14 km. They suggest this could drive an upward circulation through the tropical transition layer and lower stratosphere ("upward control"), the return meridional flow being balanced by friction. However, in simple model experiments, this did not produce the observed annual cycle in tropical tropopause temperatures. The work in this thesis indicates that Rossby waves forced by tropical convection are important, but it is wave drag produced when the waves propagate vertically into the lower stratosphere (as illustrated by Dunkerton (1995)) that is key in driving the annual cycle.

Further understanding of the links between the heat-induced tropical circulations and their influence on tropical lower stratospheric temperatures could be gained by considering the solutions given by Gill (1980). In his study it was

shown that a tropical Rossby wave (which is akin to the upper-level monsoon anticyclones) is forced to the west of the heating region, while a Kelvin wave is forced to the east of the heating region. Both these waves could vertically propagate into the stratosphere where they could dissipate to give wave driving and vertical ascent. It is likely that the generation of these equatorial waves is stronger when the heating is close to the equator compared to when it is displaced off the equator. This is what happens in the observed annual cycle of tropical heating, during Northern Hemisphere winter the heating is close to the equator, while in Northern Hemisphere summer the heating is displaced to 20°N (see Hoskins *et al.* (1989)).

The results of this thesis are not inconsistent with the results of Randel *et al.* (2002). Both studies indicate that variations in wave driving produces changes in tropical vertical ascent which creates an annual cycle in temperatures. Both studies show that the long radiative timescales at 70 hPa are responsible for the large annual cycle in temperatures at this level. However Randel *et al.* (2002) did not quantify what levels and waves produce the annual cycle in wave driving, this is examined in this thesis. Randel *et al.* (2002) also consider subseasonal variations in ascent rates and wave driving. The large scale stratospheric circulation driven by breaking extratropical planetary waves can reach deep into the tropics on these timescales because the transient response to changes in wave driving (e.g. from stratospheric warmings) has a much broader latitudinal extent (see Haynes *et al.* (1991)). This thesis only considered variations on the slower annual timescales.

7.5 Summary

To summarise, the answers to the questions asked in chapter 1 are:

What is driving the annual cycle in temperature?
Adiabatic heating and cooling is driving the rate of change of temperature in the thermodynamic equation. The diabatic heating responds to the change in temperature and opposes the adiabatic cooling.

The annual cycle in adiabatic heating and cooling is due to the annual cycle in vertical velocities, i.e. the rate of upwelling.

What is driving the annual cycle in the strength of the tropical upwelling?

From mass continuity the annual cycle in $\overline{v}^*$, or mass outflow, from the tropical latitude band 10°N to 10°S is driving the annual cycle in tropical upwelling.

In the ECMWF data the Eliassen-Palm flux divergence, or wave-driving, is driving the annual cycle in $\overline{v}^*$ in the zonal momentum equation. In the UM data the residual $\overline{X}$ is also important.

Where do the important wave dissipation regions lie?

In the mass continuity calculation the annual cycle in mass outflow at levels near 90 hPa dominates the driving of the upwelling, rather than remote, higher levels. Both the NH and SH are important for driving the annual cycle. The main contributions to the annual cycle from the horizontal and vertical components of the EP flux are due to different hemispheres.

The longitudes where there are monsoon circulations are important. The number, size and location of the monsoon circulations vary over the course of the year.

Which are the important waves?

The important waves for driving the annual cycle are Rossby planetary waves. These waves are stationary rather than transient. The horizontal wavenumbers of the waves are at least three.

From the results of this thesis a proposed mechanism for the driving of the annual cycle in temperature is:

The monsoon anticyclone circulations penetrate up into the tropical lower stratosphere where they dissipate, depositing wave momentum. Hence they produce a non-zero Eliassen-Palm flux divergence and a body force on the mean flow. The body force is balanced by meridional motion which produces net outflow from the 10°N to 10°S tropical latitude band. By mass continuity this drives a net vertical motion.

In December there are monsoon circulations over northern Australia, Africa and central America which produce anticyclones which are symmetric about the equator. In August the tropical circulation is dominated by the Asian monsoon, which is displaced well off the equator. Hence there is a strong annual cycle, at 10°N and 10°S, in EP flux divergence and this produces an annual cycle in tropical

vertical ascent. This causes an annual cycle in adiabatic heating and cooling and hence in the zonal mean temperatures.

The monsoon anticyclone circulations in the Unified Model are less well confined to the equator. Therefore the non-zero EP flux divergence due to wave dissipation from these circulations is less well confined to the equator, affecting the annual cycle in wave-driving.

Chapter 8

Further work

This chapter lists possible extensions to this research and suggestions for further areas that could be investigated.

8.1 Analysis of UM data

Fewer parts of the research were able to be done with the UM data than with the ECMWF data. This was due in part to limitations on time and computer resources. It would be interesting to do the investigation into the contributions from the stationary and transient components of the eddy terms, as discussed in section 4.4.3 for the ECMWF data, with the UM data. It would also be interesting to consider the longitudinal variations in these eddy fluxes as done in section 4.4.4 for the ECMWF data. To do this would require re-running the model to obtain the diagnostics θ, u, v and ω in all three space dimensions as well as the time dimension. Previously these diagnostics had only been obtained in the zonal mean to save disk space. Significant amounts of time would be required to produce and process this data and significant amounts of hard disk space would be required to store and process this data. It would be useful to investigate further the errors in the modelling of the monsoon circulations and in tropical tropopause temperatures.

8.2 Analysis of ERA 40 data

The ECMWF data used has a relatively low top level, at 10 hPa and a coarse stratosphere compared with state of the art models. This means that data in the top levels is less accurate. The higher resolution ERA 40 dataset has recently become available, but too late for the research presented here. ERA 40 has a lid

at 0.1 hPa and 60 model levels in the vertical compared with the 31 of ERA 15. Of these additional levels, 19 are above 90 hPa. However, there are no longer model levels at 70 hPa and 90 hPa, the nearest levels are at 67, 80 and 96 hPa. The horizontal spectral resolution is also improved, at TL159 compared with T106, although the Gaussian grid resolution is the same. ERA 40 also extends over a longer time period, from September 1957 to August 2002. It would be interesting to repeat some of the research using this improved dataset. The integration of the mass continuity would be especially interesting to repeat to see if the semi-annual behaviour at 10 hPa and the opposite sign forcing at 30 hPa are retained.

8.3 Investigation of other levels

Although during the course of this research levels other than 90 hPa were looked at, there was not time to study them in as great a detail as the 90 hPa level. It would be interesting to do a more thorough investigation of the levels adjacent to 90 hPa to see how the results compared to those presented here. This could expand on the investigation of 70 hPa presented here as well as investigate what is happening at 110 and 50 hPa for each data set. Processed data is available to do an identical investigation, although additional disk space and several weeks' processing time would be required for parts of the investigation. Use of the ERA 40 data here would enabled detailed investigation of the behaviour with finer vertical resolution.

8.4 Investigation of eddy flux terms

It would be informative to investigate the eddy flux terms in more detail. In this research we have learnt that the terms $\omega' u'$ and $v'\theta'$ are not unimportant in the tropics but contribute to the annual cycle in the EP flux divergence. However they are noisy. Using a simplified model with idealised forcing to investigate them would be useful. Forcing a model of the non-linear Gill solution with idealised heating based on the observations and then calculating the resulting eddy flux terms might help with further understanding.

8.5 Interannual variability

In this research only the annual cycle has been considered. Other timescales of variation would be interesting to consider. Specifically, it would be interesting to investigate potential links between interannual variations in wave-driving and interannual variations in tropical tropopause temperatures.

Reid and Gage (1985) studied interannual variations in tropical tropopause heights from radiosonde data. They noted a pronounced quasi-periodicity of similar period to the stratospheric quasi-biennial oscillation. They noted a link with the El Niño Southern Oscillation (ENSO) 3-5 year cycle. Gage and Reid (1987) looked at longitudinal variations in tropopause heights and temperatures, noting a quasi-biennial cycle in temperature. They also noted a difference in longitudinal behaviour of tropopause temperature during El Niño years than during non-El Niño years. The interannual variability of monsoons has been studied extensively because many agrarian societies are totally dependent on the rainfall during a monsoon season. Quasi-biennial, ENSO and interdecadal timescales have been noted in monsoon variability (Webster *et al.*, 1998). Kiladis (1998) noted substantial interannual variability of wave activity, linking it with southern oscillations and the Madden-Julian oscillation.

One timescale which would be particularly interesting to study would be the approximately two yearly or biennial timescale.

The stratospheric quasi-biennial oscillation (QBO) is a 26-28 month oscillation in equatorial zonal winds and temperature. It is known to affect the stratospheric circulation and temperature. The stratospheric QBO in temperature has an amplitude of about ± 0.5 K at 100 hPa, which is small compared with the ± 4 K annual cycle. The QBO also interacts with the annual cycle in the tropics, although this interaction is not entirely understood (Gray and Dunkerton, 1990). There is also a biennial periodicity in tropical circulations, especially the monsoon circulations (Webster *et al.*, 1998). This biennial oscillation is not correlated to the stratospheric QBO; and it is irregular in time, asymmetric in longitude and propagates slowly eastward, unlike the stratospheric QBO (Baldwin *et al.*, 2001). There are two possible different tropospheric quasi-biennial oscillations; a biennial component of the ENSO and a biennial component of the interannual variation of the Asian summer monsoon (Meehl, 1997; Baldwin *et al.*, 2001). Giorgetta *et al.* (1999) suggest that the QBO modifies the tropospheric circulation, via the tropical tropopause temperatures, including sea surface temperatures and the monsoon. These various biennial oscillations may affect the wave-driving and

therefore upwelling and temperature seen in the tropical tropopause region and it would be interesting to study this by examining the balance of terms in the TEM equations.

Another possibly timescale to study, perhaps in conjunction with the quasi-biennial timescale, would be that of ENSO. The El Niño is a warming of Pacific ocean surface temperatures which occurs on a 3–5 year timescale. This is accompanied by a change in pressure between the western and eastern Pacific oceans, known as the ENSO. ENSO changes the pattern in tropical convection and circulation (Salby, 1996). It affects the monsoon circulations and monsoon precipitation (Zahn, 2003) and there is a clear multi-year ENSO variability in the monsoon. Gray *et al.* (1992) also suggest the stratospheric QBO influences ENSO. This would be especially good to study using the longer ERA 40 dataset, which encompasses more ENSO cycles.

There is however insufficient data to look at longer timescales, such as the 11 year cycle seen in tropopause heights (Reid and Gage, 1985) or the interdecadal variability in the monsoon (Webster *et al.*, 1998).

Appendix A

List of Symbols

a	"a" coefficient for calculation of pressure of model levels (UM)
A	Mean quadratic function of wave transience
$\overline{A}$	Perturbation of the zonal momentum equation due to the analysis scheme
b	"b" coefficient for calculation of pressure of model levels (UM)
c_p	Specific heat capacity at constant pressure
c_v	Specific heat capacity at constant temperature
D	Mean quadratic function of frictional and diabatic disturbances
$\mathbf{E}$	Vector based on the Eliassen-Palm Flux, $\mathbf{F}$, but calculated from non-zonally averaged eddy terms, see equation 4.5
f	Coriolis parameter, $F = 2\Omega \sin \phi$
$\mathbf{F}$	Eliassen-Palm Flux, see equation 2.10
F_q	Source and sink term of water vapour (UM)
F_u	Source and sink term of zonal momentum (UM)
F_v	Source and sink term of meridional momentum (UM)
F_θ	Source and sink term of heat (UM)
g	Magnitude of acceleration due to gravity of the Earth
g_0	Global average of gravity at mean sea level ($9.80665\,\mathrm{m\,s^{-1}}$)
G	Departure from gradient wind balance, see equation 2.12
H	Scale height, $H = RT_s/g_0$ (7 km for $T_s \approx 240\,\mathrm{K}$ for the middle atmosphere)
L_c	Latent heat of condensation (UM)
L_f	Latent heat of fusion (UM)
p	Pressure
p_s	Constant reference pressure (1000 hPa)

p_1	Reference pressure (UM)
p_*	Surface pressure (UM)
q	Atmospheric specific humidity (UM)
q_T	Total water content (UM)
$q_c^{(L)}$	Cloud liquid water content (UM)
$q_c^{(F)}$	Ice liquid water content (UM)
Q	Diabatic heating
$\overline{Q}_{LW}$	Contribution to diabatic heating from longwave heating rates
$\overline{Q}_{SW}$	Contribution to diabatic heating from shortwave heating rates
$\overline{Q}_{\text{Residual}}$	Residual contribution to diabatic heating
r_s	Pseudo-radius (UM), see equation 5.2
R	Gas constant for dry air ($287\,\text{J}\,\text{K}^{-1}\,\text{kg}^{-1}$)
R_e	Radius of the Earth (6.371×10^6m)
t	Time
T	Temperature
T_r	Temperature reference profile (UM)
T_s	Constant reference temperature (240 K for the middle atmosphere)
T_v	Virtual temperature (UM), see equation 5.9
u	Zonal component of velocity
v	Meridional component of velocity
$\overline{v}^*$	Residual mean meridional velocity, see equation 2.8
$\overline{w}^*$	Residual mean vertical velocity (log-pressure coordinates), see equation 2.8
$\tilde{w}$	Vertical velocity (UM), see equation 5.3
X	Zonal component of non-conservative mechanical forcing
$\overline{X}_{GWD}$	Contribution to X from gravity wave drag
$\overline{X}_{\text{Residual}}$	Residual contribution to X
Y	Meridional component of non-conservative mechanical forcing
z	Log-pressure vertical coordinate, see equation 2.1

α	Wave amplitude
ϵ	Ratio of the molecular weight of water to the molecular weight of dry air (UM)
$\overline{\zeta}_a$	Absolute vorticity, see equation 3.10
η	Vertical coordinate (UM)
θ	Potential temperature
θ_L	Liquid water potential temperature (UM)
κ	$(c_p - c_v)/c_p$ (UM)
λ	Longitude
μ	(UM) see equation 5.6
Π	Exner function $\left(\frac{p}{100000}\right)^{\kappa}$ (UM)
ρ	Atmospheric density profile
τ	Wave stress due to gravity waves
ϕ	Latitude
Φ	Geopotential, $\Phi = gz$
χ	Velocity potential
ψ	Stream function
ω	Vertical component of velocity
$\overline{\omega}^*$	Residual mean vertical velocity, see equation 2.8
Ω	Rotation rate of the Earth ($7.292\times10^{-5}\mathrm{s}^{-1}$)
$\nabla.\mathbf{F}$	Eliassen-Palm flux divergence, see equation 2.11
$\nabla.\mathbf{F}^{(\phi)}$	Normalised horizontal component of Eliassen-Palm flux divergence
$\nabla.\mathbf{F}^{(p)}$	Normalised vertical component of Eliassen-Palm flux divergence
$v'u'$	Eddy momentum flux, the poleward flux of zonal momentum
$v'\theta'$	Eddy heat flux, the poleward flux of potential temperature
$\omega'u'$	Vertical flux of zonal momentum
$\omega'\theta'$	Vertical flux of potential temperature
$-\overline{\omega}^*\frac{\partial\overline{\theta}}{\partial p}$	Adiabatic heating and cooling

Appendix B

Second order differencing for first order derivatives for unequally spaced points.

B.1 Centred difference

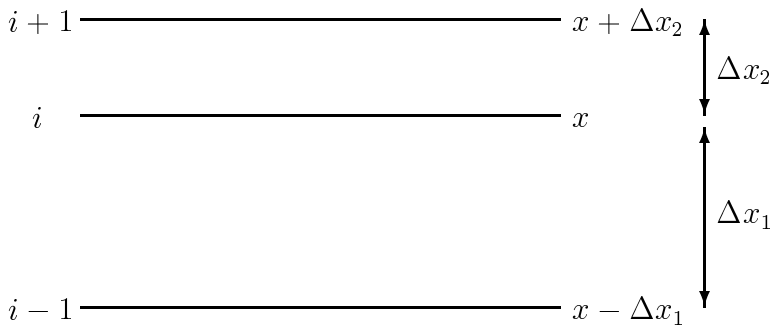

Figure B.1: Levels diagram for centred difference.

Take Taylor Series Expansions of $y(x+\Delta x_2)$ and $y(x-\Delta x_1)$:

$$\begin{aligned} y(x+\Delta x_2) &= y(x) + \frac{y'(x)\left[(x+\Delta x_2)-x\right]}{1!} + \frac{y''(x)\left[(x+\Delta x_2)-x\right]^2}{2!} + \cdots \\ &= y(x) + \Delta x_2 y'(x) + \frac{\Delta x_2^2 y''(x)}{2} + \cdots \end{aligned} \tag{B.1}$$

$$\begin{aligned} y(x-\Delta x_1) &= y(x) + \frac{y'(x)\left[(x-\Delta x_1)-x\right]}{1!} + \frac{y''(x)\left[(x-\Delta x_1)-x\right]^2}{2!} + \cdots \\ &= y(x) - \Delta x_1 y'(x) + \frac{\Delta x_1^2 y''(x)}{2} + \cdots \end{aligned} \tag{B.2}$$

Find (B.1)$\times\Delta x_1^2$:

$$\Delta x_1^2 y(x+\Delta x_2) = \Delta x_1^2 y(x) + \Delta x_1 (\Delta x_1 \Delta x_2) y'(x) + \frac{(\Delta x_1 \Delta x_2)^2}{2} y''(x) + \cdots \tag{B.3}$$

Find (B.2)$\times\Delta x_2^2$:

$$\Delta x_2^2 y(x-\Delta x_1) = \Delta x_2^2 y(x) - \Delta x_2 (\Delta x_1 \Delta x_2) y'(x) + \frac{(\Delta x_1 \Delta x_2)^2}{2} y''(x) + \cdots \tag{B.4}$$

Take (B.3)$-$(B.4), neglecting high order terms:

$$\begin{aligned} &\Delta x_1^2 y(x+\Delta x_2) - \Delta x_2^2 y(x-\Delta x_1) \\ &\qquad \approx \left(\Delta x_1^2 - \Delta x_2^2\right) y(x) + (\Delta x_1 + \Delta x_2)(\Delta x_1 \Delta x_2) y'(x) \end{aligned}$$

Rearrange for $y'(x)$:

$$y'(x) \approx \frac{\Delta x_1^2\, y(x+\Delta x_2) - \Delta x_2^2\, y(x-\Delta x_1) - \left(\Delta x_1^2 - \Delta x_2^2\right) y(x)}{(\Delta x_1 + \Delta x_2)(\Delta x_1 \Delta x_2)}. \tag{B.5}$$

Substitute $x = x_n$, $\Delta x_1 = x_n - x_{n-1}$, $\Delta x_2 = x_{n+1} - x_n$, $y(x) = y_n$, $y(x + \Delta x_2) = y_{n+1}$ and $y(x - \Delta x_1) = y_{n-1}$ into equation B.5:

$$\begin{aligned} y'(x_n) &\approx \frac{(x_n - x_{n-1})^2 y_{n+1} - (x_{n+1} - x_n)^2 y_{n-1} - \left[(x_n - x_{n-1})^2 - (x_{n+1} - x_n)^2\right] y_n}{\left[(x_n - x_{n-1}) + (x_{n+1} - x_n)\right](x_n - x_{n-1})(x_{n+1} - x_n)} \\ &\approx \frac{(x_n - x_{n-1})}{(x_{n+1} - x_{n-1})(x_{n+1} - x_n)} y_{n+1} - \frac{(x_{n+1} - x_n)}{(x_{n+1} - x_{n-1})(x_n - x_{n-1})} y_{n-1} \\ &\quad - \frac{(x_n - x_{n-1})}{(x_{n+1} - x_{n-1})(x_{n+1} - x_n)} y_n + \frac{(x_{n+1} - x_n)}{(x_{n+1} - x_{n-1})(x_n - x_{n-1})} y_n \\ &\approx \frac{(x_n - x_{n-1})(y_{n+1} - y_n)}{(x_{n+1} - x_n)(x_{n+1} - x_{n-1})} - \frac{(x_{n+1} - x_n)(y_{n-1} - y_n)}{(x_n - x_{n-1})(x_{n+1} - x_{n-1})}. \end{aligned} \tag{B.6}$$

B.2 Forward difference

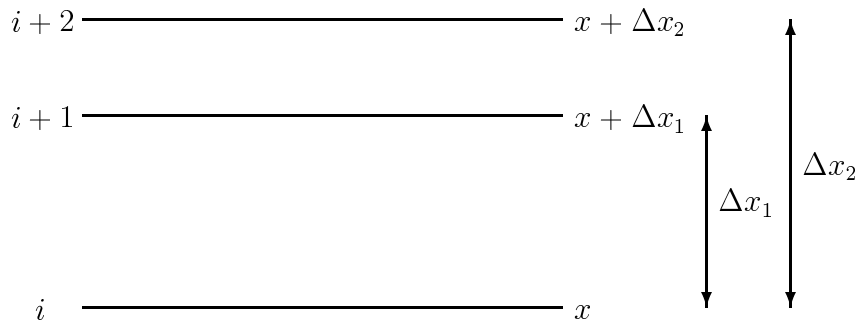

Figure B.2: Levels diagram for forward difference.

Take Taylor Series Expansions of $y(x + \Delta x_1)$ and $y(x + \Delta x_2)$:

$$\begin{aligned} y(x + \Delta x_1) &= y(x) + \frac{y'(x)\left[(x + \Delta x_1) - x\right]}{1!} + \frac{y''(x)\left[(x + \Delta x_1) - x\right]^2}{2!} + \cdots \\ &= y(x) + \Delta x_1 y'(x) + \frac{\Delta x_1^2 y''(x)}{2} + \cdots \end{aligned} \tag{B.7}$$

$$\begin{aligned} y(x + \Delta x_2) &= y(x) + \frac{y'(x)\left[(x + \Delta x_2) - x\right]}{1!} + \frac{y''(x)\left[(x + \Delta x_2) - x\right]^2}{2!} + \cdots \\ &= y(x) + \Delta x_2 y'(x) + \frac{\Delta x_2^2 y''(x)}{2} + \cdots \end{aligned} \tag{B.8}$$

Find (B.7)$\times\Delta x_2^2$:

$$\Delta x_2^2 y\left(x+\Delta x_1\right)=\Delta x_2^2 y\left(x\right)+\Delta x_2\left(\Delta x_1\Delta x_2\right)y'\left(x\right)+\frac{\left(\Delta x_1\Delta x_2\right)^2}{2}y''\left(x\right)+\cdots \tag{B.9}$$

Find (B.8)$\times\Delta x_1^2$:

$$\Delta x_1^2 y(x+\Delta x_2)=\Delta x_1^2 y(x)+\Delta x_1\left(\Delta x_1\Delta x_2\right)y'\left(x\right)+\frac{\left(\Delta x_1\Delta x_2\right)^2}{2}y''\left(x\right)+\cdots \tag{B.10}$$

Take (B.9)−(B.10), neglecting high order terms:

$$\begin{aligned}&\Delta x_2^2 y\left(x+\Delta x_1\right)-\Delta x_1^2 y\left(x+\Delta x_2\right)\\&\qquad\approx\left(\Delta x_2^2-\Delta x_1^2\right)y\left(x\right)+\left(\Delta x_2-\Delta x_1\right)\left(\Delta x_1\Delta x_2\right)y'\left(x\right).\end{aligned}$$

Rearrange for $y'\left(x\right)$:

$$y'\left(x\right)\approx\frac{\Delta x_2^2\,y\left(x+\Delta x_1\right)-\Delta x_1^2\,y\left(x+\Delta x_2\right)-\left(\Delta x_2^2-\Delta x_1^2\right)y\left(x\right)}{\left(\Delta x_2-\Delta x_1\right)\left(\Delta x_1\Delta x_2\right)}. \tag{B.11}$$

Substitute $x=x_n$, $\Delta x_1=x_{n+1}-x_n$, $\Delta x_2=x_{n+2}-x_n$, $y\left(x\right)=y_n$, $y\left(x+\Delta x_2\right)=y_{n+2}$ and $y\left(x+\Delta x_1\right)=y_{n+1}$ into equation B.5:

$$\begin{aligned}y'\left(x_n\right)&\approx\frac{\left(x_{n+2}-x_n\right)^2 y_{n+1}-\left(x_{n+1}-x_n\right)^2 y_{n+2}-\left[\left(x_{n+2}-x_n\right)^2-\left(x_{n+1}-x_n\right)^2\right]y_n}{\left[\left(x_{n+2}-x_n\right)-\left(x_{n+1}-x_n\right)\right]\left(x_{n+1}-x_n\right)\left(x_{n+2}-x_n\right)}\\&\approx\frac{\left(x_{n+2}-x_n\right)}{\left(x_{n+2}-x_{n+1}\right)\left(x_{n+1}-x_n\right)}y_{n+1}-\frac{\left(x_{n+1}-x_n\right)}{\left(x_{n+2}-x_{n+1}\right)\left(x_{n+2}-x_n\right)}y_{n+2}\\&\quad-\frac{\left(x_{n+2}-x_n\right)}{\left(x_{n+2}-x_{n+1}\right)\left(x_{n+1}-x_n\right)}y_n+\frac{\left(x_{n+1}-x_n\right)}{\left(x_{n+2}-x_{n+1}\right)\left(x_{n+2}-x_n\right)}y_n\\&\approx\frac{\left(x_{n+2}-x_n\right)\left(y_{n+1}-y_n\right)}{\left(x_{n+1}-x_n\right)\left(x_{n+2}-x_{n+1}\right)}-\frac{\left(x_{n+1}-x_n\right)\left(y_{n+2}-y_n\right)}{\left(x_{n+2}-x_n\right)\left(x_{n+2}-x_{n+1}\right)}.\end{aligned} \tag{B.12}$$

B.3 Backward difference

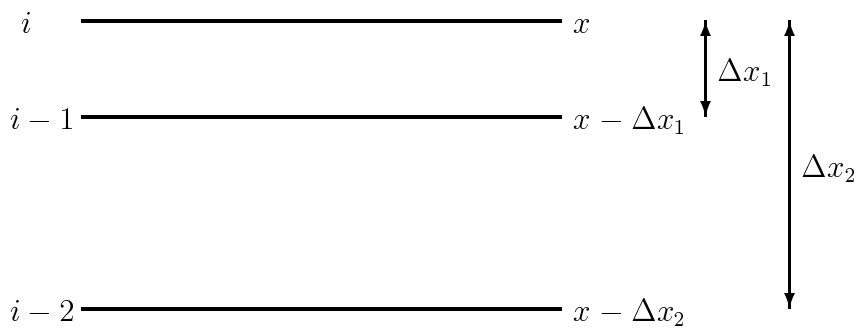

Figure B.3: Levels diagram for backward difference.

Take Taylor Series Expansions of $y(x-\Delta x_1)$ and $y(x-\Delta x_2)$:

$$\begin{aligned} y(x-\Delta x_1) &= y(x) + \frac{y'(x)\left[(x-\Delta x_1)-x\right]}{1!} + \frac{y''(x)\left[(x-\Delta x_1)-x\right]^2}{2!} + \cdots \\ &= y(x) - \Delta x_1 y'(x) + \frac{\Delta x_1^2 y''(x)}{2} + \cdots \end{aligned} \tag{B.13}$$

$$\begin{aligned} y(x-\Delta x_2) &= y(x) + \frac{y'(x)\left[(x-\Delta x_2)-x\right]}{1!} + \frac{y''(x)\left[(x-\Delta x_2)-x\right]^2}{2!} + \cdots \\ &= y(x) - \Delta x_2 y'(x) + \frac{\Delta x_2^2 y''(x)}{2} + \cdots \end{aligned} \tag{B.14}$$

Find (B.13)$\times\Delta x_2^2$:

$$\Delta x_2^2 y(x-\Delta x_1) = \Delta x_2^2 y(x) - \Delta x_2 (\Delta x_1 \Delta x_2) y'(x) + \frac{(\Delta x_1 \Delta x_2)^2}{2} y''(x) + \cdots \tag{B.15}$$

Find (B.14)$\times\Delta x_1^2$:

$$\Delta x_1^2 y(x-\Delta x_2) = \Delta x_1^2 y(x) - \Delta x_1 (\Delta x_1 \Delta x_2) y'(x) + \frac{(\Delta x_1 \Delta x_2)^2}{2} y''(x) + \cdots \tag{B.16}$$

Take (B.15)−(B.16), neglecting high order terms:

$$\begin{aligned}\Delta x_2^2 y\left(x-\Delta x_1\right)-\Delta x_1^2 y\left(x-\Delta x_2\right)&\\ \approx\left(\Delta x_2^2-\Delta x_1^2\right) y\left(x\right)-\left(\Delta x_2-\Delta x_1\right)\left(\Delta x_1 \Delta x_2\right) y'\left(x\right).&\end{aligned}$$

Rearrange for $y'\left(x\right)$:

$$y'\left(x\right) \approx \frac{\Delta x_2^2\, y\left(x-\Delta x_1\right)-\Delta x_1^2\, y\left(x-\Delta x_2\right)-\left(\Delta x_2^2-\Delta x_1^2\right) y\left(x\right)}{\left(\Delta x_1-\Delta x_2\right)\left(\Delta x_1 \Delta x_2\right)}. \tag{B.17}$$

Substitute $x=x_n$, $\Delta x_1=x_n-x_{n-1}$, $\Delta x_2=x_n-x_{n-2}$, $y\left(x\right)=y_n$, $y\left(x-\Delta x_2\right)=y_{n-2}$ and $y\left(x-\Delta x_1\right)=y_{n-1}$ into equation B.5:

$$\begin{aligned}y'\left(x_n\right) &\approx \frac{\left(x_n-x_{n-2}\right)^2 y_{n-1}-\left(x_n-x_{n-1}\right)^2 y_{n-2}-\left[\left(x_n-x_{n-2}\right)^2-\left(x_n-x_{n-1}\right)^2\right] y_n}{\left[\left(x_n-x_{n-1}\right)-\left(x_n-x_{n-2}\right)\right]\left(x_n-x_{n-1}\right)\left(x_n-x_{n-2}\right)}\\ &\approx \frac{\left(x_n-x_{n-2}\right)}{\left(x_{n-2}-x_{n-1}\right)\left(x_n-x_{n-1}\right)} y_{n-1}-\frac{\left(x_n-x_{n-1}\right)}{\left(x_{n-2}-x_{n-1}\right)\left(x_n-x_{n-2}\right)} y_{n-2}\\ &\quad-\frac{\left(x_n-x_{n-2}\right)}{\left(x_{n-2}-x_{n-1}\right)\left(x_n-x_{n-1}\right)} y_n+\frac{\left(x_n-x_{n-1}\right)}{\left(x_{n-2}-x_{n-1}\right)\left(x_n-x_{n-2}\right)} y_n\\ &\approx \frac{\left(x_n-x_{n-2}\right)\left(y_{n-1}-y_n\right)}{\left(x_n-x_{n-1}\right)\left(x_{n-2}-x_{n-1}\right)}-\frac{\left(x_n-x_{n-1}\right)\left(y_{n-2}-y_n\right)}{\left(x_n-x_{n-2}\right)\left(x_{n-2}-x_{n-1}\right)}.\end{aligned} \tag{B.18}$$

Appendix C

Decomposition of eddy terms into stationary and transient components

Recall equation 2.26, page 39:

$$\begin{aligned}\langle v'u' \rangle &= \langle (v - \overline{v})\,(u - \overline{u}) \rangle \\ &= \langle v' \rangle \langle u' \rangle + \langle v'^{*} u'^{*} \rangle \,. \end{aligned} \tag{C.1}$$

First, consider the left hand side of equation C.1 and expand $v'u'$:

$$\begin{aligned} v'u' &= (v - \overline{v})\,(u - \overline{u}) \\ &= vu - \overline{v}u - v\overline{u} + \overline{vu}. \end{aligned} \tag{C.2}$$

Take the time mean of $v'u'$, noting that $\langle a + b \rangle = \langle a \rangle + \langle b \rangle$:

$$\begin{aligned}\langle v'u' \rangle &= \langle (v - \overline{v})\,(u - \overline{u}) \rangle \\ &= \langle vu \rangle - \langle \overline{v}u \rangle - \langle v\overline{u} \rangle + \langle \overline{vu} \rangle \,. \end{aligned} \tag{C.3}$$

Now consider the first term on the right hand side of equation C.1 and expand it into its constituent terms:

$$\begin{aligned}\langle v' \rangle \langle u' \rangle &= \langle v - \overline{v} \rangle \langle u - \overline{u} \rangle \\ &= (\langle v \rangle - \langle \overline{v} \rangle)(\langle u \rangle - \langle \overline{u} \rangle) \\ &= \langle v \rangle \langle u \rangle - \langle \overline{v} \rangle \langle u \rangle - \langle v \rangle \langle \overline{u} \rangle + \langle \overline{v} \rangle \langle \overline{u} \rangle . \end{aligned} \tag{C.4}$$

Now consider the second term on the right hand side of equation C.1. Expand v'^* into its constituent terms:

$$\begin{aligned} v'^* &= v - \overline{v} - \langle v - \overline{v} \rangle \\ &= v - \overline{v} - \langle v \rangle + \langle \overline{v} \rangle \end{aligned} \tag{C.5}$$

and there is a similar result for u'^*.
Now expand $v'^* u'^*$ into its constituent terms:

$$v'^* u'^* = (v - \overline{v} - \langle v \rangle + \langle \overline{v} \rangle)(u - \overline{u} - \langle u \rangle + \langle \overline{u} \rangle) \tag{C.6}$$

$$\begin{aligned} &= vu - v\overline{u} - v \langle u \rangle + v \langle \overline{u} \rangle \\ &- \overline{v}u + \overline{vu} + \overline{v} \langle u \rangle - \overline{v} \langle \overline{u} \rangle \\ &- \langle v \rangle u + \langle v \rangle \overline{u} + \langle v \rangle \langle u \rangle - \langle v \rangle \langle \overline{u} \rangle \\ &+ \langle \overline{v} \rangle u - \langle \overline{v} \rangle \overline{u} - \langle \overline{v} \rangle \langle u \rangle + \langle \overline{v} \rangle \langle \overline{u} \rangle . \end{aligned} \tag{C.7}$$

Take the time mean of $v'^* u'^*$, noting that $\overline{a\bar{b}} = \bar{a}\bar{b}$ and $\langle a \langle b \rangle \rangle = \langle a \rangle \langle b \rangle$:

$$\begin{aligned}
\langle v'^* u'^* \rangle &= \langle vu \rangle - \langle v\overline{u} \rangle - \langle v \langle u \rangle \rangle + \langle v \langle \overline{u} \rangle \rangle \\
&\quad - \langle \overline{v}u \rangle + \langle \overline{vu} \rangle + \langle \overline{v} \langle u \rangle \rangle - \langle \overline{v} \langle \overline{u} \rangle \rangle \\
&\quad - \langle \langle v \rangle u \rangle + \langle \langle v \rangle \overline{u} \rangle + \langle \langle v \rangle \langle u \rangle \rangle - \langle \langle v \rangle \langle \overline{u} \rangle \rangle \\
&\quad + \langle \langle \overline{v} \rangle u \rangle - \langle \langle \overline{v} \rangle \overline{u} \rangle - \langle \langle \overline{v} \rangle \langle u \rangle \rangle + \langle \langle \overline{v} \rangle \langle \overline{u} \rangle \rangle \\
&= \langle vu \rangle - \langle v\overline{u} \rangle - \langle v \rangle \langle u \rangle + \langle v \rangle \langle \overline{u} \rangle \\
&\quad - \langle \overline{v}u \rangle + \langle \overline{vu} \rangle + \langle \overline{v} \rangle \langle u \rangle - \langle \overline{v} \rangle \langle \overline{u} \rangle \\
&\quad - \langle v \rangle \langle u \rangle + \langle v \rangle \langle \overline{u} \rangle + \langle v \rangle \langle u \rangle - \langle v \rangle \langle \overline{u} \rangle \\
&\quad + \langle \overline{v} \rangle \langle u \rangle - \langle \overline{v} \rangle \langle \overline{u} \rangle - \langle \overline{v} \rangle \langle u \rangle + \langle \overline{v} \rangle \langle \overline{u} \rangle \\
&= \langle vu \rangle - \langle v\overline{u} \rangle - \langle \overline{v}u \rangle + \langle \overline{vu} \rangle \\
&\quad - \langle v \rangle \langle u \rangle + \langle v \rangle \langle \overline{u} \rangle + \langle \overline{v} \rangle \langle u \rangle - \langle \overline{v} \rangle \langle \overline{u} \rangle \,. \qquad \text{(C.8)}
\end{aligned}$$

Add the result for $\langle v' \rangle \langle u' \rangle$ from equation C.4 and for $\langle v'^* u'^* \rangle$ from equation C.8:

$$\begin{aligned}
\langle v' \rangle \langle u' \rangle + \langle v'^* u'^* \rangle &= \langle v \rangle \langle u \rangle - \langle \overline{v} \rangle \langle u \rangle - \langle v \rangle \langle \overline{u} \rangle + \langle \overline{v} \rangle \langle \overline{u} \rangle \\
&\quad + \langle vu \rangle - \langle v\overline{u} \rangle - \langle \overline{v}u \rangle + \langle \overline{vu} \rangle \\
&\quad - \langle v \rangle \langle u \rangle + \langle v \rangle \langle \overline{u} \rangle + \langle \overline{v} \rangle \langle u \rangle - \langle \overline{v} \rangle \langle \overline{u} \rangle \\
&= \langle vu \rangle - \langle \overline{v}u \rangle - \langle v\overline{u} \rangle + \langle \overline{vu} \rangle \,, \qquad \text{(C.9)}
\end{aligned}$$

comparing this to equation C.3

$$= \langle v'u' \rangle \,. \qquad \text{(C.10)}$$

Thus equation 2.26 holds.

Bibliography

AMIP UKMO documentation. *AMIP UKMO Unified Model Documentation*. `http://www-pcmdi.llnl.gov/modeldoc/amip2/ukmo_98a/index.html`.

Andrews, D. (1987). On the interpretation of the Eliassen–Palm flux divergence. *Q. J. R. Meteorol. Soc.*, **113**, 323–338.

Andrews, D. G. and McIntyre, M. E. (1978). Generalized Eliassen–Palm and Charney–Drazin theorems for waves on axisymmetric mean flows in compressible atmospheres. *J. Atmos. Sci.*, **35**, 175–185.

Andrews, D. G., Holton, J. R., and Leovy, C. B. (1987). *Middle Atmosphere Dynamics*, volume 40 of *International Geophysics Series*. Academic Press, Inc.

Baldwin, M. P., Gray, L. J., Dunkerton, T. J., Hamilton, K., Haynes, P. H., Randel, W. J., Holton, J. R., Alexander, M. J., Hirota, I., Horinouchi, T., Jones, D. B. A., Kinnersley, J. S., Marquardt, C., Sato, K., and Takahashi, M. (2001). The quasi-biennial oscillation. *Rev. of Geophys.*, **39**(2), 179–229.

Bethan, S., Vaughan, G., and Reid, S. J. (1996). A comparison of ozone and thermal tropopause heights and the impact of tropopause definition on quantifying the ozone content of the troposphere. *Q. J. R. Meteorol. Soc.*, **122**, 929–944.

Boehm, M. T. and Lee, S. (2003). The implications of tropical Rossby waves for tropical tropopause cirrus formation and for the equatorial upwelling of the Brewer-Dobson circulation. *J. Atmos. Sci.*, **60**, 247–261.

Bresser, G., Manning, A. J. L., Pawson, S., and Rodgers, C. D. (1995). A new parameterization of scale-dependent radiative rates in the stratosphere. *JAS*, **52**(24), 4429–4447.

Brewer, A. W. (1949). Evidence for a world circulation provided by the measurements of helium and water vapour distribution in the stratosphere. *Q. J. R. Meteorol. Soc.*, **75**, 351–363.

Callis, L. B., Boughner, R. E., and Lambeth, J. D. (1987). The stratosphere: climatologies of the radiative heating and cooling rates and the diabatically diagnosed net circulation fields. *J. Geophys. Res.*, **92**(D5), 5585–5607.

Clough, S. A. and Iacono, M. J. (1995). Line-by-line calculation of atmospheric fluxes and cooling rates 2. application to carbon dioxide, ozone, methane, nitrous oxide and the halocarbons. *JGR*, **100**(D8), 16519–16535.

Cole, H. P. (1975). An investigation of a possible relationship between the height of the low-latitude tropopause and the sunspot number. *J. Atmos. Sci.*, **32**, 998–1001.

Cullen, M. (1993). The unified forecast/climate model. *Meteorol. Mag*, **122**, 81–94.

Cullen, M. J. P., Davies, T., and Mawson, M. H. (1993). Conservative finite difference schemes for a unified forecast/climate model. Technical report, UK Meteorological Office. Crown Copyright.

Danielsen, E. F. (1968). Stratospheric-tropospheric exchange based on radioactivity, ozone and potential vorticity. *J. Atmos. Sci.*, **25**, 502–518.

Danielsen, E. F. (1982). A dehydration mechanism for the stratosphere. *Geophys. Res. Lett.*, **9**(6), 605–608.

Danielsen, E. F. (1993). In situ evidence of rapid, vertical, irreversible transport of lower tropospheric air into the lower tropical stratosphere by convective cloud turrets and by larger-scale upwelling in tropical cyclones. *J. Geophys. Res.*, **98**(D5), 8665–8681.

Dunkerton, T. J. (1995). Evidence of meridional motion in the summer lower stratosphere adjacent to monsoon regions. *J. Geophys. Res.*, **100**, 16675–16688.

ECMWF Analysis. *Operational analysis and forecasting system history*. `http://www.ecmwf.int/products/data/operational_system/index.html`.

ECMWF ERA-15. *ERA-15 Project Home Page*. `http://www.ecmwf.int/research/era/ERA-15/`.

Edmon Jr., H. J., Hoskins, B. J., and McIntyre, M. E. (1981). Eliassen-Palm cross sections for the troposphere. *J. Atmos. Sci.*, **37**, 2600–2616.

Eluszkiewicz, J., Crisp, D., Zurek, R., Elson, L., Fishbein, E., Froidevaux, L., Waters, J., Grainger, R. G., Lambert, A., Harwood, R., and Peckham, G. (1996). Residual circulation in the stratosphere and lower mesosphere as diagnosed from Microwave Limb Sounder data. *J. Atmos. Sci.*, **53**, 217–240.

Fels, S. B. (1982). A parametrization of scale-dependent radiative damping rates in the middle atmosphere. *JAS*, **39**, 1141–1152.

Forster, P., Freckleton, R., and Shine, K. (1997). On aspects of the concept of radiative forcing. *Climate Dynamics*, **13**, 547–560.

Frederick, J. E. and Douglass, A. R. (1983). Atmospheric temperatures near the tropical tropopause: temporal variations, zonal asymmetry and implications for stratospheric water vapour. *Mon. Wea. Rev.*, **111**, 1397–1403.

Gage, K. S. and Reid, G. C. (1987). Longitudinal variations in tropical tropopause properties in relation to tropical convection and El Niño-Southern Oscillation events. *J. Geophys. Res.*, **92**(C13), 14197–14203.

Gates, W. L. (1992). AMIP: the atmospheric model intercomparison project. *Bull. Amer. Meteor. Soc.*, **73**(12), 1962–1970.

Gates, W. L., Boyle, J. S., Covey, C., Dease, C. G., Doutriaux, C. M., Drach, R. S., Fiorino, M., Gleckler, P. J., Hnilo, J. J., Marlais, M. S., Phillips, T. J., Potter, G. L., Santer, B. D., Sperber, K. R., Taylor, K. E., and Williams, D. N. (1999). An overview of the results of the atmospheric model intercomparison project (AMIP I). *Bull. Amer. Meteor. Soc.*, **80**(1), 29–55.

Gettelman, A. and Forster, P. M. d. F. (2002). A climatology of the tropical tropopause layer. *J. Meteor. Soc. Japan*, **80**(4B), 911–924.

Gettelman, A., Salby, M. L., Randel, W. J., and Sassi, F. (2001). Convection in the Tropical Tropopause region and Stratosphere-Troposphere Exchange. In SPARC Newsletter 17, also available at `http://www.aero.jussieu.fr/~sparc/News17/17_Gettelman.html`.

Gettelman, A., Salby, M. L., and Sassi, F. (2002). Distribution and influence of convection in the tropical tropopause region. *J. Geophys. Res.*, **107**(D10), ACL 6–1–6–14.

Gibson, J. K., Kållberg, P., Uppala, S., Hernandex, A., Nomura, A., and Serrano, E. (1999). ECMWF re-analysis project report series: 1 ERA-15 description. Technical report, ECMWF, Reading, United Kingdom. Available at `http://www.ecmwf.int/research/era/ERA-15/Report_Series/`.

Gill, A. E. (1980). Some simple solutions for heat-induced tropical circulation. *Q. J. R. Meteorol. Soc.*, **106**, 447–462.

Gille, J. C., Lyjak, L. V., and Smith, A. K. (1987). The global residual mean circulation in the middle atmosphere for the northern winter period. *J. Atmos. Sci.*, **44**, 1437–1452.

Giorgetta, M. A., Bengtsson, L., and Arpe, K. (1999). An investigation of QBO signals in the east Asian and Indian monsoon in GCM experiments. *Climate Dynamics*, **15**, 435–450.

Gray, L. J. and Dunkerton, T. J. (1990). The role of the seasonal cycle in the quasi-biennial oscillation of ozone. *J. Atmos. Sci.*, **47**(20), 2429–2451.

Gray, W. M., Sheaffer, J. D., and Knaff, J. A. (1992). Influence of the stratospheric QBO on ENSO variability. *J. Meteor. Soc. Japan*, **70**(5), 975–995.

Gregory, D., Kershaw, R., and Inness, P. M. (1997). Parametrization of momentum transport by convection. II: tests in single-column and general circulation models. *Q. J. R. Meteorol. Soc.*, **123**(541), 1153–1183.

Gregory, D., Shutts, G. J., and Mitchell, J. (1998). A new gravity-wave-drag scheme incorporating anisotropic orography and low-level wave breaking: impact upon the climate of the UK Meteorological Office Unified Model. *Q. J. R. Meteorol. Soc.*, **124**, 463–494.

Hartmann, D. L., Holton, J. R., and Fu, Q. (2001). The heat balance of the tropical tropopause, cirrus, and stratospheric dehydration. *Geophys. Res. Lett.*, **28**(10), 1969–1972.

Haynes, P. and Shepherd, T. (2001). Report on the SPARC tropopause workshop. In SPARC Newsletter 17, also available at `http://www.aero.jussieu.fr/~sparc/News17/ReportTropopWorkshopApril2001/%17Haynes_Shepherd.html`.

Haynes, P. H., Marks, C. J., McIntyre, M. E., Shepherd, T. G., and Shine, K. P. (1991). On the "downward control" of extratropical diabatic circulations by eddy-induced mean zonal forces. *J. Atmos. Sci.*, **48**(4), 651–678. Comments and reply in J. Atmos. Sci., 1996, volume 53, pages 2103–2107.

Held, I. M. and Hou, A. Y. (1980). Non-linear axially symmetric circulations in a nearly inviscid atmosphere. *J. Atmos. Sci.*, **37**, 515–533.

Highwood, E. J. and Hoskins, B. J. (1998). The tropical tropopause. *Q. J. R. Meteorol. Soc.*, **124**, 1579–1604.

Holton, J. R. (1972). *An Introduction to Dynamic Meteorology*. Academic Press, Inc.

Holton, J. R. (1990). On the global exchange of mass between the stratosphere and troposphere. *J. Atmos. Sci.*, **47**, 392–395.

Holton, J. R. and Gettelman, A. (2001). Horizontal transport and the dehydration of the stratosphere. *Geophys. Res. Lett.*, **28**(14), 2799–2802.

Holton, J. R., Haynes, P., McIntyre, M. E., Douglass, A. R., Rood, R. B., and Pfister, L. (1995). Stratosphere-Troposphere exchange. *Rev. of Geophys.*, **33**(4), 403–439.

Hood, L. L. (2003). Thermal response of the tropical tropopause region to solar ultraviolet variations. *GRL*, **30**(23), ACL 10–1–10–4.

Hoskins, B. J., McIntyre, M. E., and Robertson, A. W. (1985). On the use and significance of isentropic potential vorticity maps. *Q. J. R. Meteorol. Soc.*, **111**(470), 877–946. Comments and reply in Q. J. R. Meteorol. Soc., 1987, volume 113, pages 401–404.

Hoskins, B. J., Huang-Hsiung, H., James, I. N., Masutani, M., Sardeshmukh, P. D., and White, G. H. (1989). Diagnostics of the global circulation march 1979–february 1989. Technical Report 7, UGAMP, Department of Meteorology, University of Reading.

Iwasaki, T. (1992). General circulation diagnosis in the pressure-isentrope hybrid vertical coordinate. *J. Meteor. Soc. Japan*, **70**, 673–686.

Jackson, D. R., Driscoll, S. J., Highwood, E. J., Harries, J. E., and Russell III, J. M. (1998). Troposphere to stratosphere transport at low latitudes as studied using HALOE observations of water vapour, 1992–1997. *Q. J. R. Meteorol. Soc.*, **124**, 169–192.

James, I. N. (1994). *Introduction to Circulating Atmospheres*. Cambridge Atmospheric and Space Science Series. Cambridge University Press.

Kiehl, J. T. and Solomon, S. (1986). On the radiative balance on the stratosphere. *JAS*, **43**(14), 1525–1534.

Kiladis, G. N. (1998). Observations of Rossby waves linked to convection over the eastern tropical pacific. *J. Atmos. Sci.*, **55**, 321–339.

McIntyre, M. E. (2000). On global-scale atmospheric circulations. In G. K. Batchelor, H. K. Moffat, and M. G. Worster, editors, *Developments in Fluid Mechanics: A Collection for the Millennium*, chapter 11. Cambridge University Press.

Meehl, G. A. (1997). The south Asian monsoon and the tropospheric biennial oscillation. *J. Climate*, **10**, 1921–1943.

Mlynczak, M. G., Mertens, C. J., Garcia, R. R., and Portmann, R. W. (1999). A detailed evolution of the stratospheric heat budget 2. global radiation balance and diabatic circulations. *JGR*, **104**(D6), 6039–6066.

Mote, P. W., Rosenlof, K. H., McIntyre, M. E., Carr, E. S., Gille, J. C., Holton, J. R., Kinnersley, J. S., Pumphrey, H. C., Russel, J. M., and Waters, J. W. (1996). An atmospheric tape recorder: the imprint of tropical tropopause temperatures on stratospheric water vapour. *J. Geophys. Res.*, **101**(2), 3989–4006.

Newell, R. E. and Gould-Stewart, S. (1981). A stratospheric fountain? *J. Atmos. Sci.*, **38**, 2789–2796.

Newman, P. A. and Rosenfield, J. E. (1997). Stratospheric thermal damping times. *GRL*, **24**(4), 433–436.

Norton, W. A. (2003). *Encyclopedia of Atmospheric Sciences*, chapter Middle Atmosphere: Transport Circulation. Academic Press, Inc.

Olaguer, E. P., Yang, H., and Tung, K. K. (1992). A reexamination of the radiative balance of the stratosphere. *J. Atmos. Sci.*, **49**, 1242–1263.

Peltier, W. R. and Clark, T. L. (1979). The evolution and stability of finite amplitude mountain waves. Part II: surface wave drag and severe downslope windstorms. *J. Atmos. Sci.*, **36**, 1489–1529.

Plumb, R. A. (2002). Stratospheric transport. *J. Meteor. Soc. Japan*, **80**(4B), 793–809.

Plumb, R. A. and Eluskiewicz, J. (1999). The Brewer–Dobson circulation: dynamics of the tropical upwelling. *J. Atmos. Sci.*, **56**, 868–890.

Pope, V. D., Gallani, M. L., Rowntree, P. R., and Stratton, R. A. (2000). The impact of new physical parametrisations in the Hadley Centre climate model: HadAM3. *Climate Dynamics*, **16**, 123–146.

Pope, V. D., Jackson, D. R., Pamment, J. A., and Slingo, A. (2001). The representation of water vapour and its dependence on vertical resolution in the Hadley Centre climate model. *J. Climate*, **14**, 3065–3085.

Ramanathan, K. R. (1958). Monsoons and the general circulation of the atmosphere. In S. Basu, K. R. Ramanathan, P. R. Pisharoty, and U. Bose, editors, *Symposium on Monsoons of the World*, pages 53–64. India Meteorological Department.

Ramanathan, V., Pitcher, E. J., Malone, R. C., and Blackmon, M. L. (1983). The response of a spectral general circulation model to refinements in radiative processes. *JAS*, **40**, 605–630.

Randel, W. J., Garcia, R. R., and We, F. (2002). Time-dependent upwelling in the tropical lower stratosphere estimated from the zonal-mean momentum budget. *J. Atmos. Sci.*, **59**, 2141–2152.

Reed, R. J. and Vlcek, C. L. (1969). The annual temperature variation in the lower tropical stratosphere. *J. Atmos. Sci.*, **26**, 163–167.

Reid, G. C. and Gage, K. S. (1981). On the annual variation in height of the tropical tropopause. *J. Atmos. Sci.*, **38**, 1928–1938.

Reid, G. C. and Gage, K. S. (1985). Interannual variations in the height of the tropical tropopause. *J. Geophys. Res.*, **90**(D3), 5629–5635.

Reid, G. C. and Gage, K. S. (1996). The tropical tropopause over the western pacific: wave driving, convection and the annual cycle. *J. Geophys. Res.*, **101**(D16), 21233–21241.

Rosenlof, K. H. (1995). Seasonal cycle of the residual mean meridional circulation in the stratosphere. *J. Geophys. Res.*, **100**(D3), 5173–5191.

Rosenlof, K. H. and Holton, J. R. (1993). Estimates of the stratospheric residual circulation using the downward control principle. *J. Geophys. Res.*, **98**, 10465–10479.

Russell, P. B., Pfister, L., and Selkirk, H. B. (1993). The tropical experiment of the Stratosphere-Troposphere Exchange Project (STEP): Science objectives, operations, and summary findings. *J. Geophys. Res.*, **98**, 8563–8589.

Salby, M. L. (1996). *Fundamentals of Atmospheric Physics*, volume 61 of *International Geophysics Series*. Academic Press, Inc.

Selkirk, H. B. (1993). The tropopause cold trap in the Australian monsoon during STEP/AMEX 1987. *J. Geophys. Res.*, **98**, 8591–8610.

Shepherd, T. G. (2000). The middle atmosphere. *J. Atmos. Sol-Terr. Phy.*, **62**, 1587–1601.

Shepherd, T. G. (2002). Issues in stratosphere-troposphere coupling. *J. Meteor. Soc. Japan*, **80**(4B), 769–792.

Sherwood, S. C. and Dessler, A. E. (2001). A model for transport across the tropical tropopause. *J. Atmos. Sci.*, **58**, 765–779.

Simmons, A. J., Untch, A., Jakob, C., Kållberg, P., and Undén, P. (1999). Stratospheric water vapour and tropical tropopause temperatures in ECMWF analyses and multi-year simulations. *Q. J. R. Meteorol. Soc.*, **125**, 353–386.

Slingo, J. M., Guilyardi, E., Hodges, K., Hoskins, B. J., Inness, P. M., Lawrence, D. M. ., Neale, R. B., Osborne, T. M., Spencer, H., and Yang, G.-Y. (2003). How good is the hadley centre climate model? research at cgam on identifying and understanding model systematic errors: 1999—2002. Technical report, CGAM/NCAS. This is not a refereed paper.

SPARC Report 3 (2002). Intercomparison of middle atmosphere climatologies. SPARC Report No. 3, WRCP Report No. 116, WMO/TD No. 1142.

Staley, D. O. (1962). On the mechanism of mass and radioactivity transport from stratosphere to troposphere. *J. Atmos. Sci.*, **19**, 450–467.

Thuburn, J. and Craig, G. C. (1997). GCM tests of theories for the height of the tropopause. *J. Atmos. Sci.*, **54**, 869–882.

Thuburn, J. and Craig, G. C. (2000). Stratospheric influence on tropopause height: The radiative constraint. *J. Atmos. Sci.*, **57**, 17–28.

Thuburn, J. and Craig, G. C. (2002). On the temperature structure of the tropical substratosphere. *J. Geophys. Res.*, **107**(D1D2), ACL 10–1–10–2.

Waliser, D. E. and Gautier, C. (1993). A satellite-derived climatology of the ITCZ. *J. Climate*, **6**, 2162–2174.

Webster, P. J., Magaña, V. O., Palmer, T. N., Shukla, J., Tomas, R. A., Yanai, M., and Yasunari, T. (1998). Monsoons: Processes, predictability, and the prospects for prediction. *J. Geophys. Res.*, **103**(C7), 14451–14510.

Webster, S. (2002). Personal Communication.

White, A. A. and Bromley, R. A. (1995). Dynamically consistent, quasi-hydrostatic equations for global models with a complete representation of the Coriolis force. *Q. J. R. Meteorol. Soc.*, **121**, 399–418.

Yulaeva, E., Holton, J. R., and Wallace, J. M. (1994). On the cause of the annual cycle in tropical lower stratospheric temperatures. *J. Atmos. Sci.*, **51**(2), 169–174.

Zahn, R. (2003). Monsoon linkages. *Nature*, **421**, 324–325.

Zhang, C. (1993). Large-scale variability of atmospheric deep convection in relation to sea surface temperature in the tropics. *J. Climate*, **6**, 1898–1913.